

*ÉCOLE DOCTORALE de Physique et Chimie-Physique (ED182)*

Institut de Physique et Chimie des Matériaux de Strasbourg  
(UMR 7504 CNRS – Unistra)

# THÈSE

présentée par :

**Mathias DOLCI**

soutenue le : **15 février 2018**

pour obtenir le grade de : **Docteur de l'université de Strasbourg**

Discipline/ Spécialité : Chimie-Physique des Matériaux

**Design of magnetic iron oxide nanoparticle  
assemblies supported onto gold thin films  
for SPR biosensor applications**

**THÈSE dirigée par :**

**M. PICHON Benoît**

Maitre de conférences, université de Strasbourg

**RAPPORTEURS :**

**Mme GOGLIO Graziella**

Professeur, université de Bordeaux

**Mme SZUNERITS Sabine**

Professeur, université de Lille

---

**AUTRES MEMBRES DU JURY :**

**M. CLOAREC Jean-Pierre**

Professeur, Ecole Centrale de Lyon

**M. SCHAAF Pierre**

Professeur, Université de Strasbourg



A Nina  
pour notre complicité éternelle



# Remerciements

Je profite de ces quelques lignes qui me permettent une liberté personnelle totale pour énoncer quelque chose que personne n'oublie mais qui est trop souvent tût : une thèse ne se fait pas seul ! Ainsi j'aimerais remercier toutes les personnes qui ont œuvrés pour ce travail de façon directe ou indirecte. Sans vous, la suite de ce manuscrit n'aurait pas pu aboutir, j'espère que vous prendrez conscience, en lisant ces quelques lignes, de l'importance de votre contribution.

Je remercie Stephan Haacke et Pierre Rabu pour m'avoir accueilli respectivement au sein de l'IPCMS et du DCMI.

Evidemment mon travail de thèse n'aurait pu être mené à bien sans l'aide précieuse de mon « papa de thèse ». Ces remerciements te sont adressés Benoît. Merci à toi, nous avons parcouru tout ce chemin ensemble, trois ans c'est long et pourtant j'ai l'impression que tout s'est passé très vite. Merci pour cette formation, puisqu'au final c'est de cela qu'il s'agit et en effet j'ai appris énormément avec toi autant d'un point de vue scientifique avec ta rigueur qui te tient à cœur de ne pas avancer trop vite sans qu'on soit sûr à 101% de ce qu'on fait mais aussi de ton énergie à vouloir faire plein de nouvelles choses (peut-être même trop de choses), autant d'un point de vue personnel avec tes paroles de sage-philosophe et tes blagues (un peu moins sages). Dans tous les cas merci, grâce à toi j'ai passé une excellente thèse et je te remercie de tout cœur. J'espère que l'avenir nous réservera de belles surprises.

Bien sûr, s'il y a un « papa » à cette thèse, il y a aussi une « maman », une mère protectrice qui protège ses petits doctorants et n'hésite pas une seconde à s'impliquer s'ils ont le moindre souci. Sylvie, merci pour ton chaleureux accueil dans l'équipe. Nous avons travaillé « de loin » pour cette thèse, mais je savais que tu étais là, juste derrière moi et que je pouvais m'appuyer sur toi si besoin. A toi aussi je te souhaite le meilleur, et à très bientôt je l'espère.

Pour compléter la famille il faut nécessairement que je remercie les membres de l'équipe avec qui j'ai travaillé. Merci à Damien, le « grand frère » (ou le petit ?), merci pour les discussions de stabilité colloïdale, de fonctionnalisation de nanoparticules et de Pokémons. Merci également pour le TEM et le temps que tu y as passé (merci Lina de ne pas avoir mis le feu au microscope). J'aimerais évidemment remercier mes plus que collègues de chimie 5 avec qui j'ai passé le plus grand de mon temps. Merci à toi Céline, depuis le début on en a vécu des aventures... grâce à toi je sais me servir de l'infrarouge, trier les solvants et tirer des flèches sur des cochons. Merci aux autres membres du labo, Geoffrey, Francis (mon frère), Paula, Kevin, je vous souhaite une bonne continuation pour la suite.

Merci à Cédric, excellent microscopiste et mauvais partenaire de course (ou l'inverse, je ne me souviens plus), je pense que tu garderas un bon souvenir de moi, en tout cas tu garderas un souvenir...

Merci aux autres membres du départements avec qui j'ai eu des vives et moins vives discussions, Guillaume, Emilie (tatie), Didier, Silviu, Nathalie, Geneviève, Pierre, Christophe, Anne, François, Marc et Guido. Merci à vous de m'avoir fait passer un bon séjour au DCMI que je n'oublierais pas de sitôt.

Merci également à Sophie et Gilles. Le troisième étage était bien plus rigolo avec vous, merci de m'avoir aidé lorsque j'en avais besoin, merci pour les galettes, petits pains, chasse aux œufs et tout le reste qui a contribué à la bonne ambiance du troisième.

Je remercie Bobby, Bobby et Bobby, sans vous cette aventure aurait été bien différente. Grâce à vous, j'ai l'impression d'avoir passé trois ans de franche rigolade et je regrette déjà les discussions au détour d'un couloir du troisième. Merci Bobby pour m'avoir accompagné entre midi et deux pour rejoindre notre charmante forêt et revenir au boulot en mode « serpillère », je te souhaite plein de réussite et j'espère qu'on pourra se revoir incessamment sous peu. Merci Bobby pour toutes les discussions qu'on ait pu avoir sur des sujets allant de l'eurodance des années 2000 à la politique communiste du bloc soviétique. Merci également pour ces fameuses soirées crêpes qui ont fortement contribué à augmenter mon cholestérol et me faire douter d'un éventuel déclenchement d'un diabète de type II dans mon organisme. Enfin merci Bob, on en a vécu des choses toi et moi, entre complicité extrême et rivalité scientifique permettant d'avancer ensemble dans une ambiance détonante. Je ne pense pas retrouver une ambiance au labo comme celle que nous avons eu, écouter France Gall et Daniel Balavoine le volume à fond tout en chantant pendant mes manip me manquera j'imagine... Je ne te dis pas au revoir, mais à bientôt, car nous devons encore faire une collab' ensemble.

Je tenais à remercier également toutes les personnes extérieures à l'équipe qui m'ont apporté leur aide pour la réalisation de ce travail de thèse.

Merci à mes collègues « parisien » sans qui je n'aurais pas pu développer toute la partie "SPR" de ma thèse. Merci Greg, pour toute l'aide et les explications qui vont avec sur la résonance plasmon ainsi que pour ton enthousiasme et ta bonne humeur. Le jeune padawan est devenu grand maintenant, j'espère un jour devenir maître ! Merci J-F, pour ton accueil et la patience que tu as eu de m'aider à faire les mesures pendant la finalisation de ton manuscrit. J'espère que le stress occasionné ne laissera aucune rancœur à mon égard. Merci Julien pour les très intéressantes discussions et les explications détaillées que j'ai pu avoir sur la SPR. A tous les trois, merci et bonne continuation, j'espère que nos chemins scientifiques (et personnels) se recroiseront.

Je tiens à remercier vivement Fouzia et Déborah qui m'ont permis de poursuivre mes études SPR sur place à Strasbourg. Un bon quart de ma thèse a pu être fait grâce à l'accès au banc SPR de l'ICS, c'est dire à quel point ce fut important. Merci Fouzia pour cette fructueuse collaboration. Déborah un immense merci pour m'avoir « sauvé la vie » face à cet appareil SPR, je pense que sans tes interventions j'aurais abandonné mon dernier chapitre.

Je tenais également à remercier Philippe et Anne pour leur aide et la belle collaboration qui a pu commencer, même si j'ai l'impression que je quitte l'aventure alors qu'elle n'est encore qu'un bourgeon. J'espère qu'elle donnera de jolies fleurs et vous souhaite à tous les deux une bonne continuation.

Un grand merci à Spiros et Vaso. Vous avez été très gentils avec moi, à prendre le temps de me montrer comment fonctionnait l'XPS, de m'aider à interpréter les données, de me passer des échantillons, même si la file d'attente s'étalait sur des mois.

Merci à toi Simon pour les mesures PM-IRRAS, ta gentillesse et ta bonne humeur étant toujours au rendez-vous c'était toujours avec grand plaisir (et un peu de nostalgie) que je me rendais à Mulhouse.

Je remercie Xavier et Didier, bien évidemment pour l'aide informatique et l'ATG, mais aussi pour les « délicieuses » discussions du bureau qui agrémentaient mes journées.

J'aimerais faire une mention spéciale pour le bureau 2006 qui a vu passer pas mal de monde depuis mon arrivée en tant que petit nouveau et à présent je suis l'ancien qui laisse sa place aux nouveaux. Merci à Julien, Mathilde, Xiaojie, Mathilde, Zo, Elodie, Florian et Kübra pour avoir parsemé le bureau d'une ambiance « chaleureuse », pleine d'assiduité, de thé et de belles chansons. Matoutou,

on n'en a passé des bons moments ensemble, la sueur des joueurs de foot devenait de l'eau bénite, je te souhaite une bonne continuation là où le vent te portera (et voudra de toi). Mathilde, je ne pense pas trouver un autre bureau que nos éructations puissent embaumer comme le bureau 2006, bonne continuation à toi aussi. Elodie, je te souhaite plein de réussite, toi aussi tu es une « grande » maintenant, tu n'as plus besoin de t'appuyer sur les gens, laisse les gens s'appuyer sur toi.

Merci aux gens qui m'ont aidé le long de la route, parfois juste de passage, mais qui m'ont aidé bien plus qu'ils ne le pensent. Merci à maman Yu qui a su diriger d'une main de fer chimie 5 lorsqu'on était encore que des « bébés », Aurélie ma première partenaire de course qui m'a sauvé la vie plus d'une fois. Merci Cristina, sans toi je n'aurais jamais su comment jurer ni même connaître le générique de DBZ en espagnol. Merci aux personnes du DMO qui m'ont aidé malgré mes (fortes) lacunes en chimie, merci à Catalina, Mathilde, Audrey et Emilie. Malgré le fait que je détestais faire de la chimie, c'était toujours avec plaisir que je venais vous demander de l'aide, merci d'avoir été gentilles et patientes avec moi. Merci à Zo, on s'est rencontrés quand j'étais en stage, après tu es revenu, on a même partagé un bureau. J'aimerais te remercier pour les échanges qu'on a eu, ce fut très agréable (pas tout le temps, mais la majorité du temps), je te souhaite une bonne continuation. Merci à Andra, pour moi tu reste la première roumaine à qui j'ai parlé et regarde, aujourd'hui je parle presque roumain ! Je te souhaite le meilleur, prends soin de toi. Merci à tous les autres doctorants qui ont parsemé ma thèse de bons moments, merci à Stas, Ivan, Julien, Beata, Jérôme, Ouda, Lydia, Juliane, Melania, Etienne, Michal, Guillaume, Florian et Ufuk.

Je remercie mes amis de master Ziyad, Kassio et Kübra. Grâce à vous j'ai pu passer une merveilleuse expérience humaine et je ne saurais jamais assez vous remercier. Kübra, nous t'attendons avec impatience, dépêche-toi de devenir docteur ! Je voulais te remercier pour les pauses thé, les discussions personnelles (t'étais un peu mon psy), et toutes les belles choses que tu as faites pour moi. Ziyad je ne sais même pas ce que je peux te souhaiter, car je sais que tu vas réussir ce que tu entreprendras, merci pour m'avoir fait réfléchir, questionner à chaque paroles (check). Kassio merci à toi également, je te souhaite plein de bonne choses, ta gentillesse est au-delà de tout ce que j'imaginai avant de te rencontrer, prends soin de toi.

Je remercie enfin les stagiaires que j'ai pu encadrer et qui m'ont aidé dans cette aventure. Merci à Emelyne, Solène, Eduard, Tom, Romain, Sorina, Kévin, Yu-ting et Pierre qui prend la relève. Mention spéciale à Mégane (Musch Musch), merci à toi, je te félicite d'avoir réussi à allier rigueur scientifique et franche rigolade...on s'est bien marré. Je te souhaite plein de réussite. Merci également à tous les stagiaires qu'ils soient d'ici ou d'ailleurs pour le temps passer à apprendre et jouer au tarot. Merci à l'équipe de Roumanie : Petronela, Mihail, Antonia, Roxana, Andra, Laura, Adelina et Valentina. Je remercie pêle-mêle Pedro, Maria, Connor, Maëlle, Clémence, Frédérique, Camille, Salma, Debora, Camille, Wenja et tous ceux que j'ai oublié. Je remercie également l'équipe brésilienne Antonia, Camilla, Isis, Pedro et Hermano pour leur accueil chaleureux qui me donne fortement envie de retourner à Brasilia.

Je n'oublie bien sûr pas les foteux, merci à vous les gars pour les moments de détente (toujours) dans la bonne ambiance. Merci à Christophe, Rémi, Micka, Gad, Sylvain, Laure, Anna, Marvin, Michel, Vincent, Tom, Maria, et bien sûr tous ceux que j'ai oublié en cours de route.

Pour finir j'aimerais remercier les personnes totalement extérieures à ce travail de thèse, mais qui pourtant était là quand j'en avais besoin et qui m'ont apporté le soutien moral qui m'a permis d'arriver au bout. Merci à mes parents, Nina ma sœur et Valentina ma compagne pour m'avoir soutenu jusqu'au bout même dans les moments les plus durs.

A vous tous, merci.



I. CHAPITRE I - State of Art .....	5
A. Fe <sub>3</sub> O <sub>4</sub> Nanoparticles .....	6
1. Iron oxide properties in bulk .....	6
a) Crystalline structure .....	6
b) Magnetic properties .....	7
c) Electronic properties .....	8
d) Optical properties.....	8
2. Iron oxide nanoparticles synthesis.....	10
a) Main synthesis method .....	10
b) Thermal decomposition synthesis.....	10
c) Composition as function of the size of the nanoparticle .....	12
B. Nanoparticles assembly.....	13
1. Nanoparticle assembly methods.....	13
a) Assembly through substrate functionalization .....	14
(1) Self-assembled monolayer of organic molecules.....	14
(2) Mixed self-assembled monolayer .....	15
b) Nanoparticle assembly through chelating interactions .....	16
c) Nanoparticle assembly through covalent binding.....	17
d) Nanoparticle assembly through multiple hydrogen binds .....	18
2. Magnetic and optical properties of nanoparticles.....	20
a) Magnetic properties of nanoparticles.....	20
(1) Magnetic properties of a single nanoparticle .....	20
(2) Magnetization dynamics .....	22
(3) Surface effect.....	23
b) Magnetic properties of nanoparticle assembly.....	24
(1) Dipolar interactions .....	24
(2) Influence of the inter-particle distance.....	24
C. Bio-sensors .....	26
1. Generalities of biosensors.....	26
2. Surface plasmons .....	26
a) Historical context.....	26
b) Theory.....	27
c) Excitation condition of surface plasmons with Kretschmann configuration .....	28

d)	Influence of parameters on plasmons excitation.....	30
(1)	Choice of the material .....	30
(2)	Metal permittivity.....	31
(3)	Temperature and metal thickness.....	32
(4)	Refractive index at the surface.....	33
(5)	Penetration depth .....	33
3.	Plasmonic biosensors .....	35
a)	Generalities on plasmonics biosensors .....	35
b)	Localized surface plasmon resonance sensors (LSPR).....	36
(1)	Colorimetric assays.....	38
(2)	Surface nanostructured architecture .....	38
c)	Propagative surface plasmon resonance (SPR) .....	39
4.	Plasmonics biosensors optimization .....	40
a)	Intrinsic properties .....	40
b)	Surface functionalization.....	43
5.	Iron oxide nanoparticles based biosensors .....	44
D.	Bibliography.....	47
II.	CHAPITRE II - Structuration of Iron Oxide Nanoparticle Assemblies.....	55
A.	Nanoparticle synthesis .....	56
1.	Experimental details.....	56
a)	Nanoparticles synthesis conditions .....	56
b)	Purification of the nanoparticles .....	58
2.	Structural characterizations .....	61
a)	Size and morphology of the nanoparticles.....	61
b)	Colloidal stability of nanoparticle suspension.....	62
c)	Structural characterization of the nanoparticles .....	63
3.	Magnetic characterizations .....	64
a)	Magnetic measurements as function of the applied field .....	64
b)	Magnetic measurements as function of the temperature.....	66
4.	Conclusion .....	68
B.	Nanoparticle and substrate functionalization.....	69
1.	Nanoparticle functionalization .....	69
a)	Experimental section .....	69
b)	Characterization after functionalization .....	70

2.	Substrate functionalization .....	72
a)	Synthesis of 11-mercapto-undecyn.....	73
b)	Self-assembled monolayer formation.....	74
c)	Characterization of self-assembled monolayers .....	75
3.	Conclusion .....	76
C.	Nanoparticle assembly prepared by “click” chemistry .....	78
1.	Assembly of 10 nm nanoparticles .....	78
a)	Assembly protocol.....	78
b)	Scanning electron microscopy characterization.....	79
2.	Study of the kinetics of the assembly.....	80
3.	Variation of assembly parameters .....	82
a)	Nanoparticle sizes.....	82
b)	Concentration of the nanoparticle suspensions .....	85
c)	Stability of the assembling solution in time .....	87
4.	Conclusions.....	89
D.	Characterization of the nanoparticle assemblies.....	90
1.	Composition and structural characterizations .....	90
a)	Atomic force microscopy.....	90
b)	Water contact angle .....	90
c)	Polarized Modulated Infrared Reflection Absorption Spectroscopy .....	91
d)	X-Ray Photoelectron Spectroscopy .....	92
2.	Magnetics characterization .....	93
a)	Cycles of magnetization as function of external field .....	93
b)	Magnetic measurements as function of the temperature.....	97
3.	Conclusion .....	99
E.	General conclusion .....	100
F.	Bibliography.....	101
III.	CHAPITRE III –Nanoparticle self-assembly by multiple hydrogen binding between nucleosides 103	
A.	Nanoparticle assembly through nucleosides .....	104
1.	Substrate post-functionalization .....	104
a)	Experimental procedure.....	105
b)	Characterization .....	106
(1)	Water contact angle .....	106

(2)	X-Ray photoelectron spectroscopy .....	107
(3)	Phase Modulated Infrared reflection absorption spectroscopy .....	107
2.	Nanoparticle post-functionalization.....	108
a)	Control of the quantity of azide groups at the surface .....	108
(1)	FT-IR spectroscopy measurements .....	109
(2)	DLS measurements.....	110
b)	Post-functionalization with thymine groups .....	111
c)	Characterization of the NP@Thym.....	111
(1)	TEM analysis .....	111
(2)	FT-IR measurements.....	112
(3)	DLS measurements.....	113
3.	Molecular recognition through nucleosides .....	115
a)	Experimental protocol.....	115
b)	Influence of experimental parameters.....	116
(1)	Assembly time .....	116
(2)	Influence of the quantity of functional groups at the nanoparticle and SAM surfaces 117	
(a)	On the SAM surface.....	117
(b)	On the nanoparticle surface.....	118
(3)	Solvent influence .....	119
c)	Influence of the temperature.....	122
d)	Influence of the rinsing step.....	122
B.	Conclusion .....	123
C.	Bibliography.....	124
CHAPITRE IV - Biomolecules Recognition mediated by iron oxide nanoparticle assemblies supported onto gold thin films .....		
D.	Biotin-Streptavidine .....	128
1.	Design of the bio-platform .....	128
a)	Grafting of an alkyne derivative of biotin onto nanoparticle assembly.....	128
b)	Characterizations.....	129
(1)	Microscopy characterizations.....	129
(2)	Water Contact Angle .....	130
(3)	X-Ray Photoelectron Spectroscopy .....	131
(4)	Phase Modulation Infrared Reflection Absorption Spectroscopy measurements..	132

c)	Monitoring of the bio-platform build-up by surface plasmon resonance measurements	134
d)	Performing SPR measurements to determine nanoparticle density .....	136
2.	Detection of streptavidin .....	139
a)	Influence of nanoparticle assembly on the detection.....	139
(1)	Detection of streptavidin by performing angular interrogation .....	140
(2)	Detection of streptavidin by performing spectral interrogation .....	141
b)	Understanding the role of nanoparticle assembly on the detection .....	142
(a)	Decay length .....	143
(b)	Sensitivity factor .....	143
(c)	Available surface area .....	146
3.	Detection platform optimization.....	150
a)	Influence of the spatial distribution of biotin groups at the nanoparticle surface .....	150
(1)	Preliminary study: influence of the accessibility of the biotin groups on a gold surface	151
(a)	SEM analysis .....	152
(b)	PM-IRRAS measurements.....	152
(c)	SPR measurements.....	154
(2)	Variation of the size of the nanoparticles .....	155
4.	Kinetics measurements .....	159
(1)	Kinetic measurement and determination of the limit of detection of the Streptavidin	160
(2)	Determination of the association constant by the coefficient rate method .....	162
(3)	Determination of the association constant by the Langmuir binding isotherm .....	164
5.	Biofouling.....	165
6.	Conclusion .....	167
E.	Iminosugar – Glycosidase .....	168
1.	Context and motivation.....	168
2.	Substrate post functionalization by iminosugar.....	168
a)	Experimental protocol.....	168
b)	Characterizations.....	169
(1)	Scanning electron microscopy.....	169
(2)	Water contact angle .....	170
(3)	XPS.....	170
(4)	PM-IRRAS.....	171

(5)	Construction of the film followed by Surface Plasmon Resonance Measurements	172
3.	SPR measurements for the glycosidase	173
a)	$\alpha$ -Mannosidase solution preparation	173
b)	SPR measurements	174
c)	Kinetics measurements	176
(1)	Sensorgrams	176
(2)	Determination of the rate constant affinity of the iminosugar and $\alpha$ -mannosidase couple	177
d)	Competitive association	179
e)	Regeneration of the surface	181
4.	Biofouling	183
a)	Control experiment: $\alpha$ -mannosidase on NPs@N <sub>3</sub> surface	183
b)	Control experiment: BSA on iminosugar surface	184
5.	Conclusion	185
F.	General conclusion	186
H.	Bibliography	187

# Introduction

Iron oxide nanoparticle assemblies represent a high interest in the development of nano-devices for application in spintronics such as high data storage, magneto-resistive devices and sensors. Iron oxide is a very well known, low-cost and abundant material which presents advantageous magnetic and optical properties. The main interest in nanoparticles comes from their properties resulting from their high surface/volume ratio in comparison to the bulk state.

Therefore, the design and synthesis of iron oxide nanoparticles became a hot-topic owing to their intrinsic properties which directly dependent of their shape, size and composition. During the last decades, synthesis techniques considerably evolved and the current challenges are today to control the formation of more complex structures such as new morphologies or core/shell composition. In this context, the thermal decomposition technique opened wide perspectives towards the fine design of nanoparticles by adapting carefully the operating conditions.

Although nanoparticles can be easily studied as powders, the preparation of highly ordered assemblies onto surfaces is a promising way to investigate their individual versus collective properties. Therefore, a main challenge is to develop new and efficient strategies to finely control the spatial arrangement of such nano-building blocks. Therefore, in the frame of the bottom-up approach, highly stable colloidal suspensions are required.

The control of the assembly of nanoparticles can be easily performed through specific interactions between functional groups localized at both nanoparticle and substrate surfaces. In this context, the “click” chemistry approach is very efficient and easy to process. The “click” chemistry allows controlling the assembly through robust and covalent binding. Another interesting way is multiple hydrogen bonds which are also highly specific to control the assembly of nanoparticles.

Then, the control of the spatial arrangement allows studying the physical properties of the nanoparticles such as the optical or magnetic properties. Moreover, the properties of the substrate which supports the nanoparticles can also be controlled. Indeed, plasmonic materials such as gold thin films present surface plasmon resonance which can be tuned as function of the structuration of nanoparticle assembly. These plasmonic properties allow performing biosensing to detect different species in solution. Therefore, the nanoparticle assemblies supported onto plasmonic substrates are very appealing for biosensing.

This manuscript will be divided in 4 sections:

- The first chapter presents the state of art related to the synthesis and assembly of iron oxide nanoparticles and their structural, magnetic and optical properties. Two assembling methods will be presented: the covalent linkage of the nanoparticles to the surface by the CuAAC “click” chemistry and the reversible boundary through multiple hydrogen bonds between nanoparticles and substrates. Moreover, it focuses on the way surface plasmon resonance present a particular interest for biosensing applications.
- The second chapter is dedicated to the elaboration of iron oxide nanoparticles by thermal decomposition and their assembly onto a gold substrate thanks to the CuAAC “click” chemistry reaction. The structural properties of the nanoparticles and their assemblies were studied. The collective magnetic properties were studied as function of the size and the spatial arrangement of the nanoparticles.

- The third chapter focuses on the assembly of nanoparticles via multiple hydrogen bonds. We took advantage on the “click” reaction to graft complementary nucleosides groups on the surface of the nanoparticles and the substrates. The mechanism of the assembly is then studied as function of different assembling parameters such as solvent, temperature and quantity of functional groups.
  
- Finally, the fourth chapter is dedicated to the design of a new and versatile approach to produce SPR biosensors. We took advantage of the nanoparticle assemblies presented in chapter 2 as an original detection platform which can be functionalized by specific bioreceptors. We show how iron oxide nanoparticles can be of interest to enhance the sensitivity of a gold thin film. We present the different parameters in order to design the most efficient detection platform. We studied the kinetics of two different biomolecular recognition processes which are among the most popular in biomedicine: the detection of proteins and enzymes.



## I. CHAPITRE I - State of Art

## A. Fe<sub>3</sub>O<sub>4</sub> Nanoparticles

### 1. Iron oxide properties in bulk

#### a) Crystalline structure

Magnetite (Fe<sub>3</sub>O<sub>4</sub>) exhibits a spinel structure AB<sub>2</sub>X<sub>4</sub> where A and B represent the cations and X the anions.<sup>[1]</sup> It crystallizes in a cubic system (Fd<sub>3</sub>m space group) with a lattice parameter of 0.8394 nm. The oxygen atoms form a face centered cubic (FCC) arrangement with octahedral (Oh) and tetrahedral (Td) sites where the cations can be inserted (figure I-1). A unit cell is composed of 32 oxygen atoms which define 64 Td sites which one eighth are occupied (A site) and 32 Oh sites which half are occupied (B site). Magnetite is a mixed oxide constituted of Fe<sup>2+</sup> and Fe<sup>3+</sup> in an reverse spinel (Fe<sup>3+</sup>)<sub>Td</sub>(Fe<sup>3+</sup>Fe<sup>2+</sup>)<sub>Oh</sub>(O<sup>2-</sup>)<sub>4</sub> where the tetrahedral sites are occupied by Fe<sup>3+</sup> and octahedral sites occupied by Fe<sup>3+</sup> and Fe<sup>2+</sup>.

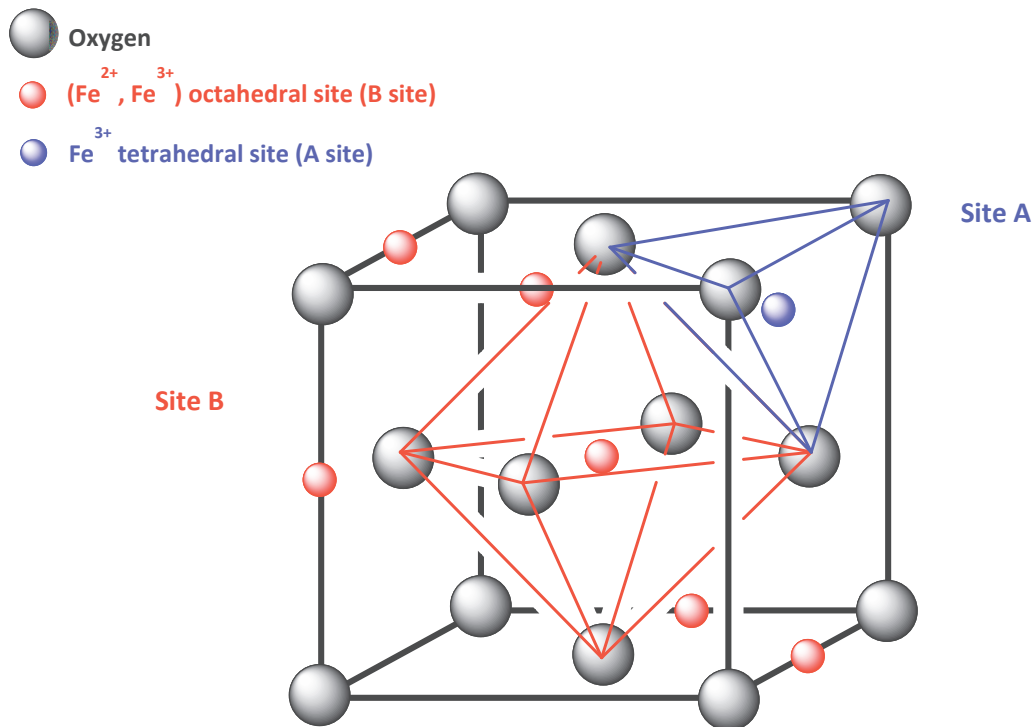


Figure I-1. Schematic representation of the magnetite structure

Maghemite (γ-Fe<sub>2</sub>O<sub>3</sub>) is the oxidized form of the magnetite and in this case the iron cations are all trivalent Fe<sup>3+</sup> which induce vacancies in the structure noted □. The resulting structure of maghemite is (Fe<sup>3+</sup>)<sub>Td</sub>[(Fe<sup>3+</sup>)<sub>5/3</sub>□<sub>1/3</sub>]<sub>Oh</sub>(O<sup>2-</sup>)<sub>4</sub>. The structures of magnetite and maghemite are very similar and it requires different characterization techniques to differentiate them. X-Ray diffraction (XRD) measurements combined to pattern refinement allow determining the lattice parameter which is slightly different between magnetite (8.396 ± 0.001 Å, JCPDS file n°00-019-0629) and maghemite (8.338 ± 0.001 Å, JCPDS file n°00-013-0458).

b) *Magnetic properties*

Magnetic properties in a material are defined by the magnetic moments carried by each atom. Therefore, the magnetization of a material for a given volume is equal to the sum of all magnetic moments which constitute the material. Applying a magnetic field to the material allows aligning these magnetic moments along the field. Therefore, the susceptibility of the material corresponds to the ratio of its magnetization  $M$  versus the applied field  $H$ :

$$\chi = \frac{M}{H} \quad \text{Equation I.1}$$

Two classes of material can be distinguished as function of their behavior when an external magnetic field is applied.

The first class corresponds to weak interactions between the atoms. Therefore, the material does not present a spontaneous magnetization. This non-cooperative magnetism is composed of:

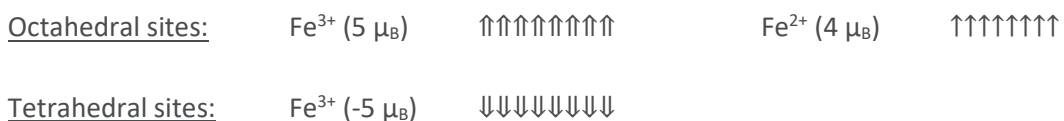
- Diamagnetism, where the atoms do not present magnetic moments without external field and in presence of magnetic field will create weak dipoles with moments in opposition of the field. The susceptibility is therefore negative and low.
- Paramagnetism, where the magnetic moments are randomly oriented without magnetic field. The presence of an external magnetic field will align the moments in the direction of the field. The susceptibility of these materials is therefore positive but low.

The second class presents exchange interactions between their magnetic moments. In this case of cooperative magnetism, a spontaneous order appears without external magnetic field:

- Ferromagnetism (FM), where the magnetic moments are parallel between them and present a long range order without magnetic field, e.g. permanent magnetization.
- Anti-ferromagnetism (AFM), where the magnetic moments have an anti-parallel configuration and compensate, e.g. no macroscopic magnetization.
- Ferrimagnetism (FiM), where magnetic moments have an anti-parallel configuration but do not totally compensate, e.g. lower permanent magnetization than FM.

This magnetic order exists below a temperature which is called the Curie temperature ( $T_C$ ) for ferromagnetic and ferrimagnetic materials or Néel temperature ( $T_N$ ) for anti-ferromagnetic materials. Above this temperature, the spontaneous order disappears and the material becomes paramagnetic.

Magnetite is a ferrimagnetic material. The  $\text{Fe}^{3+}$  ions have a moment of  $5 \mu_B$  and the  $\text{Fe}^{2+}$  have a moment of  $4 \mu_B$ . Magnetic order in reverse spinel is driven by the exchange interactions between A and B sites. Magnetic moments of  $\text{Fe}^{3+}$  ions in  $O_h$  and  $T_d$  sites are aligned but their antiparallel configuration result in their compensation. Therefore, the net magnetization of  $4 \mu_B$  only accounts from the  $\text{Fe}^{2+}$  in  $O_h$  sites.



According to cell multiplicity, the magnetic moment per unit cell is  $32 \mu_B$ .<sup>[2]</sup> In bulk state, the saturation magnetization for magnetite is 92 emu/g. In the case of maghemite, one  $Fe^{3+}$  is located in octahedral sites and 5/3 in tetrahedral sites which lead to a theoretical magnetization of  $10/3 \mu_B$ .<sup>[3]</sup> This corresponds to a lower saturation magnetization of 74 emu/g.

### c) *Electronic properties*

Magnetite is considered as a half-metal and has a high conductivity at 300 K for an oxide ( $200\text{-}300 \Omega^{-1}\cdot\text{cm}^{-1}$ ) which is attributed to electron hopping between  $Fe^{2+}$  and  $Fe^{3+}$ . However, magnetite has many conductive regimes as function of the temperature which does not follow any law. At room temperature, the magnetite has a band gap around 0.1 eV.<sup>[4, 5]</sup> The maghemite, instead has the behavior of a semi-conductor with a 2.03 eV band gap.<sup>[6]</sup>

### d) *Optical properties*

The optical properties of iron oxide are directly dependent on its refractive index. The refractive index  $n$  of a material corresponds to the ratio of light celerity in vacuum  $c$  compared to the phase velocity of the light  $v$  in the material:

$$n = \frac{c}{v} \quad \text{Equation I.2}$$

Maxwell's equations predict that celerity  $c$  of an electromagnetic wave (such as light) which propagates through vacuum is related to the dielectric permittivity  $\epsilon_0$  and the magnetic permeability  $\mu_0$  as:

$$c = \frac{1}{\sqrt{\epsilon_0 \mu_0}} \quad \text{Equation I.3}$$

Therefore in a material with a dielectric permittivity  $\epsilon$  and magnetic permeability  $\mu$ , the phase velocity of light is:

$$v = \frac{1}{\sqrt{\epsilon \mu}} \quad \text{Equation I.4}$$

Given the equation I.2, the refractive index of a material is defined as:

$$n = \sqrt{\epsilon_r \mu_r} \quad \text{Equation I.5}$$

with  $\epsilon_r = \frac{\epsilon}{\epsilon_0}$  the relative permittivity and  $\mu_r = \frac{\mu}{\mu_0}$  the relative permeability of the material. The magnetic permeability is directly linked with the magnetic susceptibility of the material by:

$$\mu_r = 1 + \chi \quad \text{Equation I.6}$$

In the case of diamagnetic or paramagnetic materials, the susceptibility is very low ( $< 10^{-5}$ ) which reduces the permeability to 1. For magnetite, at room temperature, the susceptibility still remains very ( $\chi \approx 10^{-3}$ ).<sup>[7-10]</sup> The approximation of  $\mu_r = 1$  can be done and the refractive index will only be dependent of the relative permittivity of the material:

$$n = \sqrt{\epsilon_r}$$

Equation I.7

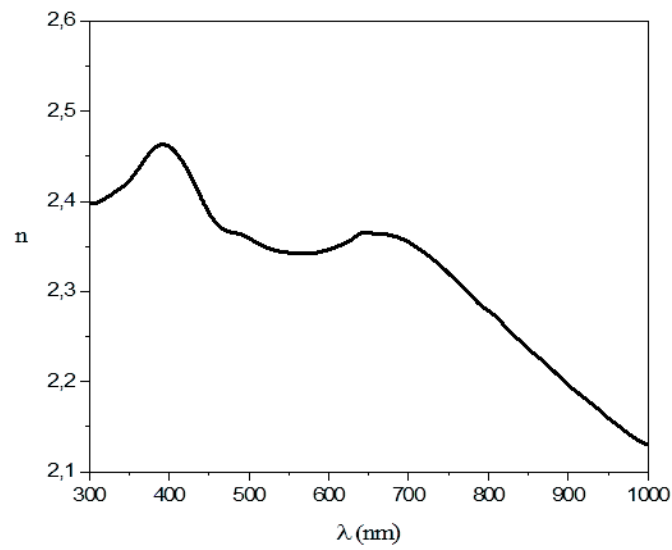


Figure I-2. Evolution of the refractive index as function of the incident wavelength in magnetite. From Query et al.<sup>[11]</sup>

The refractive index is energy dependent and the relation of  $n$  and the wavelength of the illuminating light have been given by Query in 1985 (Figure I-2).<sup>[11]</sup> In our study, we will consider the domain of visible light, in the range 400-800 nm. The refractive index of iron oxide oscillates between 2.46 and 2.28.

## 2. Iron oxide nanoparticles synthesis

The development of new chemical synthesis strategies recently allowed unprecedented control on size, shape, composition and structure of nanoparticles.<sup>[12-15]</sup> Furthermore, highly stable suspensions of nanoparticles can be prepared which is important for anyone who wants to consider isolated nanoparticles. Therefore, unprecedented control of physical properties of nanoparticles, especially new and unexpected physical properties can be achieved.

### a) *Main synthesis method*

Many techniques have been developed to synthesize iron oxide nanoparticles which present different advantages and drawbacks.<sup>[16-19]</sup> The main purpose of these methods is to improve the control of the size and the shape of the nanoparticles such as micro-emulsion synthesis<sup>[20]</sup>, hydrothermal synthesis<sup>[21]</sup> and polyol synthesis<sup>[22]</sup>.

The co-precipitation synthesis remains the most used method since it is the easiest to perform; the solvent used is usually water and conduct to high yields. Nanoparticles are formed with the addition of a base in acid aqueous solution of iron salts  $\text{Fe}^{2+}$  and  $\text{Fe}^{3+}$ . High quantities of nanoparticles in water with size range from 2 nm to 50 nm can be synthesized. However, the narrow size distribution is difficult to control and the nanoparticles tend to aggregate which is not suitable for further control of the arrangement of the nanoparticles.

### b) *Thermal decomposition synthesis*

The thermal decomposition allows preparing nanoparticles with a high control on the size and morphology and a good stability in suspension. Therefore, this synthesis method has been chosen for our work.

The thermal decomposition has been initially developed for the synthesis of quantum-dots and semi-conductor nanocrystals with a high control on the size and the morphology.<sup>[23, 24]</sup> Later, this method has been used to form metal oxide nanoparticles. It consists in the decomposition of a metal precursor in a high boiling temperature organic solvent in presence of stabilizing agent. This method promotes the formation of well crystallized nanoparticles functionalized with organic molecules thus providing high colloidal stability in organic solvent.<sup>[18, 25]</sup>

The synthesis process is driven by the nucleation and growth mechanisms. LaMer theory describes that the nanoparticles formation consists in three phases (figure I-3).<sup>[26]</sup> Phase 1 corresponds to pre-nucleation step, where the metallic precursor decomposes in monomers which are the base units of the iron oxide nanocrystals. After the increase of the monomer concentration above supersaturation level ( $C_s$ ), a rapid self-nucleation happens after reaching a maximal concentration ( $C_{max}$ ) (phase 2). When the monomer concentration goes down below a critical concentration ( $C_{min}$ ), the self-nucleation stops and the monomers contributes to nanoparticle growth (phase 3).

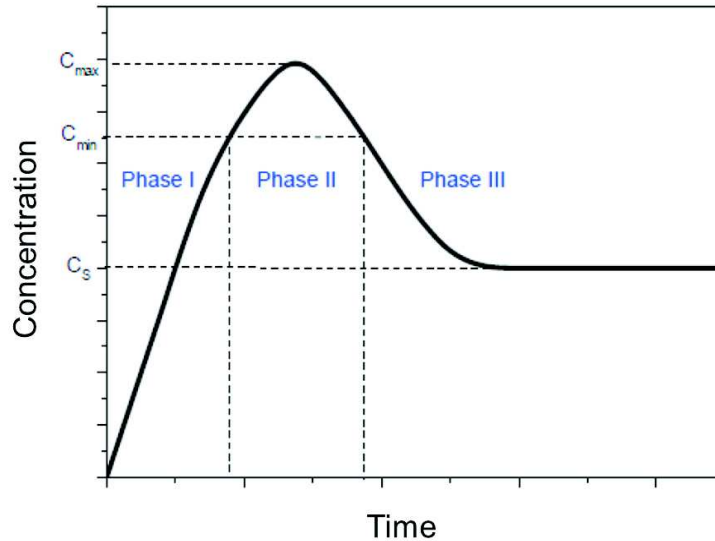


Figure I-3. Precursor concentration as function of the reaction time. From LaMer V. K et al.<sup>[26]</sup>

This method presents the advantage to separate the self-nucleation and growth steps. The fine control of experimental parameters, especially the temperature rate, results in a narrow size distribution of the nanoparticles. Moreover, the size and the morphology can be tuned by varying the synthesis parameters such as the solvent, the temperature ramp, the reaction time, the precursor concentration and the nature of ligand (figure I-4).<sup>[27, 28]</sup> During the synthesis the nanoparticles are covered with a stabilizer, the oleic acid which acknowledges the good stability of nanoparticle suspension in a variety of organic solvents and allows easily performing ligand exchange for further processes.

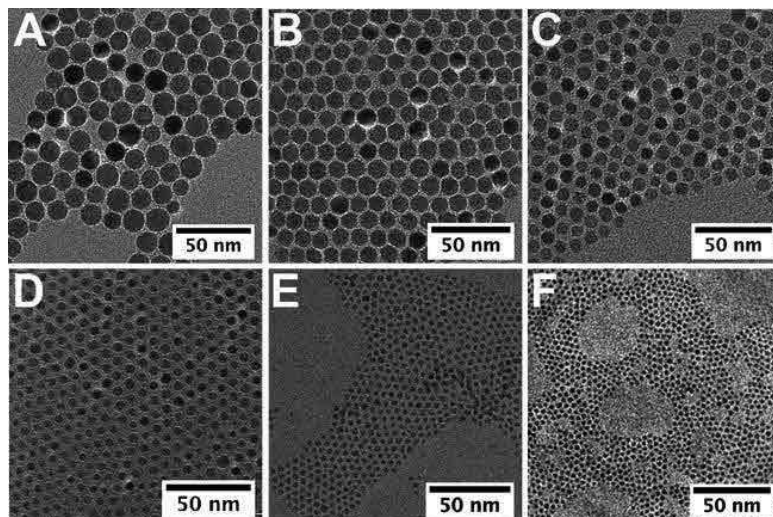


Figure I-4. TEM images of iron oxide nanoparticles synthesized with different solvents. The sizes of the nanoparticles are ranging from 2.5 nm to 14 nm. From Demortière et al.<sup>[28]</sup>

The investigation on the commercial precursor low purity which altered significantly reproducibility led our team to develop an in-house precursor.<sup>[29]</sup> This synthesis method allowed developing the nanoparticle design to form complex architectures such as nanoparticles with different compositions or Fe<sub>3</sub>O<sub>4</sub>@CoO core/shell structures.<sup>[30]</sup>

### c) Composition as function of the size of the nanoparticle

As seen previously, the surface of magnetite is partially oxidized in maghemite. Therefore, nanoparticles display an oxidized layer at their surface which consists in a thickness of few nanometers.<sup>[27]</sup> Therefore, the proportion of maghemite is more important for small nanoparticles with a larger surface/volume ratio.<sup>[31]</sup> It becomes obvious that  $\gamma$ -Fe<sub>2</sub>O<sub>3</sub> is the dominant phase in small iron oxide nanoparticles, whereas the proportion of the Fe<sub>3</sub>O<sub>4</sub> gradually increases with the particle size (figure I-5.a).

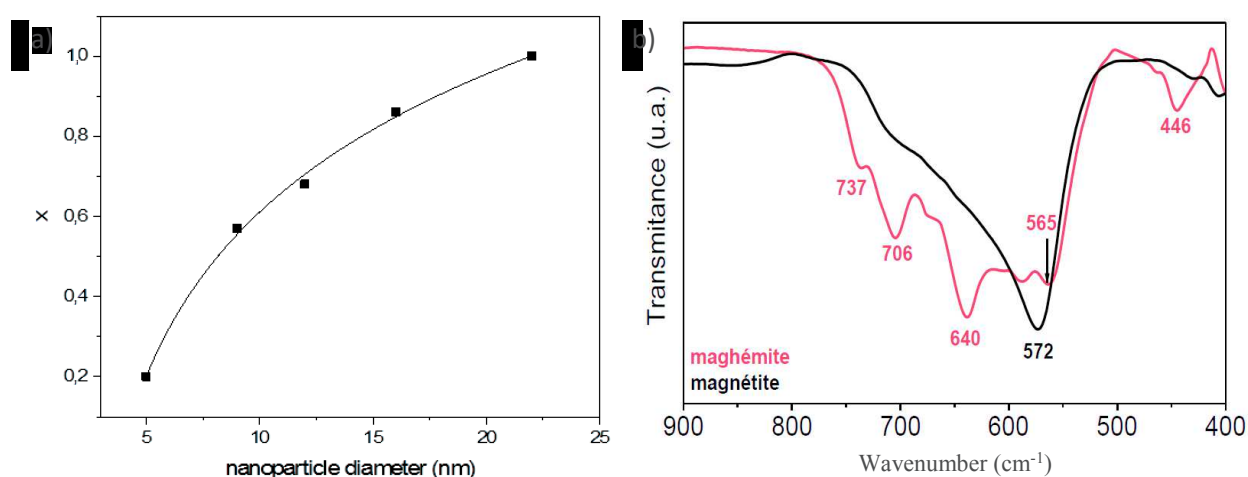


Figure I-5. a) Magnetite proportion as function of the nanoparticle size in  $(\gamma\text{-Fe}_2\text{O}_4)_{1-x}@\text{(Fe}_3\text{O}_4)$  and b) Infrared spectra of magnetite (black curve) and maghemite (red curve) in the Fe-O region. Extracted from a) data of Park et al.<sup>[31]</sup> and b) Baaziz et al.<sup>[27]</sup>

Moreover, infrared spectroscopy showed that magnetite and maghemite present different signatures. The magnetite spectrum shows a unique band at 570-580 cm<sup>-1</sup> whereas the maghemite exhibits many bands localized in the area 400-800 cm<sup>-1</sup> (figure I-5.b).<sup>[32]</sup>

The characterizations by infrared spectroscopy and X-ray diffraction allow identifying the presence of the maghemite phase in the nanoparticles. However, it is not sufficient to determine precisely the stoichiometry of maghemite in the structure. The Mossbauer spectroscopy is an accurate technique to determine the oxidation state of iron atoms.<sup>[33]</sup>

The synthesis of iron oxide nanoparticles in the Fe<sub>3</sub>O<sub>4</sub> phase implies necessarily a layer of  $\gamma$ -Fe<sub>2</sub>O<sub>3</sub>. This partial oxidation is not predominant in the case of large nanoparticles (> 10 nm). However, this composition may impact the intrinsic properties of the nanoparticles.

## B. Nanoparticles assembly

The physical properties of nanoparticles are also dependent of their close environment. Therefore, interactions with neighbor are of particular interest. The control of the spatial arrangement of nanoparticles (control of the inter-particle distance and the dimensionality of assembly) represents great challenges. Many assembly techniques can be used to graft nanoparticles onto surfaces. The structuration of these assemblies and the linkage with the surface will be dependent of the method used.

### 1. Nanoparticle assembly methods

The assembly of nanoparticles onto a surface can be controlled through specific interactions between functional groups. Three approaches can be considered (figure I-6):

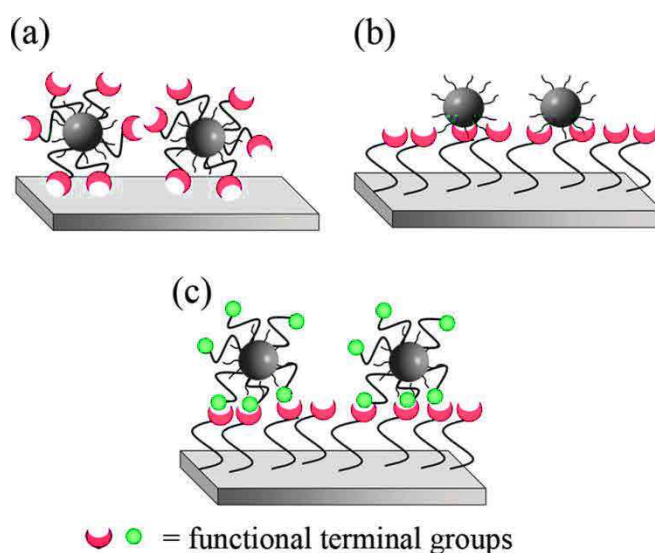


Figure I-6. Schematic representation of the assembly strategies: a) functionalization of the nanoparticles, b) functionalization of the surface and c) functionalization of both nanoparticles and substrate. From Bellido et al.<sup>[34]</sup>

- The first approach consists in the assembly of functionalized nanoparticles where the functional groups directly interact with the substrate surface. Many techniques have been used to assemble nanoparticles onto substrates such as drop casting<sup>[34]</sup>, dipping<sup>[34]</sup>, spin coating, dip coating, Langmuir-Blodgett<sup>[2, 35-37]</sup> and layer-by layer.<sup>[38]</sup> These techniques allow easily assembling nanoparticles in mono or multilayers, but suffer from a lack of the structuration control.
- The second approach consists in the substrate functionalization with molecules carrying functional groups which interact with the nanoparticle surface.
- The third approach is a combination of both methods by a functionalization of nanoparticle and substrate surface. The considerable advantage of this method is the specificity which allows a good control of the assembly structuration.

This last method of assembly will be the most interesting in our case since the high specificity will allow the control of the structuration of the nanoparticle assembly. The main advantages in the

surface functionalization of substrate for nanoparticle grafting are the easiness to process by simple dipping of substrate in nanoparticle suspensions and the high versatility.

Therefore, the molecular patterning onto surface will allow controlling the spatial distribution of the grafted nanoparticles. Thus, it requires the functionalization of substrates by molecules carrying specific functional groups.

### a) *Assembly through substrate functionalization*

#### (1) Self-assembled monolayer of organic molecules

Self-assembled monolayers (SAM) of organic molecules are an easy and versatile method to functionalize and to modulate the surface properties of a substrate.<sup>[39-45]</sup> Adsorbed molecules onto a substrate spontaneously self-organize thanks to the Van der Waals and hydrophobic interactions between the molecules (figure I-7).<sup>[45, 46]</sup>

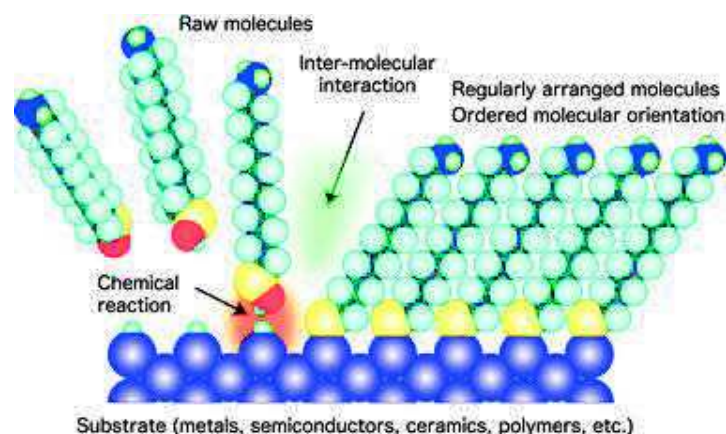


Figure I-7. Schematic representation of the self-assembled monolayer formation. From Sugimura, Kyoto.

The molecules are composed of an anchoring group, a spacer and a terminal functional groups:

- The anchor group depends of the substrate surface. In the case of SiO<sub>2</sub> surface, trialkoxysilanes are mainly used.<sup>[47-49]</sup> For metal oxides, phosphonic acids are preferred.<sup>[49-51]</sup> Thiol groups are the most used in the case of gold surface<sup>[52-54]</sup> among others such as thioacetate, di-sulfurs or di-azonium salts. In our case, gold substrates will be used with thiols molecules because of the strong interaction with gold<sup>[52, 53, 55]</sup> which is described as an intermediate between a covalent and non-covalent binding, about 50 kcal/mol.<sup>[39]</sup>
- The spacer constitutes a physical barrier between the anchoring groups and the terminal head groups and ensures a thickness of the SAM. The size of the spacer is crucial since the anchoring groups is rapidly grafted on the substrate surface and the molecules process in a slow rearrangement in *all-trans* configuration to maximize the interactions between chains.<sup>[46, 56]</sup> Alkyl chains are mostly used to maximize the packing between chains, but other types of chains with phenylene or ethylene glycol can be used.<sup>[57-59]</sup>

- The functional head group represents the essential part of the SAM since it defines the interface and the surface properties. The choice of the functional group will depend of the target interactions.

In our study, the substrate is a gold thin film supported on a silica wafer since this metal is inert and its functionalization is well described. Moreover, this metal presents plasmonic properties from which we will take advantage.

## (2) Mixed self-assembled monolayer

The surface functionalization can be modulated by mixing different molecules (with different terminal functional groups and/or different chain lengths) in the SAM. Here, the objective is to increase the reactivity by spacing the active with inactive head groups. Thus, the SAM structuration will depend of the phase segregation phenomenon leading to enriched domains with one of the thiols and thus influences the spatial repartition of the nanoparticles.<sup>[60]</sup>

Few methods can be performed in order to generate mixed SAM (figure I-8). A first one consists in the immersion in a solution of different thiols. A second consists in the preparation of a SAM with a single thiol and then to perform a partial chemical reaction in order to generate two different terminal groups.<sup>[61]</sup> A third one which consists to prepare a SAM with an asymmetric disulfur which carried two different terminal groups.<sup>[62]</sup>

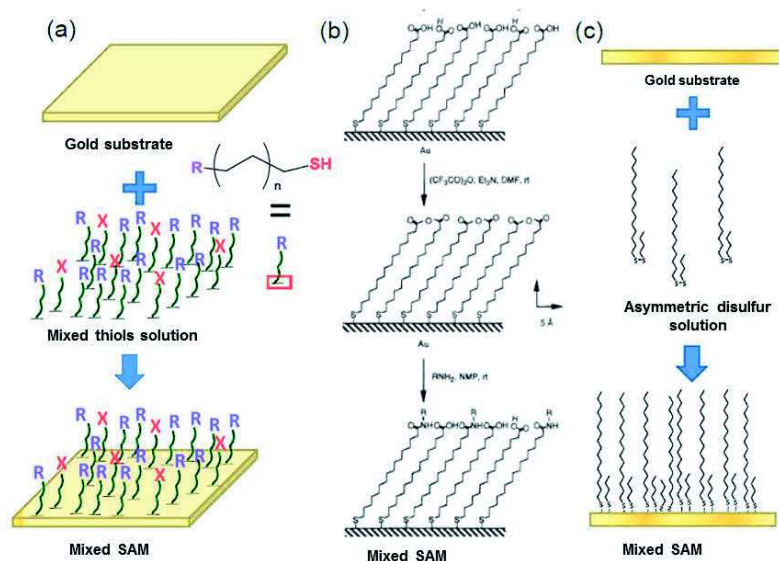


Figure I-8. Mixed SAM formation strategies: a) mixed thiols adsorption, b) anhydride method adapted from Yan et al.<sup>[61]</sup> and c) asymmetric disulfur adsorption

The characterization of mixed SAMs is not easy especially for determining the spatial distribution of the different molecules. Several techniques are used such as the infrared spectroscopy with grating incidence, photo-electron spectroscopy, ellipsometry and water contact angle. Some structural characterizations are also used such as atomic force microscopy or scanning tunneling microscopy.<sup>[60]</sup> Moreover, simulation showed that the spatial repartition of molecules in mixed SAMs<sup>[63]</sup> can lead to segregated structures.

## b) Nanoparticle assembly through chelating interactions

Indirect characterization can give also information on the SAM structure by grafting ferrocenes<sup>[52]</sup> or nanoparticles.<sup>[64]</sup> In our team, iron oxide nanoparticles coated with oleic acid have been assembled onto mixed SAMs of mercaptododecane (MDD) and mercapto-undecanoic acid (MUA) which present alkyl chains with the same length (figure I-9).

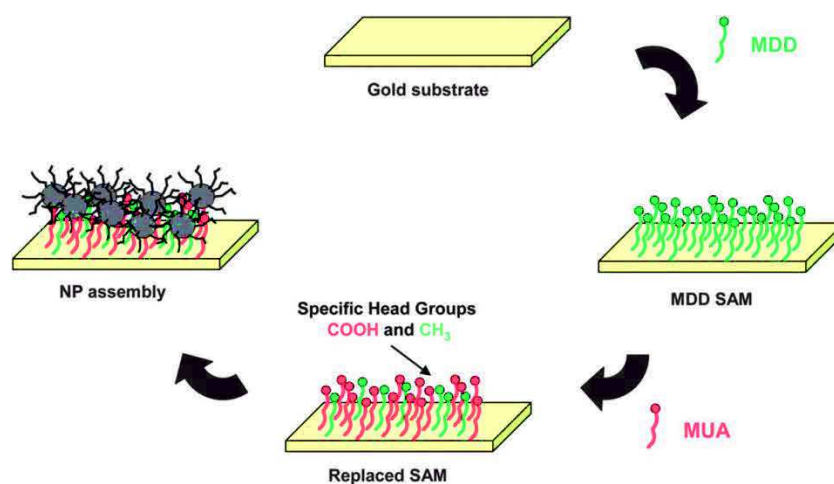


Figure I-9. Mixed SAM preparation by adsorption of mercaptododecane (MDD) and mercapto-undecanoic acid (MUA) following by iron oxide nanoparticle assembly.

The methyl terminal groups  $-CH_3$  is non-chelating for the nanoparticles in contrast to the carboxylic function ( $-COOH$ ) which is chelating for the iron oxide surface of nanoparticles. SAMs were prepared with different ratios of MUA/MDD and were immersed in an oleic acid coated nanoparticle suspension (figure I-10).

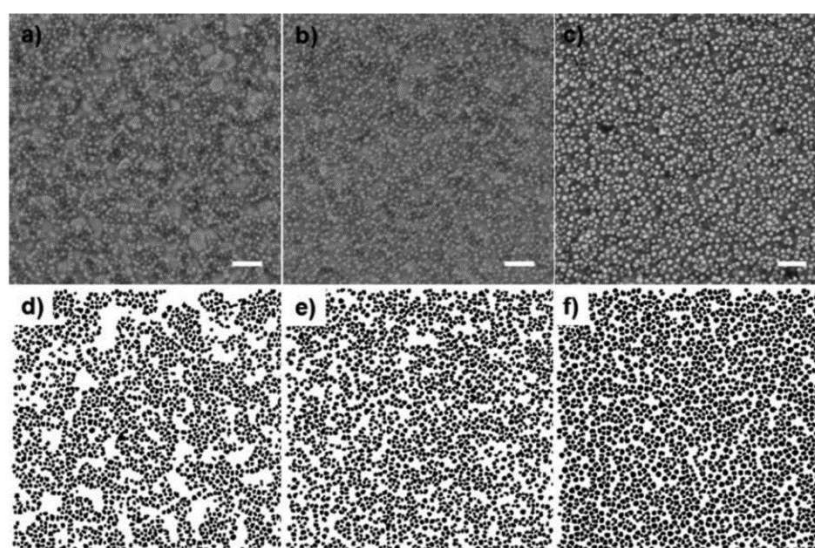


Figure I-10. Nanoparticle assembly onto SAM with ratio of MUA/MDD of a,d) 20%, b,c) 50% and c,f) 80%. a,b,c) scanning electronic microscopy images and d,e,f) binary images. Scale bar: 100 nm

The spatial distribution is different as function of the mixed SAM composition. For low quantity of active groups the presence of nanoparticle domains confirms the phase segregation of the thiols within the SAM. For a larger amount of COOH, the phase segregation disappears and the nanoparticles arrangement becomes more uniform. The weak interaction between the nanoparticles and the surface may lead to their rearrangement through the magnetic dipolar interactions.

### c) Nanoparticle assembly through covalent binding

The “click” chemistry, introduced by Sharpless in 2001<sup>[65]</sup> is an ensemble of reaction between functional groups which satisfied several requirements among which are high reproducibility, robustness and easiness to process. “Click” chemistry is mainly associated to cycloaddition reactions involving heteroatoms, such as hetero-Diels-Alder<sup>[66]</sup> and 1,3-dipolar cycloadditions.<sup>[67]</sup>

One of the most studied click reaction is the Huisgen cycloaddition also named Copper-Catalyzed Azide-Alkyne Cycloaddition (CuAAC) (figure I-11).

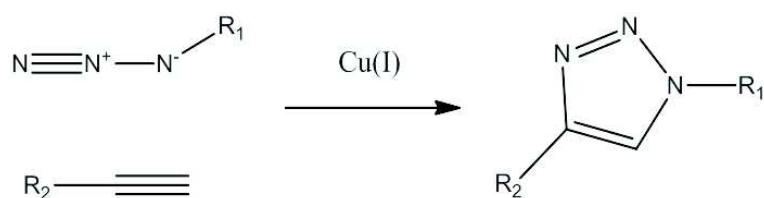


Figure I-11. Schematic representation of the reaction between an alkyne and an azide in presence of a copper (I) catalyst (CuAAC "click" chemistry)

This reaction creates a triazole bridge after reaction of alkyne ( $\text{C} \equiv \text{C}$ ) and azide ( $\text{N}_3$ ) groups. In 2004, the click reaction was used for the immobilization of functional materials on SAMs (figure I-12).<sup>[68-70]</sup>

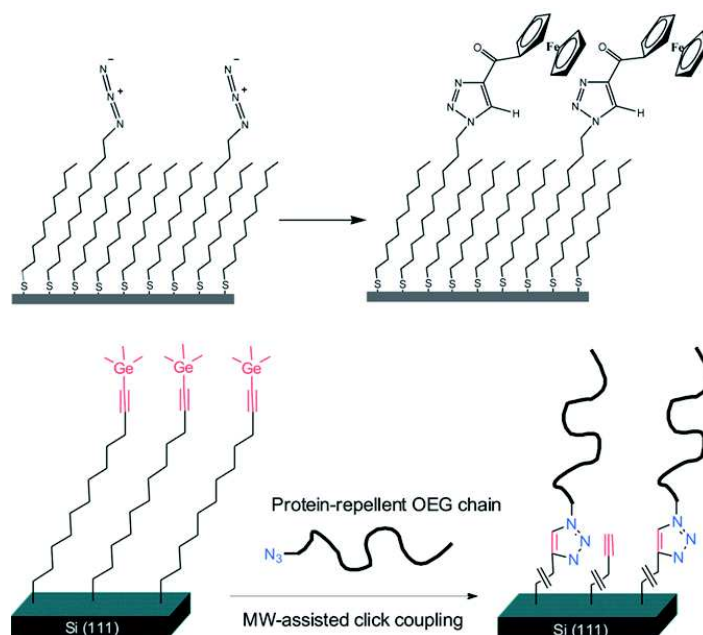


Figure I-12. CuAAC « click » reaction onto SAMs with a) electrochemically active molecules and b) protein-repellent molecules. Adapted from a) Collman et al.<sup>[68]</sup> and b) Li et al.<sup>[70]</sup>

This concept has found a great interest in surface chemistry and more recently in the assembly of nanoparticles.<sup>[71-75]</sup>

One of the great advantages of this assembly method is the covalent bond between the substrate and the nanoparticles. It allows the strong and irreversible grafting of the nanoparticles without possible rearrangement.

Another advantage of this method is to be versatile by functionalizing a variety of substrates and nanoparticles with complementary azide and alkyne groups. Kinge et al. reported first an alkyne-terminated FePt nanoparticle assembly onto an azido-terminated SAM.<sup>[75]</sup> However, previous work in our group showed that the best configuration consist in alkyne terminated gold substrate and azide-terminated nanoparticles.<sup>[76]</sup>

#### d) Nanoparticle assembly through multiple hydrogen binds

Nanoparticles can also be assembled onto surfaces through non covalent binding in order to favor the rearrangement of the nanoparticles at the surface. This method can be done by two different manners (figure I-13):

- The use of interactions where the association constant is high ( $> 10^5 \text{ M}^{-1}$ ) such as host-guest recognition. Many systems have been performed through this recognition,<sup>[77, 78]</sup> and the most used example is the cyclodextrin which constitutes a supramolecular trap for hydrophobic molecules such as adamantane or ferrocene groups.<sup>[79-82]</sup>
- The use of multiple weak interactions within one molecule to take advantage of the multiplicity effects.<sup>[83-85]</sup> Here, the stability is ensured by the high number of bonds between molecules. Examples of multiple hydrogen bonding can be found in literature

such as the interaction between Hamilton receptor and barbituric acid<sup>[78, 86, 87]</sup> and base pairing between complementary nucleosides.<sup>[85, 88, 89]</sup>

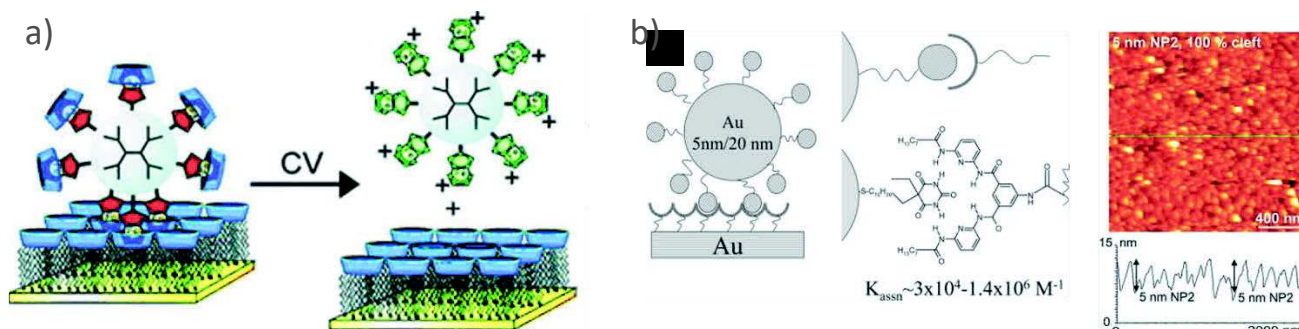


Figure I-13. a) Nanoparticle binding mediated by Hamilton-type receptors and b) cyclopetides assembled through host-guest recognition. Adapted from a) Zirbs et al.<sup>[87]</sup> and b) Nijhuis et al.<sup>[82]</sup>

Moreover, many assembly parameters can influence the recognition between the two elements. The nature of the solvent, the temperature, the number of specific groups can impact the binding energy. Therefore, it can be used as a tool to control the structured nanoparticles assemblies (figure I-14).<sup>[90, 91]</sup>

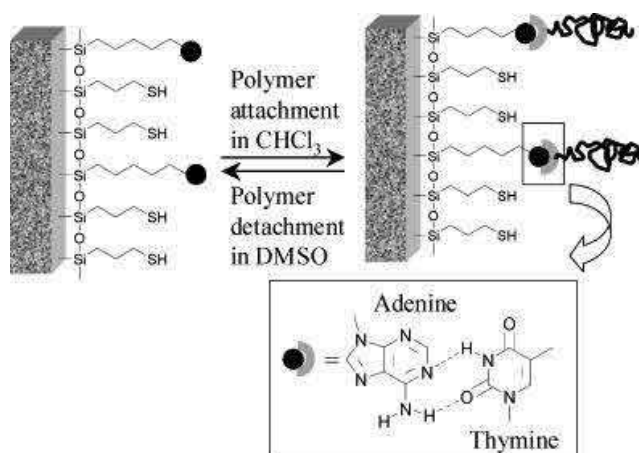


Figure I-14. Schematic representation of proposed molecular recognition between a silicon surface modified with adenine and polymer functionalized with thymine. From Viswanathan et al.<sup>[92]</sup>

Viswanathan et al. showed that the recognition process is promoted when chloroform (aprotic) is used and no recognition happens in DMSO (protic).<sup>[90, 91]</sup> The change of solvent allows the total reversibility of the self-assembly process.

The recognition process at the surface takes advantage of the high number of groups at the surface of a SAM to enhance the formation of hydrogen bonds. To obtain stable binding of nanoparticles onto a surface, the strength of interactions between the nanoparticles and the surface need to be controlled. Therefore, the association constant between molecular receptors located between the nanoparticles and the surface should be sufficiently strong and is often increased by multivalent effects.

In literature, the grafting of nanoparticles through hydrogen bonds is often performed in solution or onto polymeric surfaces. The team of Reinhoudt showed the attachment of silica nanoparticles through the host-guest recognition by using cyclodextrin.<sup>[78, 79, 81]</sup> Gold nanoparticles have been grafted onto substrate through the Hamilton receptor and barbituric acid.<sup>[87, 93]</sup> Moreover, gold nanoparticles were grafted through DNA strands which is also a recognition process involving hydrogen binding.<sup>[94-99]</sup> However, the assembly of iron oxide onto substrate through such weak interactions has been poorly reported.<sup>[100]</sup>

The assembly of nanoparticles through multiple hydrogen bonding requires a specific choice of solvent and a particularly attention at the density of groups on the considered surface. However, the high specificity coupled with low energy interactions allow flexible and dynamic coupling between nanoparticles and substrate and may favor rearrangement by playing with solvent or temperature.<sup>[101]</sup>

## 2. Magnetic and optical properties of nanoparticles

### a) Magnetic properties of nanoparticles

#### (1) Magnetic properties of a single nanoparticle

To understand the magnetic properties of magnetite nanoparticles, we will consider first the bulk state and study the effect of the reduction of the size. In a magnetic material, the total magnetic energy can be described as the sum of different contributions:

$$E = E_{ex} + E_a + E_d + E_Z \quad \text{Equation I.8}$$

The exchange energy ( $E_{ex}$ ) corresponds to the interaction between the spins of metal ions in the crystal structure. This very strong and short range interaction explains the collective behavior of magnetic moments in ferro- and ferrimagnetic materials. The anisotropy energy ( $E_a$ ) conducts to align the magnetic moments in a specific direction of the structure. The dipolar energy ( $E_d$ ) is a long range contribution which comes from the interaction between magnetic moments. The Zeeman energy ( $E_Z$ ) is an interaction between the magnetic moments and an external magnetic field.

To minimize the total energy, the magnetite presents a structure in domain separated by walls called Bloch wall (figure I-15).

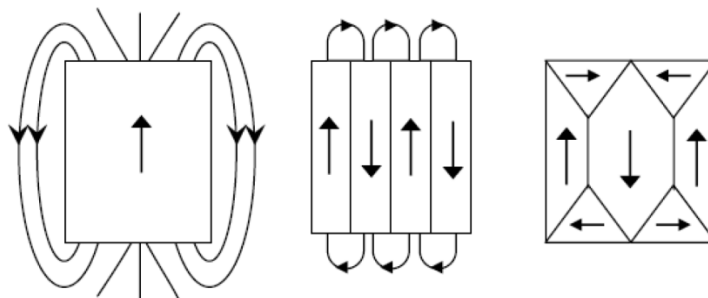


Figure I-15. Schematic representation of the energy diminution to create Bloch walls in a magnetic material

All the magnetic moments are parallel inside the same domain. When an external magnetic field is applied, the moments tend to align in the direction of the field and the Bloch walls are displacing. Therefore, the magnetization of the material can be measured as function of the applied field. A hysteresis cycle is obtained and is characterized by its saturation magnetization  $M_s$ , remanent magnetization  $M_r$  and coercive field  $H_c$  (figure I-16).

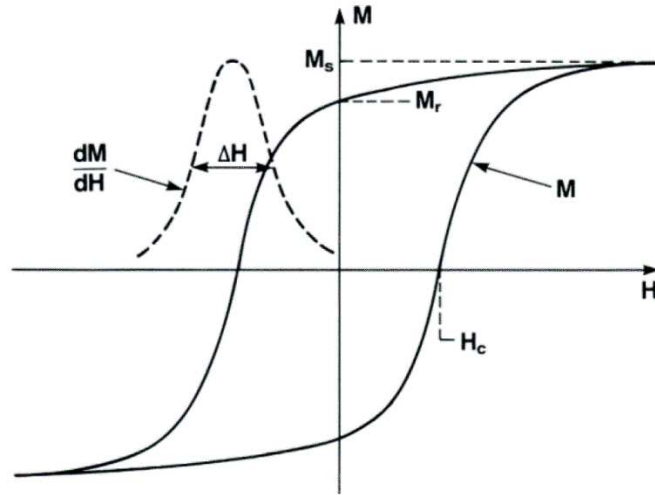


Figure I-16. Hysteresis cycle of the magnetization  $M$  as function of the applied magnetic field  $H$

Nevertheless, creating a Bloch wall requires energy. Below a critical size  $r_c$ , the best configuration becomes a single domain with a magnetization following a specific direction. In this case, the nanoparticle is composed of a unique magnetic domain with a stable magnetization at room temperature: the nanoparticle consists in a single blocked domain. Therefore, we use the macro-spin approximation which assimilates each nanoparticle to a single dipole representing the total magnetization of the nanoparticle.

In this case, the anisotropy energy  $E_a$  tends to align the magnetic moment of a single nanoparticle in a specific direction. This energy is the sum of different contributions (detailed in appendix A). Here, the magnetocrystalline energy will be considered predominant and additional component such as surface, shape and volume contribution can be neglected to explain the magnetization dynamic.

The magnetocrystalline energy  $E_{MC}$  favors the alignment of the magnetic moments in a specific direction of the crystal lattice, the magnetization easy axis. For a single nanoparticle, the magnetocrystalline energy at first order is:

$$E_a = KV \sin^2(\theta) \quad \text{Equation I.9}$$

with  $K$  the anisotropy constant which depends of chemical composition of the material,  $V$  the volume of the nanoparticle and  $\theta$  the angle between the magnetization and the easy axis (figure I-17). Therefore, the magnetization of a nanoparticle presents two minima of energy ( $\theta = 0$  and  $\theta = \pi$ ) separated by an energy barrier  $E_B = KV$  ( $\theta = \pi/2$ ).

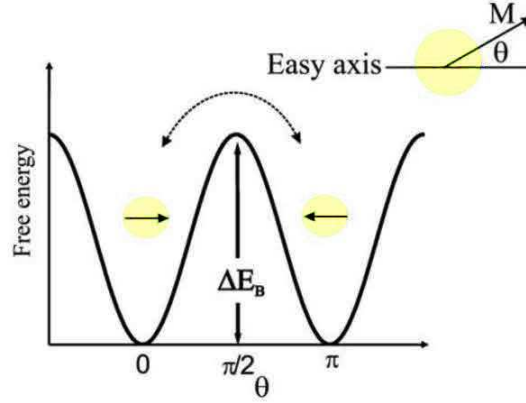


Figure I-17. Schematic representation of the free energy of a nanoparticle as function of the magnetization direction. From Bendanta et al.<sup>[102]</sup>

For  $\text{Fe}_3\text{O}_4$  the magnetization easy axis is parallel to the [111] direction, whereas the  $\gamma\text{-Fe}_2\text{O}_3$  the magnetization easy axis is parallel to the [110] direction. Without external magnetic field, the nanoparticle magnetization will be oriented parallel or anti-parallel to the magnetization easy axis.

## (2) Magnetization dynamics

If the diameter of the nanoparticle still decreases below a certain size, the product  $KV$  becomes lower than the thermal energy. In this case, the magnetization of the nanoparticles rotates from a direction of easy axis to another without external magnetic field. The Neel-Brown law shows that for non-interacting nanoparticles, the switch of direction happens for a characteristic relaxation time  $\tau$ :

$$\tau = \tau_0 e^{\frac{KV}{k_b T}} \quad \text{Equation I.10}$$

with  $\tau_0 \approx 10^{-9}\text{-}10^{-11}$ ,  $k_b$  the Boltzmann constant,  $K$  the anisotropy constant and  $V$  the volume of the nanoparticle. This equation shows that the relaxation time increases when the temperature decreases and the volume of the nanoparticle increases. For a low temperature or a nanoparticle with a size large enough,  $\tau$  becomes longer than the measurement time  $\tau_m$  (depending on the equipment) and the magnetization is blocked.

On the contrary, if the temperature is high enough or the nanoparticle size sufficiently small, the relaxation time will be shorter than the measurement time  $\tau_m$ ; it is the superparamagnetic regime. In this case the magnetic moments of the nanoparticles will oscillate during the measurement and the resultant magnetization will appear to be zero. This behavior is characterized by the disappearance of the coercive field and remanent magnetization.

The temperature when the regime is changing ( $\tau = \tau_m$ ) is called the blocking temperature  $T_b$ :

$$T_B = \frac{KV}{k_b \ln\left(\frac{\tau_m}{\tau_0}\right)} \quad \text{Equation I.11}$$

Usually, the magnetic measurements performed by SQUID (Superconducting Quantum Interference Devices) have  $\tau_m = 100$  s and  $\tau_0 = 10^{-9}$  s, the equation I.11 becomes:

$$KV = 25k_bT_b \quad \text{Equation I.12}$$

Therefore, the blocking temperature is depending of the size of the nanoparticle, the anisotropy and the measuring time. A sample of nanoparticle is never monodisperse and presents a size distribution which conducts to a distribution of blocking temperatures. Moreover, this equation does not take in account the interactions between nanoparticles. We will see later that the dipolar interaction in nanoparticle assembly have an effect on the blocking temperature.

(3) Surface effect

When the size of a nanoparticle decreases, the surface/volume ratio increases strongly, thus surface effects does. The diminution of neighboring atoms at the surface leads to a break of the symmetry and creates disorder of the spins at the surface of the nanoparticle. The direct consequence of this size reduction is that the disordered layer at the surface display a spin glass magnetic behavior where the magnetization of surface atom is different of the one in the volume of the nanoparticle. This effect is called spin canting and is responsible of the reduction of saturation magnetization in nanoparticles. The spin canting is strongly dependent of the size of the nanoparticle but also of the synthesis method and the ligand bound to the surface atoms.<sup>[103, 104]</sup> Safronov and al showed in 2013 the dependence of magnetization as function of the thickness of the canting spin layer:<sup>[8]</sup>

$$M_S = M_{bulk} \left(1 - \frac{2\Delta}{D}\right)^3 \quad \text{Equation I.13}$$

where  $M_{bulk}$  is the saturation magnetization of the bulk (92 emu/g for the magnetite),  $D$  is the diameter of the nanoparticle and  $\Delta$  the thickness of the spin canting layer. By considering a constant canted layer of 2 nm, we can easily calculate the saturation magnetization as function of the nanoparticle size.

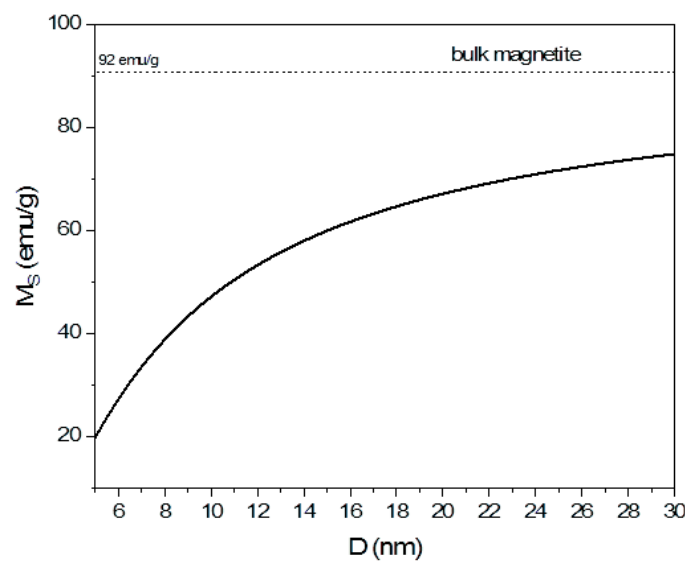


Figure I-18. Saturation magnetization as function of the size by taking in account a canted layer of 1 nm at the nanoparticle surface. Adapted from Safronov et al.<sup>[22]</sup>

The magnetization of the nanoparticle is strongly dependent of their size especially for small nanoparticles. Although, the magnetization tends to stabilize for nanoparticles larger than 20 nm, the saturation magnetization never reaches the magnetization of the bulk due to such surface disorder.

### b) *Magnetic properties of nanoparticle assembly*

We have shown that the magnetic properties are dependent of the size of the nanoparticles; however they are also dependent of the interactions between the nanoparticles. Nanoparticles can interact with their neighbors through dipolar interactions, exchange interactions or super-exchange at the interface. In our case, the nanoparticles are coated with an organic layer and the dominant interactions are the dipolar interactions.

#### (1) Dipolar interactions

The dipolar interaction between two nanoparticles is long range and anisotropic. It depends of the magnetization of each nanoparticle and of the inter-particle distance. In the case of the macro-spin approximation,<sup>[2]</sup> each nanoparticle is assimilated to a unique dipole carrying the total magnetization. In a random distribution of nanoparticles (powder state), the dipolar energy between two nanoparticles is:<sup>[2, 37, 105]</sup>

$$E_d = \frac{\mu_0 \mu^2}{4\pi a^3} \quad \text{Equation I.14}$$

with  $\mu$ , magnetization carried by a nanoparticle and  $a$  the distance between two nanoparticle centers. In the case of 2D triangular array of nanoparticles:

$$E_d = 2.8 \frac{\mu^2}{a^3} \quad \text{Equation I.15}$$

Nevertheless, in the case of a monolayer of nanoparticles with a random orientation, the dipolar energy cannot be simplified and has to be studied experimentally.

#### (2) Influence of the inter-particle distance

The influence of the inter-particle distance on the dipolar interactions can be investigated by studying the variation of the blocking temperature.

Frankamp et al.<sup>[106]</sup> and Fleutot et al.<sup>[105]</sup> studied the influence of the blocking temperature by functionalizing iron oxide nanoparticles with ligand with different sizes. The blocking temperature increased with the decrease of the inter-particle distance which resulted in stronger dipolar interactions (figure I-19.a).

Moreover, Poddar et al.<sup>[107]</sup> studied the blocking temperature as function of the dimensionality of nanoparticle assembly (figure I-19.b) prepared by the Langmuir-Blodgett technique and by dispersing nanoparticles into a polymer matrix.

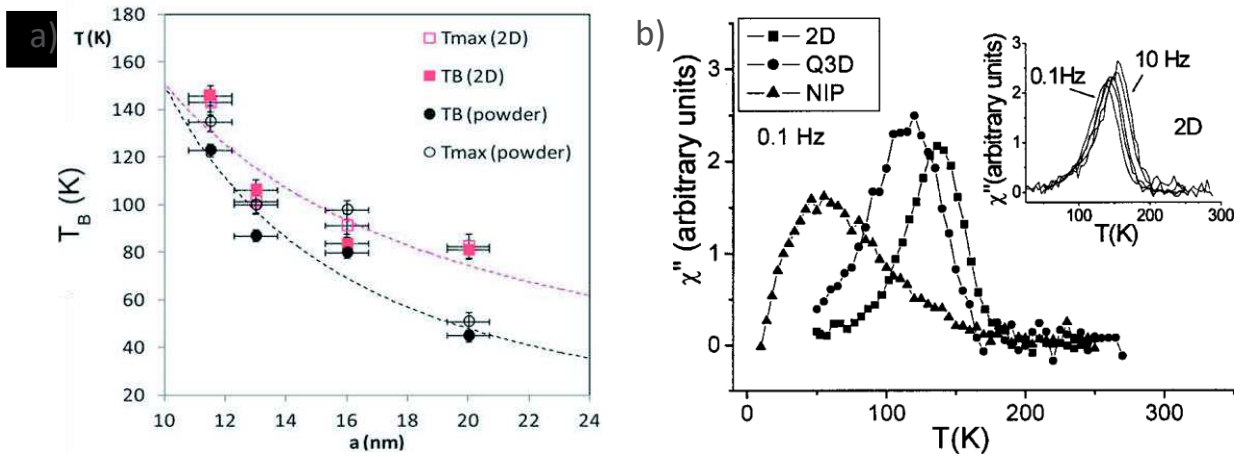


Figure I-19. Evolution of  $T_B$  as function of inter-particle distance  $a$  and b) Imaginary component of the susceptibility as function of the temperature of non-interacting nanoparticle (NIP), monolayer (2D) and multilayers (Q3D) nanoparticles. From a) Fleutot et al.<sup>[105]</sup> and b) Poddar et al.<sup>[107]</sup>

$T_B$  markedly increased from dispersed nanoparticles to a monolayer. Moreover, the monolayer also has a higher blocking temperature than the multilayer. The higher anisotropy in a 2D assembly due to all the magnetic moments aligned in the plane of the substrate requires a high energy to reverse the magnetization. However, the multilayer presents a component out of the plane and therefore a weaker energy barrier to pass. Similar studies in the team showed similar collective properties of nanoparticle assemblies.<sup>[2, 76]</sup>

The influence of the dipolar interactions on the hysteresis cycle is not trivial and the observations reported in literature are contradictory. Most of the study (theoretical and experimental) showed that the coercive field  $H_C$  is decreasing when the dipolar interactions is increasing<sup>[2, 106, 108, 109]</sup> and the ratio of the remanent magnetization on the saturation magnetization  $M_R/M_S$  increase.<sup>[107, 108, 110, 111]</sup> However, these values are also dependent of the anisotropy energy and therefore are dependent of the size of the nanoparticles.<sup>[37, 112]</sup>

## C. Bio-sensors

### 1. Generalities of biosensors

The aim of a biosensor is to detect species such as ions, molecules or proteins. Nowadays the detection of different molecules became really important for food safety, environmental, medical and security purpose.<sup>[113, 114]</sup> Moreover knowing the concentration especially for diagnosis applications is critical. The use of fluidic system where the analyte can be in contact with the recognition element allow the creation of portative and easy to use devices which give raise to the current interest of biosensing. Biosensors are composed of a biological recognition element integrated with a transducing element. Therefore, an analyte will give a biological response which is converted in an optic or electric signal thanks to the transducer. Such monitoring coupled with the versatility of the recognition methods allow detecting variety of analytes which tells about the growing interest for biosensing.

Biosensors can be classified as function of the element to detect or of the type of signal which is measured. Therefore, we can have among other, amperometric, voltametric or optic detection.<sup>[113]</sup> In each case, a crucial factor for the detection is the recognition of the receptor with the target element. We will focus on biosensors with optic transducers which use materials carrying plasmonic properties. The main advantages of such plasmonics sensors are the use of label-free detection protocols which allow detecting biomolecules in their natural forms, in-situ and in real time. The sensitivity and the limit of detection allow small quantities of analyte to detect. These sensors usually use the propagative or localized surface plasmon resonance of plasmonic materials such as noble metals. After presenting historical and theoretical part to generate and excite surface plasmon, we will focus on its interest to perform biosensing and how to improve the efficiency of such devices.

### 2. Surface plasmons

Surface plasmon occurs at the surface of metallic materials and refers to the collective oscillation of the conduction electrons. These oscillations can be coupled with an incident light in order to give birth to a resonance phenomenon called surface plasmon resonance (SPR). The SPR is used to probe the change of the environment at the metal surface since it depends of the change in refractive index.

#### a) *Historical context*

The first and most famous observation of optical phenomenon due to surface plasmon dates back to the IV<sup>e</sup> century with the Lycurgus cup (figure I-20). The color of the cup is different depending on the illumination's orientation (green with the reflected light - when the illumination comes from outside and red with the transmitted light - when the illumination comes from inside the cup). This typical behavior is due to the presence of gold and silver nanoparticles which exhibit plasmonic properties. We have to wait the beginning of the XX<sup>e</sup> century for the identification of the surface plasmon by Wood who highlighted anomalies in the diffraction spectrum of reflected light through diffracting grating.<sup>[115]</sup> In 1941, Fano gave an explanation to this phenomenon and showed that these

anomalies are due to the excitation of electromagnetic waves.<sup>[116]</sup> It is only in 1956 that the term “plasmon” is introduced by Pines<sup>[117]</sup> and the next year by Ritchie who first described the theory of surface plasmon.<sup>[118]</sup> In 1968, Ritchie introduced the concept of “surface plasmon resonance”<sup>[119]</sup> and at the same time Otto<sup>[120]</sup> and Kretschmann<sup>[121]</sup> provided two distinct configurations to excite surface plasmon on a thin film by using a prism. These works established a simple and efficient way to exploit surface plasmons giving rise to different possible applications.<sup>[122, 123]</sup> The main use of the plasmon resonance (and the one we are interested in) is in biosensors.<sup>[123, 124]</sup> In the early 1990, the first commercial biosensors appear on the market (Biacore©) following by a strong enthusiasm with the development of many devices based on plasmonic materials.



Figure I-20. Lycurgus cup under external illumination (left) and internal illumination (right) by light.

## b) Theory

To understand the mechanisms of surface plasmon resonance, it is interesting to study first the behavior of the electronic oscillations at the surface of a metal. These oscillations (often called surface plasmon waves - SPW or surface plasmon polaritons - SPP) can be defined by an excitation at the interface between a metal medium and a dielectric. The description of the surface plasmons is based on the equation of propagation of electromagnetic waves called Maxwell equations.

The detailed description of the surface plasmon which leads to the determination of the relation of dispersion is given in (appendix B). The results obtained conduct to different properties of the surface plasmons:

- Surface plasmons are described by the dispersion relation:

$$\beta_{sp} = k_0 \sqrt{\frac{\epsilon_d \epsilon_m}{\epsilon_d + \epsilon_m}} \quad \text{Equation I.18}$$

- Real part of the metal permittivity has to be negative in the range of wavelength used, it is true for noble metal such as gold and silver :  $\epsilon_m < 0$
- $\epsilon_d < -\epsilon_m$  this condition is verified for an interface metal/dielectric
- Surface plasmons can exist only for the radial polarization TM of the light

After these conclusions, we know that surface plasmons can be studied in different systems based on their dispersion relation. Moreover the existence of a metal/dielectric interface is necessary to generate the plasmon.

To generate the resonance phenomenon, the surface plasmon has to be coupled with light. We can distinguish several different cases which are used for biosensing, but the two mains are:

- Localized surface plasmon resonance (LSPR), when the surface plasmon is confined to a metallic nanostructure of a size comparable to the wavelength of light. In this case, the collective oscillation of the free electrons of the nanoparticle becomes coherent with the electric field of the incoming light giving the resonance phenomenon. Therefore, the incident light can excite the surface plasmon without need of specific coupling.
- Propagative surface plasmon resonance (SPR), when the surface plasmon is confined into a thin metallic film. In this case, the incident light cannot excite directly the surface plasmon. A specific configuration is necessary to create the resonance phenomenon.

There are different techniques to excite the surface plasmon on thin metallic layer. The excitation can be performed by waveguide coupling when a guided mode propagating along the surface or by grating coupling by using a diffraction grating.<sup>[125]</sup> Nevertheless, the configuration by prism coupling is the most conventional and the most used. This configuration using a prism with a high refractive index is detailed in the next part using optic laws.

### *c) Excitation condition of surface plasmons with Kretschmann configuration*

The excitation of the surface plasmon on a thin film is based on the coupling of light in a prism by using the technique of total internal reflection (TIR). To excite the plasmon, Kretschmann geometry is used where the metallic layer is directly deposited on the prism surface. Plasmonic resonance requires the coupling of the surface plasmon at the metal/dielectric interface with the evanescent wave generated by the TIR method. The total reflection phenomenon appears when an incident light incomes at the interface between two medium with different refractive index with an angle over the value of a critical angle  $\theta_c$ . In this case, there is no transmitted light and only reflected light. Moreover, close to the interface, an evanescent wave is generated which decreases rapidly with the distance to the surface. This condition happens at the critical angle defined by the Snell-Descartes law.

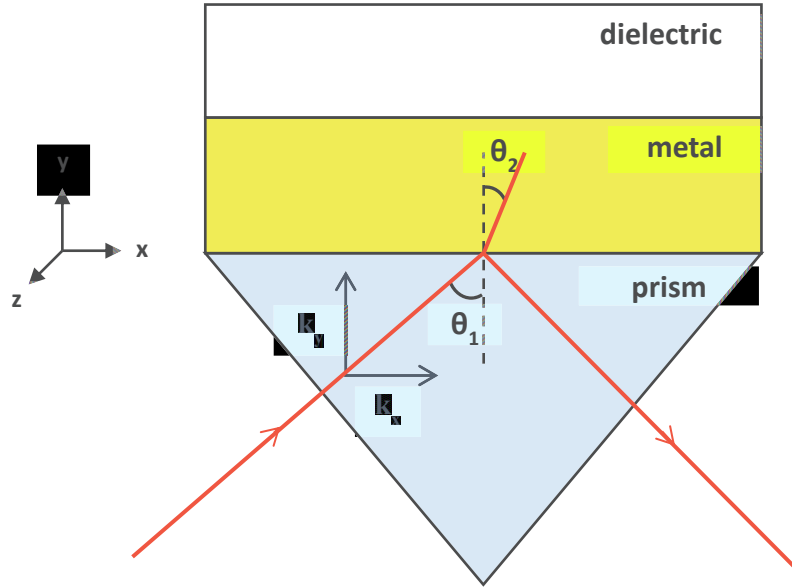


Figure I-21. Schematic representation of the coupling resonance phenomenon by using a prism in the Kretschmann configuration

Considering a medium 1 (prism) with a refractive index  $n_1$  crossed by an incident light forming an angle with the normal at the interface  $\theta_1$  (Figure I-21). This incident light will be reflected with the same angle  $\theta_1$  and transmitted with an angle  $\theta_2$  in the medium 2 (metal) with a refractive index  $n_2$ . The Snell Descartes law gives us:

$$n_1 \sin(\theta_1) = n_2 \sin(\theta_2) \quad \text{Equation I.19}$$

We deduct:

$$\sin(\theta_2) = \frac{n_1}{n_2} \sin(\theta_1) \quad \text{Equation I.20}$$

In the case where the medium 2 is more refractive than the medium 1 ( $n_2 > n_1$ ), the equation I.19 can be true for every angles. However if  $n_1 > n_2$ , this relation is no longer defined for every value of  $\theta$ . Indeed, if  $\frac{n_1}{n_2} \sin(\theta_1) > 1$  it cannot be possible to have a transmitted light: it is the total internal reflection. In our case, the refractive index of the prism is larger than the metal refractive index (gold) so this condition is respected for angle  $\theta$  given by:

$$\theta_1 \geq \arcsin\left(\frac{n_2}{n_1}\right) \quad \text{Equation I.21}$$

In this case, the totality of the incident energy is reflected and an evanescent wave appears in the medium 2 and can only propagate at the vicinity of the surface.

The resonance phenomenon occurs when the wave vector  $k$  transmitted in the metal is equal to the wave vector of the surface plasmon  $\beta_{SP}$ . The wave vector of the transmitted light in the medium 2 has a tangential component and a normal component at the interface between the two medium and is defined by:

$$\vec{k}_t = \begin{cases} k_x = \frac{\omega}{c} n_2 \sin(\theta_2) \\ k_y = \frac{\omega}{c} n_2 \cos^2(\theta_2) \\ k_z = 0 \end{cases} \quad \text{Equation I.22}$$

By using Descartes law and the property  $\cos^2\theta + \sin^2\theta = 1$ , we have:

$$\vec{k}_t = \begin{cases} k_x = \frac{\omega}{c} n_1 \sin(\theta_1) \\ k_y = \frac{\omega}{c} \sqrt{n_2^2 - n_1^2 \sin^2(\theta_1)} \\ k_z = 0 \end{cases} \quad \text{Equation I.23}$$

We can observe that the component  $k_y$  is real when  $0 < n_1 \sin(\theta_1) < n_2$  and is pure imaginary when  $n_1 \sin(\theta_1) > n_2$ . In this last case, we find again the limit where the incident light is only reflected and the transmitted wave in the medium 2 is evanescent.

The plasmon resonance condition will exist when both the propagation constant of the surface plasmon and the tangential component of the evanescent wave are equal. We obtain this resonance condition by equalizing the equation I.18 and I.23:

$$k_x = \beta_{SP} \quad \text{Equation I.24}$$

$$\frac{\omega}{c} n_1 \sin(\theta_1) = \frac{\omega}{c} \sqrt{\frac{\epsilon_d \epsilon_m}{\epsilon_d + \epsilon_m}} \quad \text{Equation I.25}$$

Or:

$$n_1 \sin(\theta_1) = \sqrt{\frac{\epsilon_d \epsilon_m}{\epsilon_d + \epsilon_m}} \quad \text{Equation I.26}$$

Equation I.26 gives us the resonance condition to generate and excite surface plasmon at the metal/dielectric interface. This condition is true for a single incident angle and for a given wavelength. Moreover, the SPR phenomenon can be monitored since the intensity of the reflected light decreases and gives a minimum of intensity for the resonance condition. This minimum of intensity (called "resonance peak") is dependent either on the incident angle or the wavelength, we talk about angular or spectral interrogation respectively.

#### d) *Influence of parameters on plasmons excitation*

Several parameters can influence the resonance of the surface plasmons such as the refractive index of the prism, the permittivity of the metal and of the dielectric. Some of these parameters have to be controlled in order to satisfy the versatility of the measurements.

##### (1) Choice of the material

The material used has a strong influence on the position of the resonance. Most of metal present plasmonics properties (gold, silver, aluminum, copper). However, gold and silver are preferably used since their plasmon resonance occurs in the visible which allows their characterization with UV-visible spectroscopy and even use naked-eye in the case of colloidal suspensions. Moreover, gold surface can be easily functionalized with different molecules as seen previously.<sup>[39, 40]</sup> Nevertheless, silver suffers from a poor chemical stability and SPR devices should use a protective layer in order to protect the metal from the oxidation and make easier functionalization.<sup>[126]</sup>

Gold surface remains the perfect candidate since its functionalization is easily afforded with self-assembled monolayers (cf. II.A.1).

(2) Metal permittivity

Different points have to be highlighted after considering the dispersion relation (equation I.18) of the surface plasmon. First, it is important to notice that the permittivity of the metal is a function of the pulsation  $\varepsilon_m(\omega)$  and can be described by the Drude model for the free electron in the metal:<sup>[127]</sup>

$$\varepsilon_m(\omega) = 1 - \frac{\omega_p^2}{\omega^2 + i\omega\gamma_l} \quad \text{Equation I.27}$$

with  $\gamma_l$  the damping factor and  $\omega_p$  the plasma pulsation given by:

$$\omega_p = \sqrt{\frac{ne^2}{m\varepsilon_0}} \quad \text{Equation I.28}$$

with  $n$  the electron density of the material,  $e$  the electron charge and  $m$  the electron mass.

In the visible light domain (400 - 800 nm) the metal is considered without losses<sup>[127]</sup> and therefore the damping factor is equal to zero and the equation I.27 becomes:

$$\varepsilon_m(\omega) = 1 - \frac{\omega_p^2}{\omega^2} \quad \text{Equation I.29}$$

Knowing that the pulsation is given by:

$$\omega = \frac{2\pi c}{\lambda} \quad \text{Equation I.30}$$

The permittivity of the metal is given for each excitation wavelength. In the plasmon dispersion relation (equation I.18), if we replace the permittivity according to the Drude model without losses (equation I.29), we can notice the denominator is cancelled for  $\varepsilon_d + \varepsilon_m = 0$ . Therefore for the frequencies  $= \pm \frac{\omega_p}{\sqrt{1+\varepsilon_d}}$ ,  $k$  tends to the infinite. These are the frequencies of the system allowing the determination of the asymptote from the dispersion relation (figure I-22). If the dielectric at the surface is water the asymptote equation will be  $\omega = \frac{\omega_p}{\sqrt{2}}$ .<sup>[127]</sup>

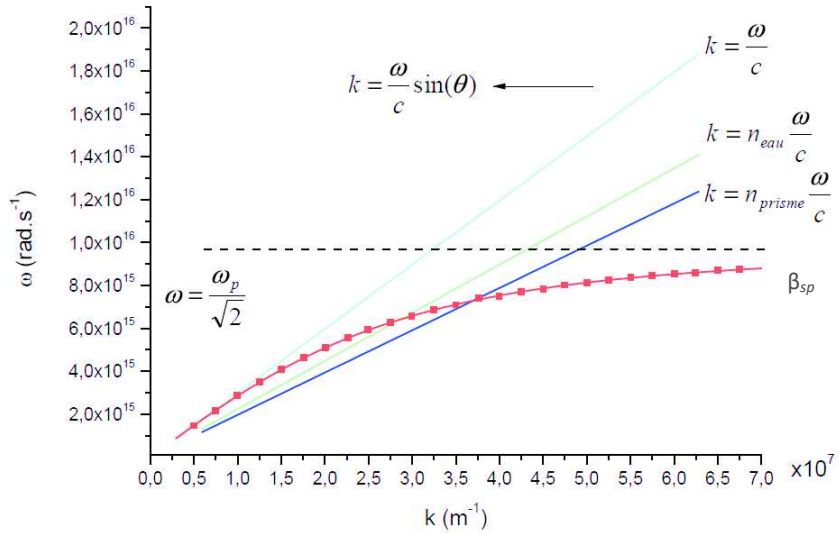


Figure I-22. Dispersion relation of surface plasmon as function of the surrounding medium. From Bryche.<sup>[127]</sup>

As we can see from the dispersion relation (equation 1.26); the coupling between the propagation of the incident light and the surface plasmon occurs when the curves representing the dispersion relation of the plasmon and the incident light are crossing. Here, we see how the medium supporting the incident light is critical to excite the surface plasmon and therefore explain the use of a prism with high refractive index.

### (3) Temperature and metal thickness

We can also take in account the influence of the temperature which is dependent of the metal conductivity. The plasma frequency is therefore dependent of the temperature and linked by the relation:<sup>[127]</sup>

$$\omega_p = \frac{\omega_{p0}}{\sqrt{1 + \alpha(T - T_0)}} \quad \text{Equation I.31}$$

with  $T_0$  the reference temperature,  $\omega_{p0}$  the plasma frequency and  $\alpha$  the thermal dilatation coefficient. The temperature is a parameter that could modify the resonance condition. Therefore the temperature is critical and will be controlled during the SPR measurement (18°C-21°C in our study).

Another parameter is the thickness of the metallic layer. Obviously the thickness of the metal should be thin enough otherwise the evanescent wave will not reach the interface with the dielectric. In another hand, the permittivity of the metal can be impacted by the film thickness.<sup>[128]</sup> Some variations can be observed as function of the thickness due to the losses of the metal permittivity which is represented by the increase of the imaginary part.<sup>[129]</sup> This should be importantly considered and therefore working with metallic films with the same thickness. In our study we will consider a continuous and homogenous metal film with thickness of 30 nm or 50 nm.<sup>1</sup>

<sup>1</sup> The study will be realized on different substrates, the thickness of the metallic layer will be constant for each study, but different samples will be characterized either with a 30 nm either a 50 nm gold thickness.

(4) Refractive index at the surface

The previous parameters can be settled to measure the samples in the same conditions. However, the condition of excitation of the plasmon (equation 1.26) shows a strong dependence on the dielectric permittivity  $\epsilon_d$ . Indeed, the change of permittivity at the surface of the metal will therefore induce a change in the spectral or angular peak position. The figure I-24 represents the resonance angle as a function of the permittivity of the dielectric when the medium 1 is a prism of BK7 with a refractive index of 1.51. Here, we can observe that the incident angle is higher for shorter wavelength.

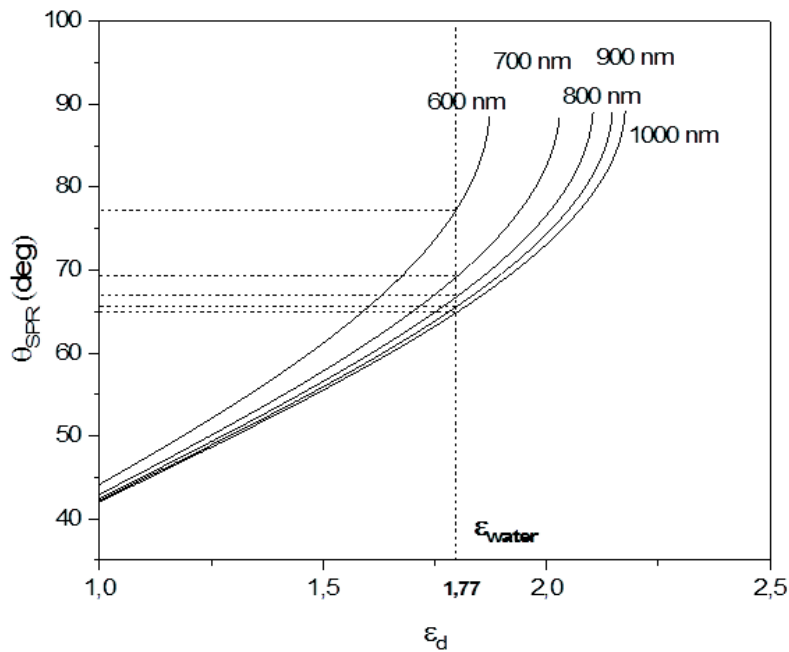


Figure I-23. Change of the angular response as function of the dielectric constant at the surface for different working wavelengths

From the equation 1.26, we can easily see that the incident angle is strongly dependent of the permittivity of the dielectric  $\epsilon_d$  at the metal surface. It is also observed that a change of permittivity creates a larger change in the incidence angle for shorter wavelengths. This better sensitivity for the shorter wavelengths have been explained by Liedberg and al<sup>[130, 131]</sup> who showed that the material have a larger absorption (due to the increase of the imaginary part of  $\epsilon_m$ ) for shorter wavelengths.

(5) Penetration depth

One property which is critical for the understanding of the surface plasmon is the penetration depth which corresponds to the distance that the evanescent wave can reach from the metal surface. The evanescent wave has a progressive structure on the normal direction of the metal/dielectric interface (y axis) and its amplitude decays exponentially as:

$$E_y(y) = E_z(0)e^{-k_y y} \quad \text{Equation I.32}$$

with

$$k_y^2 = k_x^2 - \frac{\omega^2}{c^2} \varepsilon_d \quad \text{Equation I.33}$$

Assuming this, the decay electric field of the evanescent wave can be written:

$$E_y(y) = E_z(0)e^{-\frac{y}{\delta}} \quad \text{Equation I.34}$$

with  $\delta$  the penetration depth expressed as:

$$\delta = \frac{c}{2\omega} \sqrt{\left| \frac{\varepsilon_m + \varepsilon_d}{\varepsilon_d^2} \right|} = \frac{\lambda}{4\pi} \sqrt{\left| \frac{\varepsilon_m + \varepsilon_d}{\varepsilon_d^2} \right|} \quad \text{Equation I.35}$$

The penetration depth increases with the wavelength of excitation and decreases when the dielectric constant increases at the surface. This exponential decay is the reason why the plasmon can be detected only at the vicinity of the surface. This value is important since it determines the range and the volume of sensing at the metal surface. In the early 90s, Liedberg et al. showed that the sensitivity is the best, the closest to the surface by modeling dielectric matrix at different distances from the metal (Figure I-25).<sup>[131]</sup>

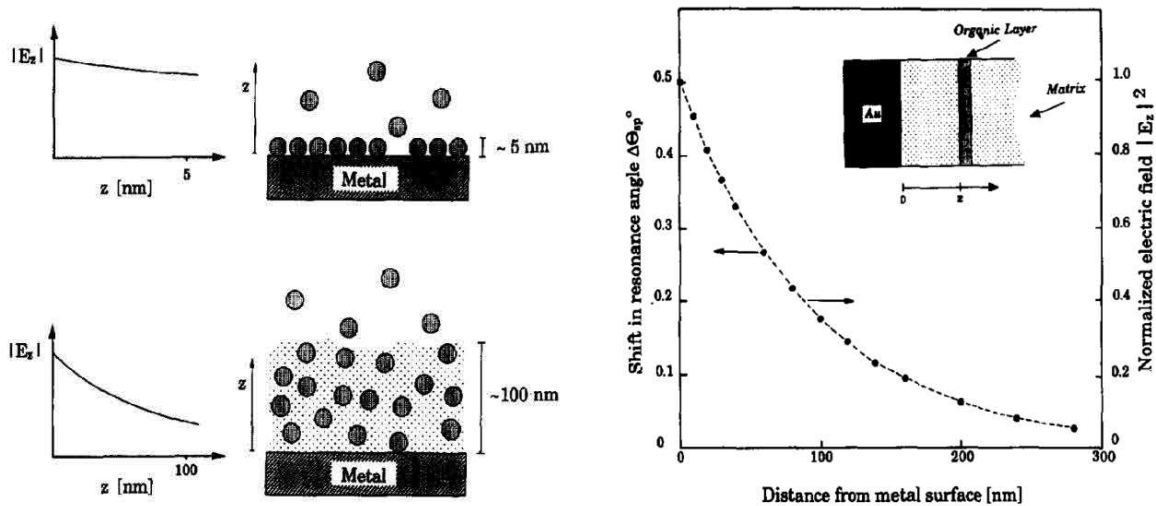


Figure I-24. (a) Attenuation of the electric field for two model with a direct surface interaction (top) or extended matrix (bottom) and (b) calculation of the SPR response as function of the distance from the metal interface of an organic layer. From Liedberg et al.<sup>[131]</sup>

Therefore performing biosensing requires detecting the analyte at the vicinity of the metal in order to ensure a good sensitivity and an optimization of the biosensor. We will see how changing the parameters can influence the penetration depth and what are the consequences on the sensitivity of the sensors.

To conclude, the surface plasmon of a gold substrate can be excited with light in the visible range when it is coupled with a prism in the Kretschmann configuration. The variation of permittivity (and therefore refractive index) at the surface of the gold substrate will induce a change in the resonance condition which will be monitored in order to detect adsorbed species.

### 3. Plasmonic biosensors

#### a) Generalities on plasmonics biosensors

The sensitivity to change in refractive index allows plasmonics sensors to detect the binding events at the surface of the metal. The main goal of a biosensor is to give a response by binding an analyte with the best sensitivity meaning the maximum response for a minimum change of refractive index. As shown in the previous part, the signal of the SPR is strongly dependent of the dielectric properties on the surrounding environment. Therefore, plasmonic sensors are used for biosensing devices and require several characteristics:

- A sensing surface including an organic receptor to adsorb the target molecules through molecular recognition process
- A microfluidic system allowing the injection in-situ and real time of the analyte
- An optical configuration linked to an online computer to measure the change in the reflected light (as function of the incident angle or wavelength)

Therefore, the key parameter is the functionalization of the surface by recognition elements which has to be highly specific to detect the target molecules. For the material, gold and silver are the most common materials used as biosensors because of their strong resonance peak in the visible. Moreover, these metallic surfaces present an easy and well described functionalization in literature which allows the grafting of receptor molecules by different approaches. Indeed a significant aspect is the way the bioreceptors are anchored to the surface. The molecules are either physisorbed,<sup>[132-134]</sup> either chemically attached.<sup>[132]</sup> Covalent binding is preferred as it provides stronger and stable binding.

The performances of SPR sensing are driven by several characteristics which are specific to the device and allow understanding the performances but also the limitations of the biosensors:

- Resolution or limit of detection (LOD); it corresponds to the lowest concentration which can be detected and differentiated from the noise.
- Sensitivity; it corresponds to the ratio between the variation of the response and the change of corresponding refractive index.
- Selectivity; the capacity to differentiate two different analytes.
- Accuracy; the difference between the measured value and the real value.

This kind of devices present multiple advantages such as the rapid and real time analysis, in-situ detection, a low limit of detection and it does not require the labeling of the analyte. This is why using SPR as biosensing presents a great interest. Several species such as protein, DNA, enzyme, cell, nucleic acid, antigen–antibody, and microorganism have been detected below the pM<sup>[113, 122, 135, 136]</sup> which makes the SPR sensing a powerful tools (table I-1).

Table I-1. Limit of detection of different analytes. Extract from Fan et al.<sup>[114]</sup>

Technology platform	Optical structures	Analyte	Detection limit	References
Surface plasmon resonance	Surface plasmon resonance	Bulk solution	$10^{-5}$ - $10^{-8}$ RIU	[137-142]
	Long range SPR	Bulk solution	$10^{-7}$ - $10^{-8}$ RIU	[143-145]
	Surface plasmon resonance	Bulk solution	$10^{-5}$ - $10^{-7}$ RIU	[146-149]
	Imaging (SPRi)	Protein	1 nM	[150]
	Optical heterodyne SPR	Protein	0.2 nM	[151]
	Phase sensitive SPR	Protein	1.3 nM	[152]
	Wavelength modulated SPR	DNA	10 pM	[153]
	SPRi	DNA and RNA	10 nM	[154]
	Flow injection SPR	DNA	54 fM, 1.38 fM	[155]
	Angle modulated SPR	Protein	0.15 ng/mL	[156]
	Surface plasmon resonance	Protein	66.7 unit/mL	[157]
	Surface plasmon resonance	Protein	50 ng/mL	[158]
	Prism-based SPR	Bacteria (E.coli)	$10^6$ cfu/mL	[159]
		Salmonella	100 cfu/mL	[160]
Biacore 2000 SPR	Bacteria	25 cfu/mL	[161]	

Nevertheless, SPR biosensing have limits such as the detection of small molecules or very diluted concentrations.<sup>[162]</sup> These limits have to be pushed in order to improve the detection this is why, the optimization of the SPR sensing becomes necessary.

Progress and achievements of the two different kinds of sensors (propagative and localized plasmon resonance) are showed in the following parts.

#### b) *Localized surface plasmon resonance sensors (LSPR)*

LSPR biosensors are based on the use of metallic nanostructures which can generate plasmons. In these cases, the incident electric field will induce a uniform displacement of the conduction electrons. LSPR can be directly excited by incident field if the nanostructure is smaller than the wavelength of light particularly because of the geometry of the nanostructure (figure I-26).<sup>[163]</sup>

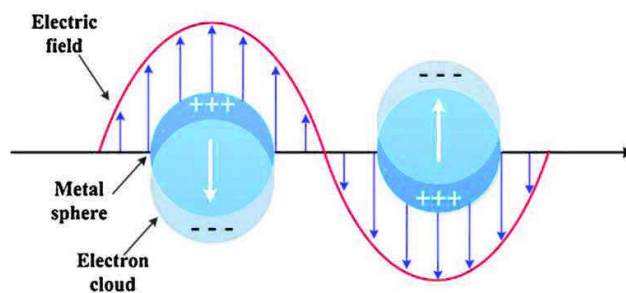


Figure I-25. Schematic representation of the localized surface plasmon generated by electric field on metal nanoparticle

In this case, the Mie theory<sup>[164]</sup> describes the properties of the nanostructures and explains the adsorption and scattering phenomenon. In this case, the resonance is expressed as:

$$\omega_{LSPR} = \frac{\omega_p}{\sqrt{(1+2\epsilon_d)}} \quad \text{Equation I.36}$$

with  $\omega_p$  the plasma frequency of bulk material. As seen before, the LSPR frequency is strongly dependent of the surrounding dielectric at the surface of the metallic nanostructure.

Gold, silver and aluminum are the common metals used because of their plasmonic resonance which is set in the visible light domain. The optical extinction of the nanoparticles displays a maximum at the plasmon resonance frequency which occurs in the visible domain for noble metals, explaining the color of metallic nanoparticle suspensions. Thanks to these properties, nanostructures can be used as biosensors by functionalizing their surface with various bio-receptors. Thus, the recognition can be easily monitored with spectroscopy techniques.

The shape and size of nanostructures modify their absorption band (figure I-27) which can allow a spectral tenability of the SPR signal.<sup>[162, 165]</sup> The surrounding medium affects also the absorption band and the adsorption of molecules at the surface changes the spectroscopy measurements.

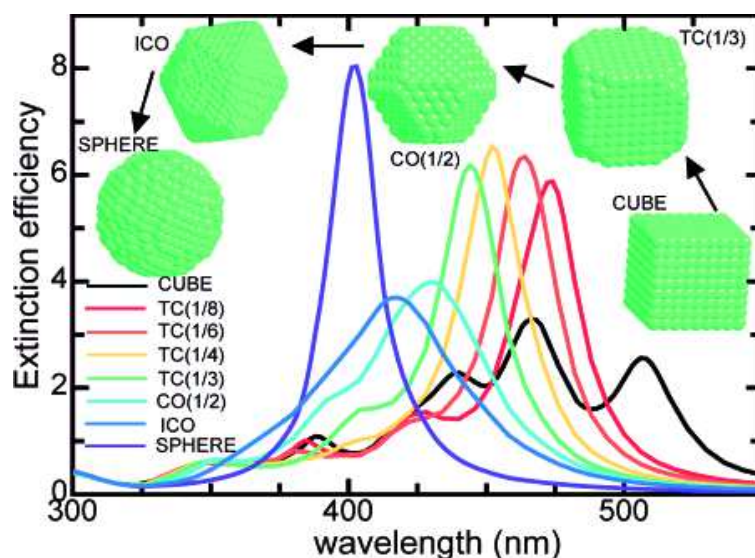


Figure I-26. Absorption bands of gold nanoparticles as function of their shape. From Noguez.<sup>[165]</sup>

UV-vis spectroscopy is a good technique to monitor the change at the nanoparticle surface.<sup>[166]</sup> Moreover, the use of noble metal nanoparticles such as gold or silver gives an absorption in the visible light which makes possible the detection with naked eye. It gives rise to two different approaches to use plasmonic nanostructures for biodetection; the first one using nanoparticles in solution (colorimetric assays) and the second using nanostructures onto substrates to form arrays.

#### (1) Colorimetric assays

Noble metal nanoparticles are used in plasmonic biosensors for detection. Indeed, the aggregation of metallic nanoparticles causes the change of the surrounding environment and creates coupling interactions between them.<sup>[167]</sup> The stability of the suspension is therefore a key parameter and the introduction of the target molecules, which act as a molecular linker between the nanostructures, will lead to the formation of aggregates in solution and to the change of the solution coloration.<sup>[168]</sup> The use of recognition elements such as the biotin-streptavidin couple has been widely used. The gold nanoparticles can be easily functionalized by thiol groups with a biotin group at the surface in order to detect streptavidin in a solution. The streptavidin with its four binding sites can link the nanoparticles together and form array of nanoparticles in suspension.<sup>[169, 170]</sup> The group of Kikuchi et al. used functionalized gold nanoparticles to detect glycosidases (Figure I-28).<sup>[171]</sup> The presence of glycosidase in the nanoparticles suspension triggered the aggregation through electrostatic interactions. Gold nanoparticles have also been crosslinked with DNA strands.<sup>[172, 173]</sup> The nanoparticles are functionalized with aptamers and the presence of the complementary aptamers in the suspension led to their aggregation.

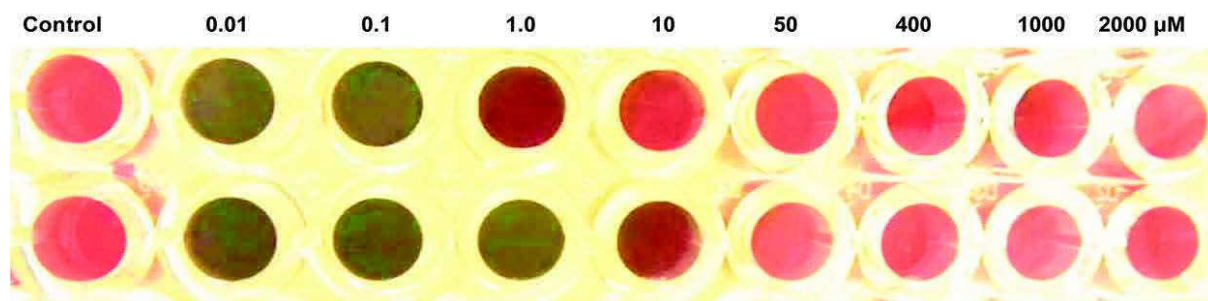


Figure I-27. Different concentration of  $\beta$ -galactosidase and  $\beta$ -glucosidase showing the change of coloration of gold nanoparticles caused by aggregation. From Zeng et al.<sup>[171]</sup>

These colorimetric assays are an easy and real time way to detect in solution the presence of various analytes such as proteins, enzymes or aptamers. The controlled aggregation in suspension of the nanostructures is the key parameter as long as it is responsible of the color change of solution observed by naked eye.

#### (2) Surface nanostructured architecture

Plasmonic nanostructures can also be used on a surface in a Kretschmann configuration to detect local changes of the refractive index with a fluidic channel. The top-down (lithography) and

bottom-up (assembly of nano-objects) approaches are both used to create devices using nanostructures with localized surface plasmons onto substrates.<sup>[174]</sup> The different assembling methods (cf. I.B.1) allow controlling the structuration of plasmonic nanoparticles onto a surface with a good control of shape and size ranging from 2 nm until 100 nm.<sup>[166, 175]</sup>

In another hand, different lithography processes allow a fine control of the size and the shape with a high density on large areas but cannot reach size below hundreds of nanometer. Nanostructures on the surface<sup>[176-178]</sup> or nanopatterning popularized by Van Duyn<sup>[179]</sup> (Figure I-29) have been used to create nanostructured surfaces. These systems highlighted a good sensitivity because of the confinement of the electromagnetic energy in the nanostructures and considerably reduced the penetration depth (cf. I.C.1.d).<sup>[177, 180]</sup>

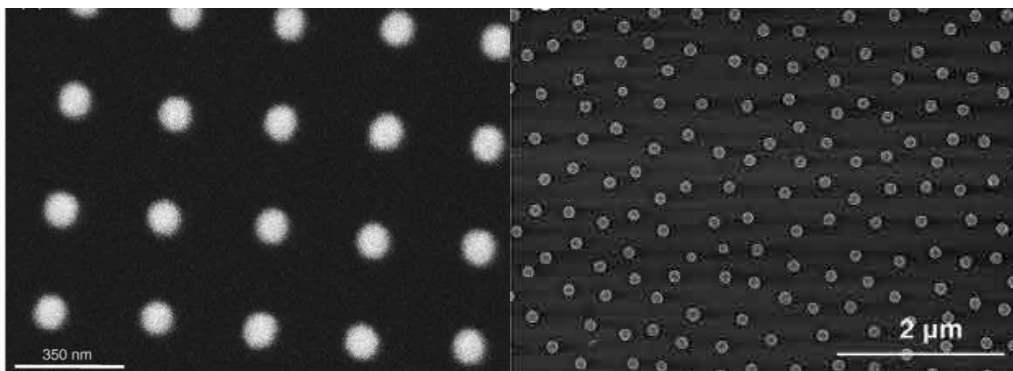


Figure I-28. Scanning electron microscopy of gold nanodiscs deposited on a substrat. From Barbillon et al.<sup>[177]</sup>

These lithography approaches are widely used but the processes are expensive and slow. Therefore, top-down approach is not suitable to achieve fast and cheap nanostructured surfaces. The use of nanomaterials in order to improve the performance of sensors is often more preferred.

### c) Propagative surface plasmon resonance (SPR)

As seen in section (I.C.2.c) the SPR displayed by thin metallic films cannot be excited by free space radiations and therefore has to be coupled with a prism with a high refractive index. However, different methods exist to couple light with the surface plasmon of thin films (figure I-30):<sup>[114, 181]</sup>

- Waveguide coupling: the light propagates in a waveguide through total internal reflection and generates an evanescent field at the waveguide–metal interface and excites the surface plasmon as for the prism configuration.<sup>[128, 182]</sup>
- Optical fibers: in the same way, the light is carried by the fiber which can have different configurations such as side-polished single mode or multimode, tip-polished, polarization maintaining or D-shaped fiber.<sup>[183-186]</sup>
- Grating coupling: the incident light is coupled with a periodic array at the substrate surface.<sup>[187, 188]</sup>
- Long/short-range surface plasmon: the plasmonic substrate is surrounded by two dielectric layers that have similar refractive index. The surface plasmons from both interfaces are coupled and generate two modes called long and short range surface plasmons.<sup>[126, 145, 189-191]</sup>

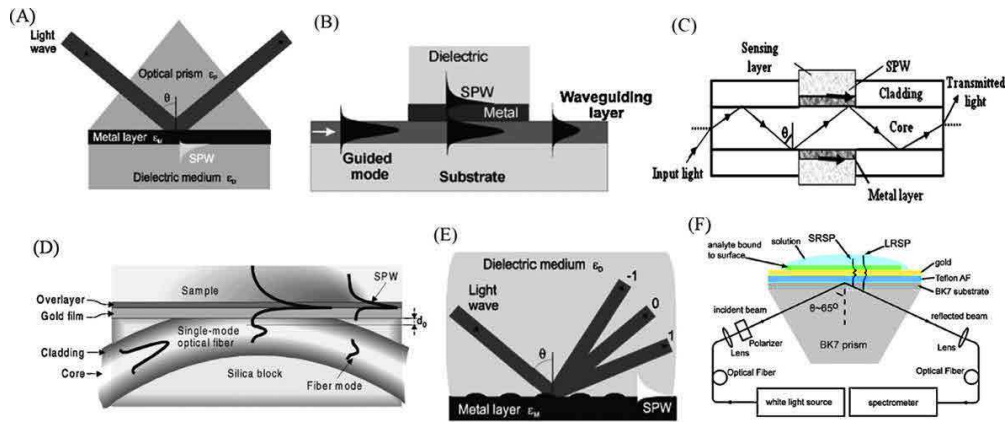


Figure I-29. Schematic representation of various SPR sensor configurations. (A) Prism coupling, (B) waveguide coupling, (C) optical fiber coupling, (D) side-polished fiber coupling, (E) grating coupling and (F) long-range and short-range surface plasmon (LRSP and SRSP). Adapted from Fan et al.<sup>[114]</sup>

The feature of the propagative SPR lies in the larger volume sensing in comparison with the LSPR. Indeed, the large penetration depth allows sensing over few hundred of nanometers which is a great advantage to detect very large objects such as cells or bacteria.<sup>[123]</sup> However, this large penetration depth reduces the sensitivity. Long-range SPR, despite the large sensing depth, allows a good sensitivity and a narrow SPR feature.<sup>[192]</sup>

In conclusion, each configuration presents different advantages and propagative and localized SPR can even be coupled in order to combine both properties and enhanced the sensitivity.<sup>[127, 193]</sup>

#### 4. Plasmonics biosensors optimization

As we saw previously, many techniques have been used to perform bio-sensing using plasmonic properties of noble metal materials. The efficiency of these sensors can be increased by two methods; improving the intrinsic optical properties and the characteristics of surface functionalization.

##### a) Intrinsic properties

The first method to improve the performance consists to decrease the sensing volume. Indeed, as shown by equation I.35, the penetration depth is representing the distance that the evanescent wave can probe and so be effective for sensing.

The response of a SPR measurement can be expressed as function of  $\lambda$  or  $\theta$  and is dependent of the change of refractive index at the surface of the metal. The response of a sensing system  $R$  is given by:

$$R = m\Delta n = m(n_{eff} - n_s) \quad \text{Equation I.37}$$

with  $m$  the sensing factor,  $n_{eff}$  the effective refractive index of the adlayer at the surface of the metal and  $n_s$  the refractive index of the solvent. The intensity of light is the field strength squared, so

it decays with height  $y$  above the metal surface as  $e^{\frac{-y}{l_d}}$  with  $l_d$  the decay length in the dielectric layer which is linked with the penetration depth  $\delta$  by:

$$l_d = 2\delta \quad \text{Equation I.38}$$

The weighting factor for determining the average refractive index is therefore  $e^{\frac{-y}{l_d}}$ . This was indeed proven to be very accurate through Maxwell's equations by Liedberg et al.<sup>[131]</sup> The effective refractive index is therefore calculated with the integral:<sup>[194]</sup>

$$n_{eff} = \frac{2}{l_d} \int_0^{\infty} n(y) e^{\frac{-y}{l_d}} dy \quad \text{Equation I.39}$$

Considering a bilayer structure we have,  $n(y) = n_d$  when  $0 < y < d$  and  $n(y) = n_s$  when  $y > d$  and the integral becomes:

$$n_{eff} = n_s + (n_d - n_s) \left[ 1 - e^{\frac{-d}{l_d}} \right] \quad \text{Equation I.40}$$

and  $R$  becomes:

$$R = m(n_d - n_s) \left[ 1 - e^{\frac{-d}{l_d}} \right] \quad \text{Equation I.41}$$

The response,  $R$ , is most of the time corresponding to a spectral shift measured with a constant incident angle ( $\Delta\lambda$ ) or an angular shift measured with a constant wavelength ( $\Delta\theta$ ). By the equation I.39, we can easily see that the sensitivity can be increased by two different factors for a given change of refractive index at the surface:

- by decreasing the decay length  $l_d$
- by increasing the sensitivity factor  $m$

Decreasing the decay length, and therefore the penetration depth, corresponds to decrease the sensing volume and therefore to increase the contribution of the analyte refractive index on the surface of the sensor. The penetration depth, given by equation I.35, is dependent of the excitation wavelength in the metal and the permittivity of the dielectric layer  $\epsilon_d$ . We can easily see that the penetration depth increases directly with the wavelength. Therefore, the sensitivity of the detection can be improved by changing the incident wavelength. The penetration depth can also be tuned by the nanostructuring of the metal at the surface.<sup>[177]</sup> Indeed, the decay length (ranging from 100 nm up to 1  $\mu\text{m}$  for classic SPR system) can be confined in nanostructure and reaches values down to 20 nm.<sup>[175, 180]</sup> The main drawback we can highlight is that the confinement around the nanostructures. It decreases the sensing volume and does not allow the detection above few nanometers from the surface of the nanostructures.

The sensitivity factor  $m$  (or refractive index sensitivity) corresponds to the slope of the variation of the measured shift (spectral or angular) for a change in effective refractive index at the surface. It becomes crucial for detecting small analytes (lower than 500 Da) to have a strong sensitivity. The sensitivity factor increases when the analyte is close to the surface but decreases with the distance from the surface.<sup>[131]</sup> The sensitivity is also dependent of the nanostructuring of SPR material, the operating wavelength and the instrumentation.<sup>[195]</sup>

The SPR and LSPR have similar magnitude order for the sensitivity. While propagation SPR has a large penetration depth and sensitivity factor, in contrast the LSPR has a low sensitivity factor but short decay length. To improve the total sensitivity of such nanodevices, different configurations of sensors are used (table I-2).

Table I-2. Summarize of SPR performances for different configurations. Extract from Roh et al.<sup>[125]</sup> References correspond to the cited article.

Optical structure	Characteristics	RI range	Wavelength	Sensitivity	Ref
<i>Kretschmann configuration</i>					
Typical sensor	Au, Ag metal film	1.33–1.34	400–800 nm	100–300 deg./RIU	35
	Ag film, low index prism	1.328–1.332	1,310 nm	500 deg./RIU	13
Over layer	Au metal film	~1.35	500–1,000 nm	7,500 nm/RIU, 10 <sup>-8</sup> RIU	18
	Au and Si, ZrO <sub>2</sub> thin film	1.325–1.335	632.8 nm	50–230 deg./RIU	16
	Ag-Au bimetallic layer	1.33–1.34	632.8 nm	7.85 × 10 <sup>-6</sup> RIU	17
Nanostructured sensor	Au nano cylindrical array	1.33–1.335	632 nm	10-7/RIU	25
	Au nanorod metamaterial	~1.33	1200–1300 nm	30,000 nm/RIU	26
	M-D mixed grating	1.33–1.36	633 nm	~120 deg./RIU	22
Multichannel sensor	Dual channel, D over-layer	1.33–1.34	550–1150 nm	5 µg/mL α-DNA	20
	Angled polishing prism	1444–1.450	500–900 nm	2,710, 8,500 nm/RIU	19
<i>Fiber-Optic SPR sensors</i>					
Symmetrical cladding off	Au, Ag metal film	1.33–1.34	400–650 nm	2,000–4,500 nm/RIU	28
Grating	Cascaded LPG	1.33–1.39	~1520 nm	-23.45 nm/RIU	
Nano-structured sensor	Au metallic grating	1.33–1.34	900–1,600 nm	4,000–9,800 nm/RIU	28
<i>Nano-structured-coupling</i>					
Grating-coupling	Au surface grating	1.33–1.34	~600 nm	440 nm/RIU	
	Al-Au bimetallic layer	1.32–1.37	900 nm	187.2 deg./RIU	37
Metamaterial-like	Au nano-structured layer	1.332–1.372	~150 THz (~2,000 nm)	588 nm/RIU	39
<i>Nanoparticle based sensors</i>					
Nano-structure	Single or double-square periodic nanoparticle array	1.333–1.420	400–950 nm	200–350 nm/RIU	73
	Nanoparticle pair, disk pair	1–1.5	500–900 nm	172,434 nm/RIU	53
	Unperiodic array		300–700 nm	165 nm/RIU	74
	Gold nano-ring array	1–1.3	300–1,800 nm	637.3 nm/RIU	75

Despite of the advantages that provide the nanostructures for LSPR, the sensitivity of this kind of sensors remains low. Nanostructured layers can provide a higher sensitivity due to the electric field enhancement between nanoparticles. Jain and al have demonstrated than the sensitivity of sensors using gold nanoparticles is higher when the nanostructures are closer but remain below 500 nm/RIU.<sup>[196]</sup> In another hand nanostructured film based biosensors can achieve a higher sensitivity up to 30000 nm/RIU by using metamaterials based on gold nanorods which support a guided mode onto a porous surface (Figure I-31).<sup>[162]</sup>

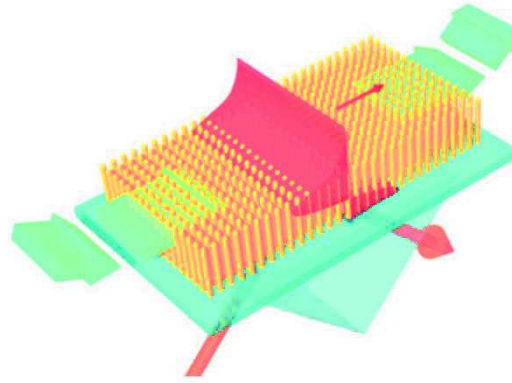


Figure I-30. Schematic representation of the nanostructured surface of gold nanorods. From Kabashin et al.<sup>[162]</sup>

### b) Surface functionalization

The sensitivity of these sensors is tuned by controlling the nanostructuring of plasmonic materials at the surface. Furthermore, the sensitivity can be increased by tuning the surface chemistry. Indeed, tuning the quantity of receptor molecules can improve the detection of the target analyte. The detection of proteins or large molecule implies a steric hindrance at the surface which can be optimized by diluting the recognition elements.<sup>[197-200]</sup>

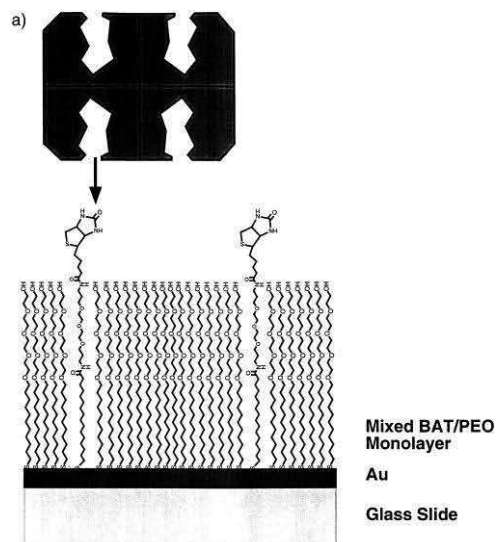


Figure I-31. Schematic representation of streptavidin adsorption onto mixed biotinylated-SAM. From Jung et al.<sup>[200]</sup>

The use of mixed SAMs onto a gold surface allowed the good recognition of the analyte (Figure I-32). Controlling the spacing between functional recognition groups can therefore increase the sensitivity by adsorbing more target molecules. Indeed, Perez et al. showed that the recognition of streptavidin on a mixed SAM surface is optimal when the concentration of biotin groups at the surface is about 20%.<sup>[199]</sup> The correct functionalization and homogenous spatial arrangement of receptor molecules at the surface is critical to have efficient sensing.

As we saw, the sensitivity of plasmonics biosensors is controlled by the structuration of the plasmonic material deposited onto and the configuration and the chemical recognition at the surface. Nevertheless, non-plasmonic materials have been also used for biosensing and can achieved a great enhancement in sensitivity.<sup>[126, 201-204]</sup>

## 5. Iron oxide nanoparticles based biosensors

Nan-plasmonic materials can be of interest to enhance markedly sensitivity. Indeed, high refractive index materials deposited onto gold thin films allow shifting strongly the resonance peak. As seen previously, sandwich immunoassay gives rise to the sensitivity of biosensors. Indeed, the signal is not sufficient to detect small analytes adsorbed on the surface. Nevertheless, coupling the analyte to a nanoparticle or to an object with large dimensions will give a larger shift after the adsorption. Gold nanoparticles which have been first used to amplify the SPR response.<sup>[205, 206]</sup> Other kinds of nanoparticles such as latex beads or silica nanoparticles with higher refractive index also induce a larger shift.<sup>[207, 208]</sup>

The use of iron oxide nanoparticles gives a better sensitivity thanks to its high refractive index which generates a larger shift and acts as a detection amplifier. Sun and al were the first in 2007 to use magnetite to improve the sensitivity of SPR sensors.<sup>[209]</sup> Therefore the magnetite nanoparticles coated with antibody are trapped onto a gold substrate using magnetic force. The detection of the specific antigen occurs at the surface of the nanoparticles. The main advantage of this approach is the reuse of the sensors by removing the magnetic microbeads support when the magnetic force is withdrawn. Soeldberg and al in 2009 used magnetic nanoparticles coated with streptavidin to bind a biotinylated antibody at the substrate surface.<sup>[210]</sup> The recognition of antibody alone is not sufficient to generate a large shift, but the presence of the antibody will indirectly bring 50 nm iron oxide nanoparticles which will create a strong shift. Similar and extended studies have been reported with different sizes of nanoparticles allowing the detection of multiple analytes at concentration below nM by using sandwich assays.<sup>[211-213]</sup> The magnetic field can also be used for trapping aggregated nanoparticles which are stable in solution but form aggregates on the plasmonic substrate in presence of the targeted analyte (Figure I-33).<sup>[214-216]</sup> In this case, the SPR response is linked to the analyte concentration in solution and the system can afford to determine the limit of detection.

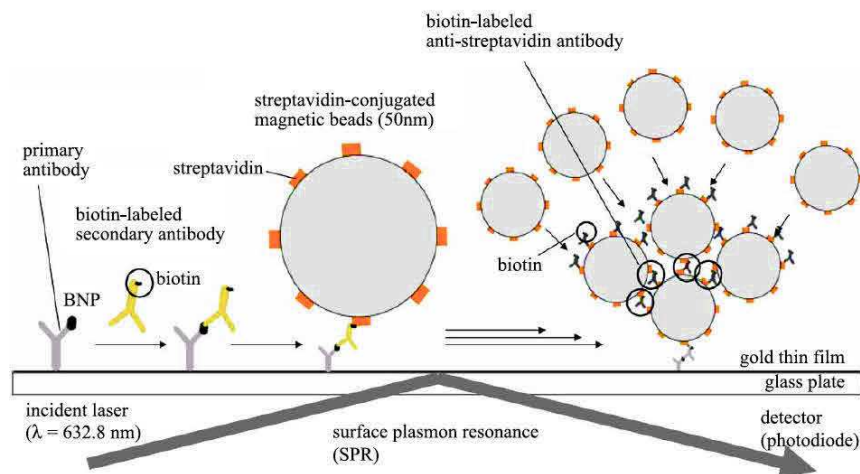


Figure I-32. Schematic representation of a sandwich assay to increase the sensitivity of SPR sensors by using iron oxide nanoparticles. From Teramura et al.<sup>[216]</sup>

These techniques based on the use of iron oxide nanoparticles allow the increase of the sensitivity and the limit of detection below nM for different proteins. In these examples, the nanoparticles are conjugated to a recognition element for detecting the analyte and then trapped onto the surface by applying magnetic field.<sup>[214, 215]</sup> The refractive index increases strongly at the surface and gives a higher SPR response. Moreover the high surface/volume ratio of nanoparticles leads to a high density of biomolecules at their surface which contributes to enhance the signal.<sup>[216]</sup> A crucial point is the non-aggregation of the nanoparticles in suspension before starting analysis in order to monitor precisely the variation of the refractive index at the surface.

Nanoparticles have been used in sandwich assay to enhance the detection of small molecules. Nevertheless it has not been reported as intermediate to increase directly the sensitivity factor. Pichon et al. showed the use of iron oxide nanoparticles to control the position of the plasmon resonance peak by grafting iron oxide nanoparticles onto a gold surface (Figure I-34).<sup>[64]</sup> The control of the peak position as well as the increase of the surface area is suitable to improve the sensitivity of the detection. Furthermore, the functionalization by receptor molecules on nanoparticle surfaces with a high curvature radius can increase the accessibility of molecules receptors and favor the molecular recognition with the target biomolecules.<sup>[217, 218]</sup>

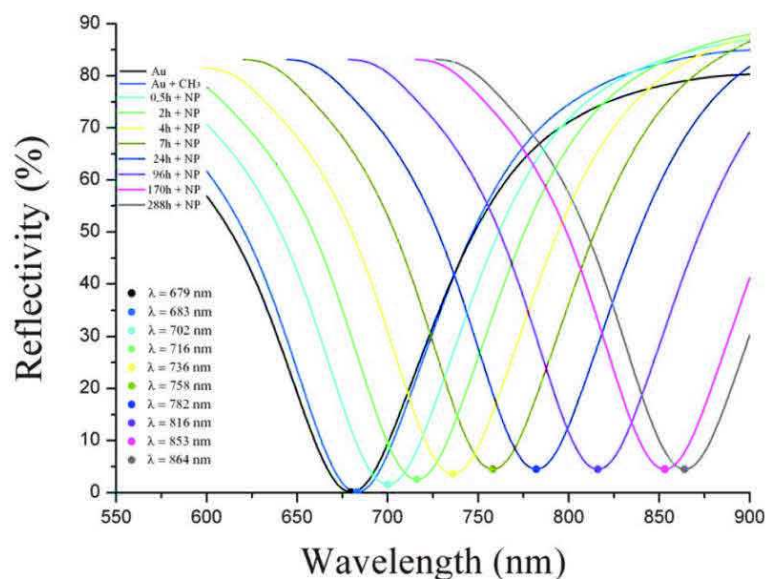


Figure I-33. Position of the plasmon peak resonance as function of the density of magnetite nanoparticles. From Pichon et al.<sup>[64]</sup>

The strategy developed in this manuscript is based on the assembly of magnetite nanoparticles onto gold surfaces. Indeed, as we have seen before, gold is an excellent candidate since it fulfills the condition to generate surface plasmon and allow an easy functionalization by thiol derivatives. Moreover, the iron oxide presents a high refractive index in the visible range which will allow controlling the plasmonic properties of gold substrate. Therefore, the assembly of magnetite nanoparticles by CuAAC “click” chemistry is a good opportunity since the synthesis and assembling processes are well controlled on gold surface which were functionalized by SAMs. The assembly of  $\text{Fe}_3\text{O}_4$  nanoparticles through covalent binding to the surface using click chemistry brings many advantages such as:

- Versatility; terminal head groups at the surface can be chosen in a variety of different functions.
- Specificity; crucial point for the preparation of nanoparticle and further assembly for the grafting of bio-receptors which are essential for the SPR detection of analytes.
- Size; detection happening in the vicinity of the metal, thin layer of materials is convenient to optimize the signal.

Synthesis and assembly processes allow the control of the size and density of the nanoparticles to tailor the plasmonic properties of the gold substrate. The grafting of receptor molecules at the surface of nanoparticles can be done by reusing the CuAAC “click” chemistry. Indeed molecules functionalized with functional groups available for the “click” reaction are grafted on the assembly of magnetite nanoparticles.

## D. Bibliography

- [1] T. F. W. Barth, E. P., *Zeitschrift für Kristallographie*, (1932) **82**, 325.
- [2] Pauly, M., *Université de Strasbourg*, (2010),
- [3] R. M. Cornell, U. S., *The Iron Oxides: Structure, Properties, Reactions, Occurrences and Uses*, VCH, W. Ed. (2003).
- [4] P. Novak, H. S., J. Englich, J. Kohout, V. A. M. Brabers, *Physical Review B*, (2000) **61**, 1256.
- [5] Antonov, V. N.; Harmon, B. N.; Antropov, V. P.; Perlov, A. Y.; Yaresko, A. N., *Physical Review B*, (2001) **64**,
- [6] Nanoparticles, V. C. d. O. o. l., *JACS*, (2007) **129**, 10358.
- [7] M. Jackson, B. M., J. Bowles, *The Iron Quarterly*, (2011) **20**, 1.
- [8] Safronov, A. P.; Beketov, I. V.; Komogortsev, S. V.; Kurllyandskaya, G. V.; Medvedev, A. I.; Leiman, D. V.; Larrañaga, A.; Bhagat, S. M., *AIP Advances*, (2013) **3**, 052135.
- [9] Santoyo Salazar, J.; Perez, L.; de Abril, O.; Truong Phuoc, L.; Ihiwakrim, D.; Vazquez, M.; Greneche, J.-M.; Begin-Colin, S.; Pourroy, G., *Chemistry of Materials*, (2011) **23**, 1379.
- [10] Sandulyak, A. A.; Sandulyak, A. V.; Ershova, V.; Pamme, N.; Ngmasom, B.; Iles, A., *Journal of Magnetism and Magnetic Materials*, (2017) **441**, 724.
- [11] Query, M. R., (1985),
- [12] Ali, A.; Zafar, H.; Zia, M.; Ul Haq, I.; Phull, A. R.; Ali, J. S.; Hussain, A., *Nanotechnology, science and applications*, (2016) **9**, 49.
- [13] Salata, O., *Journal of Nanobiotechnology*, (2004) **2**, 3.
- [14] F. Hasany, S.; Ahmed, I.; J, R.; Rehman, A., *Nanoscience and Nanotechnology*, (2013) **2**, 148.
- [15] Xu, J.; Sun, J.; Wang, Y.; Sheng, J.; Wang, F.; Sun, M., *Molecules*, (2014) **19**, 11465.
- [16] Gupta, A. K.; Gupta, M., *Biomaterials*, (2005) **26**, 3995.
- [17] S. Laurent, D. F., M. Port, Al. Roch, C. Robic, L. Vander Elst, R. N. Muller, *Chemical reviews*, (2008) **108**, 2064.
- [18] Figuerola, A.; Di Corato, R.; Manna, L.; Pellegrino, T., *Pharmacological research*, (2010) **62**, 126.
- [19] Lu, A. H.; Salabas, E. L.; Schuth, F., *Angew Chem Int Ed Engl*, (2007) **46**, 1222.
- [20] J. A. Lopez-Pérez, M. A. L.-Q., J. Mira, and J. Rivas, *IEEE Transactions on magnetics*, (1997) **33**, 4359.
- [21] D. Chen, R. X., *Materials Research Bulletin*, (1998) **33**, 1015.
- [22] Wan, J.; Cai, W.; Meng, X.; Liu, E., *Chem Commun (Camb)*, (2007), 5004.
- [23] Zeng, S. S. a. H., *JACS*, (2002) **124**, 8204.
- [24] Shouheng Sun, H. Z., David B. Robinson, Simone Raoux, Philip M. Rice, Shan X. Wang, and Guanxiong Li, *JACS*, (2004) **126**, 273.
- [25] U. Jeong, X. T., Y. Wang, H. Yang, Y. X., *Advanced materials*, (2006) **19**, 33.
- [26] Victor K. LaMer, R. H. D., *JACS*, (1950) **72**, 4847.
- [27] Baaziz, W.; Pichon, B. P.; Fleutot, S.; Liu, Y.; Lefevre, C.; Greneche, J.-M.; Toumi, M.; Mhiri, T.; Begin-Colin, S., *The Journal of Physical Chemistry C*, (2014) **118**, 3795.
- [28] Demortiere, A.; Panissod, P.; Pichon, B. P.; Pourroy, G.; Guillon, D.; Donnio, B.; Begin-Colin, S., *Nanoscale*, (2011) **3**, 225.
- [29] Cotin, G., *Université de Strasbourg* (2017).
- [30] Xiaojie LIU, B. P. P., Corinne Ulhaq, Christophe Lefevre, Jean-Marc Greneche, Dominique Begin, and Sylvie Begin-Colin, *Chem Mater*, (2015) **27**, 4073.
- [31] Park, J.; An, K.; Hwang, Y.; Park, J. G.; Noh, H. J.; Kim, J. Y.; Park, J. H.; Hwang, N. M.; Hyeon, T., *Nature materials*, (2004) **3**, 891.
- [32] Liese, H. C., *The American Mineralogist*, (1967) **52**, 1198.
- [33] Baaziz, W., *Université de Strasbourg*, (2011),
- [34] Bellido, E.; Domingo, N.; Ojea-Jimenez, I.; Ruiz-Molina, D., *Small*, (2012) **8**, 1465.

- [35] F. C. Meldrum, N. A. K., and J. H. Fendler, *J Phys Chem* (1994) **98**, 4506.
- [36] F. Mammeri, Y. L. B., T. J. Daou, J-L. Gallani, S. Colis, G. Pourroy, B. Donnio, D. Guillon, S. Beégin-Colin, *J Phys Chem B*, (2009) **113**, 734.
- [37] Pauly, M.; Pichon, B. P.; Panissod, P.; Fleutot, S.; Rodriguez, P.; Drillon, M.; Begin-Colin, S., *Journal of Materials Chemistry*, (2012) **22**, 6343.
- [38] Pichon, B. P.; Louet, P.; Felix, O.; Drillon, M.; Begin-Colin, S.; Decher, G., *Chemistry of Materials*, (2011) **23**, 3668.
- [39] J. C. Love, L. A. E., J. K. Kriebel, R. G. Nuzzo, G. M. Whitesides, *Chemical reviews*, (2005) **105**, 1103.
- [40] Morel, A. L.; Volmant, R. M.; Methivier, C.; Krafft, J. M.; Boujday, S.; Pradier, C. M., *Colloids and surfaces. B, Biointerfaces*, (2010) **81**, 304.
- [41] Bedford, E. E.; Spadavecchia, J.; Pradier, C. M.; Gu, F. X., *Macromolecular bioscience*, (2012) **12**, 724.
- [42] Briand, E.; Humblot, V.; Landoulsi, J.; Petronis, S.; Pradier, C. M.; Kasemo, B.; Svedhem, S., *Langmuir*, (2011) **27**, 678.
- [43] Francisco Palazon, P. R. R., Ali Belarouci, Céline Chevalier, Hassan Chamas, Éliane Souteyrand, Abdelkader Souifi, Yann Chevolut and Jean-Pierre Cloarec, *Nanopackaging: From Nanomaterials to the Atomic Scale*, Springer Ed. (2015).
- [44] Palazon F., M. M., Chevolut Y., Souteyrand E., Cloarec J-P., *Journal of Colloid Science and Biotechnology*, (2013) **2**, 249.
- [45] Vericat, C.; Vela, M. E.; Benitez, G.; Carro, P.; Salvarezza, R. C., *Chemical Society reviews*, (2010) **39**, 1805.
- [46] G. E. Poirier, E. D. P., *Science*, (1996) **272**, 1145.
- [47] Onclin, S.; Ravoo, B. J.; Reinhoudt, D. N., *Angew Chem Int Ed Engl*, (2005) **44**, 6282.
- [48] Schilardi, P. L.; Dip, P.; dos Santos Claro, P. C.; Benitez, G. A.; Fonticelli, M. H.; Azzaroni, O.; Salvarezza, R. C., *Chemistry*, (2005) **12**, 38.
- [49] Gang, T.; Yildirim, O.; Kinge, S.; Duan, X.; Reinhoudt, D. N.; Blank, D. H. A.; Rijnders, G.; van der Wiel, W. G.; Huskens, J., *Journal of Materials Chemistry*, (2011) **21**, 14800.
- [50] Yildirim, O.; Gang, T.; Kinge, S.; Reinhoudt, D. N.; Blank, D. H.; van der Wiel, W. G.; Rijnders, G.; Huskens, J., *International journal of molecular sciences*, (2010) **11**, 1162.
- [51] Guerrero, G.; Alauzun, J. G.; Granier, M.; Laurencin, D.; Mutin, P. H., *Dalton Trans*, (2013) **42**, 12569.
- [52] J. P. Collman, N. K. D., T. P. A. Eberspacher, C. E. D. Chidsey, *Langmuir*, (2006) **22**, 2457.
- [53] F. Tielens, E. S., *J Phys Chem C*, (2010) **114**, 9444.
- [54] S. Lee, W. L., C. Kuo, M. Karakachian, Y. Lin, B. Yu, J. Shyue, *J Phys Chem C*, (2010) **114**, 10512.
- [55] M. I. Béthencourt, L. S., P. Chinwangso, T. R. Lee, *Langmuir*, (2008) **25**, 1265.
- [56] R. K. Smith, S. M. R., P. A. Lewis, J. D. Monnell, R. S. Clegg, K. F. Kelly, L. A. Bumm, J. E. Hutchison, P. S. Weiss, *J Phys Chem C*, (2001) **105**, 1119.
- [57] J. P. Folkers, P. E. L., G. M. Whitesides, *Langmuir*, (1992) **8**, 1330.
- [58] Yu, Q.; Chen, S.; Taylor, A. D.; Homola, J.; Hock, B.; Jiang, S., *Sensors and Actuators B: Chemical*, (2005) **107**, 193.
- [59] Valiokas, R.; Malysheva, L.; Onipko, A.; Lee, H.-H.; Ruželè, Ž.; Svedhem, S.; Svensson, S. C. T.; Gelius, U.; Liedberg, B., *Journal of Electron Spectroscopy and Related Phenomena*, (2009) **172**, 9.
- [60] Smith, R. K.; Lewis, P. A.; Weiss, P. S., *Progress in Surface Science*, (2004) **75**, 1.
- [61] L. Yan, C. M., A. Terfort, G. M. Whitesides, *Langmuir*, (1997) **13**, 6704.
- [62] J. Noh, T. M., K. Nakajima, H. Lee, M. Hara, *J Phys Chem B*, (2000) **104**, 7411.
- [63] F. Tielens, V. H., C-M. Pradier, M. Calatayud, F. Illas, *Langmuir*, (2009) **25**, 9980.
- [64] Pichon, B. P.; Barbillon, G.; Marie, P.; Pauly, M.; Begin-Colin, S., *Nanoscale*, (2011) **3**, 4696.
- [65] H. C. Kolb, M. G. F., K. B. Sharpless, *Angew Chem Int Ed*, (2001) **40**, 2004.
- [66] L. F. Tietze, A. S., *Eur. J. Org. Chem.*, (1998) **189**, 1629.
- [67] K. V. Gothelf, K. A. J., *Chemical reviews*, (1998) **98**, 863.
- [68] J. P. Collman, N. K. D., C. E. D. Chidsey, *Langmuir*, (2004) **20**, 1051.

- [69] T. Lummerstorfer, H. H., *J Phys Chem B*, (2004) **108**, 3963.
- [70] Li, Y.; Wang, J.; Cai, C., *Langmuir*, (2011) **27**, 2437.
- [71] Upadhyay, A. P.; Behara, D. K.; Sharma, G. P.; Bajpai, A.; Sharac, N.; Ragan, R.; Pala, R. G.; Sivakumar, S., *ACS applied materials & interfaces*, (2013) **5**, 9554.
- [72] Rianasari, I.; de Jong, M. P.; Huskens, J.; van der Wiel, W. G., *International journal of molecular sciences*, (2013) **14**, 3705.
- [73] Toulemon, D.; Pichon, B. P.; Cattoen, X.; Man, M. W.; Begin-Colin, S., *Chem Commun (Camb)*, (2011) **47**, 11954.
- [74] Toulemon, D.; Pichon, B. P.; Leuvre, C.; Zafeiratos, S.; Papaefthimiou, V.; Cattoën, X.; Bégin-Colin, S., *Chemistry of Materials*, (2013) **25**, 2849.
- [75] Kinge, S.; Gang, T.; Naber, W. J. M.; van der Wiel, W. G.; Reinhoudt, D. N., *Langmuir*, (2011) **27**, 570.
- [76] Toulemon, D., *Université de Strasbourg*, (2013),
- [77] Mark A. Olson, A. C., Rafal Klajn, Lei Fang, Sanjeev K. Dey, Kevin P. Browne, Bartosz A. Grzybowski, J. Fraser Stoddart, *Nano Letters*, (2009) **9**, 3185.
- [78] Kinge, S.; Crego-Calama, M.; Reinhoudt, D. N., *Chemphyschem : a European journal of chemical physics and physical chemistry*, (2008) **9**, 20.
- [79] V. Mahalingam, S. O., M. Peter, B. Jan Ravoo, J. Huskens, D. N. Reinhoudt, *Langmuir*, (2004) **20**, 11756.
- [80] J. Huskens, M. A. D., D. N. Reinhoudt, *Angew Chem Int Ed*, (2002) **47**, 4467.
- [81] Mulder, A.; Onclin, S.; Péter, M.; Hoogenboom, J. P.; Beijleveld, H.; ter Maat, J.; García-Parajó, M. F.; Ravoo, B. J.; Huskens, J.; van Hulst, N. F.; Reinhoudt, D. N., *Small*, (2005) **1**, 242.
- [82] Christian A. Nijhuis, F. Y., Wolfgang Knoll, Jurriaan Huskens, David N. Reinhoudt, *Langmuir*, (2005) **21**, 7866.
- [83] M. Mammen, S. C., G. M. Whitesides, *Angew Chem Int Ed*, (1998) **37**, 2754.
- [84] A. Mulder, J. H., D. N. Reinhoudt, *Org. Biomol. Chem.*, (2004) **2**, 3409.
- [85] F. Pincet, E. P., *Faraday Communications*, (1995) **91**, 4329.
- [86] Wolfgang H. Binder, C. K., Marina Josipovic, Christoph J. Straif, Gernot Friedbacher, *Macromolecules*, (2006) **39**, 8092.
- [87] Ronald Zirbs, F. K., Peter Hinterdorfer, and Wolfgang H. Binder, *Langmuir*, (2005) **21**, 8414.
- [88] Singh, P.; Ménard-Moyon, C.; Kumar, J.; Fabre, B.; Verma, S.; Bianco, A., *Carbon*, (2012) **50**, 3170.
- [89] Sessler, J. L.; Lawrence, C. M.; Jayawickramarajah, J., *Chemical Society reviews*, (2007) **36**, 314.
- [90] Viswanathan, K.; Long, T. E.; Ward, T. C., *Langmuir*, (2009) **25**, 6808.
- [91] Kalpana Viswanathan, H. O., Casey L. Elkins, Cheryl Heisey, Thomas C. Ward, Timothy E. Long, *Langmuir*, (2006) **22**, 1099.
- [92] K. Viswanathan, H. O., C. L. Elkins, C. Hese, T. C. Ward, T. E. Long, *Langmuir*, (2006) **22**, 1099.
- [93] Andrew K. Boal, F. I., Jason E. DeRouchey, Thomas Thurn-Albrecht, Thomas P. Russell & Vincent M. Rotello, *Nature*, (2000),
- [94] A. Csaki, R. M., J. M. Köhler, W. Fritzsche, *Nucleic Acids Research*, (2000) **28**, 91.
- [95] A. Csaki, R. M., W. Straube, J. M. Köhler, W. Fritzsche, *Nucleic Acids Research*, (2001) **29**, 29.
- [96] C. M. Niemeyer, B. C., S. Gao, L. Chi, S. Peschel, U. Simon, *Colloid Polym Sci*, (2001) **279**, 68.
- [97] Derfus, A. M.; von Maltzahn, G.; Harris, T. J.; Duza, T.; Vecchio, K. S.; Ruoslahti, E.; Bhatia, S. N., *Advanced Materials*, (2007) **19**, 3932.
- [98] Mehmet Veysel Yigit, D. M., and Yi Lu, *Bioconjugate Chem*, (2008) **19**, 412.
- [99] Frédéric Geinguenaud, C. B., Antoine F. Carpentier, and Laurence Motte, *Nanomaterials*, (2015) **5**, 1588.
- [100] Boal, A. K.; Frankamp, B. L.; Uzun, O.; Tuominen, M. T.; Rotello, V. M., *Chemistry of Materials*, (2004) **16**, 3252.
- [101] Jin Seon Park, G. S. L., Yun-Jo Lee, Yong Soo Park, and Kyung Byung Yoon, *JACS*, (2002) **124**, 13366.

- [102] Bedanta, S.; Kleemann, W., *Journal of Physics D: Applied Physics*, (2009) **42**, 013001.
- [103] Roca, A. G.; Niznansky, D.; Poltierova-Vejpravova, J.; Bittova, B.; González-Fernández, M. A.; Serna, C. J.; Morales, M. P., *Journal of Applied Physics*, (2009) **105**, 114309.
- [104] T. J. Daou, J. M. G., G. Pourroy, S. Buathong, A. Derory, C. Ulhaq-Bouillet, B. Donnio, D. Guillon, and S. Begin-Colin, *Chem Mater*, (2008) **20**, 5869.
- [105] Fleutot, S.; Nealon, G. L.; Pauly, M.; Pichon, B. P.; Leuvrey, C.; Drillon, M.; Gallani, J. L.; Guillon, D.; Donnio, B.; Begin-Colin, S., *Nanoscale*, (2013) **5**, 1507.
- [106] B. L. Frankamp, A. K. B., M. T. Tuominen, V. M. Rotello, *JACS*, (2005) **127**, 9731.
- [107] Poddar, P.; Telem-Shafir, T.; Fried, T.; Markovich, G., *Physical Review B*, (2002) **66**,
- [108] Kechrakos, D.; Trohidou, K. N., *Journal of Nanoscience and Nanotechnology*, (2008) **8**, 2929.
- [109] Dorothy Farrell, Y. C., R. William McCallum, Madhur Sachan, Sara A. Majetich, *J Phys Chem C*, (2005) **109**, 13409.
- [110] C. Petit, Z. L. W., M. P. Pileni, *J Phys Chem B*, (2005) **109**, 15309.
- [111] Morup, S.; Tronc, E., *Phys Rev Lett*, (1994) **72**, 3278.
- [112] Trohidou, D. K. a. K. N., *physical Review B*, (1997) **58**, 12169.
- [113] Lafleur, J. P.; Jonsson, A.; Senkbeil, S.; Kutter, J. P., *Biosensors & bioelectronics*, (2016) **76**, 213.
- [114] Fan, X.; White, I. M.; Shopova, S. I.; Zhu, H.; Suter, J. D.; Sun, Y., *Analytica chimica acta*, (2008) **620**, 8.
- [115] Wood, R. W., *Proceedings of the Physical Society of London*, (1902) **18**, 269.
- [116] Fano, U., *Journal of the Optical Society of America*, (1941) **31**, 213.
- [117] Pines, D., *Reviews of Modern Physics*, (1956) **28**, 184.
- [118] Ritchie, R. H., *Physical Review*, (1957) **106**, 874.
- [119] Ritchie, R.; Arakawa, E.; Cowan, J.; Hamm, R., *Physical Review Letters*, (1968) **21**, 1530.
- [120] Otto, A., *Zeitschrift fffir Physik*, (1968) **216**, 398.
- [121] Raether, E. K. a. H., *Zeitschrift für Naturforschung*, (1968) **23**, 2135.
- [122] Zeng, S.; Baillargeat, D.; Ho, H. P.; Yong, K. T., *Chemical Society reviews*, (2014) **43**, 3426.
- [123] Ming Li, S. K. C. a. N. W., *Analyst*, (2015) **140**, 386.
- [124] Estevez, M. C.; Otte, M. A.; Sepulveda, B.; Lechuga, L. M., *Analytica chimica acta*, (2014) **806**, 55.
- [125] Roh, S.; Chung, T.; Lee, B., *Sensors (Basel)*, (2011) **11**, 1565.
- [126] Szunerits, S.; Shalabney, A.; Boukherroub, R.; Abdulhalim, I., *Reviews in Analytical Chemistry*, (2012) **31**,
- [127] Bryche, J.-F., (2016),
- [128] Srivastava, T.; Das, R.; Jha, R., *Plasmonics*, (2012) **8**, 515.
- [129] A. Hoffmann, N. K., Z. Lenkefi, Z. Szentirmay, *Surface science*, (1996) **352-354**, 1043.
- [130] Stefan Löfas, M. M., Inger Rönnerbergd, Esa Stenberg, *Sensors and Actuators B: Chemical*, (1991) **5**, 79.
- [131] B. Liedberg, I. L., *Sensors and Actuators B: Chemical*, (1993) **11**, 63.
- [132] Mayer, K. M.; Hafner, J. H., *Chemical reviews*, (2011) **111**, 3828.
- [133] Amanda J. Haes, S. Z., Jing Zhao, George C. Schatz, Richard P. Van Duyne, *JACS*, (2006) **128**, 10905.
- [134] Sepúlveda, B.; Angelomé, P. C.; Lechuga, L. M.; Liz-Marzán, L. M., *Nano Today*, (2009) **4**, 244.
- [135] Zhang, D.; Liu, Q., *Biosensors & bioelectronics*, (2016) **75**, 273.
- [136] He, L.; Pagneux, Q.; Larroulet, I.; Serrano, A. Y.; Pesquera, A.; Zurutuza, A.; Mandler, D.; Boukherroub, R.; Szunerits, S., *Biosensors and Bioelectronics*, (2017) **89**, 606.
- [137] Tao, N. J.; Boussaad, S.; Huang, W. L.; Arechabaleta, R. A.; D'Agnesse, J., *Review of Scientific Instruments*, (1999) **70**, 4656.
- [138] Radan Slavik, J. H., Jiri Ctyroky, *Sensors and Actuators B*, (1999) **54**, 74.
- [139] Monzón-Hernández, D.; Villatoro, J., *Sensors and Actuators B: Chemical*, (2006) **115**, 227.
- [140] Suzuki, A.; Kondoh, J.; Matsui, Y.; Shiokawa, S.; Suzuki, K., *Sensors and Actuators B: Chemical*, (2005) **106**, 383.

- [141] Chien, F. C.; Lin, C. Y.; Yih, J. N.; Lee, K. L.; Chang, C. W.; Wei, P. K.; Sun, C. C.; Chen, S. J., *Biosensors & bioelectronics*, (2007) **22**, 2737.
- [142] Dostálek, J.; Homola, J.; Miler, M., *Sensors and Actuators B: Chemical*, (2005) **107**, 154.
- [143] G.G. Neningera, P. T., J. Homolaa, S.S. Yee, *Sensors and Actuators B*, (2001) **74**, 145.
- [144] J. T. Hastings, J. G., P. D. Keathley, P. B. Kumaresh, Y. Wei, S. Law, L. G. Bachas, *Optics Express*, (2007) **15**, 17661.
- [145] Slavík, R.; Homola, J., *Sensors and Actuators B: Chemical*, (2007) **123**, 10.
- [146] Jennifer S. Shumaker-Parry, C. T. C., *Analytical chemistry*, (2004) **76**, 907.
- [147] Alexander Zybin, C. G., Vladimir M. Mirsky, Jurgen Kuhlmann, Otto S. Wolfbeis, Kay Niemax, *Analytical chemistry*, (2005) **77**, 2393.
- [148] Piliarik, M.; Vaisocherova, H.; Homola, J., *Biosensors & bioelectronics*, (2005) **20**, 2104.
- [149] Timothy M Chinowsky, M. S. G., Kyle S Johnston, Kjell Nelson, Thayne Edwards, Elain Fu, Paul Yager, *Biosensors & bioelectronics*, (2007) **15**, 2208.
- [150] Hye Jin Lee, D. N., Robert M. Corn, *Analytical chemistry*, (2006) **78**, 6504.
- [151] Wen-Chuan Kuo, C. C., and Hsieh-Ting Wu, *Optics Letters*, (2003) **28**, 1329.
- [152] Law, W. C.; Markowicz, P.; Yong, K. T.; Roy, I.; Baev, A.; Patskovsky, S.; Kabashin, A. V.; Ho, H. P.; Prasad, P. N., *Biosensors & bioelectronics*, (2007) **23**, 627.
- [153] Lin He, M. D. M., Sheila R. Nicewarner, Frank G. Salinas, Stephen J. Benkovic, Michael J. Natan, and Christine D. Keating, *JACS*, (2000) **122**, 9071.
- [154] B.P. Nelson, T. E. G., M.R. Liles, R.M. Goodman, R.M. Corn, *Analytical chemistry*, (2001) **73**, 1.
- [155] Yao, X.; Li, X.; Toledo, F.; Zurita-Lopez, C.; Gutova, M.; Momand, J.; Zhou, F., *Anal Biochem*, (2006) **354**, 220.
- [156] Besselink, G. A.; Kooyman, R. P.; van Os, P. J.; Engbers, G. H.; Schasfoort, R. B., *Anal Biochem*, (2004) **333**, 165.
- [157] Chung, J. W.; Bernhardt, R.; Pyun, J. C., *Sensors and Actuators B: Chemical*, (2006) **118**, 28.
- [158] Teramura, Y.; Iwata, H., *Anal Biochem*, (2007) **365**, 201.
- [159] Percin, I.; Idil, N.; Bakhshpour, M.; Yilmaz, E.; Mattiasson, B.; Denizli, A., *Sensors (Basel)*, (2017) **17**,
- [160] Oh, B. K.; Kim, Y. K.; Park, K. W.; Lee, W. H.; Choi, J. W., *Biosensors & bioelectronics*, (2004) **19**, 1497.
- [161] J.W. WASWA, C. D. a. J. I., *Journal of Food Process Engineering*, (2006) **29**, 373.
- [162] A. V. Kabashin, P. E., S. Pastkovsky, W. Hendren, G. A. Wurtz, R. Atkinson, R. Pollard, V. A. Podolskiy and A. V. Zayats, *Nature Material*, (2009) **8**, 867.
- [163] Sun, L.; Chen, P.; Lin, L., (2016),
- [164] Mie, G., *ANNALEN DER PHYSIK*, (1908) **3**, 377.
- [165] Noguez, C., *J Phys Chem C*, (2007) **111**, 3806.
- [166] Focsan, M.; Campu, A.; Craciun, A. M.; Potara, M.; Leordean, C.; Maniu, D.; Astilean, S., *Biosensors & bioelectronics*, (2016) **86**, 728.
- [167] Pal, S. K. G. a. T., *Chemical reviews*, (2007) **107**, 4797.
- [168] Halas, N. J.; Lal, S.; Chang, W. S.; Link, S.; Nordlander, P., *Chemical reviews*, (2011) **111**, 3913.
- [169] Kadir Aslan, C. C. L., and Victor H. Pérez-Luna, *J Phys Chem B*, (2004) **108**, 15631.
- [170] Mei Li, K. K. W. W., and Stephen Mann, *Chem Mater*, (1999) **11**, 23.
- [171] Zeng, Z.; Mizukami, S.; Kikuchi, K., *Analytical chemistry*, (2012) **84**, 9089.
- [172] James J. Storhoff, A. A. L., Robert C. Mucic, Chad A. Mirkin, Robert L. Letsinger, and George C. Schatz, *J. Am. Chem. Soc.*, (2000) **122**, 4640.
- [173] Chad. A. Mirkin, R. L., R. Mucic, J. Storhoff, *Letter to Nature*, (1996) **382**, 607.
- [174] Szunerits, S.; Boukherroub, R., *Chem Commun (Camb)*, (2012) **48**, 8999.
- [175] Stuart, D. A.; Haes, A. J.; Yonzon, C. R.; Hicks, E. M.; Van Duyne, R. P., *IEE proceedings. Nanobiotechnology*, (2005) **152**, 13.
- [176] Barbillon, G., *Micromachines*, (2012) **3**, 21.
- [177] Barbillon, G.; Bijeon, J. L.; Plain, J.; Royer, P., *Thin Solid Films*, (2009) **517**, 2997.

- [178] Chen, S.; Svedendahl, M.; Kall, M.; Gunnarsson, L.; Dmitriev, A., *Nanotechnology*, (2009) **20**, 434015.
- [179] Duyne, A. J. H. a. R. P. V., *JACS*, (2002) **124**, 10596.
- [180] G. Barbillon, J.-L. B., J. - S. Bouillard, J. Plain, M. Lamy De La Chapelle, P.-M. Adam, P. Royer, *Journal of Microscopy*, (2007) **229**, 270.
- [181] Akjouj, A.; Lévêque, G. t.; Szunerits, S.; Pennec, Y.; Djafari-Rouhani, B.; Boukherroub, R.; Dobrzyński, L., *Surface Science Reports*, (2013) **68**, 1.
- [182] A. Shalabney, I. A., *Optics Letters*, (2012) **37**, 1175.
- [183] Hong-Yu Lin, W.-H. T., Yu-Chia Tsao, and Bor-Chiou Sheu, *Applied Optics*, (2007) **46**, 800.
- [184] Ma, Y.; Farrell, G.; Semenova, Y.; Chan, H. P.; Zhang, H.; Wu, Q., *Photonics and Nanostructures - Fundamentals and Applications*, (2014) **12**, 69.
- [185] Yee, R. C. J. a. S. S., *Sensors and Actuators B*, (1993) **12**, 213.
- [186] Ming-Hung Chiu, S.-F. W. a. R.-S. C., *Optics Letters*, (2005) **30**, 233.
- [187] Oliner, A. H. a. A. A., *Applied Optics*, (1965) **4**, 1275.
- [188] Lakowicz, J. R., *Plasmonics*, (2006) **1**, 5.
- [189] Méjard, R.; Dostálek, J.; Huang, C.-J.; Griesser, H.; Thierry, B., *Optical Materials*, (2013) **35**, 2507.
- [190] Burke, J. J.; Stegeman, G. I.; Tamir, T., *Physical Review B*, (1986) **33**, 5186.
- [191] Slavík, R.; Homola, J., *Optics Communications*, (2006) **259**, 507.
- [192] Shalabney, A.; Abdulhalim, I., *Laser & Photonics Reviews*, (2011) **5**, 571.
- [193] Sarkar, M.; Besbes, M.; Moreau, J.; Bryche, J.-F.; Olivéro, A.; Barbillon, G.; Coutrot, A.-L.; Bartenlian, B.; Canva, M., *ACS Photonics*, (2015) **2**, 237.
- [194] Linda S. Jung, C. T. C., Timothy M. Chinowsky, Mimi N. Mar, and Sinclair S. Yee, *Langmuir*, (1998) **14**, 5636.
- [195] Huang, D.-W., *Optical Engineering*, (2010) **49**, 054403.
- [196] P. K. Jain, M. A. E.-S., *Nano Letter*, (2008) **8**, 4347.
- [197] Rios, F.; Smirnov, S., *ACS applied materials & interfaces*, (2009) **1**, 768.
- [198] J. Spinke, M. L., H.-J. Guder, L. Angermaier, W. Knoll, *Langmuir*, (1993) **9**, 1821.
- [199] V. H. Pérez-Luna, M. J. O. B., K. A. Opperman, P. D. Hampton, Gabriel P. Lopez, L. A. Klumb, P. S. Stayton, *JACS*, (1999) **121**, 6469.
- [200] L. S. Jung, K. E. N., C. T. Campbell, P. S. Stayton, S. S. Yee, V. Pérez-Luna, G. P. Lopez, *Sensors and Actuators B*, (1999) **54**, 137.
- [201] Chiu, N. F.; Fan, S. Y.; Yang, C. D.; Huang, T. Y., *Biosensors & bioelectronics*, (2017) **89**, 370.
- [202] Sabine Szunerits, R. B., *Langmuir*, (2006) **22**, 1660.
- [203] Lahav, A., *Journal of Nanophotonics*, (2009) **3**, 031501.
- [204] Wijaya, E.; Lenaerts, C.; Maricot, S.; Hastanin, J.; Habraken, S.; Vilcot, J.-P.; Boukherroub, R.; Szunerits, S., *Current Opinion in Solid State and Materials Science*, (2011) **15**, 208.
- [205] L. Andrew Lyon, D. J. P., and Michael J. Natan, *J. Phys. Chem. B*, (1999) **103**, 5826.
- [206] L. Andrew Lyon, M. D. M., and Michael J. Natan, *Anal. Chem*, (1998) **70**, 5177.
- [207] Besselink, G. A. J.; Kooyman, R. P. H.; van Os, P. J. H. J.; Engbers, G. H. M.; Schasfoort, R. B. M., *Analytical Biochemistry*, (2004) **333**, 165.
- [208] Ryken, J.; Li, J.; Steylaerts, T.; Vos, R.; Loo, J.; Jans, K.; Van Roy, W.; Stakenborg, T.; Van Dorpe, P.; Lammertyn, J.; Lagae, L., *Sensors and Actuators B: Chemical*, (2014) **200**, 167.
- [209] Sun, Y.; Bai, Y.; Song, D.; Li, X.; Wang, L.; Zhang, H., *Biosensors & bioelectronics*, (2007) **23**, 473.
- [210] Scott D. Soelberg, R. C. S., Ajit P. Limaye, and Clement E. Furlong, *Analytical chemistry*, (2009) **81**, 2357.
- [211] Wang, J.; Zhu, Z.; Munir, A.; Zhou, H. S., *Talanta*, (2011) **84**, 783.
- [212] Sadrolhosseini, A. R.; Naseri, M.; Kamari, H. M., *Optics Communications*, (2017) **383**, 132.
- [213] Zamfir, L.-G.; Geana, I.; Bourigua, S.; Rotariu, L.; Bala, C.; Errachid, A.; Jaffrezic-Renault, N., *Sensors and Actuators B: Chemical*, (2011) **159**, 178.
- [214] Lee, K. S.; Lee, M.; Byun, K. M.; Lee, I. S., *Journal of Materials Chemistry*, (2011) **21**, 5156.

- [215] Garibo, D.; Campbell, K.; Casanova, A.; de la Iglesia, P.; Fernández-Tejedor, M.; Diogène, J.; Elliott, C. T.; Campàs, M., *Sensors and Actuators B: Chemical*, (2014) **190**, 822.
- [216] Teramura, Y.; Arima, Y.; Iwata, H., *Anal Biochem*, (2006) **357**, 208.
- [217] Park, J.-W.; Min, H.; Kim, Y.-P.; Kyong Shon, H.; Kim, J.; Moon, D. W.; Lee, T. G., *Surface and Interface Analysis*, (2009) **41**, 694.
- [218] Kim, Y.-P.; Hong, M.-Y.; Shon, H. K.; Chegal, W.; Cho, H. M.; Moon, D. W.; Kim, H.-S.; Lee, T. G., *Applied Surface Science*, (2008) **255**, 1110.



## II. CHAPITRE II - Structuration of Iron Oxide Nanoparticle Assemblies

The aim of this chapter is to study the synthesis and the assembly of iron oxide nanoparticles onto gold substrates. The synthesis of nanoparticles allows a good control on the size and the shape of the nanoparticles in order to tune their intrinsic properties. Nanoparticles were assembled onto a surface through covalent binding by performing the CuAAC “click” chemistry which presents the advantages to be robust, highly selective, versatile and to create stable assemblies. Finally, the magnetic properties of nanoparticles were studied as function of their size and of their spatial arrangement.

## A. Nanoparticle synthesis

Iron oxide nanoparticles have been synthesized by thermal decomposition. This method allows controlling a narrow size distribution, a precise control on the morphology and a good stability in suspension. Spherical 10 nm-sized nanoparticles have been used as reference since their stability in organic solvent is very good and their synthesis and purification are well controlled. Furthermore, 5 nm and 20 nm-sized nanoparticles were synthesized by adapting carefully the experimental conditions.

### 1. Experimental details

#### a) *Nanoparticles synthesis conditions*

The nanoparticles synthesis is well mastered in our laboratory.<sup>[1, 2]</sup> An iron stearate precursor was decomposed (2.2 mmol, 1.384 g) in 20 mL of dioctylether ( $T_{\text{boil}} = 288^{\circ}\text{C}$ ) in the presence of oleic acid as a surfactant (4.4 mmol, 1.25 g). The temperature was set thanks to a thermocouple dipped in the solution and controlled by a computer. The mixture was heated at  $110^{\circ}\text{C}$  without a condenser and stirred to solubilize the reactants and to remove the water traces. Then, the mixture was heated up with a condenser with a ramp of  $5^{\circ}\text{C}$  per minute until the boiling temperature was reached. The mixture remained at this temperature for 2 hours and then was cooled down around  $100^{\circ}\text{C}$ . Figure II-1.b shows the target temperature and the temperature measured by the thermocouple. The resulting synthesized nanoparticles coated with oleic acid are noted NP10.

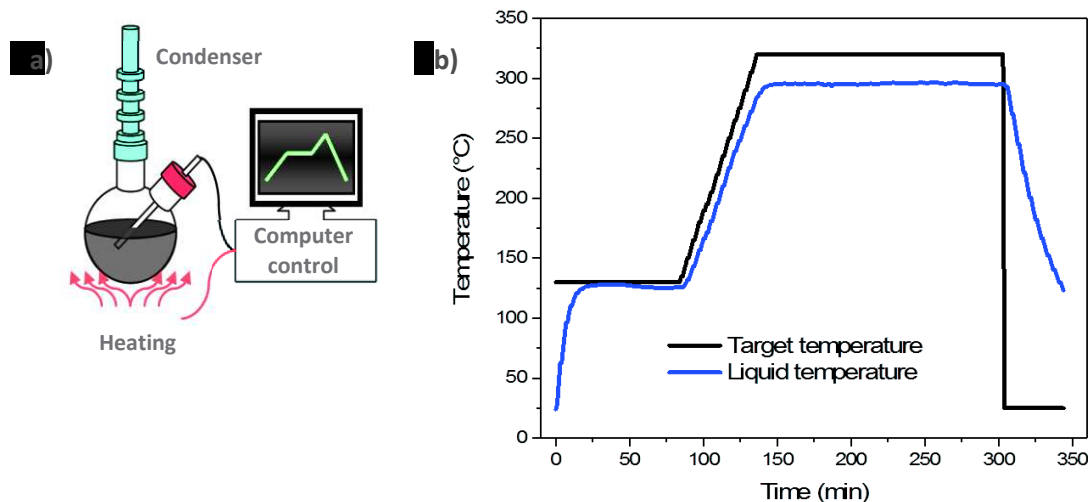


Figure II-1. a) Schematic representation of the thermal decomposition process and b) temperature profile of the setpoint and of the temperature of the reaction media

The thermal decomposition method allows controlling the size of nanoparticles by varying synthesis parameters such as solvent, temperature ramp or quantity of surfactant.<sup>[2]</sup> Therefore, spherical nanoparticles with a diameter of about 20 nm and 5 nm, and denoted NP20 and NP5 respectively, were also synthesized. The table II-1 summarizes the synthesis parameters which allow controlling the size of the nanoparticles.

Table II-1. Summarize of the synthesis parameters as function of the desired size of nanoparticles

	NP5	NP10	NP20
<b>Solvent</b> (boiling temperature)	Diocylether (288°C)	Diocylether (288°C)	Squalane + dibenzylether (470°C)
<b>Oleic acid</b>	No	yes	yes

The synthesis of 5 nm nanoparticles follows the same procedure given for the 10 nm nanoparticles except that no oleic acid was added in the reaction medium. Only the stearate chains present in the iron precursor will act as capping agent. Without oleic acid, which is used as surfactant but is also known to stabilize the iron stearate precursor (leading to its decomposition at higher temperature), the iron precursor will decompose faster and create more nuclei in the solution, thus giving smaller nanoparticles.<sup>[3]</sup>

The synthesis of 20 nm nanoparticles follows a similar protocol as reported previously for NP10 in the exception of squalane ( $T_{\text{boil}} = 470^{\circ}\text{C}$ ) which was used instead of diocylether. The iron stearate (2.9 mmol, 1.832 g) were decomposed in 19.5 mL of squalane and 0.5 mL of dibenzylether in presence of oleic acid (6.6 mmol, 1.89 g). The temperature ramp was slightly different with a first step of 1 hour at 120°C followed by a ramp of 5°C per minute and a last step at 330°C for 1 hour. The mixture was then cooled down to 90°C.

## b) Purification of the nanoparticles

The purification of the nanoparticles is an essential step to remove the excess of oleic acid, unreacted iron stearate and side products resulting from the thermal decomposition process. The control of free molecules in solution is also a crucial point to ensure a good stability of the suspension. Indeed, oleic acid molecules are characterized by an equilibrium between grafted molecules at the surface of nanoparticles and free molecules in the solvent.<sup>[4]</sup> The stability of the nanoparticle suspension is therefore dependent of this equilibrium.

The purification was realized by centrifugation to precipitate the nanoparticles. A mixture of solvents with different polarities was used to separate the nanoparticles from the free molecules. Chloroform was used because of its good affinity to the oleic acid coated nanoparticles. In contrast, acetone favored the precipitation of nanoparticles. The chloroform/acetone mixture (1:5, v:v) was added to the reaction medium and was centrifuged at 14 000 rpm for 5 minutes in order to separate nanoparticles from the other products which remained in the supernatant. This purification step was performed several times and was monitored by infrared spectroscopy until the disappearance of free oleic acid and stearate molecules. FT-IR spectra were recorded for the NP10 sample in order to monitor removal of oleic acid (figure II-2).

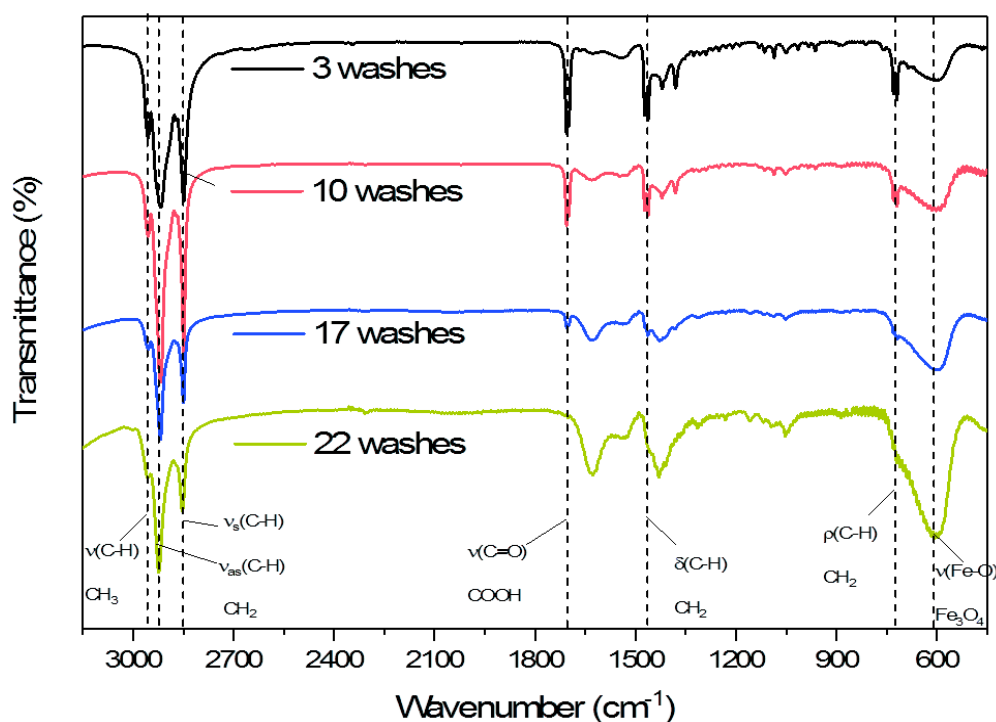


Figure II-2. Infrared spectra of NP10 after 3 washes (black curve), 10 washes (red curve), 17 washes (blue curve) and 22 washes (green curve)

Infrared spectra show the vibrational bands localized in NP10 coated with oleic acid. The broad band localized between 500 cm<sup>-1</sup> and 800 cm<sup>-1</sup> is characteristic of the stretching vibrational modes of Fe-O bonds. The bands corresponding to the symmetric and asymmetric stretching of the C-H bonds of the oleic acid and the stearate are localized at 2850 cm<sup>-1</sup> and 2920 cm<sup>-1</sup> respectively.<sup>[5]</sup> The rocking and bending modes of the C-H bonds are localized at 1460 cm<sup>-1</sup> and 720 cm<sup>-1</sup>, respectively. The vibrational band at 2960 cm<sup>-1</sup> corresponds to the stretching of the C-H binding of the methylene (CH<sub>3</sub>) terminal groups. At 1710 cm<sup>-1</sup> a narrow band is representative of the C=O bonds of the free oleic acid

in solution. The vibrational band at  $1660\text{ cm}^{-1}$  and  $1420\text{ cm}^{-1}$  are representative of the oleic acid grafted on the nanoparticle surface and correspond to the asymmetric  $\nu_{as}(\text{COO}^-)$  and symmetric  $\nu_s(\text{COO}^-)$  stretching modes, respectively.

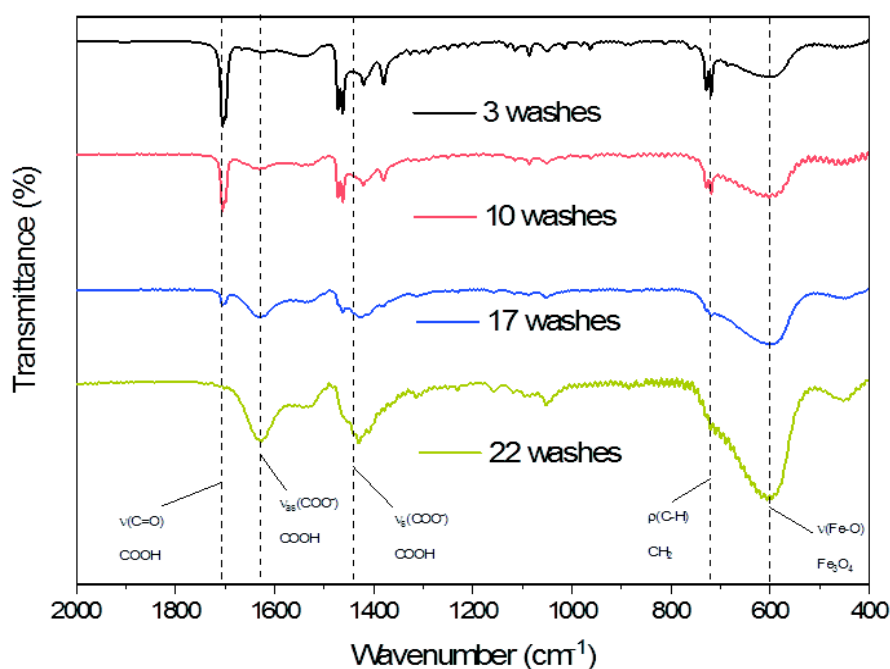


Figure II-3. Infrared spectra of NP10 after washing zoomed in the  $400\text{ cm}^{-1}$ -  $2000\text{ cm}^{-1}$  area

The purification step is evaluated as function of the peak area ratios between the different vibrational bands (table II-2). The nanoparticles coated with oleic acid were purified until the disappearance of the band corresponding to the free oleic acid C=O ( $1710\text{ cm}^{-1}$ ). The intensity ratio between the  $\nu(\text{Fe-O})$  band of iron oxide ( $580\text{ cm}^{-1}$ ) and the  $\nu(\text{C-H})$  band of the alkyl chains ( $2920\text{ cm}^{-1}$ ) has also to be close to one.

Table II-2. Surface area ratios between  $\nu(\text{C-H})$ ,  $\nu(\text{C=O})$ ,  $\rho(\text{C-H})$  and  $\nu(\text{Fe-O})$  vibrational bands.

	$\nu(\text{C=O})/\nu(\text{Fe-O})$	$\nu(\text{C-H})/\nu(\text{Fe-O})$	$\rho(\text{C-H})/\nu(\text{Fe-O})$
3 washes	<b>0.15</b>	<b>0.94</b>	<b>0.04</b>
10 washes	<b>0.07</b>	<b>0.68</b>	<b>0.02</b>
17 washes	<b>0.02</b>	<b>0.30</b>	<b>0.01</b>
22 washes	<b>&lt; 0.01</b>	<b>0.20</b>	<b>&lt;0.01</b>

The disappearance of the  $\nu(\text{C=O})$  and the  $\rho(\text{C-H})$  bands after 22 washes and the different ratios indicates that most of the free molecules in solution were removed. This purification step is different for all synthesis and the number of washes can be strongly dependent of the environmental conditions (hygroscopy, local temperature) in the laboratory. Moreover, the used of warm acetone (pre-heated before the centrifugation) led to a faster removal of the organic species which reduce considerably the number of washes.<sup>[3]</sup>

Infrared spectra were also recorded for the NP5 and NP20 after several washes to get “clean” nanoparticles. The washing step consists in removing the maximum of free molecules while avoiding the aggregation. These washing steps are strongly dependent of the size of the nanoparticles since the surface composition and therefore the binding of the carboxylic acid at the surface of iron oxide is different (cf. II.A.2.a). Infrared spectra of nanoparticles after washing was completed and shown in the figure II-4.

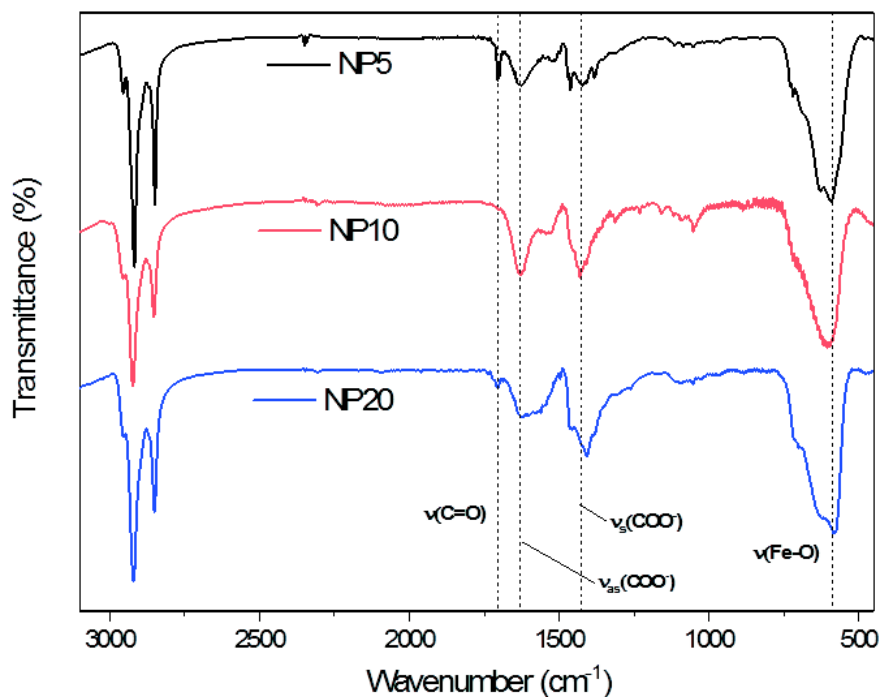


Figure II-4. Infrared spectra of NP5 (black curve), NP10 (red curve) and NP20 (blue curve) after the washing step was completed

The NP5 and NP20 were washed 11 times and 6 times respectively until the  $\nu(\text{Fe-O})/\nu(\text{C-H})$  ratio was close to one. The NP5 and NP20 still present the band of the free oleic acid at  $1710\text{ cm}^{-1}$  in low proportion. However, more washes of these nanoparticles lead to their aggregation.

The strongest dipolar interactions in the NP20 led to the formation of aggregates. An excess of oleic acid is needed and therefore, the washing steps have to be stopped much earlier than for NP10. In the case of NP5, the smaller diameter of the nanoparticles is correlated to a lower surface. Given the weak interactions between the carboxylic acid group and the iron oxide surface, the quantity of free oleic acid in solution should be higher to preserve the equilibrium between the ligand free and adsorbed at the nanoparticle surface which rule the stability of NP5 suspension.

Furthermore, the  $\nu(\text{Fe-O})$  band of iron oxide is located at  $590\text{ cm}^{-1}$  for each size of nanoparticles. A closer look shows that the NP5 and NP10 are closer from the value of the maghemite ( $638\text{ cm}^{-1}$ ) which shows an evolution of the composition. Indeed, smaller nanoparticles exhibit a higher surface/volume ratio which favors the oxidation of magnetite in maghemite (cf. II.A.2.c).<sup>[1]</sup> Moreover, a component at  $630\text{ cm}^{-1}$  can be observed especially for the NP5 and NP20 which show the presence of maghemite. Nevertheless, all the samples present a layer of maghemite due to the surface oxidation<sup>[1]</sup> and the determination of the quantity of maghemite with infrared spectroscopy is complicated because of the method of preparation which can promote the oxidation of magnetite.

## 2. Structural characterizations

### a) *Size and morphology of the nanoparticles*

The size and the morphology of the nanoparticles were characterized by transmission electron microscopy (TEM). The size distribution was calculated by measuring more than 200 nanoparticles using the ImageJ software and was fitted by a Gaussian function. The analysis was done on NP5, NP10 and NP20 (figure II-5).

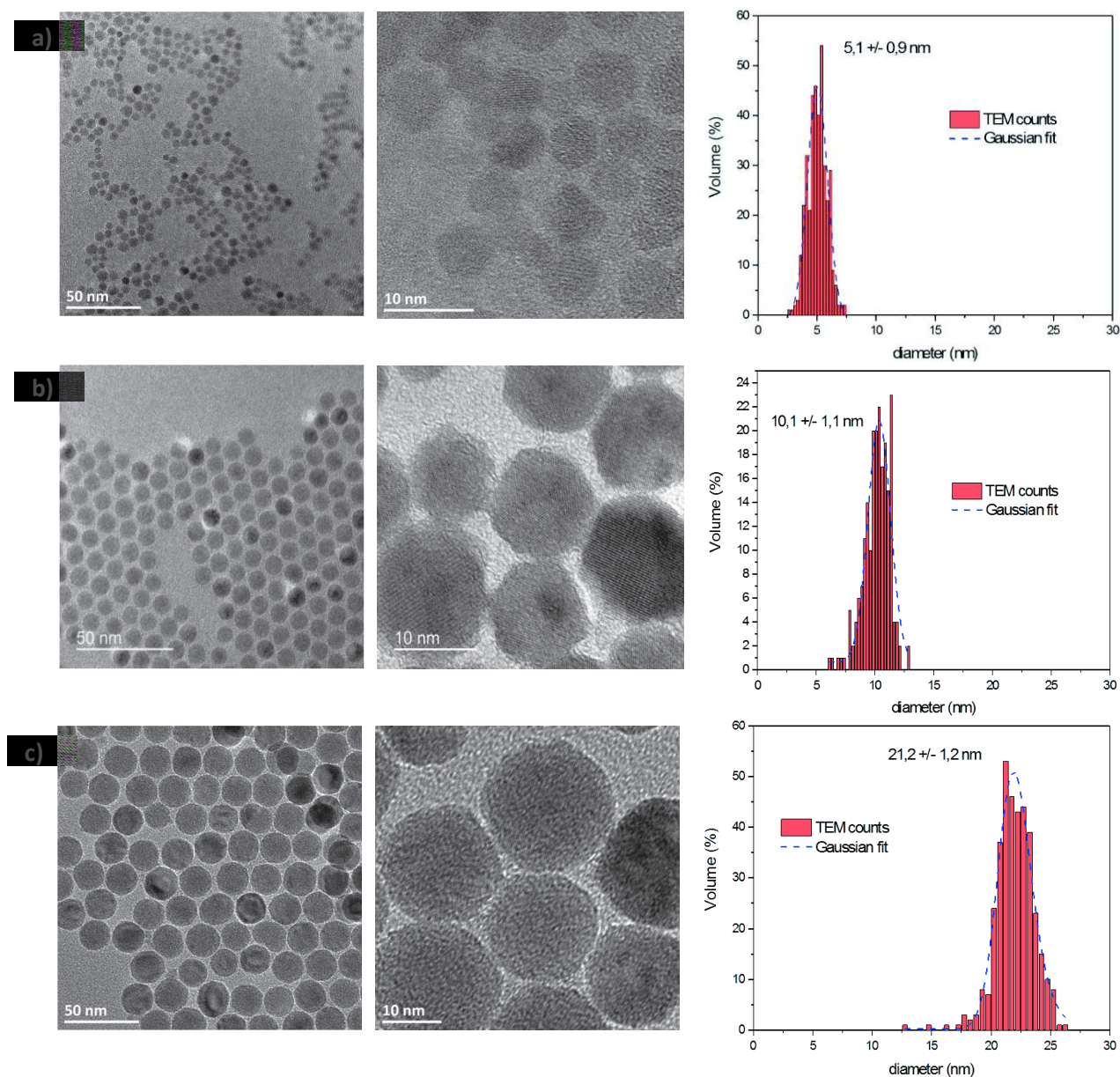


Figure II-5. TEM images of oleic acid coated nanoparticles (NP@OA) and the corresponding size distribution. a) NP5, b) NP10 and c) NP20

TEM images showed spherical morphologies for each size of nanoparticles. High resolution images showed not completely spherical objects, but faceted nanoparticles. The size distributions are narrow for each size of nanoparticles and are centered to  $5.1 \pm 0.8$  nm (16 % deviation),  $10.1 \pm 1.1$

nm (11% deviation) and  $21.2 \pm 1.2$  nm (7% deviation) for NP5, NP10 and NP20, respectively. All nanoparticles present a rather low standard deviation (below 16%). The 20 nm nanoparticles present more facets which have been previously observed.<sup>[6, 7]</sup> Indeed, the crystallographic planes do not present the same surface energy and, therefore, grow at different rates which induce facets which are more visible for the largest nanoparticles.

### b) Colloidal stability of nanoparticle suspension

The preparation of a stable suspension of nanoparticles is an essential step to assemble them onto a surface. The colloidal stability of the suspension has been investigated by granulometry measurements by dynamic light scattering (DLS) in order to determine their distribution of hydrodynamic diameters (figure II-6).

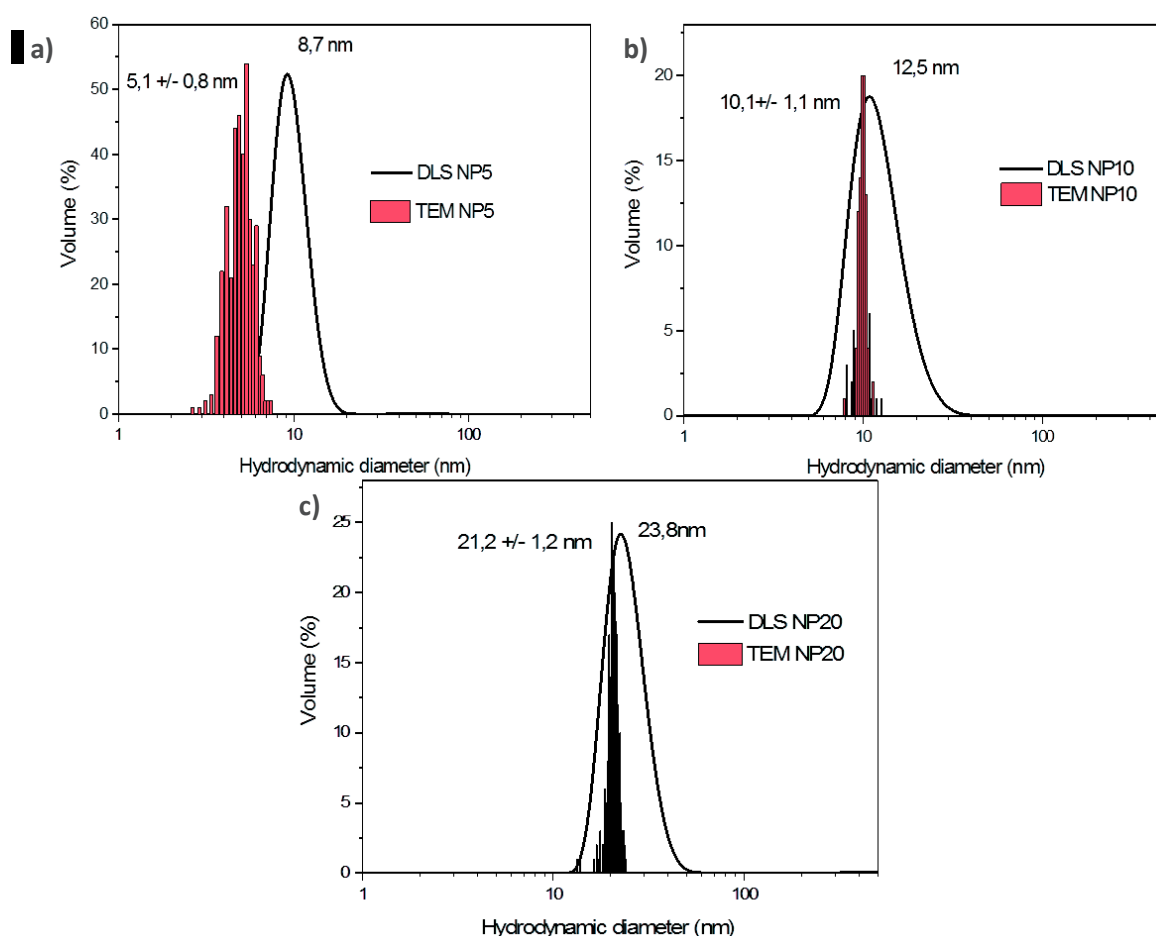


Figure II-6. Hydrodynamic diameter distributions in volume measured by granulometry and histogram of size distributions determined by TEM of a) NP5, b) NP10 and c) NP20

The hydrodynamic diameters were measured in tetrahydrofuran (THF) solvent which will be used for the assembly step. In each case, the hydrodynamic diameter distribution is monomodal with a low polydispersity index which agree with a single population of nanoparticles in suspension. The hydrodynamic diameters centered at 8.7 nm, 12.5 nm and 23.8 nm for NP5, NP10 and NP20, respectively, shows that the nanoparticles were not aggregated since these values are similar to TEM sizes. A slight shift of 2-3 nm can be observed between the size distribution measured on the TEM

images and the peak position of the value given by DLS. Indeed, the measurement of the size by TEM gives the diameter of the inorganic core of the nanoparticles whereas the DLS measurement gives the hydrodynamic diameter which includes the inorganic core, the organic shell corresponding to the oleic acid molecules and the solvation sphere. This analysis shows the good colloidal stability of the nanoparticles in THF.

### c) Structural characterization of the nanoparticles

Nanoparticles were characterized by X-ray diffraction to determine the crystalline phase and their composition. This characterization allows also calculating the size of diffracting domains and the lattice parameter. Figure II-7 shows the XRD patterns of nanoparticles of different sizes.

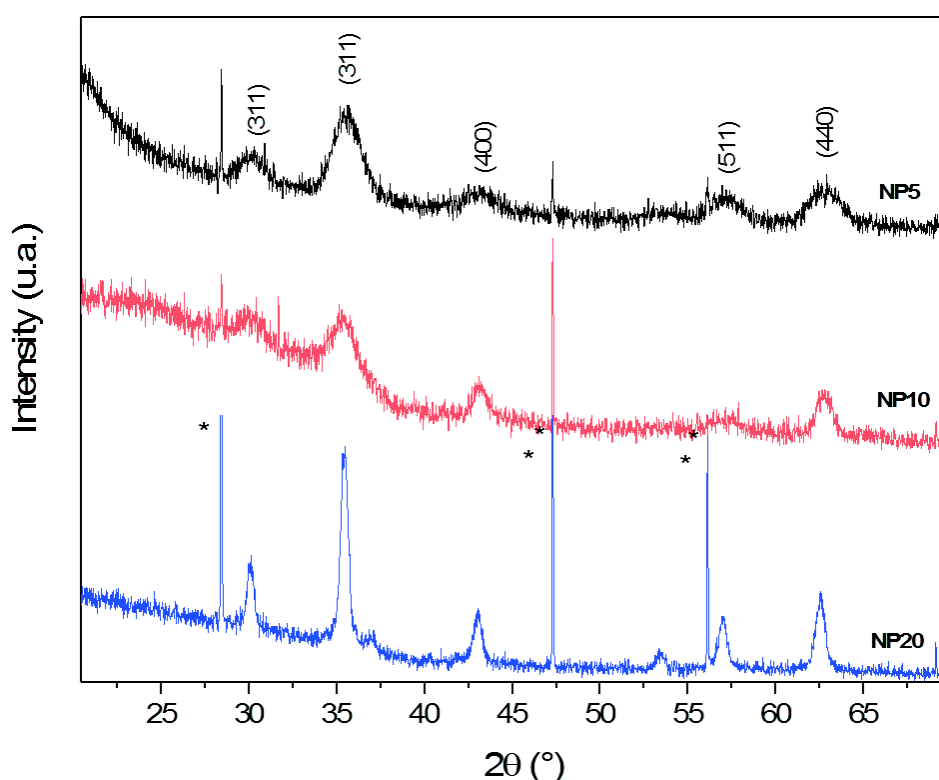


Figure II-7. XRD patterns of NP5 (black curve), NP10 (red curve) and NP20 (blue curve). Calibration silicon peaks are noted with a star

The narrow peaks (marked with a star) are assigned to silicon powder which was added to calibrate XRD patterns in order to perform Rietveld refinements.<sup>2</sup> The diffraction peaks observed for each size of nanoparticle corresponds to the spinel structure. The peak positions between magnetite and maghemite being very close, the refinement with Fullprof software allowed determining the lattice parameters and the mean crystallite sizes (table II.3).

Table II-3. Structural parameters of the nanoparticles

	NP5	NP10	NP20
Lattice parameter (Å)	8.360 ± 0.002	8.379 ± 0.002	8.391 ± 1.000
Crystallite size (nm)	3 ± 1	10 ± 1	13 ± 1

<sup>2</sup> Collaboration with C. Lefevre (IPCMS)

The lattice parameters of the three sizes of nanoparticles are intermediate between the lattice parameters of the stoichiometric magnetite ( $8.396 \pm 0.001 \text{ \AA}$ , JCPDS file n°00-019-0629) and maghemite ( $8.338 \pm 0.001 \text{ \AA}$ , JCPDS file n°00-013-0458) phases. However, the larger nanoparticles (NP20) present a lattice parameter closer to the magnetite than the maghemite. In contrast, the smallest nanoparticles display a cell parameter much closer to the one of maghemite. Indeed, NP5 and NP10 are more sensitive to the surface oxidation<sup>[6]</sup>. As seen in chapter I, the thickness of the maghemite layer at the surface of the nanoparticle is about 2-3 nm and therefore, for small nanoparticles, the contribution of the oxidized layer is the most important.

The XRD patterns show that for larger nanoparticles, the diffraction peaks are narrower meaning larger diffracting domains. Indeed, the crystallite sizes increase with the size of nanoparticles. For NP5 and NP10 the crystallite sizes are similar to the measured sizes with TEM which confirms that the nanoparticles are single crystal. For the NP20, the crystallite size is about 13 nm which is lower than the measured size at TEM (21.2 nm). This has been attributed to the presence of lattice dislocations induced by the oxidation of nanoparticles and explains the smaller structural coherence length compared to TEM size.<sup>[3, 8, 9]</sup>

### 3. Magnetic characterizations

#### a) *Magnetic measurements as function of the applied field*

Magnetic characterizations were performed on NP5, NP10 and NP20 by using a SQUID (Superconducting QUantum Interference Device) magnetometer<sup>3</sup>. Magnetization cycles were obtained by varying an external field between -5 tesla and 5 tesla. The measurements were performed at 300 K and 5 K on samples in the powder state (figure II-8). Saturation magnetization was calculated by measuring the concentration of  $\text{Fe}_3\text{O}_4$  in solution by atomic absorption spectroscopy (AAS) (see appendix A).

---

<sup>3</sup> Collaboration with Lise-Marie Lacroix, LPCNO, Toulouse

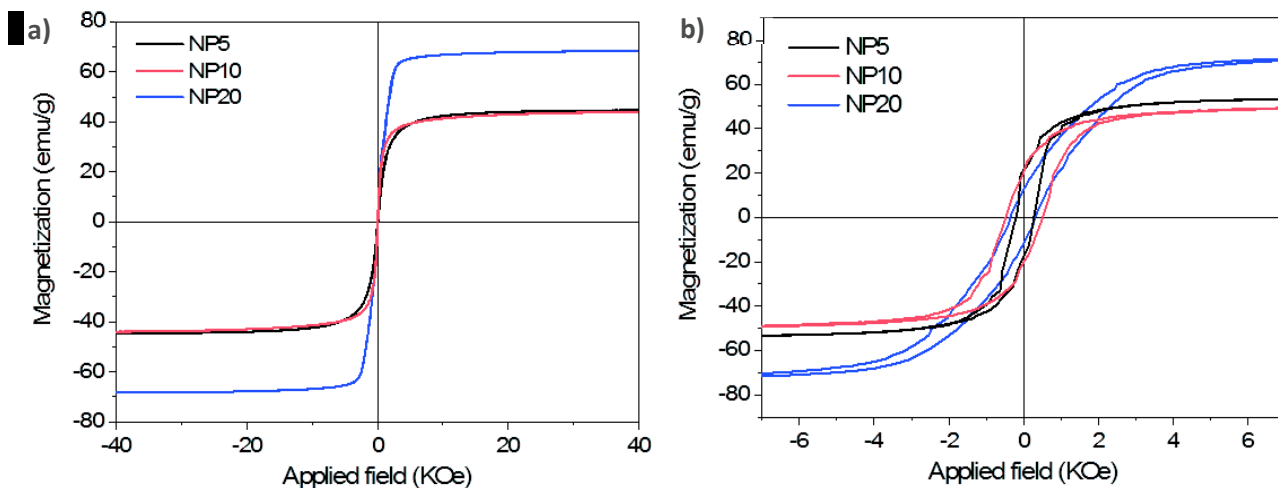


Figure II-8. Magnetization curves as function of applied field for different sizes of nanoparticles at a) 300 K and b) 5 K

No hysteresis loops ( $H_C = 0$  Oe and  $M_R/M_S = 0$ ) were observed at 300 K for the different sizes of nanoparticles which agree with a superparamagnetic behavior. At low temperature (5 K), the cycles present an opening indicating that magnetic moments are blocked. The saturation magnetization, the coercive field and the relative remanent magnetization are extracted from the magnetization curves and summarized in table II-4.

Table II-4. Coercive fields  $H_C$ , relative remanent magnetization  $M_R/M_S$  and saturation magnetization  $M_S$  for the different sizes of nanoparticles at 5 K

Sample	$H_C$ (Oe)	$M_R/M_S$	$M_S$ (emu/g)
NP5	$240 \pm 30$	$0.36 \pm 0.05$	$55 \pm 5$
NP10	$495 \pm 30$	$0.35 \pm 0.05$	$55 \pm 5$
NP20	$330 \pm 30$	$0.16 \pm 0.05$	$75 \pm 5$

The saturation magnetization is lower than the magnetite in the bulk state (92 emu/g). This lower magnetization can be explained by the presence of the oxidized layer at the nanoparticle surface. Indeed, the saturation magnetization of the maghemite (74 emu/g) is lower than the magnetite. The lower  $M_S$  for smaller nanoparticles is due to the composition closer from the maghemite as shown by the structural characterizations. Moreover, defects and surface effect may cause the lower magnetization. A disorder of the magnetic moments can exist at the nanoparticle surface. This phenomenon is called spin canting and induces a diminution of the saturation magnetization.<sup>[1, 7]</sup> For smaller nanoparticles, the contribution of the spin canting is more important which explains the lower  $M_S$  for NP5 and NP10.

The remanent magnetization is the same between NP10 and NP5 ( $M_R/M_S = 0.35$ ) and still below the theoretical value for a random orientation ( $M_R/M_S = 0.5$ ). However this ratio is lower for the NP20 ( $M_R/M_S = 0.16$ ) which results from the strong dipolar interactions which tends to align the magnetic moments. Indeed, the theoretical value corresponds to a random orientation, but the increase of the anisotropy (with the increase of the size for example) can be responsible of the decrease of the  $M_R/M_S$  ratio.

The coercive field of NP10 (495 Oe) is larger than for the NP20 (330 Oe) and the NP5 (240 Oe). This increase of the coercive field with the size of the nanoparticles but decrease for size larger than 10 nm is expected from the literature.<sup>[10-12]</sup> Moreover, the values of  $H_c$  are in accordance with the values found for similar sizes.<sup>[6, 7, 10, 13]</sup> This behavior is explained by the fact that we consider here nanoparticles with a single magnetic domain and with increase of the size the required field to reverse the magnetization increases. Nevertheless, the decrease of the coercive field for NP20 may be related to structural defects in NP20.

The magnetic and structural characterizations of the NP20 can show an ambiguity to their composition and can be relevant of a core/shell structure. The presence of a wüstite core has already been observed on large or cubic nanoparticles (e.g.  $Fe_xO@Fe_{3-6}O_4$  core/shell nanoparticles).<sup>[6, 7, 14]</sup> Moreover, XRD being sensitive to composition above 5 % in mass, we cannot rule out the presence of small amount of wüstite within the core of nanoparticles. Wüstite is antiferromagnetic (AFM) and its coupling with ferrimagnetic (FiM) material may induce exchange bias coupling between interfacial AFM and FiM spins.<sup>[15]</sup> The exchange bias can be observed easily by the shift of the hysteresis loop measured after cooling down under a magnetic field which correspond to the exchange field:

$$H_e = \frac{|H_c^-| - |H_c^+|}{2} \quad \text{Equation II.1}$$

Therefore, magnetization cycles were performed after cooling down to 5 K under an external field of 7 T. This measurement was compared with the cycle at 5 K without external field (figure II-9).

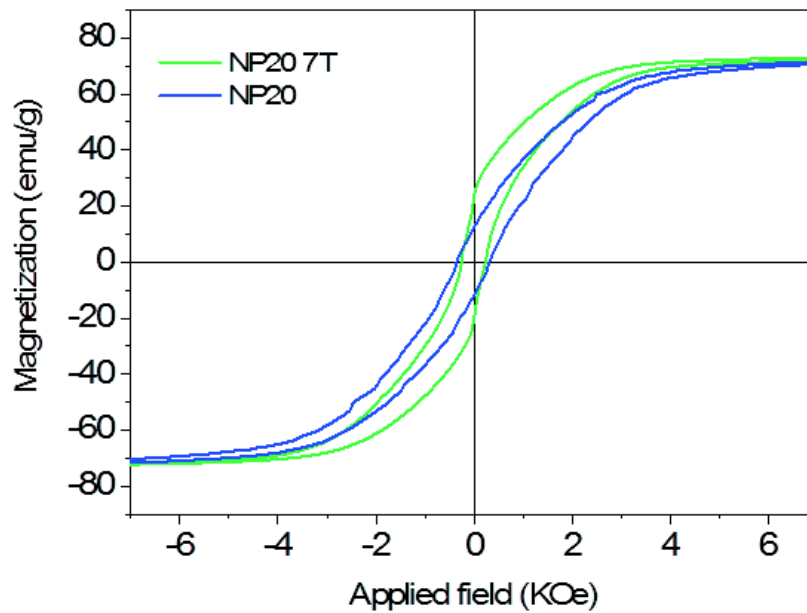


Figure II-9. Magnetization curves as function of applied field recorded at 5K after zero field cooling (ZFC) (blue curve) and field cooling (FC) (green curve) at 7 tesla.

The exchange field measured on the sample is  $H_e = 20$  Oe. This low exchange field is not significant of a wüstite/magnetite core/shell structure as shown previously.<sup>[14]</sup> Nevertheless, this small field can be induced by the coupling between the magnetite and the external spin canting layer.<sup>[1]</sup>

#### b) *Magnetic measurements as function of the temperature*

Magnetization measurements were also performed as a function of the temperature (figure II-10.a). First, magnetization was recorded from 5 K to 350 K after cooling down the sample without applying any magnetic field (Zero Field Cooled, ZFC). Second, magnetization was also recorded from 5 K to 350 K but after cooling the sample under an external magnetic field of 75 Oe (Field Cooled, FC). The ZFC and FC curves allow identifying the blocking temperature ( $T_B$ ) of the samples in the powder state. The blocking temperature is often assimilated to the maximum of the ZFC curve. However, this value is overestimated because the ZFC curve reflects a distribution of magnetic anisotropies which depend on the size distribution of the nanoparticles and of the dipolar interactions. Therefore, it is much accurate to consider that the blocking temperature corresponds to the inflection point of the ZFC curve. This inflection point can be determined by the maximum of the derivative of the difference between ZFC and FC curve (figure II-10.b).<sup>[14]</sup> Therefore the maximum of the ZFC curve is named  $T_{Max}$ .

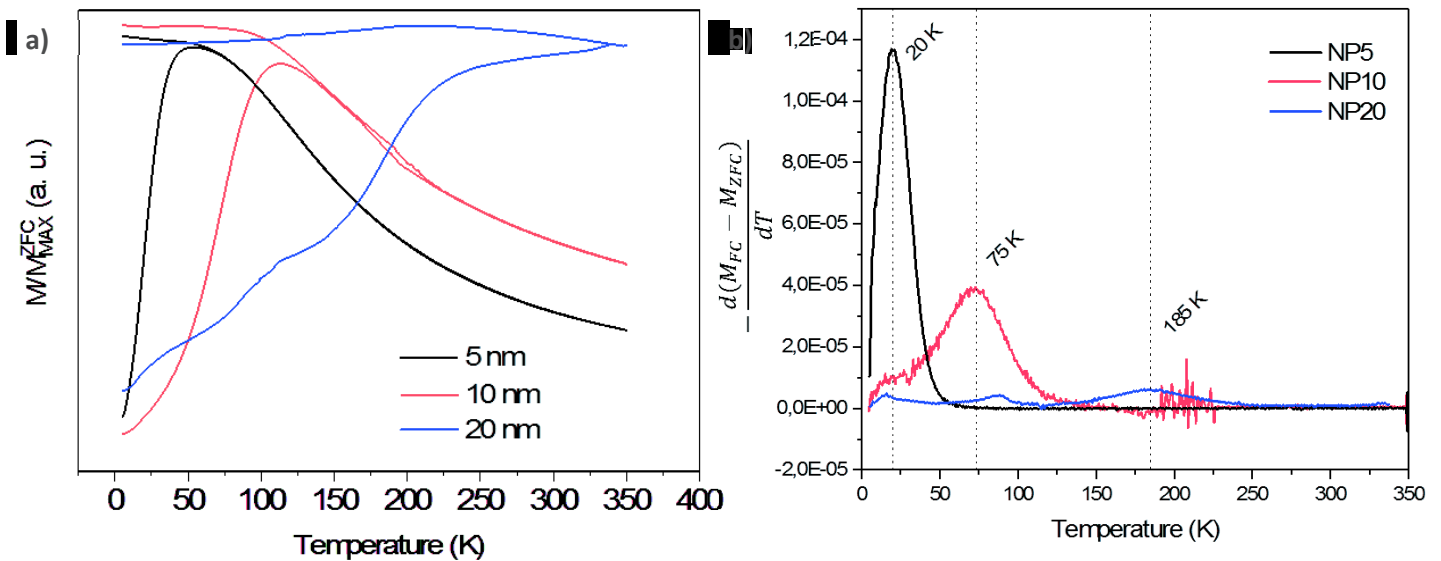


Figure II-10. a) Magnetization as function of temperature (ZFC/FC curves) for different sizes of nanoparticles and b) temperature derivative of the difference between ZFC and FC

Table II-5 summarizes  $T_{Max}$  and  $T_B$  values of the nanoparticles. These values increase with the size of the nanoparticles. Indeed, nanoparticles with larger sizes increase the magnetocrystalline energy and, therefore, a higher thermal energy ( $k_B T$ ) is required to pass the energy barrier  $KV$  (see chapter I).<sup>[6, 13]</sup> In the case of NP20, the  $M(H)$  curve recorded at 300 K agree with a blocking temperature below 300 K. Therefore,  $T_{Max}$  which is larger than 350 K is not coherent with a superparamagnetic behavior.

Table II-5.  $T_{Max}$  and  $T_B$  determined by ZFC/FC curves for different sizes of nanoparticles

Sample	$T_{Max}$	$T_B$
NP5	50 K	20 K
NP10	110 K	75 K
NP20	> 350 K	185 K, 90 K, ≈20 K

The values of  $T_B$  determined with the derivative of the difference between ZFC and FC curves are values lower than the  $T_{Max}$ . The approximation of  $T_B$  corresponding to the maximum of the ZFC values here show clearly an error on its value. Here, the  $T_B$  for each nanoparticle size is below 300 K and is coherent with the superparamagnetic behavior at room temperature showed by  $M(H)$  curves. The  $T_B$  for NP5 and NP10 (20 K and 75 K respectively) are in accordance with their sizes whereas the

NP20 at 185 K is slightly lower than expected.<sup>[6]</sup> Once again, this behavior can be caused by defect in the crystal structure of the nanoparticles. Moreover, NP20 present different contributions in the ZFC curve. A first one can be observed around 90 K and can be attributed at the Verwey transition which corresponds to a structural phase transition and can modified the physical properties of the magnetite such as its conductivity, calorific capacity and magnetization. This transition is visible for large nanoparticles in the ZFC curve.<sup>[16]</sup> A second contribution is observed around 20 K and can be attributed to the canted layer at the surface of the nanoparticles.<sup>[3]</sup>

#### 4. Conclusion

Iron oxide nanoparticles with different sizes have been synthesized by thermal decomposition. Their structural and magnetic properties have been studied. The structural characterizations showed that the size of the nanoparticles have an influence on their composition. Small nanoparticles favor the maghemite phase which has for main consequence to reduce saturation magnetization. In contrast, large nanoparticles favor the contribution of magnetite and larger magnetization saturation. Nevertheless, nanoparticles of 5 nm, 10 nm and 20 nm in the powder state display the superparamagnetic behavior at room temperature. The saturation magnetization and the blocking temperature increases with the size of the nanoparticles. Therefore, larger nanoparticles favor magnetic anisotropy collective and stronger dipolar interactions which may alter their stability as suspensions.

## B. Nanoparticle and substrate functionalization

To produce highly stable nanoparticle assemblies, iron oxide nanoparticles were covalently bound onto planar substrates. The CuAAC “click” reaction which is well known for its versatility and selectivity is well suited to assemble the iron oxide nanoparticles into stable single monolayer.<sup>[17-19]</sup> Moreover, this assembling method allows the control of the assembly structuration.<sup>[20, 21]</sup> Assemblies of nanoparticles by “click” chemistry involve the functionalization of nanoparticles and substrates by alkyne and azide complementary groups, respectively. These groups have to be available at the surface to ensure the complete reaction. Preliminary studies in our team showed that the best system consist in a gold substrate functionalized with alkyne groups while nanoparticles exhibit azide groups at their surface.<sup>[6]</sup>

### 1. Nanoparticle functionalization

In order to graft a specific group required for the CuAAC “click” reaction, a ligand exchange has to be performed to replace oleic acid on the nanoparticle surface with a molecule carrying an azide functional group. Functionalized nanoparticles are then characterized in order to control the ligand replacement at their surface as well as the suspension stability.

#### a) *Experimental section*

A direct ligand exchange was performed to replace the oleic acid by 12-azido-dodecylphosphonic acid (AP12N<sub>3</sub>). A phosphonic acid is used because the interactions with the iron oxide are stronger than with the carboxylic acid.<sup>[22-26]</sup> Therefore, phosphonic acid will spontaneously replace the oleic acid which results in the production of azido-terminated nanoparticles (NP@N<sub>3</sub>). Moreover, the long alkyne chains allow the stability of the nanoparticle suspensions in THF while the azide groups are directly available from the surface. The ligand exchange was performed in solution (figure II-11). 20 mg of AP12N<sub>3</sub> was solubilized in THF before adding a volume of 10 mL at 5 mg/mL of NP@OA. Then, the suspension was stirred for 16 hours.

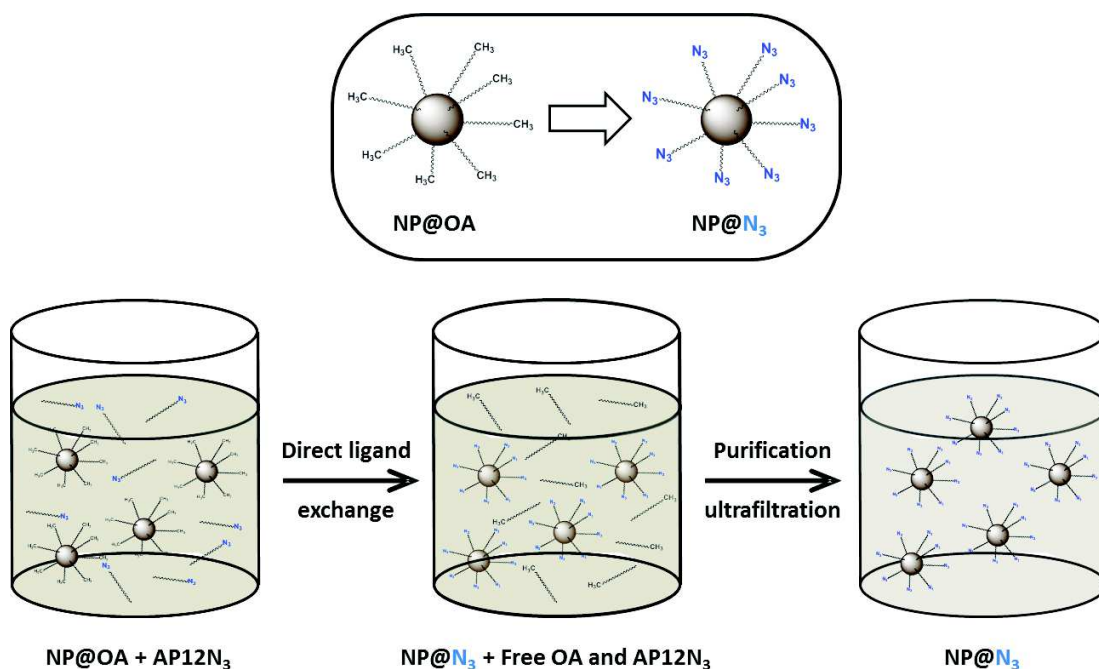


Figure II-11. Schematic representation of the preparation of NP@N<sub>3</sub> by performing the ligand exchange process

NP@N<sub>3</sub> were purified in order to remove the excess of phosphonic acid molecules which could interfere during the click reaction and the oleic acid in solution desorbed from the nanoparticle surface. The purification step was realized by ultrafiltration which consists in the filtration of the nanoparticle suspension through a cellulose membrane (30 kDa). The suspension is pushed by putting pressure with argon flux in order to eliminate the free molecules and to remain the nanoparticles which are too large to go through the membrane. The purification step is monitored by FT-IR spectroscopy to ensure the disappearance of the free molecules in the suspension.

### b) *Characterization after functionalization*

It is essential to be certain that the nanoparticles have still a good stability and do not present any aggregation prior to their assembly through CuAAC “click” chemistry. Granulometry measurements were performed to ensure having non aggregated nanostructures in suspension after the ligand exchange. Characterizations here are presented for NP10 which are the reference nanoparticles, NP5 and NP20 characterizations are presented in appendix C and the values of hydrodynamic diameter are summarized in table II-6. Figure II-12 shows a monomodal hydrodynamic diameter after the exchange with the phosphonic acid meaning a good stability of the suspension in THF. The average value of the hydrodynamic diameter (11.8 nm) is slightly smaller than before the ligand exchange (13.5 nm). It can be explained by a shorter length of the alkyl chains of AP12N<sub>3</sub> (12 carbons) than oleic acid (18 carbons).

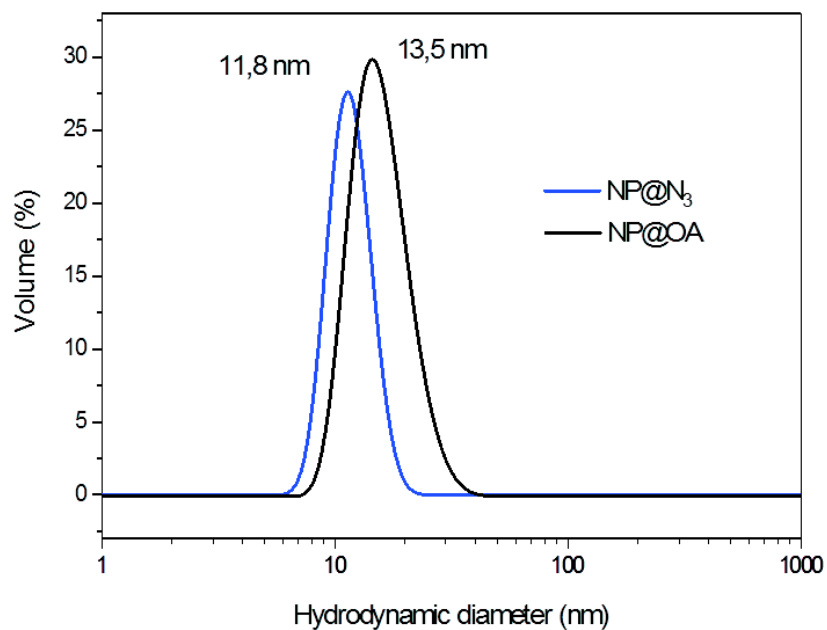


Figure II-12. Granulometry measurements of the nanoparticles in THF before (black curve) and after (blue curve) ligand exchange

Table II-6. Summarize of the hydrodynamic diameter for nanoparticles before (NP@OA) and after functionalization (NP@N<sub>3</sub>)

	NP5	NP10	NP20
NP@OA	8.7 nm	13.5 nm	23.8 nm
NP@N <sub>3</sub>	6.5 nm	11.8 nm	21.2 nm

To confirm the correct grafting of the AP12N<sub>3</sub> on the nanoparticles, FT-IR spectroscopy measurements were performed before and after the ligand exchange and on AP12N<sub>3</sub> (figure II-13).

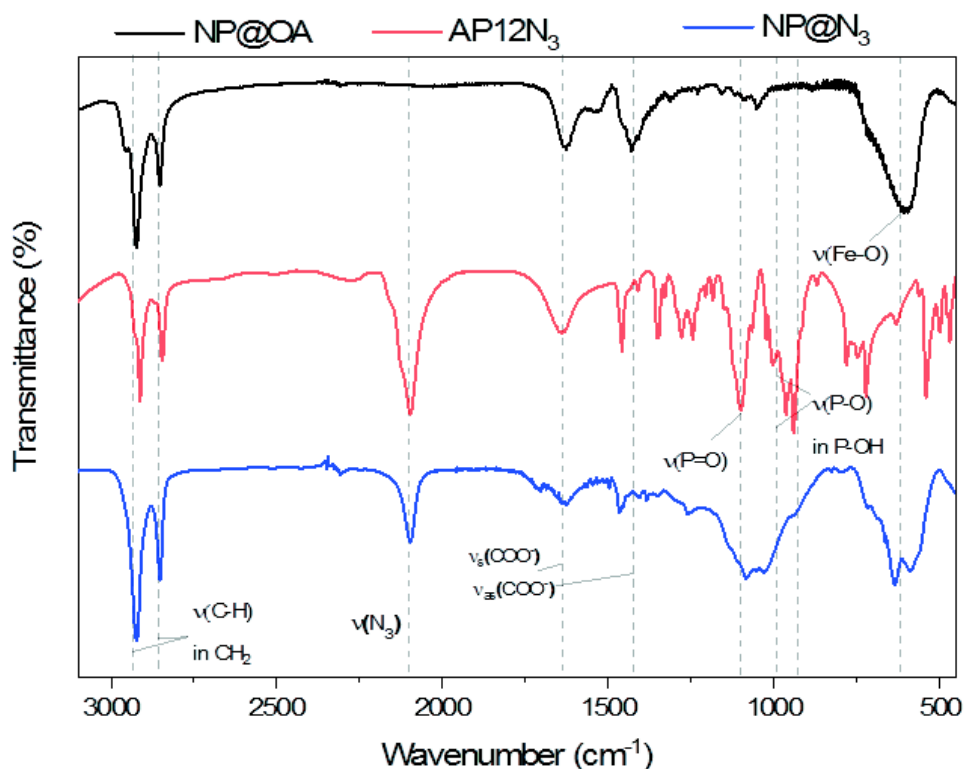


Figure II-13. Infrared spectra of the nanoparticles with oleic acid (black curve), the free molecule of AP12N<sub>3</sub> (red curve) and the NPs functionalized with the azide phosphonic acid (blue curve)

Infrared spectra of nanoparticles functionalized with oleic acid (black curve) present the characteristic peaks of iron oxide ( $\nu(\text{Fe-O}) - 600 \text{ cm}^{-1}$ ), alkyne chains ( $\nu_{\text{as}}(\text{CH}_2) - 2920 \text{ cm}^{-1}$  and  $\nu_{\text{s}}(\text{CH}_2) - 2850 \text{ cm}^{-1}$ ) and oleic acid grafted at their surface ( $\nu_{\text{as}}(\text{COO}^-) 1660 \text{ cm}^{-1}$  and  $\nu_{\text{s}}(\text{COO}^-) 1420 \text{ cm}^{-1}$ ) as described previously. After the functionalization step (blue curve), the infrared spectra of nanoparticles do not show the carboxylic vibrational bands anymore. Moreover, a singular and recognizable band at  $2100 \text{ cm}^{-1}$  is attributed to the vibrational stretching mode of the azide group ( $\nu(\text{N}\equiv\text{N})$ ).<sup>[5]</sup> The apparition of a wide band between  $900 \text{ cm}^{-1}$  and  $1150 \text{ cm}^{-1}$  is representative of the phosphonic acid bound to the iron oxide vibration ( $\nu(\text{Fe-O-P})$ ).<sup>[23]</sup> Indeed, the signal of the free molecule of phosphonic acid (red curve), shows characteristic bands of the stretching mode of the azide groups at  $2100 \text{ cm}^{-1}$ . Moreover, the stretching modes within the P-OH binding ( $\nu(\text{P-O})$ ) at  $1008 \text{ cm}^{-1}$  and at  $945 \text{ cm}^{-1}$  and the supplementary vibrational band observed at  $1110 \text{ cm}^{-1}$  corresponding to the P=O stretching mode are representative of the phosphonic acid function.<sup>[6]</sup> The replacement of the peaks at  $945 \text{ cm}^{-1}$  and  $1010 \text{ cm}^{-1}$  by the wide band located at  $1015 \text{ cm}^{-1}$  indicates the correct grafting of the AP12N<sub>3</sub> on the nanoparticle surface and the absence of free molecules of phosphonic acid in solution.

The infrared spectroscopy confirmed the replacement of the oleic acid by the AP12N<sub>3</sub>. Moreover, the purification step was done successfully with the ultrafiltration method and allowed preparing NP@N<sub>3</sub> with functional groups available at their surface. The DLS measurements confirmed the good colloidal stability after the ligand exchange, meaning suspensions ready for the “click” chemistry reaction.

## 2. Substrate functionalization

The gold surface has to be functionalized with the complementary groups for the “click” chemistry reaction. Azide groups have been localized on the nanoparticle surface, alkyne groups have to be grafted on the substrate surface. The use of a gold surface allows the formation of self-assembled monolayers (SAM) of thiol molecules. The arrangement of thiol derivatives with alkyl chains will allow having ordered and functional head groups directly available from the surface.

#### a) *Synthesis of 11-mercapto-undecyn*

In order to create SAMs terminated with alkyne groups, 11-mercapto-undecyn ( $\text{HCC}(\text{CH}_2)_9\text{SH}$ ) was synthesized following the protocol of Colmann (figure II-14).<sup>[27]</sup> The detailed procedure can be found in appendix C. The compound was then characterized by  $^1\text{H}$  NMR and FT-IR.

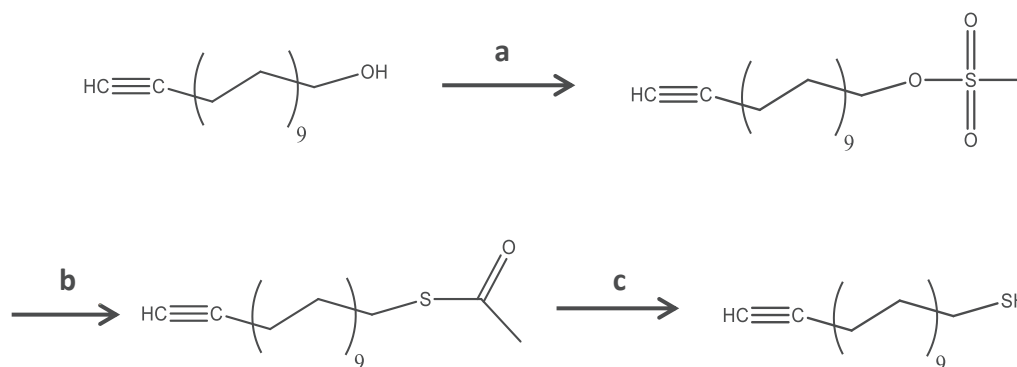


**Figure II-14. Scheme of the 11-mercapto-undecyn synthesis in 3 steps a) mesylation of the alcohol group, b) nucleophile substitution of mesyle groups by thioacetate group and c) acid hydrolysis of the thioacetate group in thiol**

Starting from the 11-hydroxy-undecyn, the first step is a mesylation of the alcohol function of the molecule to obtain the 11-methylsulfonate-undecyn. This reaction takes place in THF under reflux with mesyl chloride ( $\text{CH}_3\text{SO}_2\text{Cl}$ ) with triéthylamine to activate the reaction (Figure II-15, step a).

The methylsulfonate group was substituted by a thioacetate group to form the 11-thioacetate-undecyn. This reaction takes place with potassium thioacetate in methanol under argon for 3 hours (Figure II-15, step b).

The thiol is synthesized by acid hydrolysis of the acetate group by reacting the 11-thioacetate-undecyn with hydrochloric acid in methanol refluxed under argon for 5 hours (Figure II-15, step c).

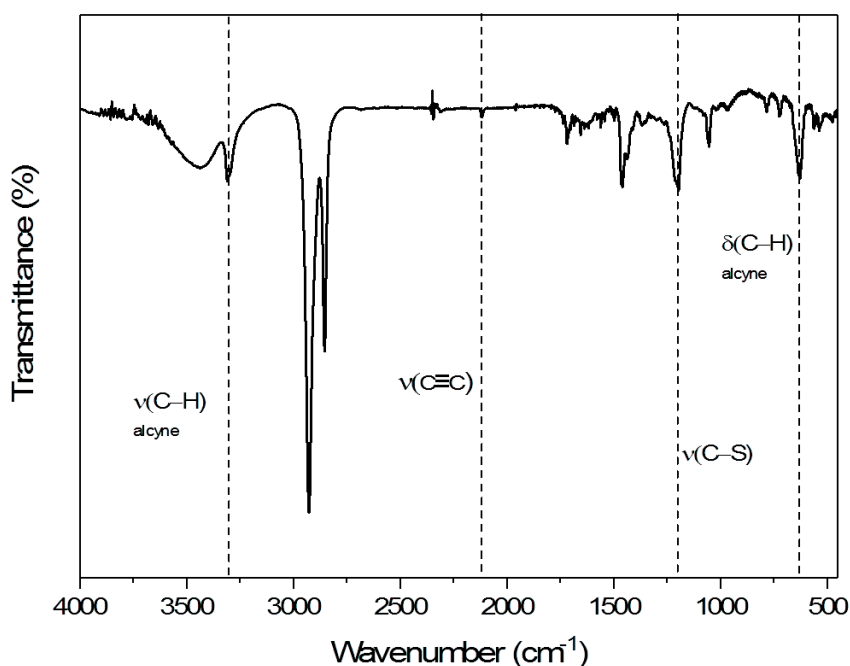


Figure II-15. Infrared spectra of the 11-mercapto-undecyn

Figure II-15 presents the infrared spectra of the synthesized compounds. The characteristic vibrational bands at  $2850\text{ cm}^{-1}$ ,  $2920\text{ cm}^{-1}$  and  $1460\text{ cm}^{-1}$  indicate the presence of the long alkane chains of the molecules. The terminal alkyne group is characterized by the specific vibrational band of the stretching mode within the C-H binding at  $3300\text{ cm}^{-1}$ , the rocking mode in the C-H binding at  $635\text{ cm}^{-1}$  and the stretching mode of the  $\text{C}\equiv\text{C}$  binding at  $2115\text{ cm}^{-1}$ .<sup>[5]</sup>

### b) Self-assembled monolayer formation

The formation of self-assembled monolayer is then realized by the following procedure. The gold substrates were first cleaned by hydrogen and oxygen plasma for 2 minutes in order to remove organic elements from the surface to activate the surface. The substrate was then immersed in an ethanolic solution at 10 mM of 11-mercapto-undecyn. The substrates remained 24 hours in the solution and were stored in the dark at room temperature before rinsing with ethanol (figure II-16). The formed self-assembled monolayer terminated with alkyne is noted SAM-CC.

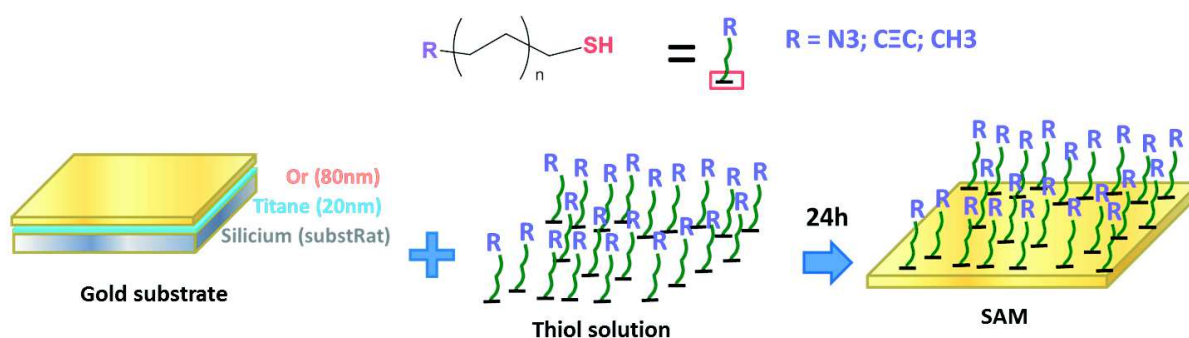


Figure II-16. Schematic representation of the formation of self-assembled monolayer. Adapted from Toulemon.<sup>[6]</sup>

### c) Characterization of self-assembled monolayers

Different surface characterizations were used to determine the arrangement and the presence of terminal head groups at the SAM surface.

The topography of the gold substrate was investigated with atomic force microscopy (AFM) before and after functionalization (figure II-17). AFM gives indications on the roughness and the thickness of the substrate.

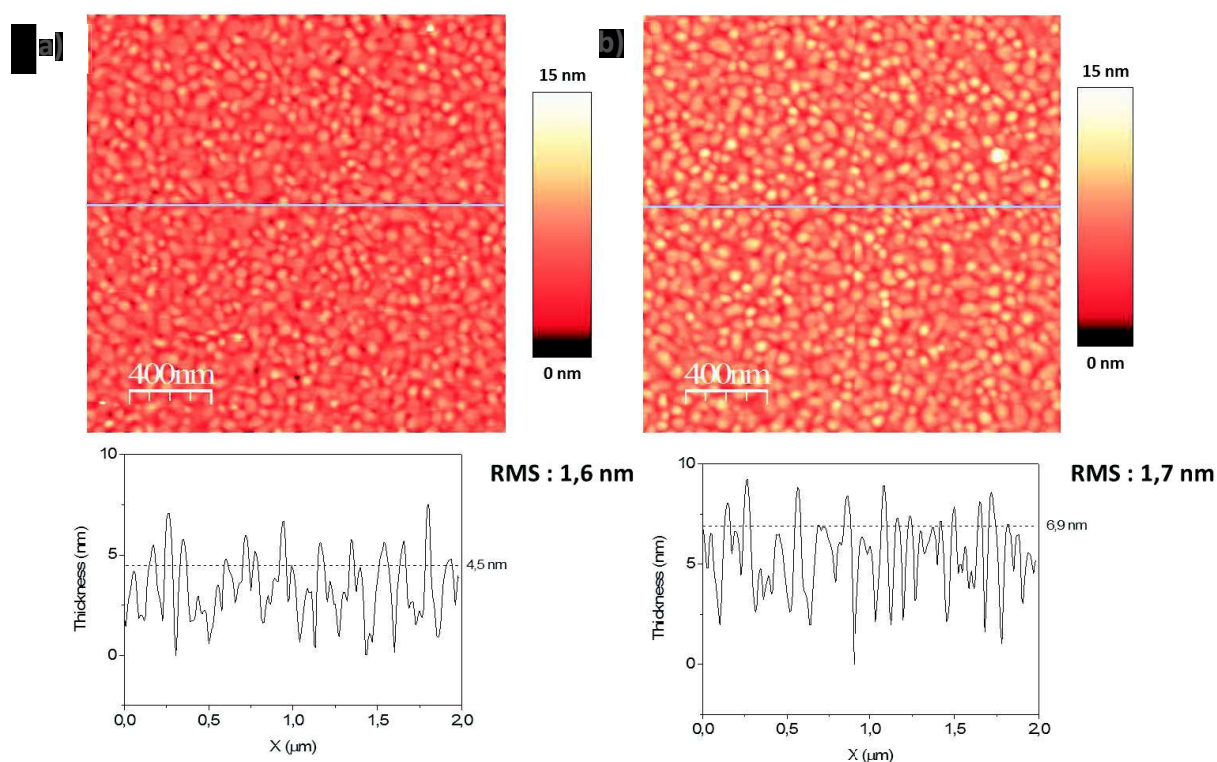


Figure II-17. AFM images of the substrates and cross-section profile measured on a) gold naked surface and b) SAM-CC surface

The gold substrate consists in gold grains with different sizes with a roughness of 1.6 nm. The image of the SAM-CC presents a similar structure. However, height profiles show a larger average thickness which are  $4.5 \pm 1.5$  nm and  $6.9 \pm 1.3$  nm for gold and SAM-CC, respectively. The height increase of about 2 nm was ascribed to the grafting of 11-mercapto-undecyn at the gold surface and to the formation of the SAM-CC.

The water contact angle (WCA) measurement was realized with the deposition of a  $5 \mu\text{L}$  water droplet on the surface to determine its wettability (figure II-18). The picture and the measured angle values were performed one minute after the droplet deposition in order to stabilize the system.

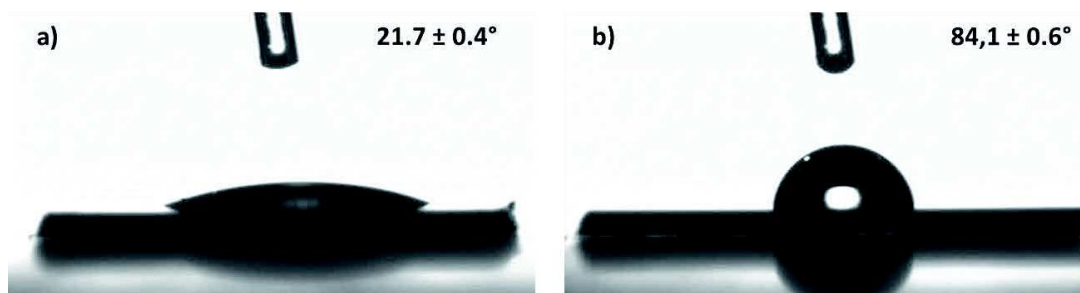


Figure II-18. Water contact angle measurements on a a) gold substrate and b) SAM-CC

The gold surface shows a contact angle of  $21.7^\circ$  which agree with a highly hydrophilic surface. After functionalization with the thiol groups, the substrate presents a contact angle of  $84.1^\circ$  which is characteristic of a hydrophobic surface. Such a significant variation of the contact angle agrees with the grafting of 11-mercapto-undecyn onto the gold surface. Indeed, the thiol molecules with their long alkyl chains and alkyne head groups induce a hydrophobic behavior of the surface.

Polarized Modulated Infrared Reflection Absorption Spectroscopy (PM-IRRAS) measurements were performed in order to characterize the self-assembled monolayer of thiol alkyne (figure II-19). The antisymmetric and symmetric stretching bands at  $2927\text{ cm}^{-1}$  and  $2856\text{ cm}^{-1}$  respectively indicates the presence of organic chains at the surface of the gold. These positions suggest a slight disorder between alkyl chains due to a gauche configuration.<sup>[28]</sup>

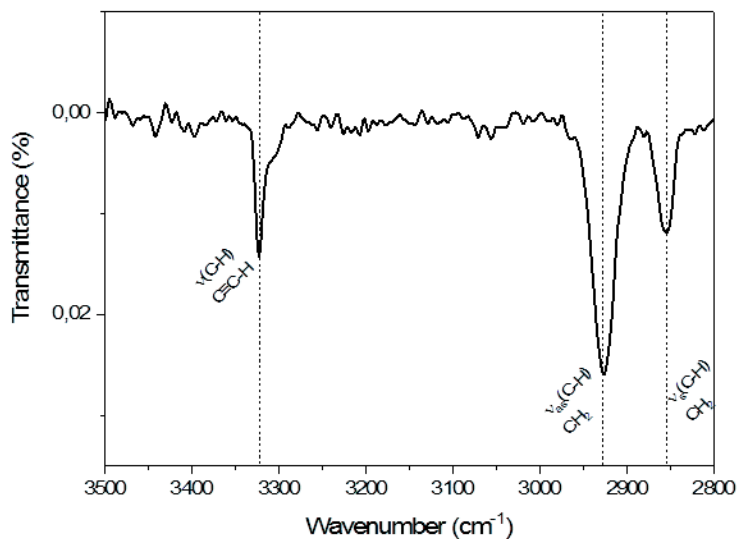


Figure II-19. PM-IRRAS spectra of the SAM surface

A characteristic band at  $3320\text{ cm}^{-1}$  is observed and correspond to the  $\nu(\text{C-H})$  vibration in the terminal methylene group  $\text{C}\equiv\text{C-H}$ .<sup>[29]</sup> Therefore, the presence of terminal alkyne groups is confirmed at the SAM surface.

### 3. Conclusion

On one hand, the nanoparticles have been successfully functionalized by azide groups. Moreover, the good stability of the suspension allows having nanoparticles available for the CuAAC

“click” chemistry. On the other hand, the gold substrate has been functionalized with the complementary alkyne groups required for the reaction.

### C. Nanoparticle assembly prepared by "click" chemistry

The assembly method used here is based on the interaction between organic groups localized on the surface of both nanoparticles and substrate. The CuAAC "click" reaction allows the strong binding of the nanoparticles to the substrate and presents the advantage of being highly selective and versatile. The CuAAC reaction usually takes place in an aqueous solution between an alkyne and an azide groups and is catalyzed by copper (I).<sup>[30]</sup> However, copper (I) has poor stability in aqueous medium and the nanoparticles are stable in organic solvent. Therefore, we performed the reaction in an organic solvent by using a copper catalyst stabilized by ligands:  $[\text{CuBr}(\text{PPh}_3)_3]$ . The "click" reaction was performed by using the protocol described by Xavier Cattoën<sup>[31]</sup> in THF in presence of triethylamine to activate the reaction (figure II-20).

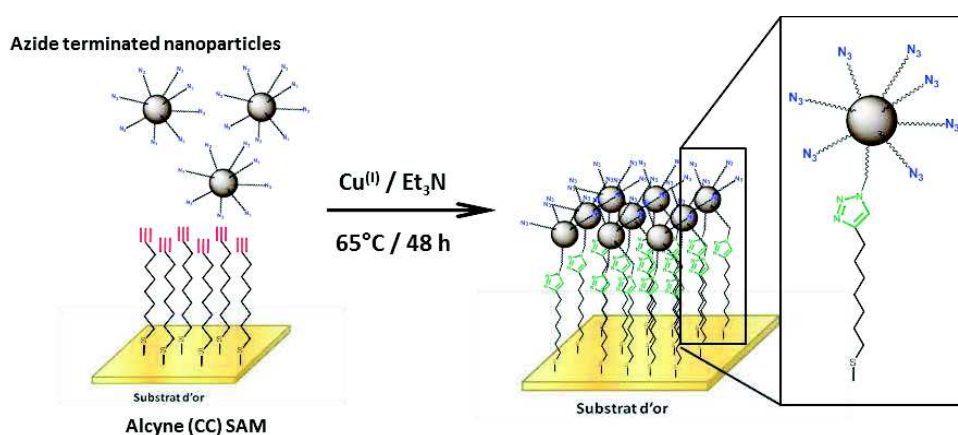


Figure II-20. Schematic representation of the "click" chemistry assembly of nanoparticles onto gold surface

The functionalization of both nanoparticles and substrate with complementary groups will allow the preparation of assemblies. The process of this reaction for different size of nanoparticles, the influence of reaction parameters and the characterizations of these assemblies will be studied in this part.

#### 1. Assembly of 10 nm nanoparticles

The protocol and control experiment will be detailed in this part as reference assembly. The concept will be presented here and the study of different sizes and parameters will be discussed afterwards.

##### a) Assembly protocol

The click chemistry reaction was performed in a reactor of 10 mL (figure II-21). A suspension of NP@N<sub>3</sub> in THF was prepared with a concentration of 1 mg/mL. A  $\text{CuBr}(\text{PPh}_3)_3$  catalyst (3% of nanoparticle weight) and triethylamine (0.5 mL) were added to foster the reaction by increasing the lability of the C-H binding in the alkyne group.<sup>[6, 31]</sup>

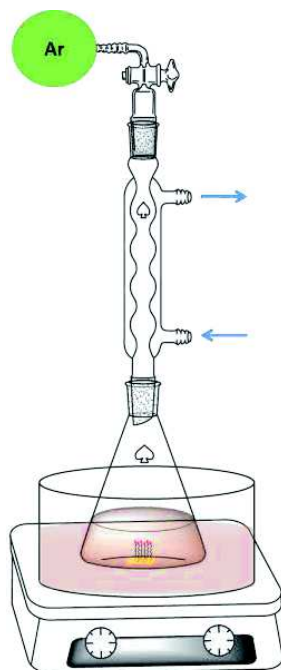


Figure II-21. Schematic representation of the apparatus required to perform nanoparticle assembling by "click" chemistry reaction

The SAM-CC was then immersed in this solution and heated at 70°C for 48 hours with a condenser under argon. The reactor was put in a silicon bath and the temperature was controlled by a thermocouple. After the reaction was completed, the substrate was removed, rinsed with THF and put in ultrasonic bath for 1 minute in order to remove the nanoparticles which are not covalently bound to the surface. The substrate was then dried under an air stream.

b) *Scanning electron microscopy characterization*

Scanning electron microscopy (SEM) is a powerful technique which allows determining the structure of the nanoparticle assemblies.

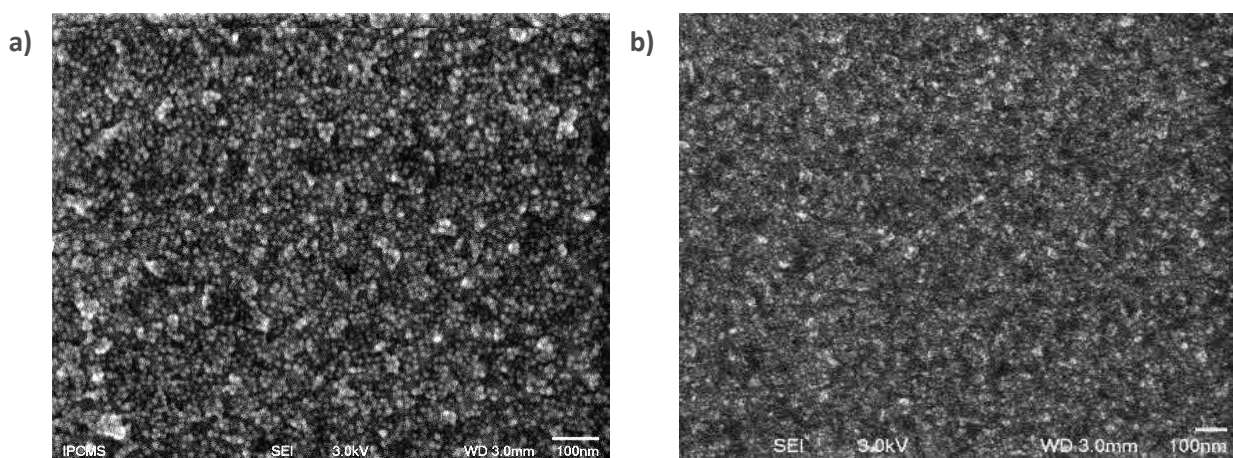


Figure II-22. SEM images of 10 nm-sized nanoparticle assemblies at magnifications a) X100000 and b) X50000

On the SEM picture showed in figure II-22, a fully covered surface of nanoparticles can be observed. The image with low magnification (X50000) shows a homogenous surface without aggregates neither holes in the assembly on a large area. The image with a higher magnification (X100000) allows determining the density of nanoparticles on the surface. The number of nanoparticles per surface unit area was measured with ImageJ software by counting nanoparticles in five different areas which allow determining an average with a standard deviation. For this sample, the density is  $4\,950 \pm 95$  NPs/ $\mu\text{m}^2$ . In order to compare the density for different sizes of nanoparticles, it was normalized to a maximal theoretical value which corresponds to the hexagonal close packing of nanoparticles onto a surface (figure II-23).

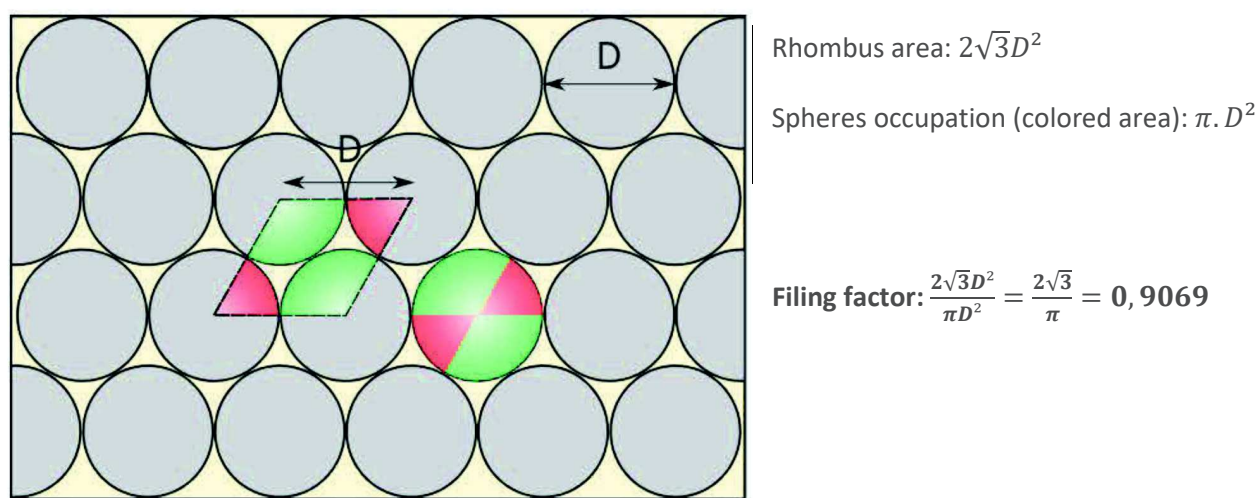


Figure II-23. Schematic representation of the nanoparticle arrangement on a hexagonal close packing

This maximal theoretical value was calculated for a hexagonal close packing of 10.1 nm spheres surrounded with an organic layer about 2 nm which is  $5\,810$  NPs/ $\mu\text{m}^2$ . Considering this, the sample showed on the figure II-22 presents 85% of the maximum theoretical density. This value is in accordance with previous studies of nanoparticle films.<sup>[4, 6]</sup> These values for 5.1 nm and 21.2 nm nanoparticles are respectively  $13\,940$  NPs/ $\mu\text{m}^2$  and  $1\,820$  NPs/ $\mu\text{m}^2$ .

## 2. Study of the kinetics of the assembly

The considerable advantage of the “click” chemistry method is to control the spatial arrangement of the assembly as function of the reaction time.<sup>[20]</sup> It is a real advantage to control the magnetic collective properties and specifically the plasmonic properties carried by the substrate.

The kinetic of the reaction allows controlling the density of the nanoparticles at the surface. A typical assembly of 10 nm of nanoparticles in a concentration of 0.8 mg/mL in  $\text{Fe}_3\text{O}_4$  has been realized by varying the reaction time between 1 hour and 48 hours. SEM analysis showed the evolution of the surface coverage and allowed measuring the nanoparticle density as function of the reaction time (figure II-24).

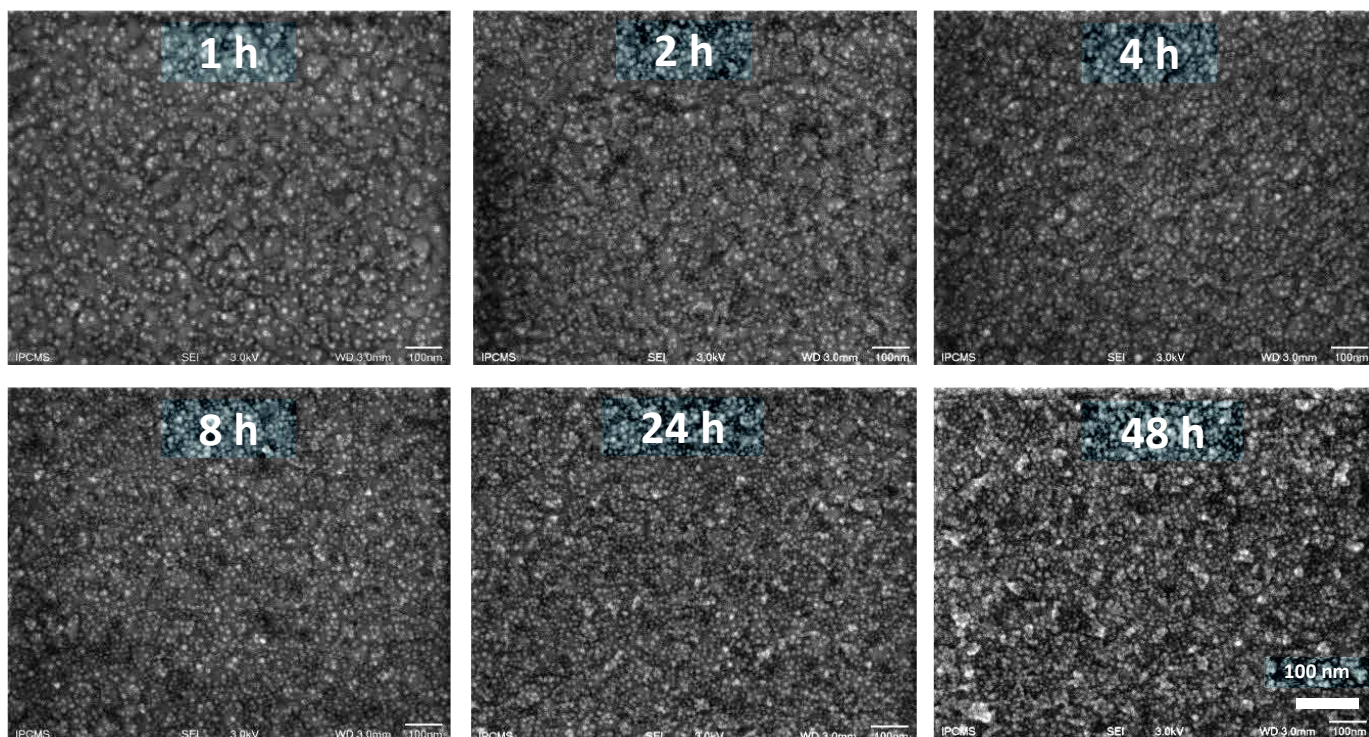


Figure II-24. SEM images of the NP10 assembly after different reaction times. Magnification X100000

After 1 hour of reaction, some azido-terminated nanoparticles were already grafted onto the alkyne-terminated SAM. Isolated nanoparticles can be observed at the gold grain boundaries where the energy necessary for the assembly should be the lowest. Alignments or packing from 3 to 6 nanoparticles promoted by magnetic dipolar interactions were also observed.<sup>[6, 32]</sup> The density increased with the reaction time until reaching a full monolayer of nanoparticles after 48 hours. After 24 hours, some aggregates were observed. This aggregation phenomenon may be caused by the evaporation of the solvent during the reaction.

The density was measured and reported to the maximal theoretical value for NP10 (5 810 NPs/ $\mu\text{m}^2$ ) as function of the reaction time (figure II-25).

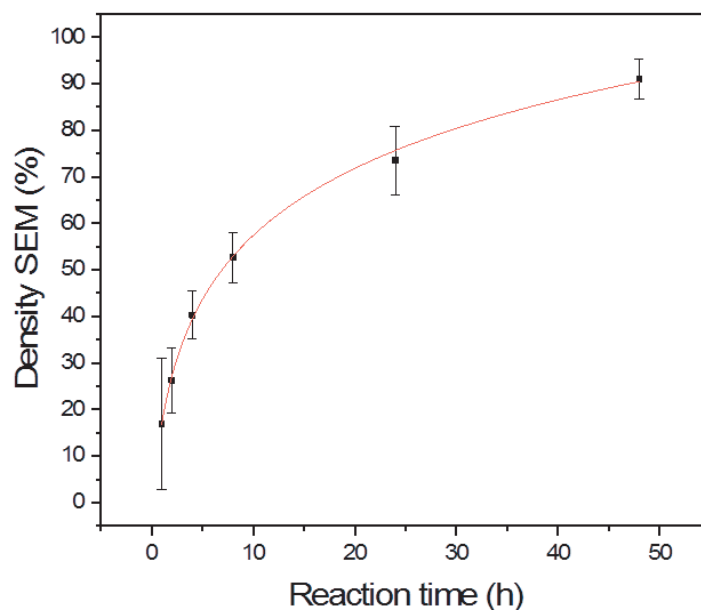


Figure II-25. Density of nanoparticles onto the gold surface as a function of the reaction time (calculated from SEM images)

The data were fitted with a logarithm function and the scale bars correspond to measurements on different areas. The evolution of the density is nonlinear and a rapid evolution is monitored until reaching 80% of the maximal coverage after 24 hours. The film of nanoparticles does not reach 100 % of the maximal theoretical density value even after 48 hours which can be explained by the random grafting of the nanoparticles at the surface which can let holes on the surface smaller than the nanoparticles size. Indeed, the maximum value was calculated for a hexagonal close packing, which is not the case for the random arrangement of the nanoparticles in these samples.

### 3. Variation of assembly parameters

The structuration of the nanoparticle assembly is crucial to control the collective and individual properties of these films. The size of nanoparticles directly influence the properties of the assembly and therefore has to be studied. Moreover, the presence of aggregates on long reaction times may question us on the influence of some parameters of the assembly. Different parameters have been studied previously in our team which showed the influence on the nanoparticle density.<sup>[6]</sup> However, the suspension concentration has not been studied yet and can influence the presence of aggregates.

#### a) Nanoparticle sizes

The kinetics of assembly reaction was studied for each nanoparticle size. Figure II-26 shows the SEM analysis for the assembly of 5 nm nanoparticles, with a concentration of 0.45 mg/mL, by varying the reaction time between 1 hour and 48 hours.

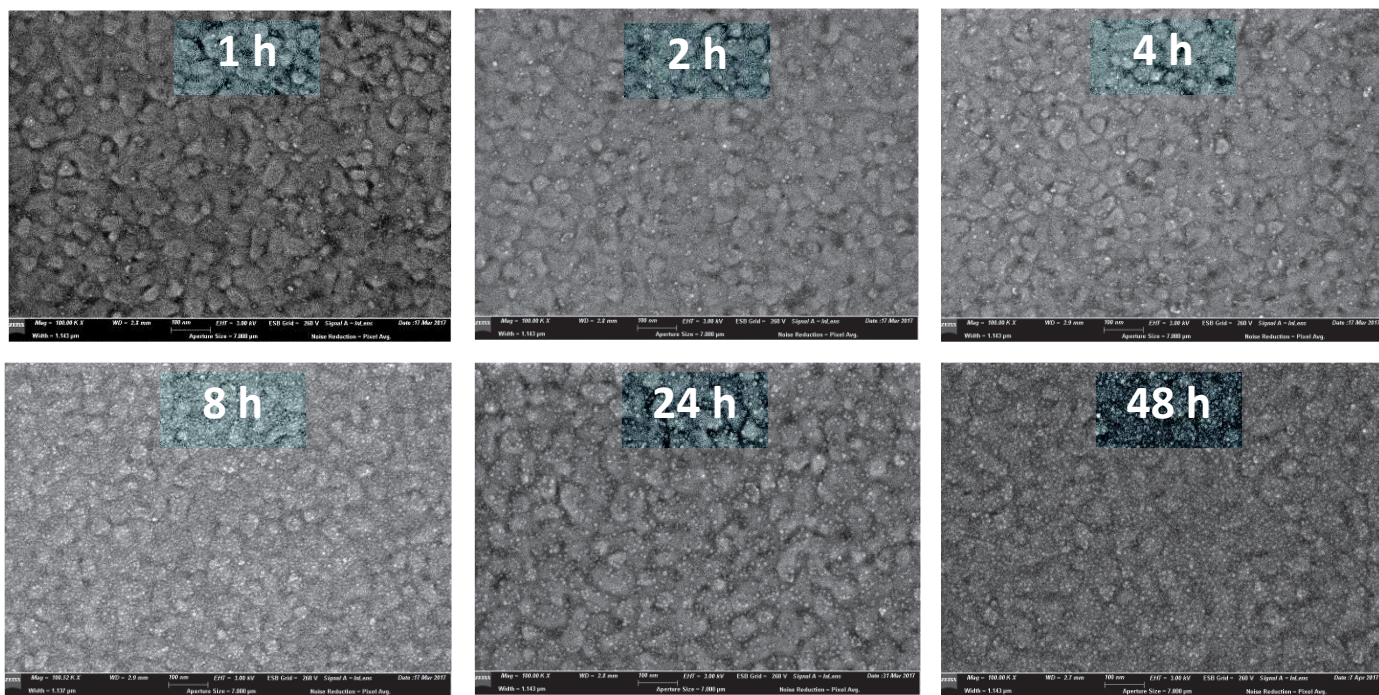


Figure II-26. SEM images of the assembly of NP5 after different reaction times. Magnification X100000

The presence of nanoparticles is observed after one hour of reaction. The density is very low until 8 hours of reaction. The nanoparticles are isolated on the surface and no alignments or clusters are observed. Contrary to the 10 nm nanoparticles, after 48 hours of reaction, the surface is not fully covered. The density as function of the reaction time is reported on figure II-27.

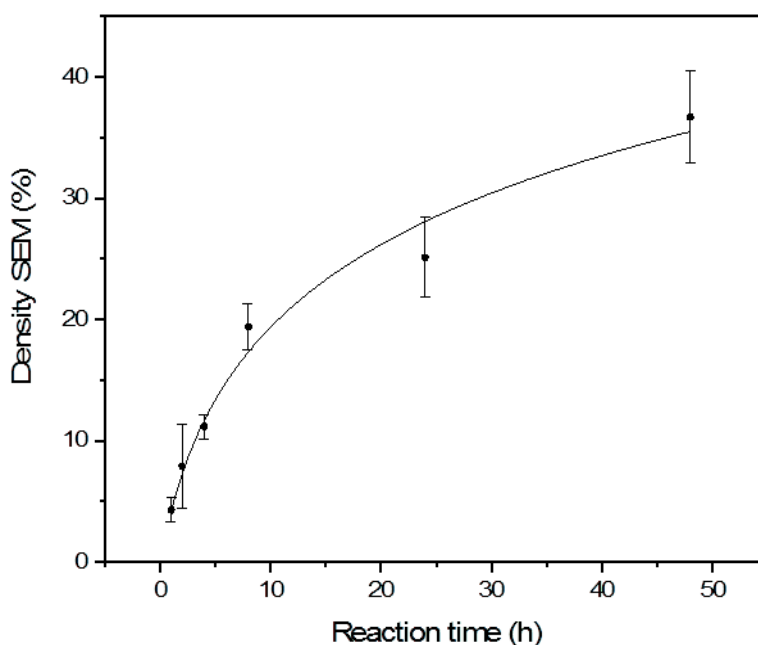


Figure II-27. Density of the NP5 at the gold surface as function of reaction time

The same behavior than for the NP10 is observed with a fast increase of the density until 24 hours of reaction. The kinetics of assembly for the NP5 is slower than for the NP10. The density value, even after 48 hours, remains low below 40 % of maximal theoretical value.

In a colloidal suspension, smaller nanoparticles have a higher mobility and therefore statically generate more encounters with the gold surface. However, the kinetic of the assembly reaction is slower in this case which disagrees with this theory. In the case of assembly of nanoparticles with “click” chemistry, the kinetic of the reaction is slow since the azide and alkyne groups have to be in presence of the copper catalyst to form the reactional intermediate. Therefore the reaction requires more time and a fast mobility of nanoparticle can reduce the kinetic of reaction. Moreover, the NP5 due to their lower surface, present less functional groups which can interact at the SAM surface. The reduction of active groups on the nanoparticle surface can also decrease the recognition process. Finally, the dipolar interactions can drive the assembly by inducing nanoparticles to get closer (see part C.3.b).<sup>[6]</sup> The smaller nanoparticles present less dipolar interactions due to their size<sup>[13]</sup> and, therefore, may contribute to such a slow kinetic.

The same study was performed with NP20 with a concentration of 0.49 mg/mL. The SEM analysis is shown on figure II-28.

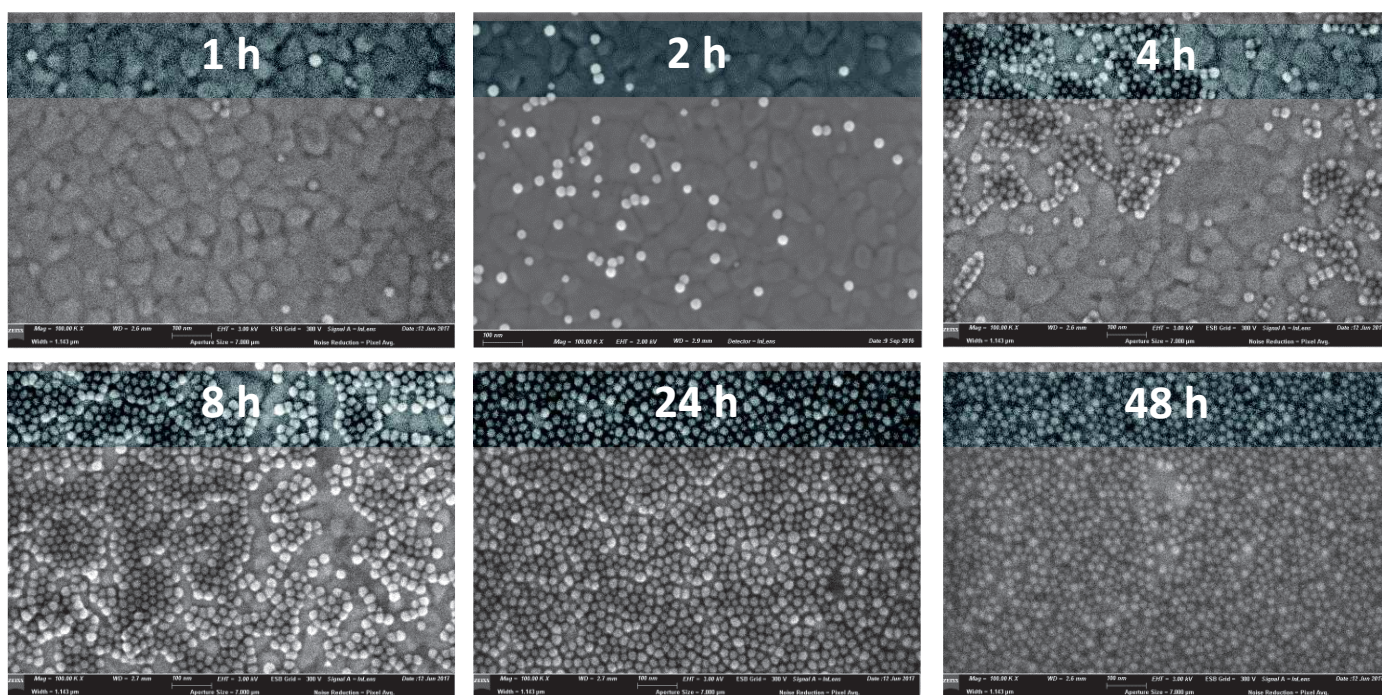


Figure II-28. SEM images of the assembly of NP20 after different reaction times. Magnification X100000

The nanoparticles can be observed onto the gold surface after one hour of reaction. After 4 hours of reaction, the density increases faster and at 8 hours the surface is almost fully covered. Moreover, the presence of clusters after 4 hours seems to indicate that the nanoparticles which were already immobilized onto the substrate favored the assembly of others next to them. The assembly after 24 hours and 48 hours of reaction present a great order of the nanoparticles which confirm the directed assembly. This is caused by the stronger dipolar interactions between 20 nm nanoparticles which induces attraction of the nanoparticles. The density of nanoparticles as function of the time is reported on figure II-29.

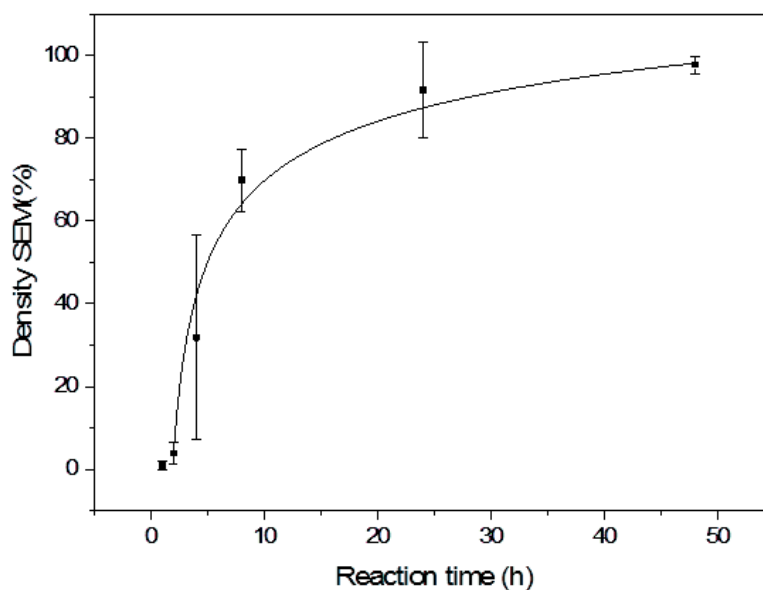


Figure II-29. Density of the NP20 onto the gold surface as function of reaction time

With the NP20, the density onto the gold surface reaches almost 100% of the maximum theoretical coverage. Such a high coverage may be explained by dipolar interactions which promote the tight packing of nanoparticles.

The assembly of nanoparticles with three different sizes showed different behaviors. The smallest nanoparticles seem to assemble the slowest and are isolated on the surface, neither clusters nor alignments were observed. In contrast, 10 nm and 20 nm sized nanoparticles assemble much faster into clusters of chains of nanoparticles. The strongest dipolar interactions between these nanoparticles favor their assembly and, in the case of NP20, create an arrangement with higher density. The magnetic properties seem to influence directly the spatial arrangement of the nanoparticles onto substrates.

#### b) *Concentration of the nanoparticle suspensions*

The concentrations of the nanoparticle suspensions were varied in order to study the influence on the kinetics of the reaction (figure II-30). For each size of nanoparticles, two different concentrations were studied: one low concentration with few nanoparticles in suspension which induce fewer encounters of the nanoparticles at the surface; and one with high concentration where the dynamic promotes the encounters between nanoparticles and functional groups at the surface. The concentrations are given in mg of  $\text{Fe}_3\text{O}_4$  per mL.

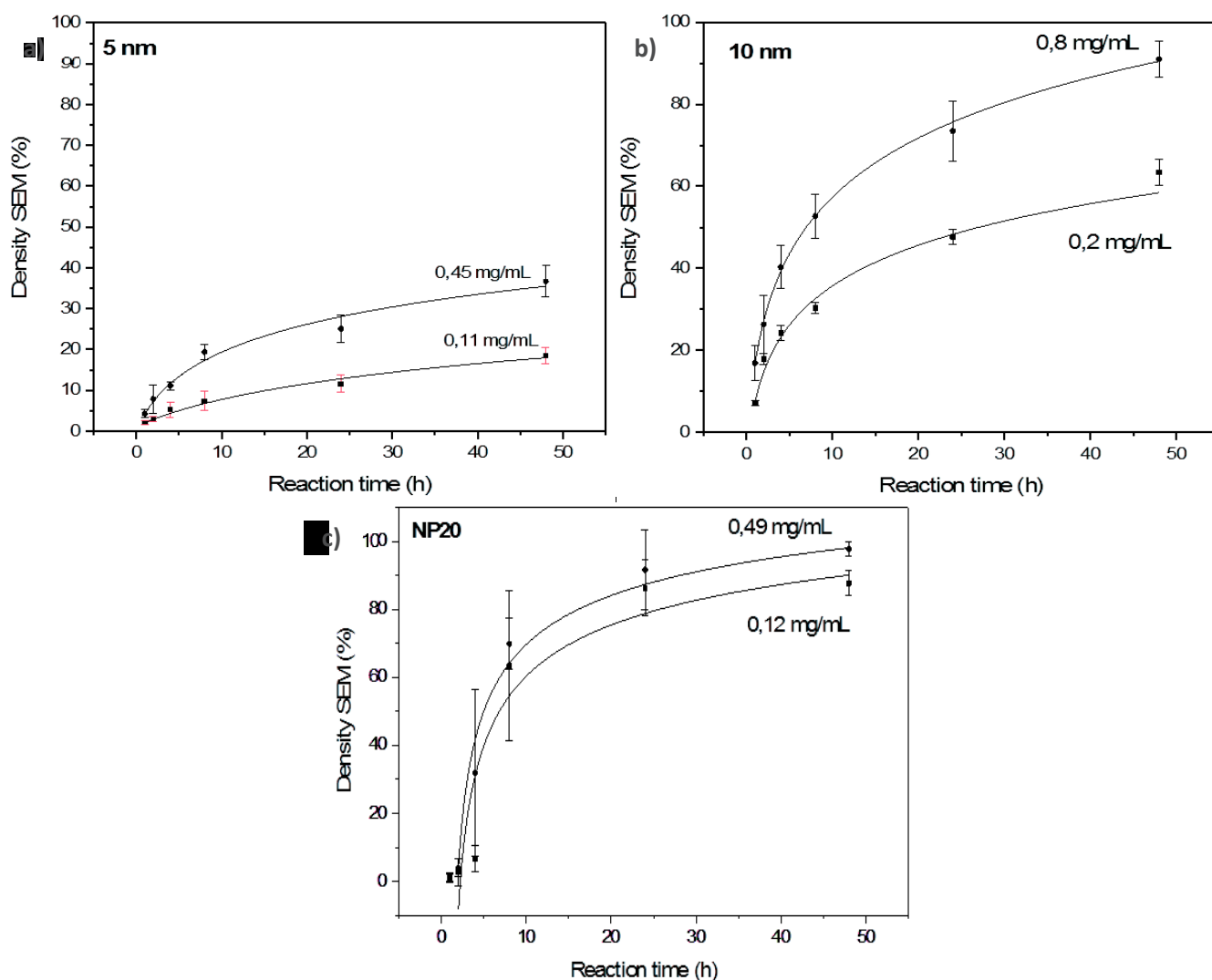


Figure II-30. Density of the a) NP5, b) NP10 and c) NP20 assembly as function of reaction time for two different concentrations

The increase of nanoparticle concentrations resulted in higher densities for the same reaction time, whatever their size. These results are ascribed to the increase of probability of nanoparticles to hit the substrate. Moreover, the highest concentrations lead to stronger dipolar interactions between nanoparticles which foster the assembly kinetic. Longer reaction times may improve the density of nanoparticles onto the substrate, but the stability of the suspensions decreased with the time. Therefore, high concentration of nanoparticles for short times of reaction is expected to increase the density of nanoparticles without aggregation at the surface.

The film thickness was also measured by performing ellipsometry. The measurement was performed on the SAM-CC to know the thickness of the organic layer. The thickness measured was  $1.4 \pm 0.2$  nm and this value was used thereafter to measure the thickness of the iron oxide layer. The refractive index used for the determination of the thickness is 2.42. This refractive index corresponds to a thin film of iron oxide. Here, the nanoparticle assembly does not form a complete film and the refractive index is overestimated. The measurements were performed on different spots of the surface of the sample to give average values with standard deviation. The thickness was measured for the two different concentrations studied and the results are show on figure II-31.

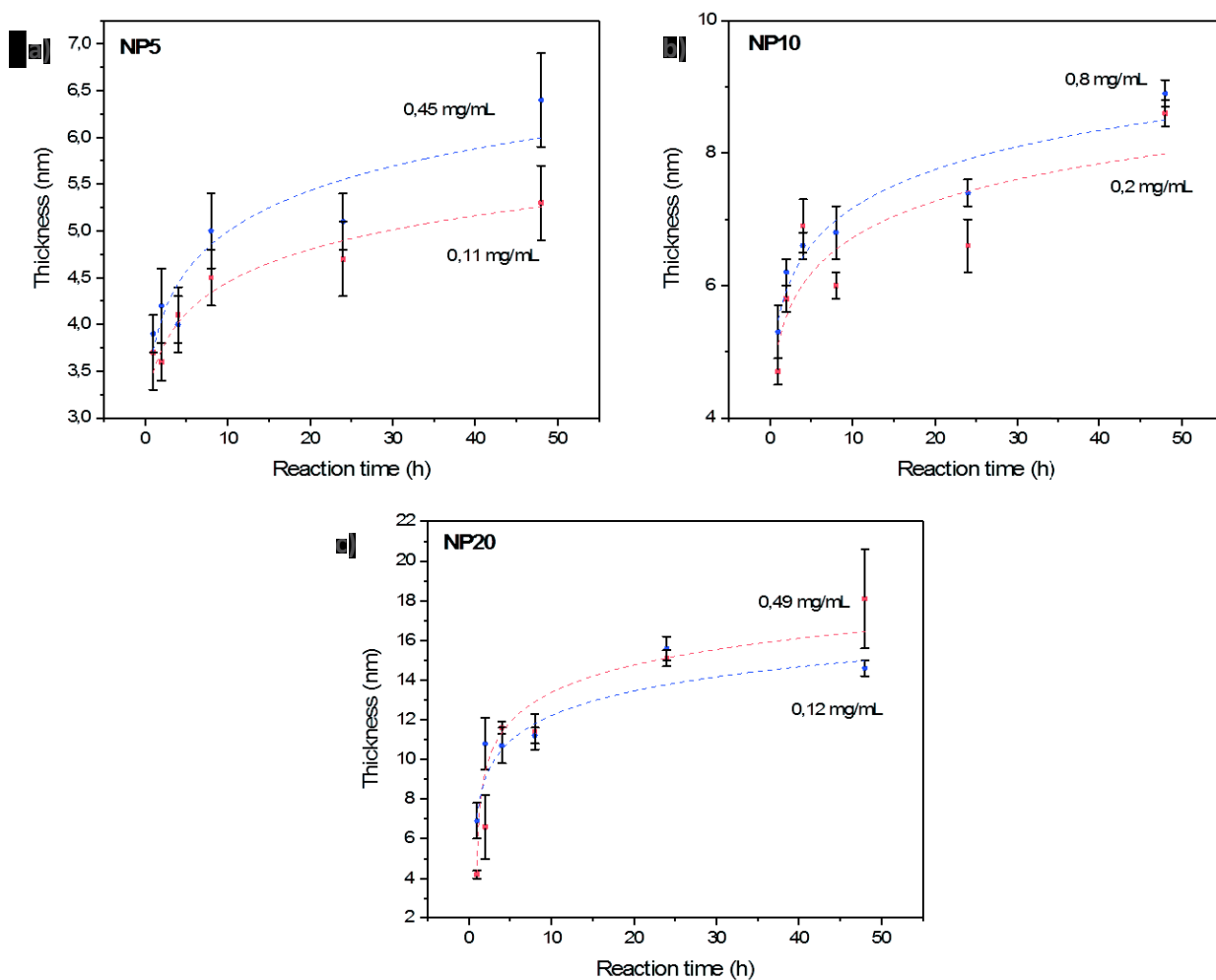


Figure II-31. Ellipsometry measurements of the a) NP5, b) NP10 and c) NP20 assembly as function of reaction time for two different concentrations

The thickness of the nanoparticle assembly increases with the reaction time for each size of nanoparticles. The trends are following the densities measured by SEM with apparition of a plateau for the NP20 and slight increase of the thickness for NP5 and NP10 after 24 hours of reaction. The values after 48 hours of reaction are close of the theoretical maximum values (which correspond to 91% of the size of the nanoparticles in the case of a close packed hexagonal arrangement) for NP10 ( $8.9 \pm 0.2$  nm) and NP20 ( $18.1 \pm 2.5$  nm). However for NP5, the value is unexpected with a thickness reaching  $6.4 \pm 0.5$  nm after 48 hours of reaction for the highest concentration. This overestimation can be due to the refractive index used (2.42) which is too high with regard to the low density of nanoparticles.

### c) Stability of the assembling solution in time

The assembly is promoted by the dipolar interactions between the nanoparticles as shown with the assembly of NP20 which form an array on the surface. However, the stability of the suspension evolves with the reaction time and the nanoparticles are aggregated at the end of the reaction (especially in the case of NP20). This aggregation is visible, but it can happen earlier during the reaction.

Therefore, to get a better understanding, the stability during the reaction was studied. For each size of nanoparticles, 1 mL of the solution was taken off for different reaction times and was characterized by granulometry (figure II-32).

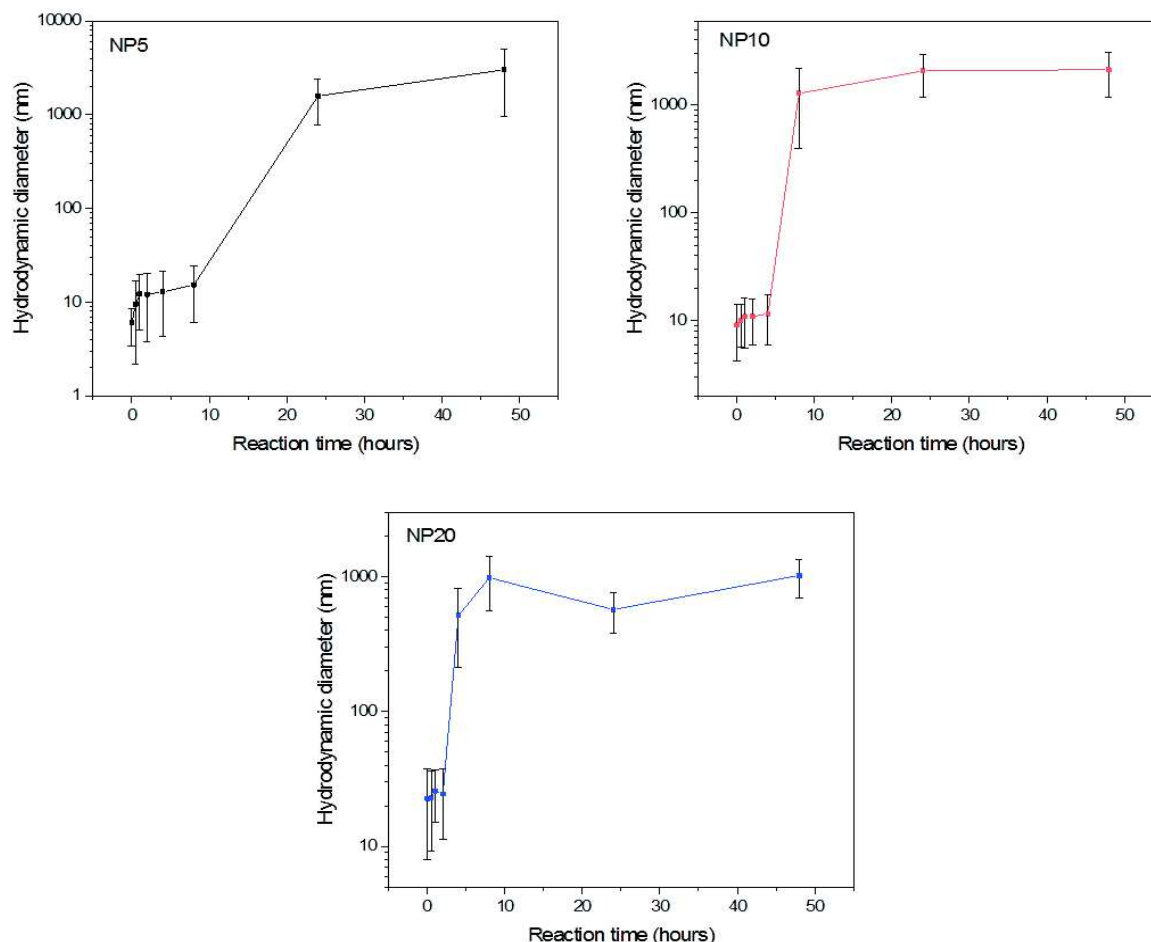


Figure II-32. Hydrodynamic diameter in volume as function of the reaction time of a) NP5, b) NP10 and c) NP20

The hydrodynamic diameter shows two phases for each size of nanoparticles. For short reaction times, the mean hydrodynamic diameter corresponds to the size of the nanoparticles, meaning a good stability of the suspension. However, for longer times, the suspensions present a huge value of hydrodynamic diameters which corresponds to aggregation phenomenon. This aggregation appears at different times as function of the size of the nanoparticles. For NP20, the aggregation is observed after 4 hours of reaction only. This aggregation appears later for smaller nanoparticles: after 8 hours for NP10 and 24h for NP5 (we can observe a slight aggregation for NP5 after the first hours of reaction). The largest nanoparticles present an aggregation earlier than the smallest nanoparticles.

This aggregation can be caused by the desorption or degradation of the ligand at the nanoparticle surface.<sup>[33]</sup> Infrared spectra were performed on the assembly solution after the “click” reaction of NP10 in order to control the stability of the phosphonic acid molecules (figure II-33).

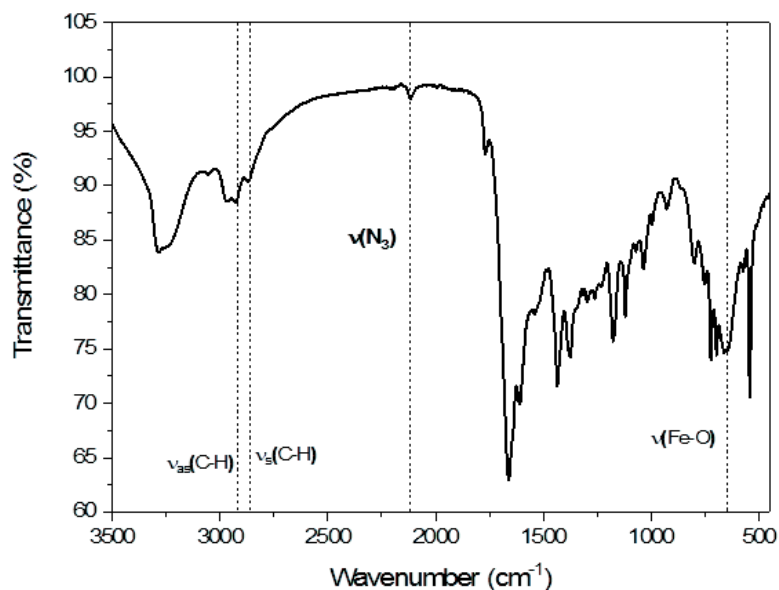


Figure II-33. Infrared spectra of the assembly solution after 48 h of reaction of NP10

The assembly solution with the presence of triethylamine, nanoparticles and the copper catalyst presents many bands which are difficult to interpret. However, the presence of azide vibrational band at  $2100\text{ cm}^{-1}$  allows to conclude that there is no degradation of the azide groups. However, the desorption of the phosphonic acid is still possible and may induce aggregation. Moreover, dipolar interactions may favor the formation of clusters in suspension which may explain the easiest aggregation in the case of the largest nanoparticles.

#### 4. Conclusions

Iron oxide nanoparticles have been assembled onto gold substrates through “click” chemistry reaction which provides a stable assembly thanks to covalent bonds. The control of the reaction time showed that the spatial arrangement can be tuned. Moreover, the density at the surface is dependent of the concentration of the nanoparticle suspension. By following the rate of coverage, dipolar interactions have been highlighted to influence the assembly. For small nanoparticles, the assembly structure consists in isolated nanoparticles. In contrast, for larger nanoparticles such as NP20, strong dipolar interactions accelerate the assembly kinetics and lead to clusters and alignments. The study of the stability of the suspensions as function of the reaction time has shown that the assembly may also be driven by the aggregation of nanoparticles in solution.

## D. Characterization of the nanoparticle assemblies

### 1. Composition and structural characterizations

The structural and composition characterizations were performed on a reference sample of a fully covered assembly of 10 nm-sized nanoparticles (NP10) obtained after 48 hours of reaction.

#### a) Atomic force microscopy

Atomic force microscopy (AFM) was performed on the NP10 assembly to have complementary information to the SEM images on the structure of the assembly. Figure II-34 shows the AFM images  $2 \times 2 \mu\text{m}$  of the surface of an assembly after 48 hours. Dense packed nanoparticles were observed on the surface. The sample is homogenous and the density of nanoparticles is constant on the image. A topographic profile has been done using WSXM software.<sup>[34]</sup> The measured height on the assembly reaches an average of 9.1 nm which agree with the nanoparticle size.

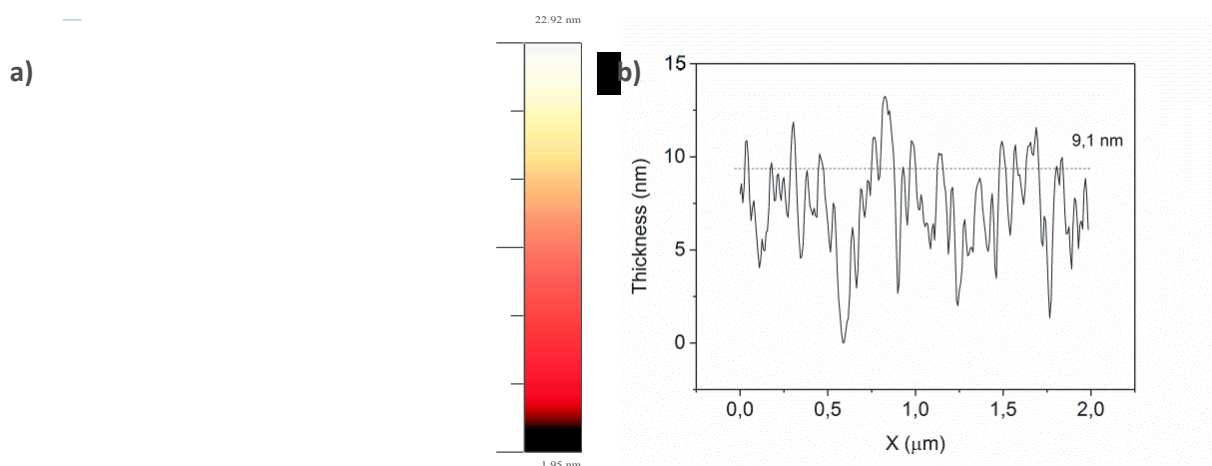


Figure II-34. a) AFM image of the 10 nanometer-sized nanoparticle assembly and b) topographic profile following the blue line

The roughness of the sample can be also extracted from these images and is evaluated to 2.6 nm. This larger value than SAM-CC can be explained by the presence of nanoparticles at the surface which increase the roughness of the assembly.

#### b) Water contact angle

Water contact angle (WCA) measurements have been performed to evaluate the hydrophobicity of the surface. The measurements have been done by depositing a  $5 \mu\text{L}$  droplet on the surface and take a picture of the sample after 1 minute in order to stabilize the system. The nature of this hydrophobicity is driven by the functional groups at the surface. Here, long alkane chains do not

present polar groups which can induce a hydrophilic surface. Indeed, figure II-35 shows a contact angle value of  $99.8^\circ$  relevant of a hydrophobic surface.

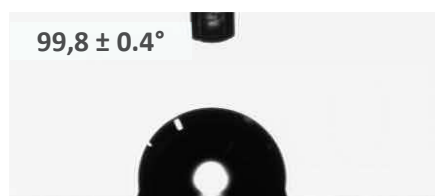


Figure II-35. Water contact angle characterization of the 10 nm-sized nanoparticle assembly

### c) Polarized Modulated Infrared Reflection Absorption Spectroscopy

Polarized Modulated Infrared Reflection Absorption Spectroscopy (PM-IRRAS) allows determining the vibrational bands of compounds grafted onto a substrate by using infrared with a grazing ( $< 5^\circ$ ) incidence (figure II-36). The presence of interferences reduces the spectral range between  $3500\text{ cm}^{-1}$  and  $900\text{ cm}^{-1}$  and avoids the observation of the iron oxide band. Nevertheless, it can be possible to observe functional groups at the surface of the nanoparticle assembly.

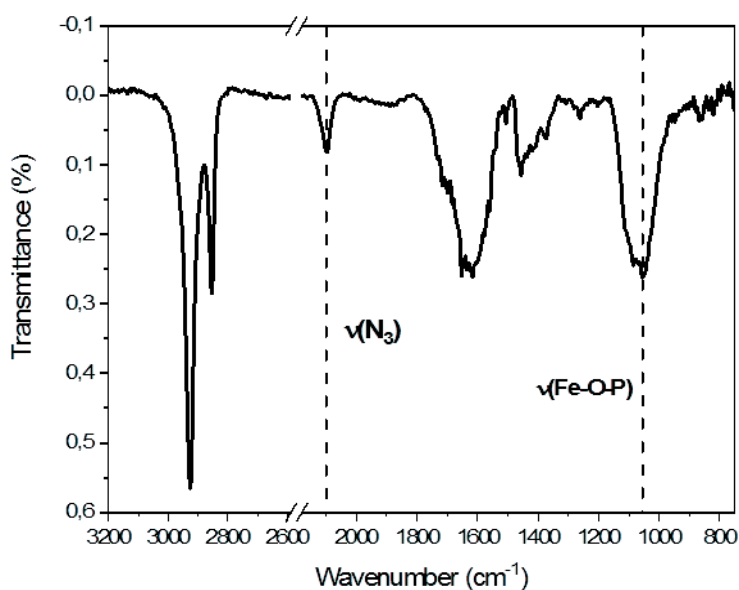


Figure II-36. PM-IRRAS spectrum of the assembly of nanoparticles of 10 nm with full density

The vibrational bands characteristics of the alkane chains are visible at  $2850\text{ cm}^{-1}$  and  $2920\text{ cm}^{-1}$ , meaning the presence of the ligands at the surface of the nanoparticles. The peak of the stretching mode ( $\nu(\text{Fe-O-P})$ ) at  $1040\text{ cm}^{-1}$  and the azide vibrational band ( $\nu(\text{N}\equiv\text{N})$ ) at  $2100\text{ cm}^{-1}$  show that  $\text{AP12N}_3$  was still grafted onto the nanoparticle surface. Moreover, it confirms the stability of  $\text{AP12N}_3$  at the nanoparticle surface after the CuAAC reaction was completed.

#### d) X-Ray Photoelectron Spectroscopy

In order to confirm the presence of azide groups at the surface and to validate PM-IRRAS results, XPS measurements have been performed (figure II-37). The  $\text{Fe}_{2p}$  region shows multiple peaks which can be attributed to  $2P_{1/2}$  and  $2P_{3/2}$  core level. Each peak can be deconvoluted in two components corresponding to  $\text{Fe}^{2+}$  and  $\text{Fe}^{3+}$  from the magnetite.<sup>[35]</sup> The satellite peaks, especially at 720 eV can be attributed at the  $\text{Fe}^{3+}$  present in the maghemite phase which indicates the oxidation of the nanoparticles.<sup>[36]</sup> However, the XPS is a surface characterization and cannot show a rigorous stoichiometry in the film which allow to estimate the quantity of maghemite. The  $P_{2p}$  core level region shows a low signal at 133.5 eV. The phosphonic acids are localized at the nanoparticle surface while they are between nanoparticle and the substrate and cannot be observed since the XPS signal does not probe beyond 9-10 nm.<sup>[37]</sup>

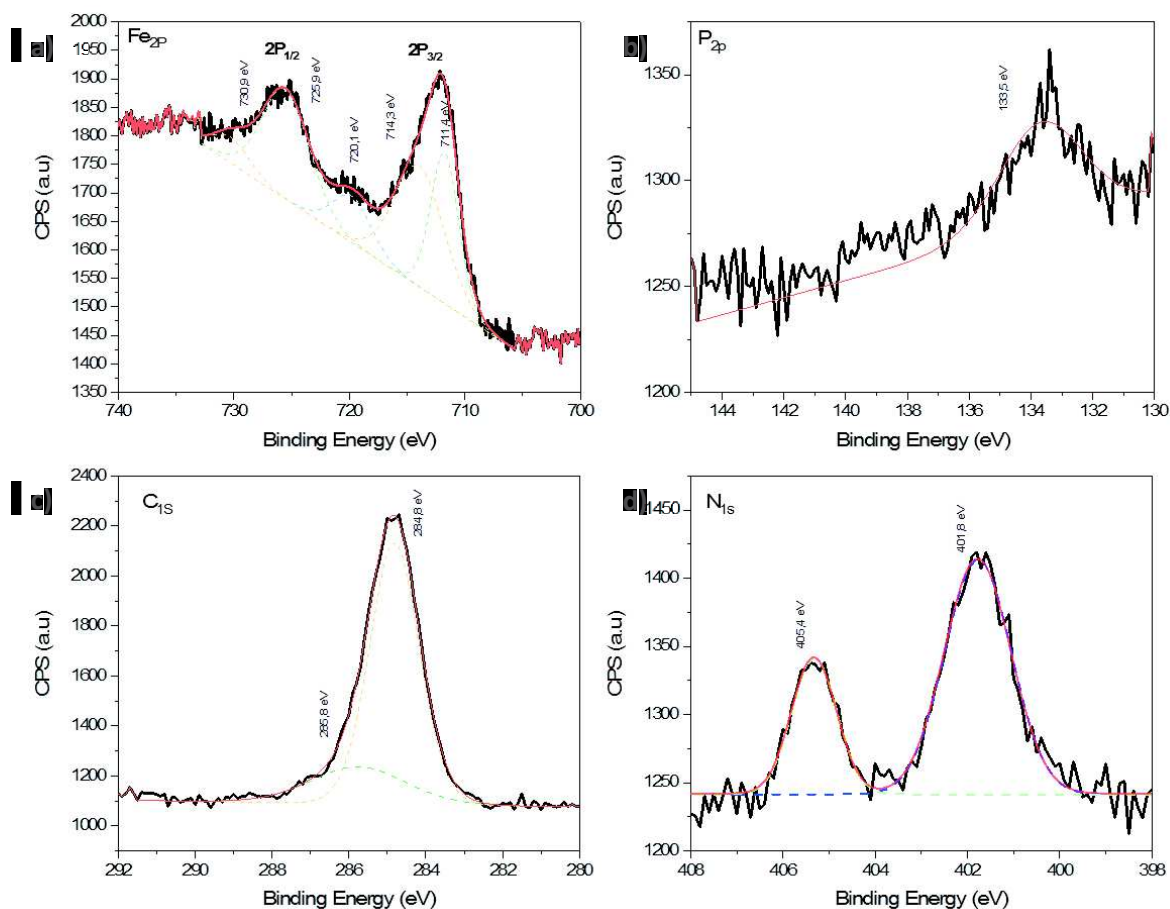


Figure II-37. XPS spectra of the NPs assembly on the region a)  $\text{Fe}_{2p}$  b)  $\text{P}_{2p}$ , c)  $\text{C}_{1s}$  and d)  $\text{N}_{1s}$

$\text{N}_{1s}$  core level region shows both characteristic peaks at 401,3 eV and 405,4 eV of the azide groups. The intense peak at 401,3 eV corresponds to the two lateral nitrogen atoms ( $-\text{N}=\text{N}=\text{N}$ ) whereas the peak at 405,4 eV correspond to the central nitrogen atom ( $-\text{N}=\text{N}=\text{N}$ ). It is confirmed by the ratio of the peak area close to 2:1.<sup>[38]</sup> These measurements confirm the presence of the azide groups at the nanoparticle assembly surface after the click reaction. The  $\text{C}_{1s}$  core level presents a large component at 284.8 eV which is attributed to the C-C and C-H bonds and a smaller one at 286.6 eV representing the C-N bonds in the triazole bridge.<sup>[39, 40]</sup>

The surface characterizations showed that the azide groups are still present at the surface of nanoparticle assembled onto substrate and are therefore available for further grafting.

## 2. Magnetism characterization

The magnetic properties of nanoparticle assemblies are strongly dependent of their spatial arrangement. Indeed, magnetic dipolar interactions are dependent on the intrinsic properties of nanoparticles (magnetization saturation) and also on the distance between nanoparticles. In the first part of this chapter, the magnetization saturation of the nanoparticles was measured for the NP20 which presents the highest  $M_s$  (75 emu/g) and that of NP5 and NP10 was lower (55 emu/g). The dipolar energy can be evaluated by knowing the inter-particle distance which is dependent of the density. Therefore, the collective and individual properties can be studied as function of the spatial distribution of assemblies. Samples with different sizes and densities were measured to evaluate the influence of magnetic dipolar interactions.

### a) Cycles of magnetization as function of external field

Magnetization was measured as function of the external applied magnetic field for assemblies of NP5, NP10 and NP20 with two different densities. Assemblies with low and high density of nanoparticles were prepared which represent two systems with weak and strong dipolar interactions respectively. The inter-particle distance is lower than 7 nm. The inter-particle distances were also calculated (see Appendix A for detailed calculus) in order to evaluate the strength of dipolar interactions. The inter-particle distance is an average value considering nanoparticles randomly dispersed onto a surface. The samples with low densities of nanoparticles present a low coverage (below 25% of the maximal theoretical value) which corresponds to inter-particle average distances larger than 10 nm. In the case of high density, the NP10 and NP20 present coverage close to 80% whereas the NP5 presents coverage of 41% of the maximal theoretical value. However, we saw (especially in the case of NP20), that the nanoparticles can form clusters and alignments onto the substrate. Therefore, this value only represents the idea of how far a first neighbor can be found. The density values are summarized in table II-7 and the SEM images are shown in figure II-38.

Table II-7. Structural characteristics of nanoparticle assemblies. density and the corresponding average inter-particle distance

		Density (NPs/ $\mu\text{m}^2$ )	Inter-particle distance (nm)
NP5	Low density	$2000 \pm 95$ ( $20 \pm 1\%$ )	$11 \pm 2$
	High density	$4019 \pm 430$ ( $41 \pm 4\%$ )	$7 \pm 2$
NP10	Low density	$1240 \pm 255$ ( $24 \pm 5\%$ )	$14 \pm 4$

	High density	3890 ± 95 (76 ± 2%)	5 ± 1
NP20	Low density	320 ± 45 (17 ± 3 %)	27 ± 5
	High density	1505 ± 60 (81 ± 3%)	6 ± 1

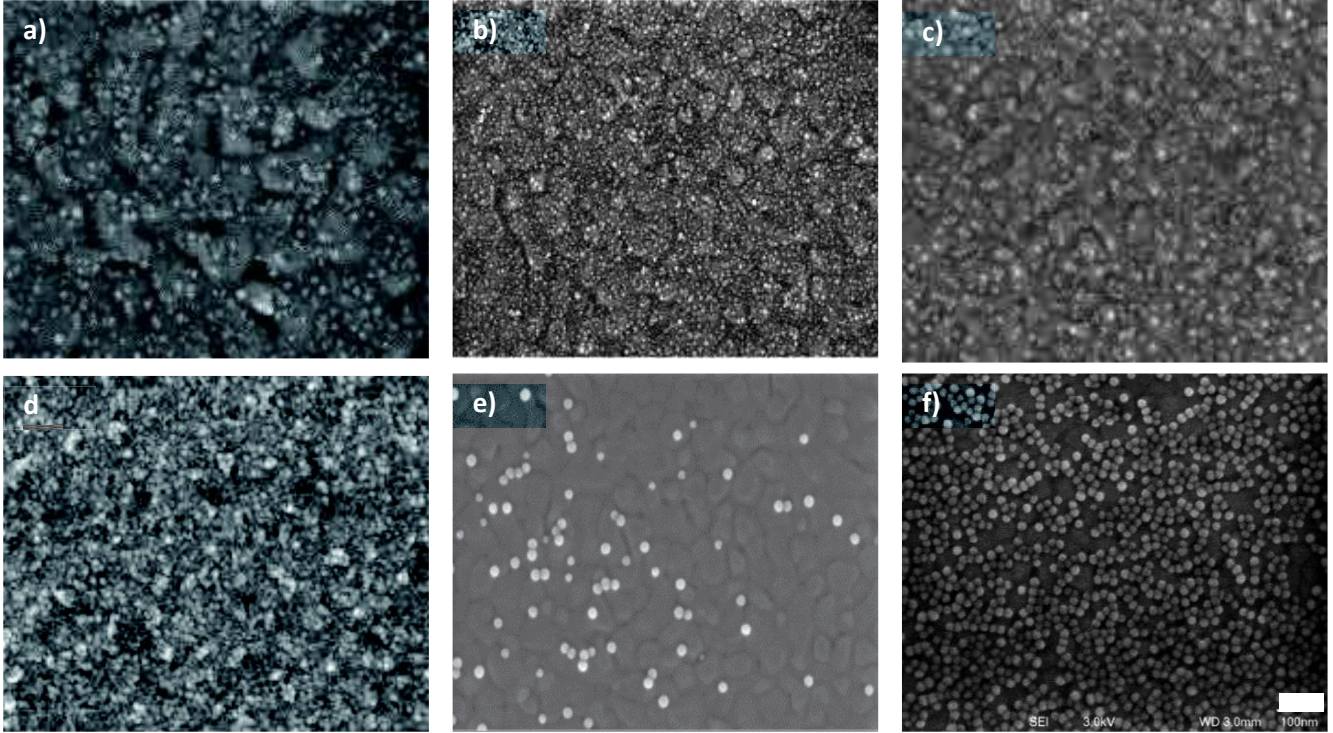


Figure II-38. SEM images of NPs assembly of a) and b) 5 nm, c) and d) 10 nm, e) and f) 20 nm at low density a),c) and e) and high density b), d) and f). Scale bar: 100 nm

The inter-particle distances here play an important role since the dipolar interactions between nanoparticles influence the collective magnetic properties of these assemblies. If we consider the macro-spin approximation and a triangular array of nanoparticles, the dipolar energy  $E_d$  can be defined as (see chapter I):

$$E_d = 2.8 \frac{\mu^2}{a^3} \quad \text{Equation II.2}$$

with  $\mu$  the nanoparticle magnetization and  $a$  the distance between center of the nanoparticles. Considering the magnetization of a nanoparticle as the saturation magnetization  $M_s$  multiplied by its volume ( $V = \pi D^3/6$ ). The distance between centers of nanoparticles corresponds to the sum of the diameter of the nanoparticle and the inter-particle distance ( $a = D + s$ ), which give:

$$E_d = 2.8 \frac{\left(M_s \frac{\pi D^3}{6}\right)^2}{(D+s)^3} \quad \text{Equation II.3}$$

with  $M_s$  the nanoparticle magnetization,  $D$  the nanoparticle diameter and  $s$  the distance between nanoparticles. Here, we can easily see the strong influence of the size of the nanoparticles on this interaction. The dipolar energy of bulk magnetite normalized with the Boltzmann constant is determined with an inter-particle distance of 4 nm which corresponds to twice the organic layer (figure

II-39.a). A strong increase of the dipolar energy can be observed for larger nanoparticles, whereas nanoparticles smaller than 10 nm exhibit a lower dipolar energy. The distance between nanoparticles influences also the dipolar energy. This effect of the distance was calculated for the three sizes of nanoparticles considered and normalized with their anisotropy energy defined by:

$$E_d = KV = K \frac{\pi D^3}{6} \quad \text{Equation II.4}$$

with K anisotropy constant of the nanoparticle. The ratio between dipolar and anisotropy energies can be expressed as:

$$\frac{E_d}{E_a} = \frac{2.8M_S}{6K} \left( \frac{D}{D+s} \right)^3 \quad \text{Equation II.5}$$

This ratio is determined with the saturation magnetization calculated for the size of each nanoparticle and with the magnetocrystalline constants of magnetite ( $K = 1.1 \times 10^5 \text{ erg/cm}^3$ ) and presented in figure II-39.b.

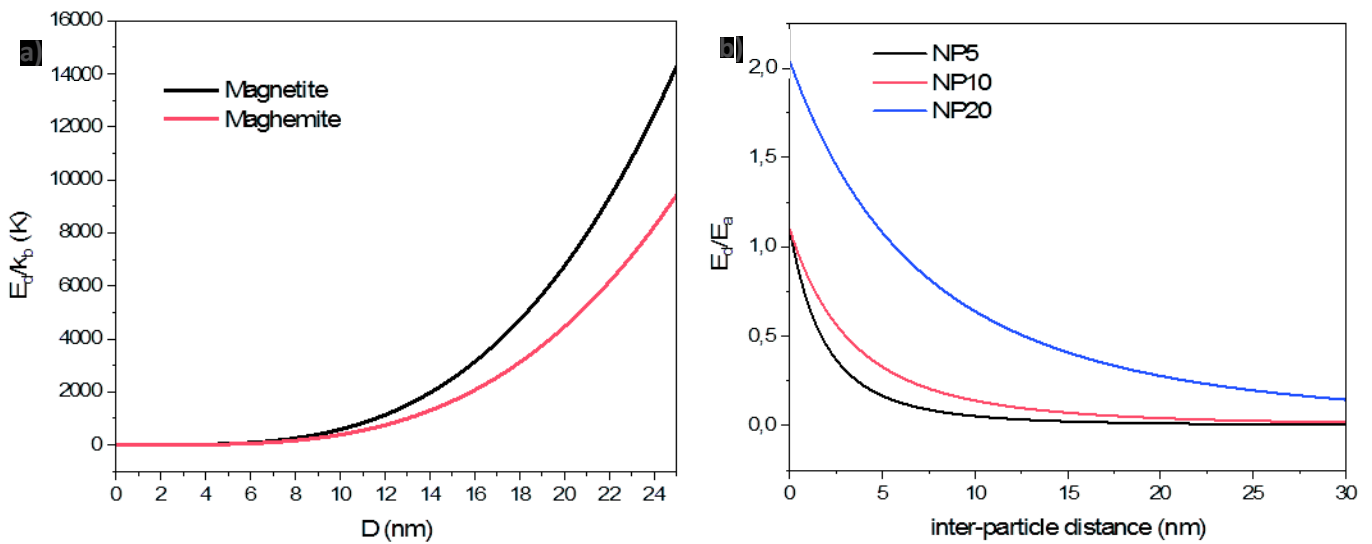


Figure II-39. a) Dipolar energy as function of the nanoparticle diameter and b) ratio between dipolar energy and anisotropy energy as function of the inter-particle distance for different sizes of nanoparticle

The dipolar energy decreases fast with the inter-particle distance especially for NP5 and NP10. In the case of NP20, the dipolar interactions stay strong even for the sample with low density and large inter-particle distance (27nm) where the ratio  $E_d/E_a$  is larger than sample NP10 with high density. These curves show the strong influence of the size of the nanoparticles on the dipolar interactions and explain the structuration of the assemblies where larger nanoparticles form alignments. These informations will help to understand the magnetic measurements performed on these assemblies.

Figure II-40 presents the hysteresis loop of the assemblies of nanoparticles from different sizes for the low (red curve) and the high density coverage (blue curve). The coercive field  $H_c$  and ratio of remanent magnetization on saturation magnetization at 5 K are summarized in table II-8.

Table II-8. Coercive field and remanent magnetization for nanoparticle assemblies of different sizes and densities compared with powder at 5 K

	$H_C$ (Oe)	$M_R/M_S$	$E_d/k_B$ (K)	$H_C$ (Oe) powder	$M_R/M_S$ powder
NP5 Low density	1100	0.38	30	240	0.36
NP5 High density	210	0.42	70		
NP10 Low density	1660	0.40	330	500	0.36
NP10 High density	370	0.42	1250		
NP20 Low density	480	0.28	3300	330	0.16
NP20 High density	550	0.31	18000		

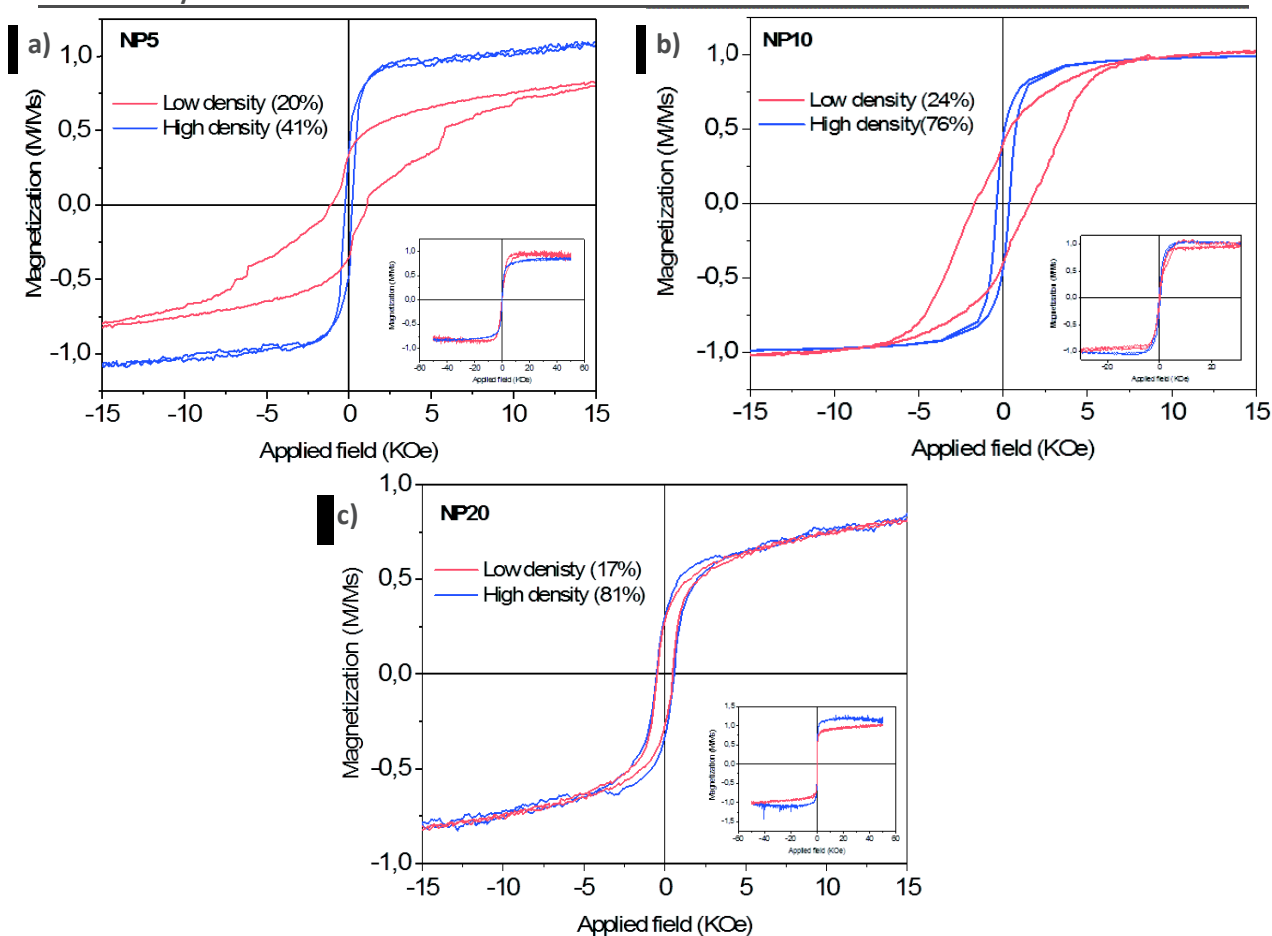


Figure II-40. Magnetization as a function of an applied magnetic field recorded at 5 K for nanoparticle monolayers with high (blue curve) and low (red curve) densities a) NP5, b) NP10 and c) NP20. Insets represent cycles at 300

The interpretation of the evolution of the coercive field and the remanent magnetization as function of the dipolar interactions and the anisotropy of assemblies is not trivial. The literature is conflicting in the evolution of  $H_C$  and  $M_R/M_S$  as function of the dipolar interactions.<sup>[13, 41-44]</sup> The coercive field and remanent magnetization should decrease when the dipolar interactions are stronger which are mostly explained by the collective properties of the nanoparticles. The force needed to reverse the magnetization of an assembly of nanoparticles will be weaker than the force to reverse an isolated nanoparticle because of the dipolar interactions will participate to reverse the magnetic moments. If

we consider the case of NP5 and NP10 which present both weak dipolar interactions, a similar behavior is observed. Indeed, a larger coercive field is observed for samples with low densities which is coherent with a high  $H_C$  for isolated nanoparticles. The dipolar energy for the NP10 sample with high density (1250 K) is almost four times higher than for the low density sample (330 K). It is correlated to the coercive field which is four times weaker (370 Oe versus 1660 Oe). In the case of the NP5 assembly with low density, the coercive field is five times larger than for high density whereas the dipolar energy is only twice weaker. This behavior can be explained by the calculated average distance which does not correspond exactly to the spatial arrangement of nanoparticles. In the case of NP10, a significant amount of clusters of nanoparticles can be observed which strengthen the dipolar interactions. Moreover, the hysteresis loop of NP5 with low coverage is not symmetric, meaning all the magnetic moments are not reversed at the same times. Different populations of nanoparticles can be responsible of this behavior such as isolated nanoparticles and clusters of nanoparticles.

In the case of NP20, this enlargement of the hysteresis loop is not observed for assembly with low density of nanoparticles. The explanation may come from the strong dipolar interactions even with large inter-particles distances. Indeed, the  $E_d/k_b$  ratio for NP20 is much larger than for NP5 and NP10 assemblies with high densities. Moreover, as shown previously, the 20 nm nanoparticles tend to easily form clusters or alignments.

The slight decrease of  $H_C$  in the dense assemblies compared to the powder state can be attributed of the increase of the anisotropy in 2D which favors in-plane magnetization reversal. However, for NP20,  $H_C$  is the largest in the nanoparticle assembly. The strong dipolar interactions can be responsible of this behavior which has been already observed.<sup>[13]</sup>

The increase of the  $M_R/M_S$  ratio in assemblies compared to powder may be due to the loss of order in the powder state. Indeed, a 2D array shows a higher order and, therefore, presents more anisotropy than powder. A random orientation is expected in the powder state which conducts to decrease the  $M_R/M_S$  value.<sup>[13]</sup>

## b) *Magnetic measurements as function of the temperature*

The measure of the magnetization as function of the temperature was performed on the nanoparticle assemblies of different sizes for low and high coverage (figure II-41).

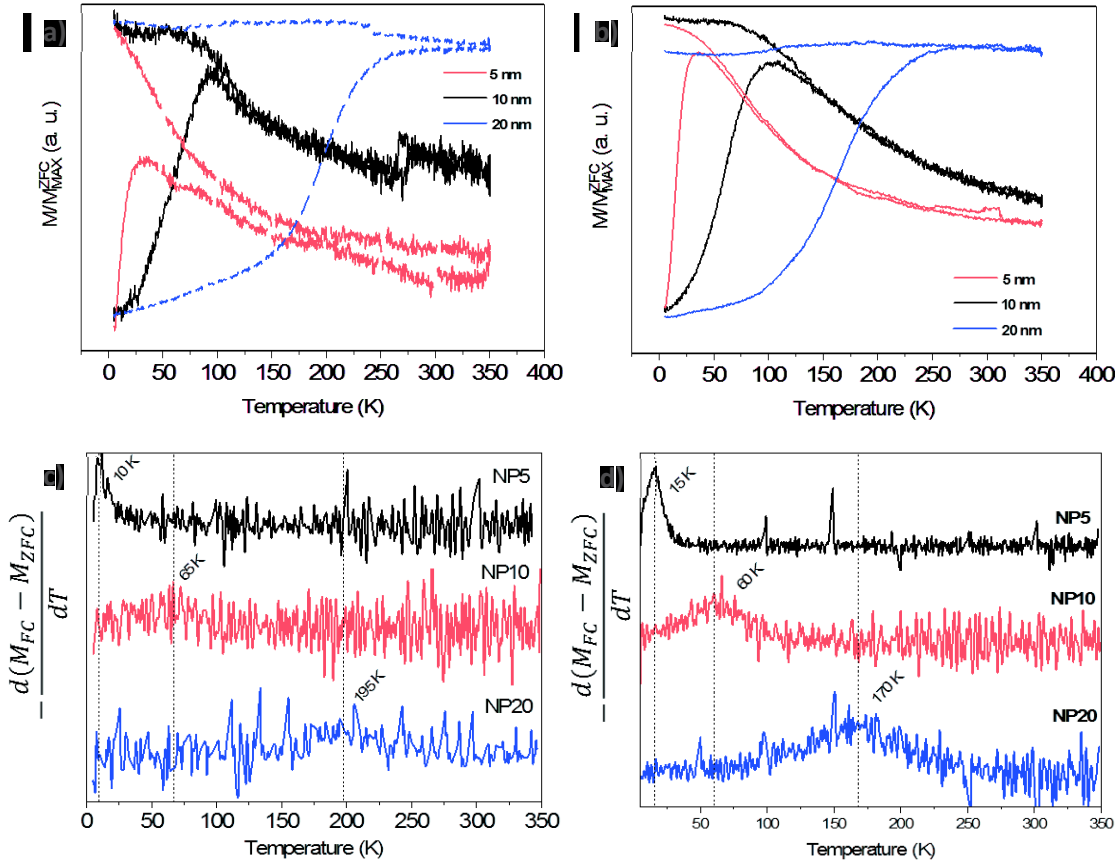


Figure II-41. a,b) ZFC/FC temperature dependent magnetization curves and c,d) temperature derivative of the difference between ZFC and FC for assemblies of nanoparticles of different sizes at a,c) low density and b,d) high density

$T_{Max}$  were extracted from the maximum of the ZFC curves. Values for the assemblies with different densities and the nanoparticles in powder state are summarized in table II-9.

Table II-9.  $T_{Max}$  values for nanoparticle assemblies of different sizes and densities and for the powder state

	NP5		NP10		NP20	
	$T_{Max}$	$T_B$	$T_{Max}$	$T_B$	$T_{Max}$	$T_B$
Low density	30 K	10 K	90 K		260 K	
High density	35 K	15 K	100 K	60 K	270 K	170 K
Powder state	50 K	20 K	110 K	75 K	> 350 K	185 K

$T_{Max}$  measured from the ZFC curves and  $T_B$  from the temperature derivatives (figure II-41). However, for low density film, the measure of  $T_B$  is complicated due to the low signal and to high noise on the measurement. Nevertheless, the values of  $T_B$  are following the same trend than  $T_{Max}$ . For all nanoparticle assemblies,  $T_{Max}$  increases with nanoparticle density which is correlated to higher magnetic anisotropy of nanoparticles.

These results have been already shown in the case of nanoparticle assemblies prepared by the Langmuir-Blodgett<sup>[13]</sup> and click chemistry<sup>[6]</sup> techniques which showed the 2D enhances collective properties by favoring anisotropy of dipolar interactions in plane.

The lower dipolar interactions for non-interacting nanoparticles explain the slightly decrease of the blocking temperature in the case of low density assemblies.<sup>[45]</sup> Nevertheless, the assemblies of nanoparticles in a 2D layer increase the anisotropy of the film and therefore require a higher energy to change the behavior of nanoparticles and to make them becoming superparamagnetic.<sup>[6]</sup>

A higher blocking temperature could be expected for high density films in comparison with powder state. Here, the  $T_{Max}$  is lower for the film than for the powder which goes against what have already been observed.<sup>[6, 13]</sup> This behavior could have been explained by the presence of aggregates or inhomogeneous density of nanoparticles assemblies, but the SEM images do not show such inhomogeneities. Nevertheless, NP5 and NP20 high density assemblies present some “holes” at the surface where no nanoparticles are grafted and so can be responsible of the smaller value of  $T_{Max}$ .

Another observation is the non-saturation of the FC curve at low temperatures for the NP5 assemblies. The dipolar interactions are weaker with the decrease of the size of nanoparticles<sup>[13]</sup>. Therefore, the FC curve will not present a plateau for the low temperature. Isolated nanoparticles or with low dipolar interactions are typical representative for this non-saturation. The combination of the small size and the low coverage on this sample makes very low dipolar interactions and the non-saturation even for low temperatures.

### 3. Conclusion

The magnetic properties of assemblies of nanoparticles with different sizes and different densities have been studied. The investigations of the dipolar interactions have highlighted two distinct behaviors between the NP5 and NP10 which present weak dipolar interactions and NP20 which presents strong dipolar interactions even in the case of the assembly with large inter-particle distance. The non-interacting nanoparticles showed a higher coercive field which is explained by the loss of collective properties. In contrast, larger nanoparticles present collective behaviors even for low coverages confirmed by similar coercive fields. The temperature of transition between ferrimagnetism and superparamagnetism for dense assemblies is surprisingly close to the powder state. The presence of defects in the films could explain this behavior.<sup>[32, 45]</sup> However, the decrease of  $T_{Max}$  for the lowest densities is coherent with non-interacting nanoparticles.<sup>[45, 46]</sup>

## E. General conclusion

The thermal decomposition method has allowed synthesizing iron oxide highly stable nanoparticle suspension in organic solvent. Three different sizes have been successfully synthesized and characterized:  $5.1 \pm 0.8$  nm,  $10.1 \pm 1.1$  nm and  $21.2 \pm 1.2$  nm.

Nanoparticles were post-functionalized by direct ligand exchange with a phosphonic acid derivative carrying azide group in order to complete the assembly through CuAAC “click” chemistry. Moreover, gold substrates were functionalized with thiol carrying alkyne complementary groups required for the “click” reaction.

The assemblies of the azido-terminated nanoparticles onto the alkyne-terminated SAM were performed by CuAAC “click” reaction and the conditions of reaction were studied. The variation of reaction time allowed controlling the spatial distribution of the nanoparticles on the gold surface from few isolated nanoparticles to a dense monolayer. The kinetic of the assembly was studied for two different concentrations and showed a faster kinetic for larger nanoparticles in contrast with small nanoparticles which do not reach the full monolayer. The investigation on the colloidal stability of the nanoparticle suspension after different reaction time showed that the aggregation of nanoparticles is favored for larger nanoparticles. The assembly kinetics seems driven by the stability of the suspension and the dipolar interactions stronger in the case of 20 nm-sized nanoparticles.

Finally, the magnetic properties of assemblies prepared with different sizes and different densities were performed. The measure of the magnetization as function of an applied field and the temperature highlighted that the NP20 present stronger dipolar interactions than the NP5 and NP10 whatever the density of nanoparticles. This behavior explains the assembly is driven by these dipolar interactions and explains the faster kinetic and stronger tight-packing of the NP20.

## F. Bibliography

- [1] Baaziz, W.; Pichon, B. P.; Fleutot, S.; Liu, Y.; Lefevre, C.; Greneche, J.-M.; Toumi, M.; Mhiri, T.; Begin-Colin, S., *The Journal of Physical Chemistry C*, (2014) **118**, 3795.
- [2] Demortiere, A.; Panissod, P.; Pichon, B. P.; Pourroy, G.; Guillon, D.; Donnio, B.; Begin-Colin, S., *Nanoscale*, (2011) **3**, 225.
- [3] Cotin, G., Université de Strasbourg (2017).
- [4] Benoit P. Pichon, A. D., Matthias Pauly, Karin Mouglin, Alain Derory, and Sylvie Bégin-Colin, *J Phys Chem*, (2010) **114**, 9041.
- [5] K, N., *Wiley: New york*, (1986),
- [6] Toulemon, D., *Université de Strasbourg*, (2013),
- [7] Baaziz, W., *Université de Strasbourg*, (2011),
- [8] Walter, A.; Billotey, C.; Garofalo, A.; Ulhaq-Bouillet, C.; Lefèvre, C.; Taleb, J.; Laurent, S.; Vander Elst, L.; Muller, R. N.; Lartigue, L.; Gazeau, F.; Felder-Flesch, D.; Begin-Colin, S., *Chemistry of Materials*, (2014) **26**, 5252.
- [9] Erik Wetterskog, C.-W. T., Jekabs Grins, Lennart Bergström, and German Salazar-Alvarez, *ACS Nano*, (2013) **7**, 7132.
- [10] Park, J.; An, K.; Hwang, Y.; Park, J. G.; Noh, H. J.; Kim, J. Y.; Park, J. H.; Hwang, N. M.; Hyeon, T., *Nature materials*, (2004) **3**, 891.
- [11] Park, J.; Lee, E.; Hwang, N. M.; Kang, M.; Kim, S. C.; Hwang, Y.; Park, J. G.; Noh, H. J.; Kim, J. Y.; Park, J. H.; Hyeon, T., *Angew Chem Int Ed Engl*, (2005) **44**, 2873.
- [12] Zhang, Q. S. a. Z. J., *J. Phys. Chem. B*, (2006) **110**, 11205.
- [13] Pauly, M., *Université de Strasbourg*, (2010),
- [14] Pichon, B. P.; Gerber, O.; Lefevre, C.; Florea, I.; Fleutot, S.; Baaziz, W.; Pauly, M.; Ohlmann, M.; Ulhaq, C.; Ersen, O.; Pierron-Bohnes, V. r.; Panissod, P.; Drillon, M.; Begin-Colin, S., *Chemistry of Materials*, (2011) **23**, 2886.
- [15] Nogués, J.; Sort, J.; Langlais, V.; Skumryev, V.; Suriñach, S.; Muñoz, J. S.; Baró, M. D., *Physics Reports*, (2005) **422**, 65.
- [16] E. J. W. Verwey, E. L. H., *The Journal of Chemical Physics*, (1947) **15**, 174.
- [17] Upadhyay, A. P.; Behara, D. K.; Sharma, G. P.; Bajpai, A.; Sharac, N.; Ragan, R.; Pala, R. G.; Sivakumar, S., *ACS applied materials & interfaces*, (2013) **5**, 9554.
- [18] Rianasari, I.; de Jong, M. P.; Huskens, J.; van der Wiel, W. G., *International journal of molecular sciences*, (2013) **14**, 3705.
- [19] Kinge, S.; Gang, T.; Naber, W. J. M.; van der Wiel, W. G.; Reinhoudt, D. N., *Langmuir*, (2011) **27**, 570.
- [20] Toulemon, D.; Pichon, B. P.; Cattoen, X.; Man, M. W.; Begin-Colin, S., *Chem Commun (Camb)*, (2011) **47**, 11954.
- [21] Toulemon, D.; Pichon, B. P.; Leuvre, C.; Zafeiratos, S.; Papaefthimiou, V.; Cattoën, X.; Bégin-Colin, S., *Chemistry of Materials*, (2013) **25**, 2849.
- [22] T. J. Daou, J. M. G., G. Pourroy, S. Buathong, A. Derory, C. Ulhaq-Bouillet, B. Donnio, D. Guillon, and S. Begin-Colin, *Chem Mater*, (2008) **20**, 5869.
- [23] Basly, B.; Popa, G.; Fleutot, S.; Pichon, B. P.; Garofalo, A.; Ghobril, C.; Billotey, C.; Berniard, A.; Bonazza, P.; Martinez, H.; Felder-Flesch, D.; Begin-Colin, S., *Dalton Trans*, (2013) **42**, 2146.
- [24] T. J. Daou, S. B.-C., J. M. Grenèche, F. Thomas, A. Derory, P. Bernhardt, P. Legare, and G. Pourroy, *Chem Mater*, (2007) **19**, 4494.
- [25] Daou, T.; Buathong, S.; Ung, D.; Donnio, B.; Pourroy, G.; Guillon, D.; Begin, S., *Sensors and Actuators B: Chemical*, (2007) **126**, 159.
- [26] Hyeon, T., *Chemical Communications*, (2003), 927.
- [27] James P. Collman, N. K. D., and Christopher E. D. Chidsey, *Langmuir*, (2004) **20**, 1051.
- [28] Ralph G. Nuzzo, B. R. Z., and Lawrence H. Dubois, *JACS*, (1986) **109**, 733.

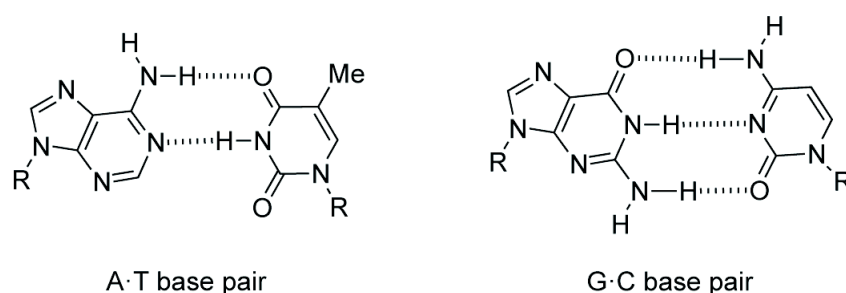
- [29] F. Tielens, V. H., C-M. Pradier, M. Calatayud, F. Illas, *Langmuir*, (2009) **25**, 9980.
- [30] H. C. Kolb, M. G. F., K. B. Sharpless, *Angew Chem Int Ed*, (2001) **40**, 2004.
- [31] Moitra, N.; Moreau, J. J.; Cattoen, X.; Wong Chi Man, M., *Chem Commun (Camb)*, (2010) **46**, 8416.
- [32] Toulemon, D.; Rastei, M. V.; Schmool, D.; Garitaonandia, J. S.; Lezama, L.; Cattoën, X.; Bégin-Colin, S.; Pichon, B. P., *Advanced Functional Materials*, (2016) **26**, 2454.
- [33] Maalouli, N.; Barras, A.; Siriwardena, A.; Bouazaoui, M.; Boukherroub, R.; Szunerits, S., *The Analyst*, (2013) **138**, 805.
- [34] Horcas, I.; Fernandez, R.; Gomez-Rodriguez, J. M.; Colchero, J.; Gomez-Herrero, J.; Baro, A. M., *The Review of scientific instruments*, (2007) **78**, 013705.
- [35] Nan, A.; Turcu, R.; Liebscher, J., *Journal of Polymer Science Part A: Polymer Chemistry*, (2012) **50**, 1485.
- [36] Cuenca, J. A.; Bugler, K.; Taylor, S.; Morgan, D.; Williams, P.; Bauer, J.; Porch, A., *Journal of physics. Condensed matter : an Institute of Physics journal*, (2016) **28**, 106002.
- [37] Gilbert, J. B.; Rubner, M. F.; Cohen, R. E., *Proceedings of the National Academy of Sciences of the United States of America*, (2013) **110**, 6651.
- [38] Gouget-Laemmel, A. C.; Yang, J.; Lodhi, M. A.; Siriwardena, A.; Aureau, D.; Boukherroub, R.; Chazalviel, J. N.; Ozanam, F.; Szunerits, S., *The Journal of Physical Chemistry C*, (2013) **117**, 368.
- [39] Baio, J. E.; Weidner, T.; Brison, J.; Graham, D. J.; Gamble, L. J.; Castner, D. G., *Journal of electron spectroscopy and related phenomena*, (2009) **172**, 2.
- [40] Vermette, P.; Gengenbach, T.; Divisekera, U.; Kambouris, P. A.; Griesser, H. J.; Meagher, L., *Journal of Colloid and Interface Science*, (2003) **259**, 13.
- [41] B. L. Frankamp, A. K. B., M. T. Tuominen, V. M. Rotello, *JACS*, (2005) **127**, 9731.
- [42] Poddar, P.; Telem-Shafir, T.; Fried, T.; Markovich, G., *Physical Review B*, (2002) **66**,
- [43] Kechrakos, D.; Trohidou, K. N., *Journal of Nanoscience and Nanotechnology*, (2008) **8**, 2929.
- [44] Dorothy Farrell, Y. C., R. William McCallum, Madhur Sachan, Sara A. Majetich, *J Phys Chem C*, (2005) **109**, 13409.
- [45] Klughertz, G.; Manfredi, G.; Hervieux, P.-A.; Pichon, B. P.; Begin-Colin, S., *The Journal of Physical Chemistry C*, (2016) **120**, 7381.
- [46] Fleutot, S. N., G. L.; Pauly, M.; Pichon, B. P.; Leuvrey, C.; Drillon, M.; Gallani, J.-L.; Guillon, D.; Donnio, B.; Begin-Colin, S., *Nanoscale*, (2013) **5**, 1507.

### III. CHAPITRE III –Nanoparticle self-assembly by multiple hydrogen binding between nucleosides

## A. Nanoparticle assembly through nucleosides

The self-assembly through multiple hydrogen bonding allow more flexible and dynamic in geometry than rigid covalent bonds. Moreover, they are directional and can be rendered highly selective by exploiting multiple hydrogen bonding molecules. Here, the strategy consists in the functionalization of nanoparticles and substrates by complementary group for click chemistry and graft subsequently modified nucleosides.

The recognition process will use the self-complementary Watson-Crick multiple hydrogen-bonding interactions nucleobases pairing. This process involves the recognition between nucleosides from the DNA: guanine-cytosine (GC) and adenine-thymine (AT)



An essential part of the assembly through nucleobase pairing is to understand the assembly process through multiple hydrogen bonds. The interaction energy for hydrogen bonds is usually defined between 10 and 50  $\text{kJ}\cdot\text{mol}^{-1}$ <sup>[1]</sup>, however this determination is not trivial since the recognition involves a high number of groups between the surfaces. Theoretical investigations have been performed to study the interaction energies between nucleobases and showed energies around 20  $\text{kJ}\cdot\text{mol}^{-1}$  (for the A-T pairs) and 50  $\text{kJ}\cdot\text{mol}^{-1}$  (for the G-C pairs).<sup>[2-4]</sup> Nevertheless, many parameters can influence the strength of the binding:

- The solvent can induce a competition to the pairing. Indeed, protic and polar solvents will favor recognition with the nucleobases and therefore not favor the base pairing in contrary to aprotic solvents which do not generate competition.
- $\pi$ -stacking between close packed rings decreases the interaction energy and therefore reduce the strength of the binding between pairs.
- The temperature can weaken the interactions between nucleobases. These binding usually break around 55°C.

These parameters shows that some requirements are needed to perform the assembly. Investigations on the solvent used for the assembly showed reversibility on the attachment of polymer onto substrate surface functionalized by complementary nucleobases.<sup>[5-8]</sup>

The couple adenine-thymine will be use in this study by functionalizing both nanoparticle and substrate surfaces with complementary nucleobases. The recognition happens by dipping the functionalized substrate in the nanoparticle suspensions at room temperature. The influence of experimental parameters such as the solvent, the pi-stacking and the temperature, was studied.

### 1. Substrate post-functionalization

In order to perform the recognition process, the surfaces have to be functionalized with nucleosides. The use of modified nucleosides with azide and alkyne groups will allow their grafting onto surfaces by CuAAC cycloaddition “click” reaction. Adenine modified by an azide group and thymine modified with an alkyne group are used (figure III-1).<sup>4</sup> The atom indexation in the ring will facilitate the infrared interpretation.

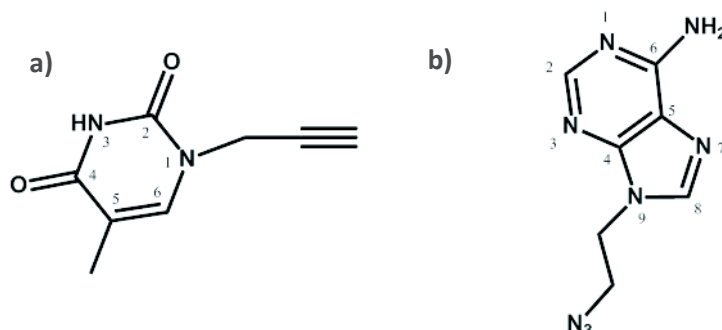


Figure III-1. Schematic representation of a) alkyne-modified thymine and b) azide-modified adenine

#### a) *Experimental procedure*

As seen in the previous chapter, the most efficient system is the alkyne-terminated SAM. The adenine modified with azide group is used to be grafted through click chemistry reaction on a SAM alkyne surface.

1-Dodecanethiol (DDT) was used to dilute alkyne groups at the surface prior to control the quantity of adenine groups at the surface. During the gold functionalization, substrates were immersed in a thiol solution with different molar ratios of DDT and 11-mercapto undecyn (MUY) with a total concentration in thiol of 10 mM. The ratio MUY/DDT was varied from 0% to 100% and SAM were called SAM-MUY/DDT 0%, 20%, 50%, 80% and 100%. Azide-modified adenine (Ade-N<sub>3</sub>) was then grafted to the alkyne on the surface of SAM prepared with different MUY/DDT ratios (figure III-2).

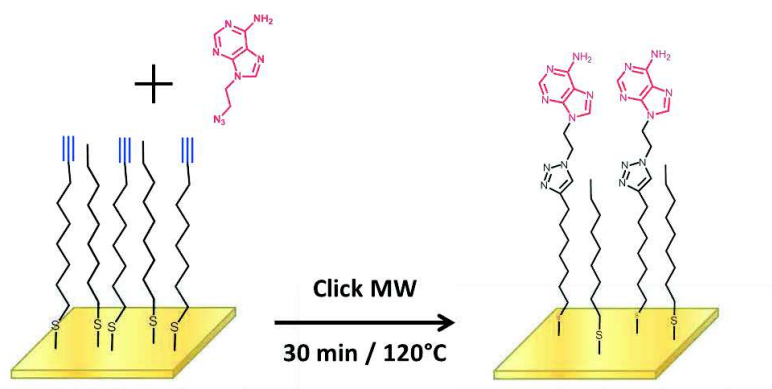


Figure III-2. Schematic representation of the substrate functionalization assisted by micro-wave (MW) irradiation

The CuAAC “click” reaction was performed by the same protocol than for the assembly of nanoparticles (chapter II) by using copper I catalyst. A large excess of modified nucleosides are used in order to promote the kinetics and diffusion of the molecules to the surface. In order to increase the

<sup>4</sup> Collaboration with X. Cattoën, Institut Néel, Grenoble.

efficiency of the process, the reaction was performed under microwave irradiations to decrease strongly the time of reaction. Indeed, the activation by micro-wave irradiation presents a different way of heating since the activation energy will directly stimulate the solvent molecules instead of classic heating process where the vessel is heated and the heat diffuse in the liquid.<sup>[9-12]</sup> The assembly solution was prepared with 6.5 mg  $\text{CuBr}(\text{PPh}_3)_3$ , 5 mL of THF, 0.5 mL of triethylamine and 10 mg (49  $\mu\text{mol}$ ) of azide-modified adenine ( $\text{Ade-N}_3$ ). The reagents were mixed in a vial, settled in a microwave reactor and heated until 120°C with a constant power of 50 W at a 2.45 GHz frequency. Then, the temperature was maintained at 120°C for 30 min before cooled at room temperature.

### b) *Characterization*

The SAM surface modified with adenine was characterized in order to study the presence of the nucleosides and to evaluate its quantity.

#### (1) Water contact angle

Contact angle measurements were performed on SAM with different MUY/DDT ratios after grafting of the adenine (figure III-3).

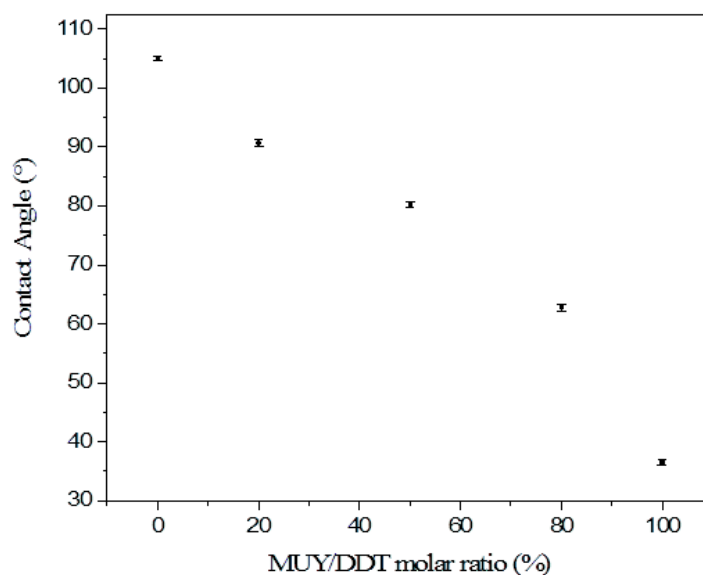


Figure III-3. Water contact angle values as function of the MUY/DDT molar ratio in solution

The water contact angle value decreases when the MUY/DDT molar ratio increase. The higher hydrophilicity of the substrate for high MUY/DDT ratio suggests a higher quantity of adenine. Indeed, the adenine presents a hydrophilic structure with the presence of polar groups. Therefore, the substrate becomes more hydrophilic with the increase of adenine. The contact angle runs from 105° when the surface is covered at 100% with DDT, to 33 % for a full coverage with adenine. The value decreases quasi-linearly which means that the quantity of adenine roughly corresponds to the ratio in solution.

## (2) X-Ray photoelectron spectroscopy

XPS measurements were performed on the SAM-Ade 100% in order to control the presence of adenine on the SAM surface. The adenine molecule presents nitrogen atoms. Thus, the  $N_{1s}$  region was probed to attest the presence of adenine groups (figure III-4).

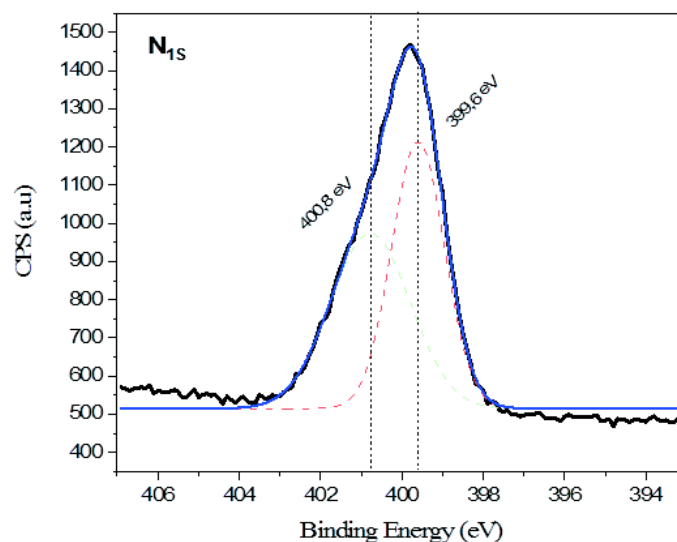


Figure III-4. XPS spectrum of the  $N_{1s}$  region for the SAM-Ade 100%

The large and intense peak around 400 eV shows the significant presence of nitrogen at the surface. The peak can be deconvoluted in two components at 399.6 eV and 400.8 eV. The first component can be attributed to the N-H and the nitrogen in aromatic ring whereas the second correspond to the N-C binding present in the position 9 of the adenine.<sup>[13-15]</sup> The component at 400.8 eV can also be attributed for the N-C binding in the triazole bridge.

## (3) Phase Modulated Infrared reflection absorption spectroscopy

PM-IRRAS were also performed on the SAM-Ade 100%. The results are compared to adenine deposited on a gold surface by drop casting (figure III-5).

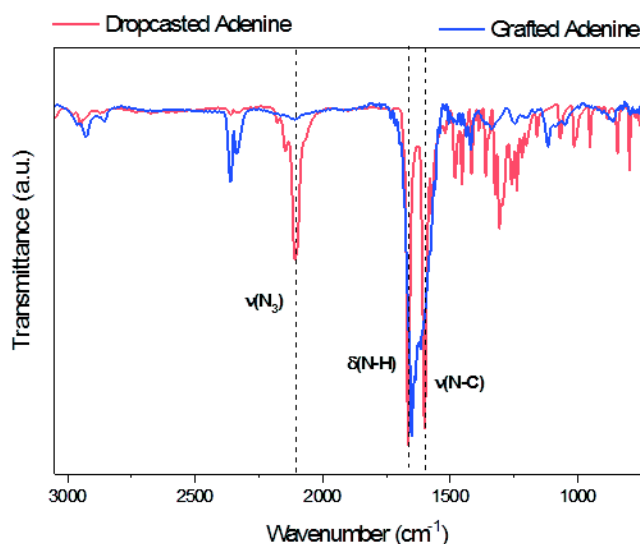


Figure III-5. PM-IRRAS spectra of adenine dropcasted on a surface (red curve) and grafted through click chemistry on alkyne SAM (blue curve)

The red curve shows the azido-modified adenine molecule deposited by drop casting on the substrate. Vibrational bands of the nucleosides can be identified in the range 800 - 2500  $\text{cm}^{-1}$ . The nucleosides present a large variety of vibrational bands between 800  $\text{cm}^{-1}$  and 1500  $\text{cm}^{-1}$  which have been listed in the literature.<sup>[16, 17]</sup> However, we will focus on the main and more intense bands at 1660  $\text{cm}^{-1}$  and 1580  $\text{cm}^{-1}$  which are attributed to the bending vibrational mode in amine  $\delta(\text{N-H})$  and the stretching mode  $\nu(\text{N}_3\text{-C}_4)$ . Moreover, the nucleoside has been modified by an azide group which can be noticed thanks to the characteristic vibrational band at 2100  $\text{cm}^{-1}$ . The blue curve shows the surface after the click chemistry reaction between the azido adenine and the alkyne SAM. The presence of adenine is confirmed by the strong vibrational band at 1660  $\text{cm}^{-1}$ . There are not anymore two fine bands, but a broad one which may be explained by the fact that the adenine groups are stacked at the nanoparticle surface in different orientations. Moreover, the characteristic band at 2100  $\text{cm}^{-1}$  is not visible which agree with the reaction of azide and alkyne groups. This last information confirms the grafting of adenine through triazole bridge to the SAM.

The XPS and PM-IRRAS showed the apparition of signature of functions present in the adenine and the disappearance of azide groups. It confirms the grafting of the adenine onto the SAM surface. Moreover, the WCA showed that different MUY/DDT ratios conduct to the quasi-linear change of the hydrophobicity of the SAM after grafting of azido-modified adenine grafting. It confirms the control of the quantity of adenine at the surface of the SAM. The substrates with different ratio in adenine were prepared in order to realize self-assembly of the nanoparticles.

## 2. Nanoparticle post-functionalization

### a) *Control of the quantity of azide groups at the surface*

The 10 nm-sized nanoparticles functionalized with azide groups (cf. chapter II) were used to graft alkyne-modified thymine (figure III-1.a). In order to control the pi-stacking, as on the substrate, thymine groups were diluted at the surface of the nanoparticles. In order to change de density of thymine groups at the surface, the nanoparticles were functionalized with different phosphonic acid

molecules. The purpose was to lead to mixed nanoparticles functionalized with azide groups and methyl groups which are inactive for the CuAAC click reaction. The functionalization was performed in THF with different ratios of 12-azido-dodecyl-phosphonic acid (AP12N<sub>3</sub>) and decyl-phosphonic acid (DPA) represented on figure III-6; 20%, 50%, 80% and 100%. The nanoparticles were then washed by ultrafiltration. The functionalization and the stability were monitored by FT-IR spectroscopy and granulometry.

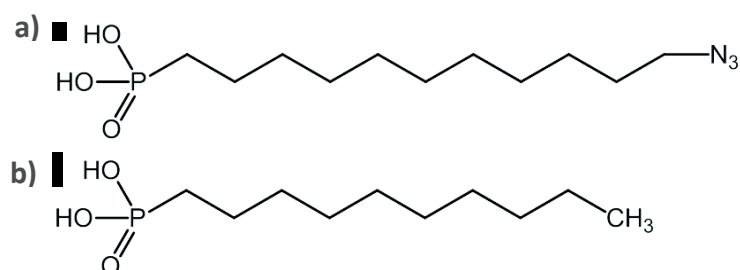


Figure III-6. Schematic representation of the a) 12-azido-dodecyl-phosphonic acid (AP12N<sub>3</sub>) and b) decyl-phosphonic acid (DPA)

The alkyl chain is slightly longer for AP12N<sub>3</sub> than DPA in order to favor the accessibility of azide groups at the nanoparticle surface.

(1) FT-IR spectroscopy measurements

The infrared spectroscopy measurements were performed in order to control the quantity of biotin groups at the nanoparticle surface (figure III-7). The spectra were normalized on the vibrational band of FeO at 590 cm<sup>-1</sup>.

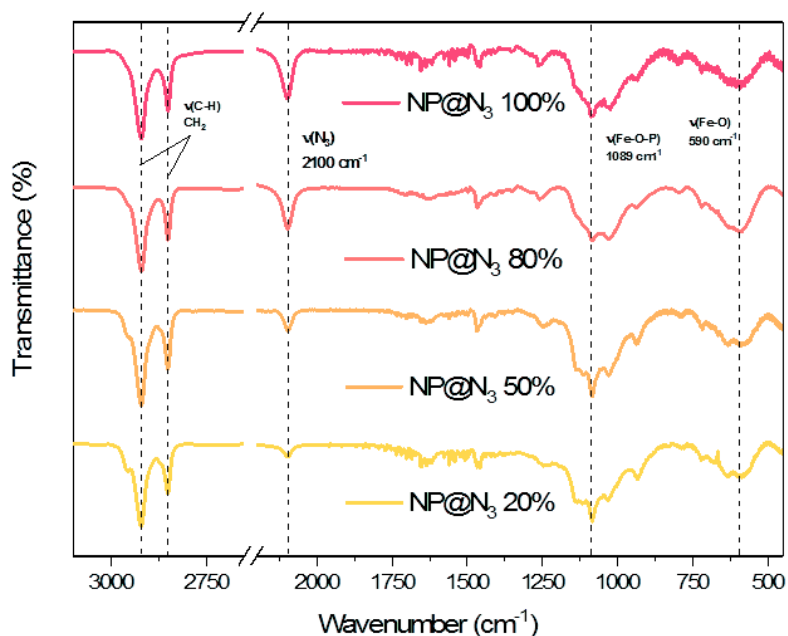


Figure III-7. FT-IR spectra of the nanoparticles functionalized with different AP<sub>12</sub>N<sub>3</sub>/DPA ratios

The FT-IR spectroscopy measurements show the vibrational bands of iron oxide, phosphonic acid and azide groups at 590 cm<sup>-1</sup>, 1080 cm<sup>-1</sup> and 2100 cm<sup>-1</sup> respectively. This indicates the correct

functionalization of the nanoparticles. The intensity ratio between iron oxide and phosphonic acid is very close whatever the AP<sub>12</sub>N<sub>3</sub>/DPA ratio which agree with similar grafting rate for both AP<sub>12</sub>N<sub>3</sub> and DPA molecules. However, the azide vibrational band decreases with the quantity of DPA molecules which were introduced in the reaction medium. Moreover, the vibrational band corresponding to the stretching modes of the CH<sub>3</sub> groups (2950 cm<sup>-1</sup>) increases with DPA molecules. The ratios of the different intensity peaks are summarized in table III-1.

Table III-1. Summarize of the intensity ratios between the vibrational bands  $\nu(\text{C-H})$  (2950 cm<sup>-1</sup>),  $\nu(\text{Fe-O})$  (580cm<sup>-1</sup>) and  $\nu(\text{N}_3)$  (2100 cm<sup>-1</sup>)

Azide phosphonic ratio in solution	Peak intensity ratios	
	CH <sub>3</sub> /Fe-O	N <sub>3</sub> /Fe-O
100 %	<b>0,36</b>	<b>1,42</b>
80 %	<b>0,37</b>	<b>0,95</b>
50 %	<b>0,78</b>	<b>0,62</b>
20 %	<b>0,83</b>	<b>0,45</b>

The ratio between azide and iron oxide vibrational bands increased with the ratio of AP<sub>12</sub>N<sub>3</sub>/DPA molar ratio in solution. In contrast, the ratio between methylene and iron oxide vibrational bands decreased. These results showed that azide groups at the nanoparticles surface can be modulated as function of the molecular ratio in solution.

## (2) DLS measurements

DLS measurements were performed in order to study the colloidal stability of the suspensions in THF after the functionalization with different molecular ratios. The results in THF are shows in figure III-8.

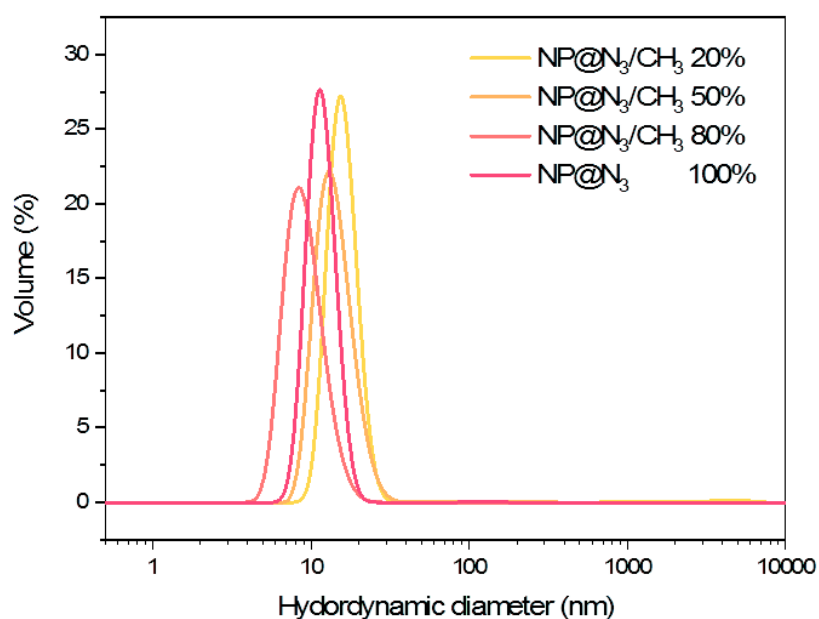


Figure III-8. DLS measurements of the nanoparticle suspensions with different AP<sub>12</sub>N<sub>3</sub>/DPA ratios in solution

The nanoparticles are stable for the four different ratios studied. The size distribution is monomodal, meaning no aggregation of the suspension and a unique size population. Some differences can be observed (from 10.1 nm to 15.5 nm) which are not discrediting the stability of these suspensions.

### b) *Post-functionalization with thymine groups*

The mixed-nanoparticles were then post-functionalized with the alkyne modified thymine groups. The CuAAC reaction was performed by using the nanoparticle suspensions with different quantities of azide groups at their surface.

As for the grafting of adenine, a large excess of modified thymine was used to promote the kinetics and diffusion of the molecules to the surface. Moreover, the reaction was performed under microwave irradiation for only 5 minutes. Indeed, the motion of nanoparticles promotes the encounter with molecules and fosters the reaction kinetics. Then, the suspension was purified by ultrafiltration in order to remove the excess of molecules and all the reagents present in the solution assembly (figure III-9).

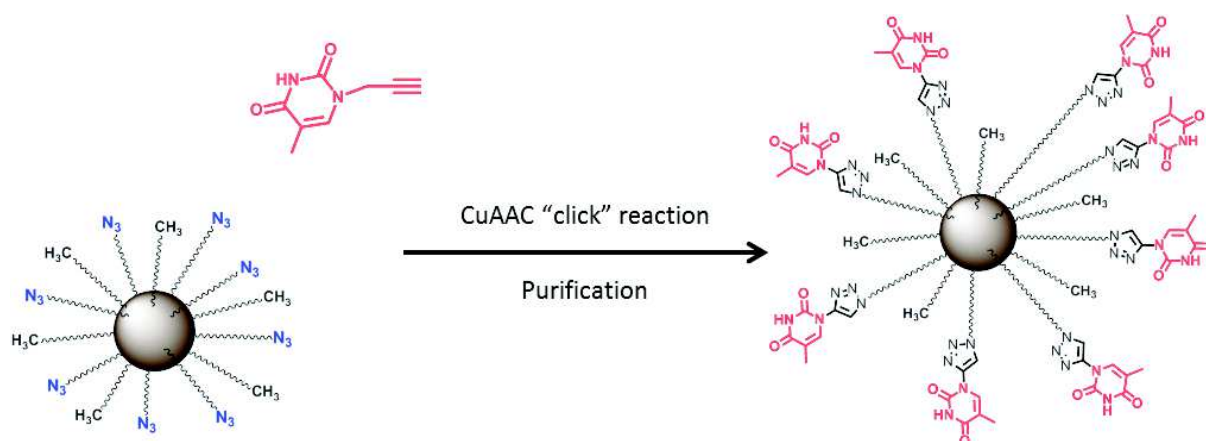


Figure III-9. Schematic representation of the "click" reaction to graft the thymine group at the nanoparticle surface

The nanoparticles after purification were characterized in order to study the presence of thymine at their surface and to control their colloidal stability. The nanoparticles functionalized with the thymine for the different AP12N<sub>3</sub>/DPA ratios are called NP@Thym 20%, 50%, 80% and 100%.

### c) *Characterization of the NP@Thym*

As for the substrate, the functionalized nanoparticles have been characterized in order to confirm the presence of the thymine species at their surface.

#### (1) TEM analysis

Transmission electronic microscopy was performed to study the size and morphology after the multiple functionalization processes (figure III-10).

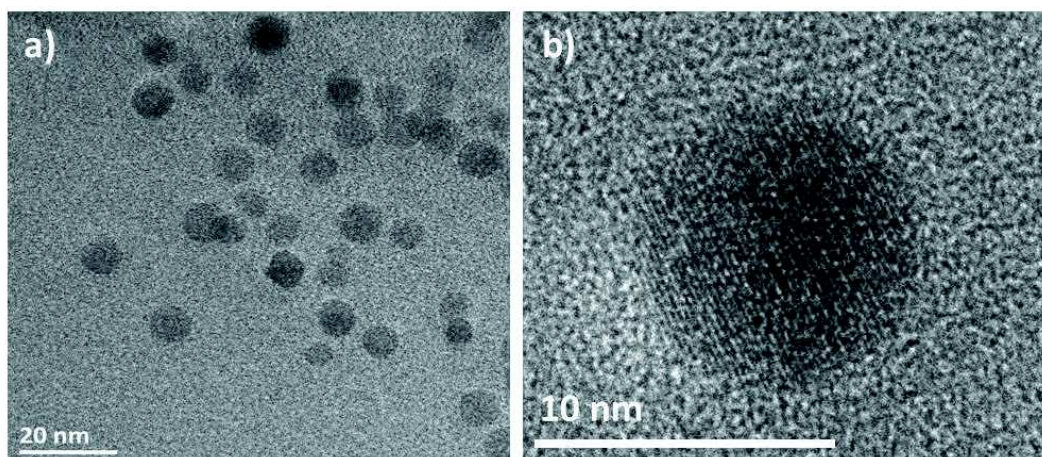


Figure III-10. TEM images of nanoparticles after functionalization with alkyne-modified thymine 100%

The morphology of the nanoparticles was not altered by the functionalization. The nanoparticle mean diameter was centered to  $8.5 \pm 0.8$  nm whereas the NP@OA was at  $9.1 \pm 0.6$  nm. The size remains constant (according to the standard deviation) even if a slight decrease can be noticed.

## (2) FT-IR measurements

FT-IR measurements were performed on the samples with different AP12N<sub>3</sub>/DPA molar ratios after the reaction with alkyne-modified thymine (figure III-11).

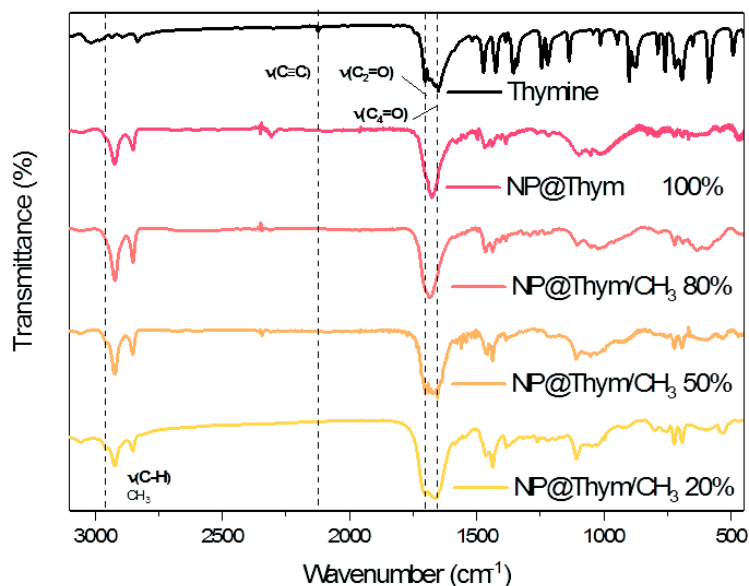


Figure III-11. Infrared spectra of NP@thym with different thymine ratio at the surface

The infrared spectrum of the free molecule of alkyne-modified thymine presents a large variety of vibrational bands in the range  $500-1700$   $\text{cm}^{-1}$ . The specific and weak band at  $2115$   $\text{cm}^{-1}$  is characteristic of the stretching mode of the alkyne binding  $\nu(\text{C}\equiv\text{C})$ . The more intense bands which allow identifying the thymine are located at  $1710$   $\text{cm}^{-1}$  and  $1660$   $\text{cm}^{-1}$ . These bands correspond to the

stretching mode of the carboxylic acid in the thymine  $\nu(\text{C}_2=\text{O})$  and  $\nu(\text{C}_4=\text{O})$ , respectively.<sup>[17, 18]</sup> The spectra of the functionalized NP@thym with different ratios exhibit for all this a large band centered around  $1680\text{ cm}^{-1}$  which agree with the presence of the thymine at the nanoparticle surface. In the case of the highest ratios of thymine, a single band at  $1680\text{ cm}^{-1}$  was observed. For the lowest ratios, two bands at  $1710\text{ cm}^{-1}$  and  $1660\text{ cm}^{-1}$  were observed as for the free molecule. The conformation of the C=O bonds is different for the high quantity of thymine at the surface, probably due to the stacking of the thymine groups at the nanoparticle surface. For low quantities of thymine, such a stacking disappears and the binding modes are closer from the molecule in solution.

The disappearance of the band at  $2115\text{ cm}^{-1}$  shows that the free thymine molecules in solution were totally removed and the purification step has been well performed. Moreover, the disappearance of the band at  $2100\text{ cm}^{-1}$  reveals that all the azide groups at the nanoparticle surface have totally reacted to form triazole bonds.

### (3) DLS measurements

Granulometry measurements have been performed on the NP@Thym in order to study the colloidal stability after the post-functionalization. The control of the aggregation in the following part becomes a crucial point. Therefore, the NP@Thym 100% will be distinguish from the others and their stability will be investigated first (figure III-12).

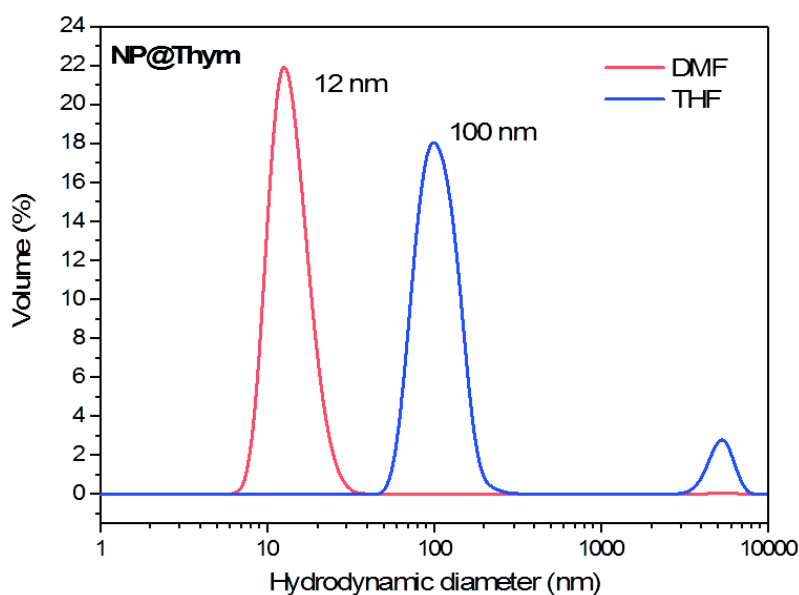


Figure III-12. DLS measurements of the NP@Thym 100% in THF (blue curve) and DMF (red curve)

The click reaction and the purification were both performed in THF. The DLS measurements (figure III-12, blue curve) exhibit a hydrodynamic diameter centered to 100 nm. Considering the average size of nanoparticles at 8.5 nm, this value indicates their aggregation in the suspension. A first hypothesis could be that the nanoparticles aggregate during the “click” reaction even after very short times (5 min). However, the DLS measurement performed after evaporation of the THF and dispersion in dimethylformamide (DMF) showed a single peak centered to 12 nm, meaning no aggregation and a

good stability of the suspension (figure III-12, red curve). This last information proves that the aggregation does not come from the “click” reaction but from the interaction with the solvent.

It is important to understand how the solvent interacts with the nanoparticle surface to manage the assembly thereafter. Here, the nanoparticles are covered with thymine which presents few polar groups which are able to create hydrogen bonding with electronegative atoms. The thymine groups at the nanoparticle surface may create bonds with another thymine group which favors the aggregation in solution. With protic solvents, bonds also exist with the thymine groups. Therefore, solvent-thymine interactions compete with thymine-thymine interactions.<sup>[8, 19, 20]</sup>

To ensure the stability of the suspension, a solvent which promotes the solvent-thymine interaction (thus limit the thymine-thymine interaction) is required. The DMF can generate easily hydrogen bonds because of the presence of hydrogen and electronegative atoms in its structure (figure III-13). Therefore, this solvent is more favorable to avoid aggregation. This aggregation is reversible by changing the solvent of the nanoparticle suspension. Indeed, the solvent exchange was performed with the same sample and the stability of the nanoparticles was the same, aggregated in THF and stable in DMF.

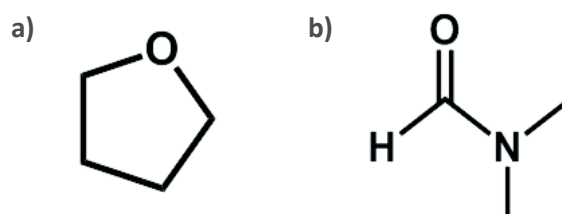


Figure III-13. Schematic representation of the molecules of a) THF and b) DMF

The stability has been studied for each ratio of thymine groups at the surface of the nanoparticles. Table III-2 summarizes the stability of the suspension as function of the solvent.

Table III-2. Stability of the NP@Thym with different ratio of azide groups at the surface as function of the solvent

	NP@Thym	100 %	80 %	50 %	20 %
Polarity ↑	H <sub>2</sub> O	X	X	X	X
	DMF	✓	✓	✓	X
	THF	X	X	✓	✓
	CHCl <sub>3</sub>	X	X	X	✓

X      aggregation in suspension  
✓      good stability of the suspension

As expected, the nanoparticles with different quantities of thymine groups at the surface have stability which varies with the solvent polarity. Nanoparticles are aggregated in water whatever the quantity of thymine at their surface. The DMF allow a good dispersion of the NP@Thym 100%, 80% and 50%, but below this value, the NP@Thym 20% are not stable. For these nanoparticles, the THF and chloroform allow a good dispersion. The DLS measurements were performed in the solvent where the nanoparticle suspension are the more stable (figure III-14).

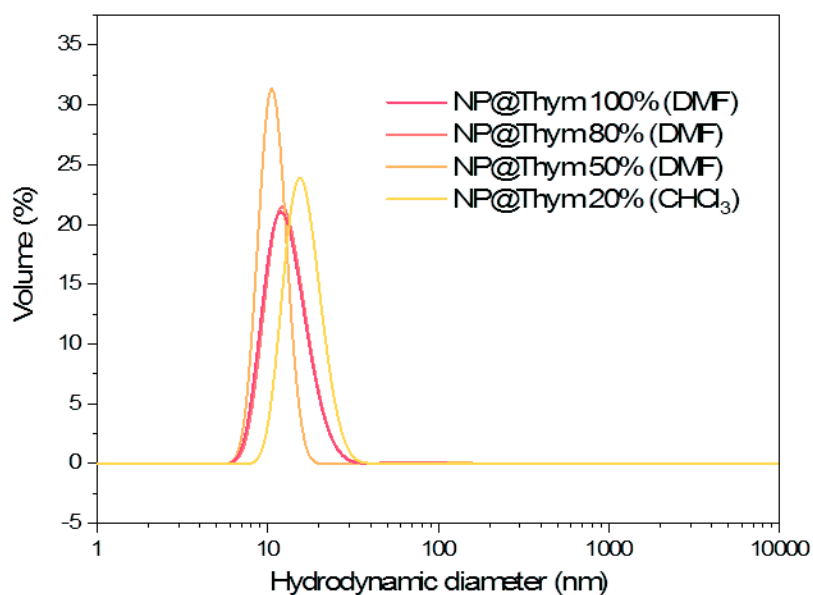


Figure III-14. DLS measurements for nanoparticles with different ratio of thymine at the surface in DMF for 100%, 80% and 50% and  $\text{CHCl}_3$  for 20% and 0%

The suspensions of NP@thym are stable and do not present aggregation as long as they are in the right solvent. The small differences of the hydrodynamic diameters may come from the formation of small clusters in solution due to the solvent.

FT-IR and DLS allow a first understanding of the mechanisms of aggregation of the nanoparticles covered with different quantities of thymine groups. The control of the stability by using the solvent is an essential point that will be useful for the assembly through the multiple hydrogen bonding.

### 3. Molecular recognition through nucleosides

The surfaces of both substrates and nanoparticles have been functionalized with complementary nucleosides adenine and thymine groups. The recognition can be established to assemble the nanoparticles at the surface. Here, the influence of the parameters such as the solvent, the density of functional groups and the temperature are investigated to understand the mechanisms of assembly through the nucleosides.

#### a) *Experimental protocol*

The assembly process is quite simple: substrates with different ratios of adenine were dipped in 5 mL of a suspension of nanoparticles with different ratios of thymine (figure III-15). The substrates were removed after one hour at room temperature. Then, they were extensively rinsed with DMF and exposed for 15 seconds in ultrasonic bath in order to remove physisorbed nanoparticles before being dried under air stream.

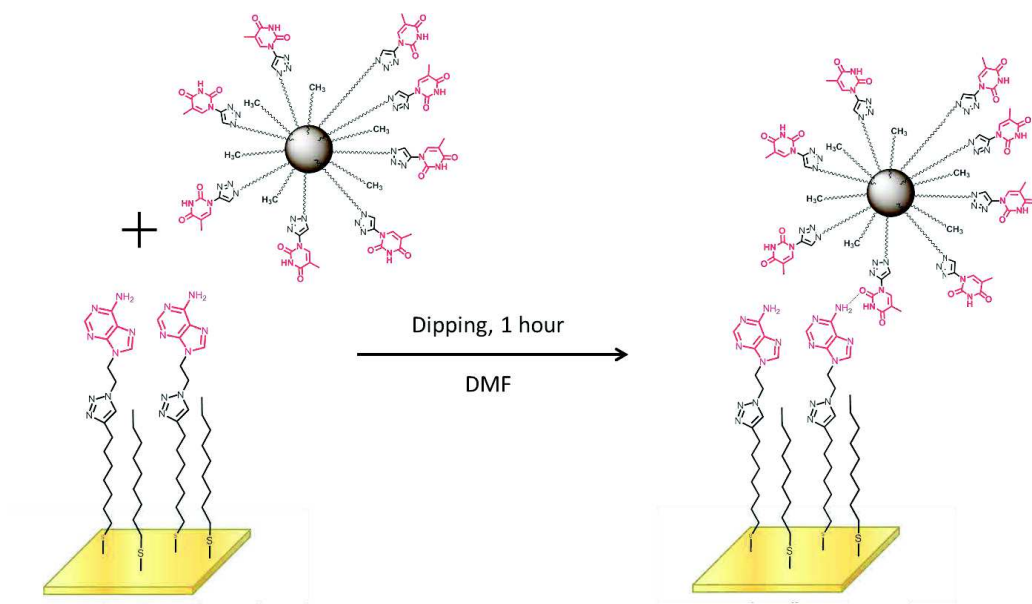


Figure III-15. Schematic representation of the assembly process through multiple hydrogen bonding

### b) Influence of experimental parameters

#### (1) Assembly time

The influence of the time where the thymine-terminated nanoparticles are in contact with the adenine-terminated SAM is important to know the kinetics of the assembly. Therefore, different immersion times of the SAM-Ade 100% in a suspension of NP@Thym 100% in DMF at the same concentration were performed. The SEM images are shown in figure III-16 and the density values were compared to maximum theoretical values calculated for a hexagonal close packed nanoparticle assembly with a mean diameter of  $8.5 \pm 0.8$  nm (table III-3).

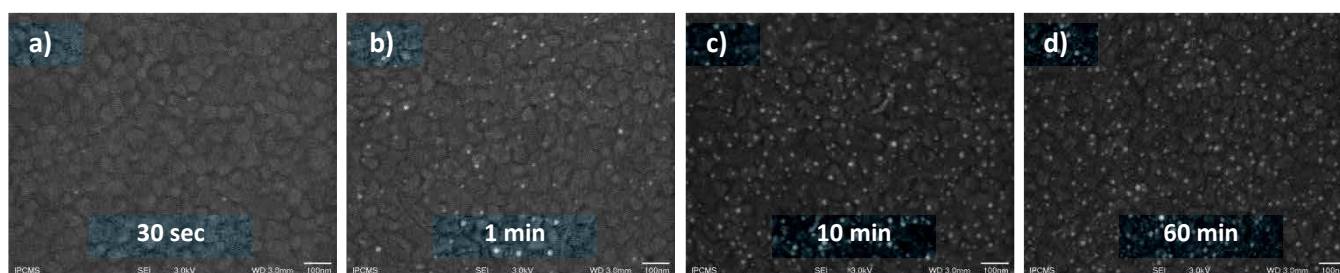


Figure III-16. SEM images of assembly of NP@Thym on SAM-Ade for different assembly times: a) 30 sec, b) 1 min, c) 10 min and d) 60 min. Magnification X100 000

The SEM images show the increase of densities of nanoparticles at the SAM surface as function of the immersion time. After 30 seconds, the recognition does not happen and there is no nanoparticles at the surface (<1% of the maximal theoretical value). After 1 minute, some nanoparticles are observed with a very low density (2.4%). After 10 minutes of immersion, the density of nanoparticles stops increasing around 13% of the maximal theoretical density.

**Table III-3. Density of nanoparticles as function of the time dipping time**

	30 sec	1 min	10 min	60 min
Density of nanoparticles (NP/ $\mu\text{m}^2$ )	<b>15 <math>\pm</math> 15</b>	<b>115 <math>\pm</math> 85</b>	<b>600 <math>\pm</math> 45</b>	<b>625 <math>\pm</math> 55</b>
Surface coverage (%)	<b>&lt; 1</b>	<b>2,4 <math>\pm</math> 0,2</b>	<b>12,6 <math>\pm</math> 1,0</b>	<b>13,2 <math>\pm</math> 1,2</b>

The density for a long reaction time remains far below the theoretical full coverage of the surface. The concentration should have an impact on the diffusion of the nanoparticles on the surface and therefore on the kinetics. However, due to the time-consuming ultrafiltration step to purify the nanoparticles, the influence of the concentration could not be studied and remains low ( $\approx 0.5$  mg/mL).

Moreover, isolated nanoparticles were observed on each sample. No clusters or chains of nanoparticles were observed in contrast with the assembly via “click” chemistry reaction. This observation shows that the assembly mechanism driven by nucleosides is different from the “click” strategy.

(2) Influence of the quantity of functional groups at the nanoparticle and SAM surfaces

One of the interactions which can prevent the recognition between nucleosides is the  $\pi$ -stacking.<sup>[2, 3, 21-23]</sup> Indeed, the stacking interaction between rings of the nucleobases, generally weakens the hydrogen bonds.<sup>[2]</sup> To study the influence of the  $\pi$ -stacking on the assembly, nucleobases on the nanoparticles and substrates surfaces have been diluted.

(a) On the SAM surface

Self-assembled monolayers were realized with different CC/DDT ratios in solution in order to mix adenine groups at the gold surface with methylene-terminal group which are non-active for the base pairing. The assemblies have been prepared by dipping SAM-Ade 0%, 20%, 50%, 80% and 100% in a NP@Thym 100% DMF solution for 30 min. The nanoparticle densities were measured from the SEM images (figure III-17) and are summarized in table III-4.

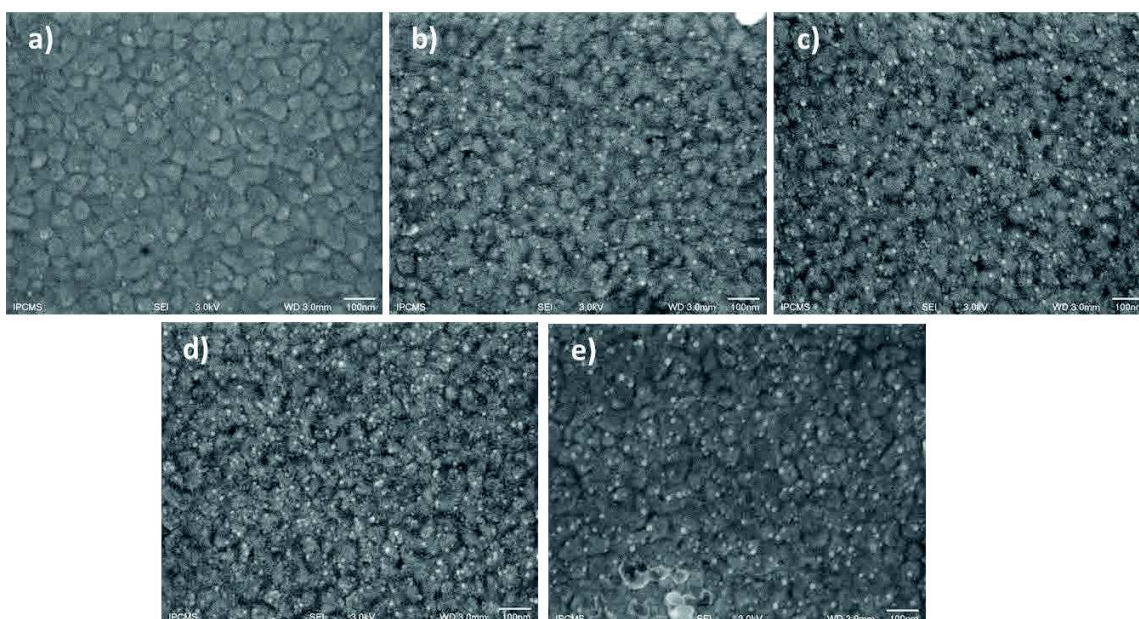


Figure III-17. SEM images SAM-Ade with different ratios: a) 0%, b) 20%, c) 50% d) 80% e) 100% after dipping in a suspension of NP@Thym 100% in DMF. Magnification X100 000

Table III-4. Surface coverage of NP@Thym 100% assemblies on SAM-Ade with different ratios of adenine at the surface.

SAM-Ade	0 %	20 %	50 %	80 %	100 %
NP@Thym 100 %	< 1 %	$6.8 \pm 1.1$ %	$8.7 \pm 1.6$ %	$11.2 \pm 1.2$ %	$9.1 \pm 0.9$ %

The surface coverage is very low for each sample (below 15% of the maximal theoretical value). Nevertheless, a trend can be observed. Indeed, the number of nanoparticles at the surface increases up to 11% with the quantity of adenine at the surface of the SAM until 80%. This trend does not seem to attest a strong influence of  $\pi$ -stacking. However, a slight decrease is observed for the SAM-Ade 100% in comparison with the 80%.

Decreasing the adenine at the surface does not allow increasing the density of nanoparticles which can be explained by reducing the number of nucleobases at the surface and so decreasing the recognition rate. The number of nanoparticles is still low at the surface and the  $\pi$ -stacking effect is not responsible for such low density.

Considering the previous results, SAM-Ade 80% will be used in the following section in order to optimize the density of nanoparticles at the surface.

(b) *On the nanoparticle surface*

In order to control the influence of  $\pi$ -stacking at the nanoparticle surface, thymine groups were diluted on the surface. The assembly took place for 30 min by dipping a SAM-Ade 80%. The densities values are summarized in table III-5.

**Table III-5. Density of NP@Thym assembly for different ratios of thymine on SAM-Ade 80%**

NP@Thym	20 %	50 %	80 %	100 %
SAM 80%	< 1 %	<b>42,1 ± 2,4 %</b>	<b>12,3 ± 1,0 %</b>	<b>11 %</b>

The results measured on the SEM images show that the best density was obtained for nanoparticles covered with 50% of thymine groups. The investigation of the influence of  $\pi$ -stacking showed that the optimal system is the one with NP@Thym 50% grafted on SAM-Ade 80%. The density of these assembly can be modulated by the quantity of nucleosides at the surface, however, other parameters can contribute to improve the recognition such as solvent and temperature.

### (3) Solvent influence

As shown previously, the solvent has a strong influence on the stability of the nanoparticles covered with thymine groups. Indeed, the solvent interacts by hydrogen bonding with the nucleosides localized on the substrates and nanoparticle surfaces. In order to improve the recognition between adenine and thymine, a solvent which does not interferes with the multiple hydrogen bonding has to be used. Two solvents have been used with different polarity to observe the effect on the assembly. Different DMF/CHCl<sub>3</sub> volume ratios were used: [4:1], [1:1] and [1:4]. The SAM-Ade 80% were dipped for 30 min at room temperature in NP@Thym 50% suspension. SEM images are shown in figure III-18.

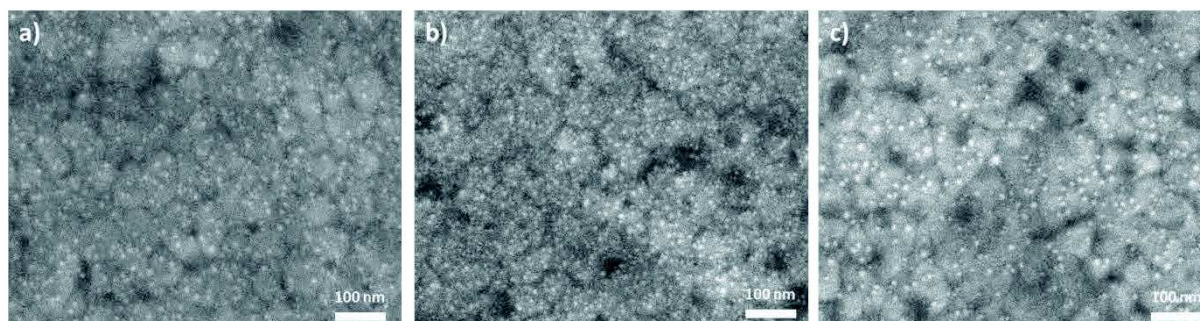


**Figure III-18. SEM images of assemblies of NP@Thym 50% on SAM-Ade 80% with different ratios of DMF/CHCl<sub>3</sub> a) [4:1], b) [1:1] and c) [1:4]**

As observed previously, the nanoparticles are isolated and do not present any clusters or alignments at the SAM surface. With the information obtained earlier, we can assume that the nanoparticles prevent the  $\pi$ -stacking effect and cannot be too close from each other because the energy required to create a binding is higher.

The density increases up to the DMF/CHCl<sub>3</sub> ratio [1:1] at 53 % before decreasing when the quantity of chloroform increases. This phenomenon can be explained with a complementary characterization method such as granulometry. DLS measurements were performed on each suspension with different ratios of DMF/CHCl<sub>3</sub> and are presented on figure III-19. The hydrodynamic diameters are summarized in table III-6.

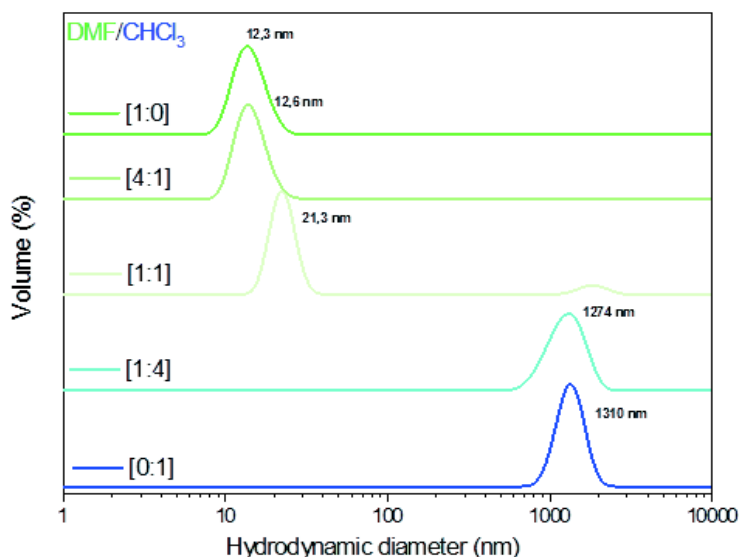


Figure III-19. DLS measurements of NP@Thym 50% in different DMF/CHCl<sub>3</sub> ratios

The hydrodynamic diameter of the nanoparticles evolves with the ratio DMF/CHCl<sub>3</sub>. The suspension of nanoparticles has a very good stability in DMF. Therefore, thymine-DMF interactions can compete with the thymine-thymine interactions. In CHCl<sub>3</sub> the suspension is totally aggregated with a single peak around 1300 nm which agrees with weak interactions between the solvent and the thymine group and thus, which promoting the recognition thymine-thymine between nanoparticles.

Table III-6. Density of NP@Thym 50% assemblies on SAM-Ade 80% for different DMF/CHCl<sub>3</sub> ratios

	[4:1]	[1:1]	[1:4]
Density	19%	53%	18%
Hydrodynamic Diameter	13,6 nm	21,3 nm	1274 nm

The stability with ratios containing few CHCl<sub>3</sub> [4:1] is similar to pure DMF without aggregation of the nanoparticles. In contrast, the one containing few DMF [1:4] is similar to CHCl<sub>3</sub> with total aggregation of the suspension. In the case of a [1:1] ratio, nanoparticles start to aggregate with a hydrodynamic diameter centered to 21 nm. The stability can be directly influenced by the polarity of the solvent which can control the hydrogen bonding between the nucleosides at the surface of the nanoparticles and gold substrate.

The stability of the nanoparticle suspension can be directly correlated to the structure of nanoparticles assembly. The energies of the different interactions in the system can be noted as follows:

- $E_{T-T}$  : the energy necessary to form thymine-thymine bonding
- $E_{T-S}$  : the energy necessary to form interaction between thymine and solvent molecule
- $E_{T-A}$  : the energy necessary to form thymine-adenine bonding

The system will always minimize the energy and allow the formation of bonds which requires the lowest energy interaction. However, the energy to form thymine-adenine bonds will always be

lower than the energy to form thymine-thymine bonds (figure III-20).<sup>[2]</sup> Immersion of a SAM-Ade in NP@Thym would technically lead to the formation of adenine-thymine bonds before thymine-thymine bonds ( $E_{T-A} < E_{T-T}$ ). Therefore, assembly of nanoparticles at the SAM surface is favored against nanoparticle aggregation in solution.

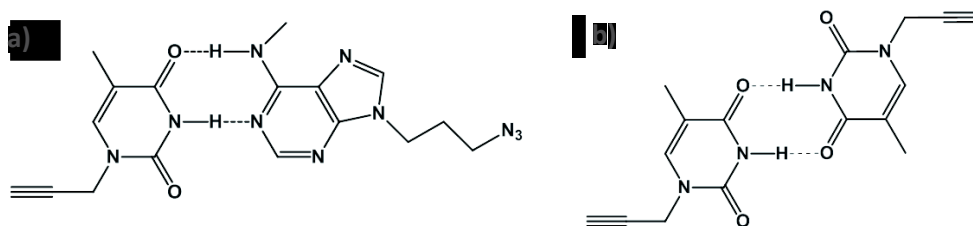


Figure III-20. Schematic representation of the hydrogen bonds between a) adenine-thymine and b) thymine-thymine

However, the interactions between the solvent and the thymine at the nanoparticle surface may compete the assembly process. Three cases have been studied as function of the solvent used:



The use of a solvent with a low polarity and thus, not able to form hydrogen bonds with nucleobases will allow the formation of bonds between nucleosides. However, in suspension, the nanoparticles will be aggregated because of the non-competition of the solvent to avoid the formation of thymine-thymine bonds. It leads to nanoparticle aggregation for low DMF/ $\text{CHCl}_3$  ratios ([1:4] and [0:1]). Moreover, the immersion of SAM-Ade leads to a low density of nanoparticles. This can be explained by the fact that aggregates do not have the energy to create bonds with the surface and lead to low nanoparticle density (18%).



In another hand, using a solvent which can create bonds with nucleosides and compete with the formation of thymine-thymine bonds does not lead to the aggregation of the suspension. Unfortunately, the use of DMF does not allow having a high density of the nanoparticles after immersion of the SAM-Ade. The explanation comes from the solvent interactions with nucleosides is too strong and disturb the recognition adenine-thymine. In this case, nanoparticles cannot be grafted on the surface because their stability in suspension is too “good”.



In order to avoid a solvent which compete too much with the recognition process between adenine and thymine and another one which promotes aggregation of the suspension, a right solvent has to be found to allow the recognition and to favor the stability of the suspension. A mixture of chloroform and DMF in ratio [1:1] shows the highest density at the surface (53%). The energy necessary to form adenine-thymine bonds is lower than the energy to form bonds with the solvent and allow the grafting of the nanoparticles. The DLS measurements show a small shift of the hydrodynamic diameter to 21.3 nm meaning the start of the aggregation. The system is slightly destabilized which allows the formation of bonds of the nanoparticles at the surface of the SAM-Ade.

The solvent has a strong influence on the recognition. Indeed it will promote or not the interactions between nucleosides localized at the surface of both nanoparticles and gold substrates.<sup>[24]</sup>

### c) *Influence of the temperature*

Hydrogen bonds can be easily broken with thermal energy. Therefore, the influence of the temperature on the structuration of the assembly was studied. A sample corresponding to an optimized density of nanoparticles (57%) was dipped in DMF which favors the solvation of the nanoparticles and heated at 60°C for 2 hours. The SEM images before and after heating are presented on the figure III-21.

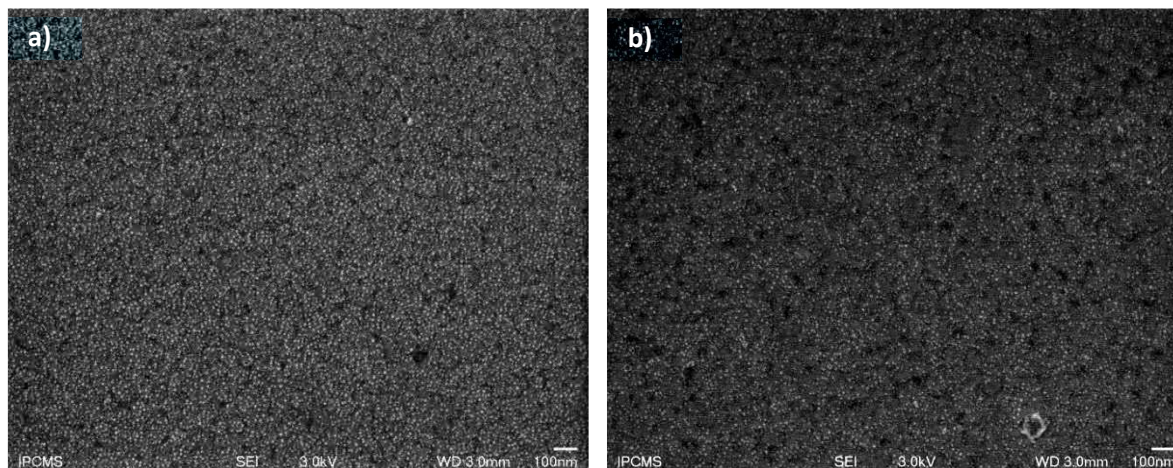


Figure III-21. SEM images of a NP@Thym 50% assembly on SAM-Ade 80% a) before and b) after heating at 60°C in DMF for 2 h

The density of nanoparticles decreases after heating in DMF and pass from 57% to 18%. It shows that the hydrogen bonds were broken with the increase of the thermal energy. However, some nanoparticles remain at the substrate surface, meaning there is not a fully desorption and shows a certain stability of the system.

### d) *Influence of the rinsing step*

The assembly of nanoparticles onto SAMs is dependent of the solvent as seen previously. The rinsing step should also have an influence on nanoparticle removal after recognition by rinsing with a solvent promoting the interactions with the nucleosides. In order to study the influence of the solvent during the rinsing step, assemblies of NP@Thym 50% on SAM-Ade 80% performed with DMF/CHCl<sub>3</sub> [1:1] mixture were rinsed with different solvents. The different solvents used and the density of nanoparticles are summarized in table III-7.

Table III-7. Density of nanoparticles as function of the rinsing solvent

DMF/CHCl <sub>3</sub>	[1:0]	[1:1]	[0:1]
Density (NPs/μm <sup>2</sup> )	2015 ± 260	2150 ± 80	2840 ± 165
Density	42.5 ± 5.5 %	45.3 ± 1.7 %	59.8 ± 3.5 %

Rinsing the assembly using CHCl<sub>3</sub> which does not interfere in the formation of adenine-thymine binding should not remove nanoparticles. In contrast, DMF should favor the removal of the

nanoparticles. Considering the density measured on the SEM image a trend can be observed with a slight increase of the density with the rinsing in  $\text{CHCl}_3$ . However, the reproducibility and the errors on the measurements show that we have to be careful with these results. The results in  $\text{CHCl}_3$  were expected as long as this solvent is not able to break the hydrogen binding between the nanoparticles and the substrate. In another hand, for the DMF and the mix DMF/ $\text{CHCl}_3$  [1:1] which are able to break the binding as shown with the DLS measurements, a removal of the nanoparticles could be expected. Instead, except a slightly decrease in density, the nanoparticles remain at the SAM surface. The system shows a certain stability since the nanoparticles stay at the surface after rinsing with DMF. This can be explained by the fact that the nanoparticles are not grafted with a single nucleoside at the surface but with few which increase the stability.

## B. Conclusion

By taking advantage of the “click” chemistry, the nanoparticles and substrates were post-functionalized with complementary nucleobases. The use of micro-wave irradiations allowed decreasing strongly the reaction time down to few minutes. The hydrogen bonds formed during the assembly were sensitive to external parameters such as the  $\pi$ -stacking, the solvent and the temperature. Understanding the influence of these parameters allow controlling the structure of nanoparticle assembly.

This work leads to perspectives. Indeed, the influence of the chain length at the surface of nanoparticle and substrate or the presence of hydrophilic groups such as PEG in their structure can be investigated.

Moreover, the control of stability of two types of nanoparticles functionalized with thymine and adenine can be investigated. The control of the stability can be done by playing with the nature of the solvent or the temperature. Such a kind of nanoparticle suspension incorporating both nucleobases may allow the control of self-assembly in multilayers.

The control of the nanoparticle assembly through base pairing could allow to go further and envisioned the assembly through more specific interactions such as the recognition through DNA strands.<sup>[25-28]</sup>

## C. Bibliography

- [1] Freek J. M. Hoeben, P. J., E. W. Meijer, and Albertus P. H. J. Schenning, *Chem. Rev.*, (2005),
- [2] Villani, G., *J Phys Chem B*, (2014) **118**, 5439.
- [3] Villani, G., *Physical chemistry chemical physics : PCCP*, (2013) **15**, 19242.
- [4] Cerny, J.; Hobza, P., *Chem Commun (Camb)*, (2010) **46**, 383.
- [5] Viswanathan, K.; Long, T. E.; Ward, T. C., *Langmuir*, (2009) **25**, 6808.
- [6] K. Viswanathan, H. O., C. L. Elkins, C. Hese, T. C. Ward, T. E. Long, *Langmuir*, (2006) **22**, 1099.
- [7] A. Sanyal, T. B. N., O. Uzun, V. M. Rotello, *Langmuir*, (2004) **20**, 5958.
- [8] Binder, W. H.; Lomoschitz, M.; Sachsenhofer, R.; Friedbacher, G., *Journal of Nanomaterials*, (2009) **2009**, 1.
- [9] Toulemon, D.; Pichon, B. P.; Leuvrey, C.; Zafeiratos, S.; Papaefthimiou, V.; Cattoën, X.; Bégin-Colin, S., *Chemistry of Materials*, (2013) **25**, 2849.
- [10] Erumpukuthickal Ashok Anumol, P. K., Parag Arvind Deshpande, Giridhar Madras, and Narayanan Ravishankar, *ACS Nano*, (2011) **5**, 8049.
- [11] Oliver Kappe, C., *Chemical Society Reviews*, (2008) **37**, 1127.
- [12] MINGOS, D. M. P., *Res. Chem. Intermed*, (1994) **20**, 85.
- [13] Mohtasebi, A.; Chowdhury, T.; Hsu, L. H. H.; Biesinger, M. C.; Kruse, P., *The Journal of Physical Chemistry C*, (2016) **120**, 29248.
- [14] Pagliai, M.; Caporali, S.; Muniz-Miranda, M.; Pratesi, G.; Schettino, V., *The Journal of Physical Chemistry Letters*, (2012) **3**, 242.
- [15] Furukawa, M.; Yamada, T.; Katano, S.; Kawai, M.; Ogasawara, H.; Nilsson, A., *Surface Science*, (2007) **601**, 5433.
- [16] Yoshimasa Kyogoku, R. C. L., and Alexander Rich, *JACS*, (1967) **89**, 496.
- [17] Pina Colarusso, K. Z., Bujin Guo, Peter E Bernath, *Chemical Physics Letters*, (1997) **269**, 39.
- [18] Singh, J. S., *Journal of Molecular Structure*, (2008) **876**, 127.
- [19] Kalpana Viswanathan, H. O., Casey L. Elkins, Cheryl Heisey, Thomas C. Ward, and Timothy E. Long, *Langmuir*, (2006) **22**, 1099.
- [20] Andrew K. Boal, F. I., Jason E. DeRouchey, Thomas Thurn-Albrecht, Thomas P. Russell & Vincent M. Rotello, *Nature*, (2000),
- [21] Goodman, R. S. P. a. J. M., *J. Chem. Inf. Model.*, (2009) **49**, 944.
- [22] Marlon N. Manalo, L. M. P., and Andy LiWang, *JACS*, (2006),
- [23] Mignon, P.; Loverix, S.; Steyaert, J.; Geerlings, P., *Nucleic acids research*, (2005) **33**, 1779.
- [24] Stolarczyk, J. K.; Ghosh, S.; Brougham, D. F., *Angew Chem Int Ed Engl*, (2009) **48**, 175.
- [25] Chevolut, Y.; Laurenceau, E.; Phaner-Goutorbe, M.; Monnier, V.; Souteyrand, E.; Meyer, A.; Gehin, T.; Vasseur, J. J.; Morvan, F., *Current opinion in chemical biology*, (2014) **18**, 46.
- [26] James J. Storhoff, A. A. L., Robert C. Mucic, Chad A. Mirkin, Robert L. Letsinger, and George C. Schatz, *J. Am. Chem. Soc.*, (2000) **122**, 4640.
- [27] A. Csaki, R. M., J. M. Köhler, W. Fritzsche, *Nucleic Acids Research*, (2000) **28**, 91.
- [28] Chad. A. Mirkin, R. L., R. Mucic, J. Storhoff, *Letter to Nature*, (1996) **382**, 607.

## CHAPITRE IV - Biomolecules Recognition mediated by iron oxide nanoparticle assemblies supported onto gold thin films

The assembly of iron oxide nanoparticles can be used to design a very efficient detection platform by taking advantage of the surface plasmon resonance (SPR) properties of the gold substrate. Receptor molecules can be easily grafted at the nanoparticle surface in order to detect target molecules through specific interactions.

We previously saw that the “click” reaction is a powerful tool for tuning the structuration of the assembly. Moreover, the versatility of this method ensures the grafting of a large variety of receptor molecules. Furthermore, the covalent binding of the receptor molecules is preferred since it provides strong and stable binding. The analyte can also be removed to regenerate the sensors without removing the receptor molecules which is strongly anchored at the surface. Therefore, receptor molecules can be modified with alkyne groups in order to perform the CuAAC “click” reaction with azide groups at the surface of nanoparticles (Figure IV.1).

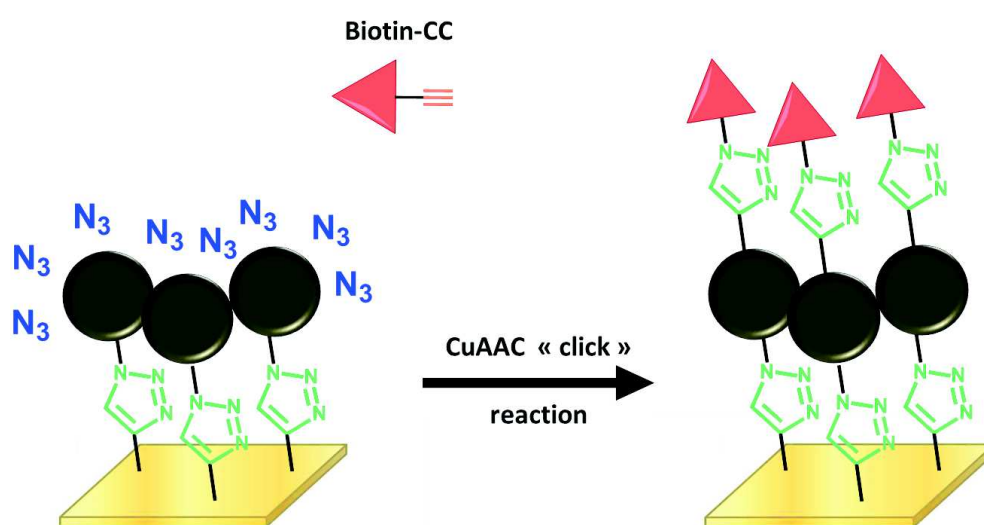


Figure 0-1. Schematic representation of the grafting of an alkynated derivative bioreceptor molecules on the azide terminated nanoparticle assembly

The grafting of biomolecules on the surface can be characterized by surface analysis techniques in order to control the chemical change at the surface of nanoparticles. This platform is then available for the detection of the recognition element. The gold surface provides a SPR signal and allows the detection of the analyte. The high surface/volume ratio of nanoparticles is expected to improve the density of bioreceptors at the surface.<sup>[1]</sup> Moreover the control of the structure of nanoparticle assembly enables the tuning of the plasmon properties<sup>[2]</sup> in order to enhance the sensitivity.

This platform will allow the study of the sensitivity of the SPR sensors, the limit of detection and the recognition mechanisms between an analyte and a receptor molecule. Indeed, the SPR measurements can be performed with microfluidic channel in order to investigate the kinetics of biomolecular recognition process between bioreceptors and analytes.

In this chapter, the efficiency of our platform will be studied by the detection of two different bio-molecules. The two couples of receptor/target molecules are:

- Biotin/streptavidin
- Iminosugar/ $\alpha$ -glycosidase

In one hand, the biotin/streptavidin was studied as a model system because this couple is very well known. Streptavidin is easy to detect thanks to its high binding affinity  $K_d = 10^{-15}$  mol/L and its high specificity. These molecules are widely used for detection systems since the mechanisms of association are known and well described.<sup>[3, 4]</sup>

In another hand, the glycosidase was studied because it is involved in several essential biological processes. Irreversible inhibitors such as iminosugar were used to covalently modify the glycosidases which is involved in many biomedical processes (Gaucher disease, cystic fibrosis, diabetes).<sup>[5, 6]</sup> The study of the immobilization of this enzyme at the surface of nanoparticles gives the opportunity to bring a better understanding of the recognition process with iminosugars in addition to studies reported from solutions.<sup>[7-10]</sup>

## D. Biotin-Streptavidine

The immobilization of proteins with maximum retention of activity and minimized nonspecific interactions is a key goal in the development of biosensing technologies. Molecular recognition processes of streptavidin with biotin supported onto modified surfaces have been importantly studied as a model system for protein immobilization. The high binding affinity allows high stability and robustness which make this couple very well used in many different applications in biotechnology. The use of self-assembled monolayer (SAM) of organic molecules is highly suited for biomolecular recognition because it allows the versatile grafting of molecular receptors onto solid surfaces. The group of Knoll in the early 90s studied the adsorption of streptavidin onto a gold surface functionalized with biotin terminated SAMs. They used the SPR technique to monitor the molecular recognition process.<sup>[3, 4, 11]</sup> The structuration of the SAM was studied to understand the mechanisms of recognition. These studies showed that the recognition mechanisms was dependent of the geometry and the orientation of biotin groups.<sup>[11, 12]</sup> More recently, different approaches have been used to detect small concentrations of streptavidin on surfaces.<sup>[13, 14]</sup> The biotin/streptavidin couple was further used to reach limit of detection below nM.<sup>[12, 15]</sup>

### 1. Design of the bio-platform

The assembly of nanoparticles represents the base of the bio-platform because of the presence of terminated azide groups at the nanoparticle surface. In order to graft irreversibly biomolecules receptors, an alkynated derivative of biotin was synthesized. The molecular receptor was then grafted on the surface of the nanoparticle film using the CuAAC “click” chemistry reaction which was used to build nanoparticle assemblies.

#### a) *Grafting of an alkyne derivative of biotin onto nanoparticle assembly*

The biotin molecule displays a terminal carboxylic acid group which allows its easy functionalization with an amine group. Therefore, alkynated biotin was synthesized from biotin and propargyl-amine in DMF for 24 h at room temperature by performing the carboxyl-to-amine crosslinking using the carbodiimide EDC and Sulfo-NHS (figure IV-2). See appendix A for experimental details.

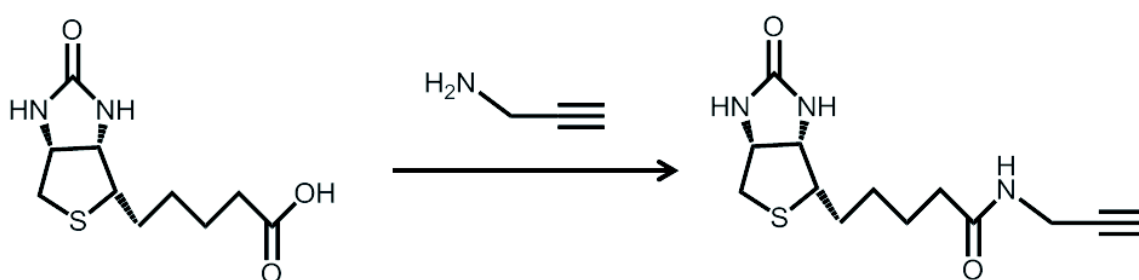


Figure 0-2. Schematic representation of the synthesis of alkynated biotin

Fourier transform infrared spectroscopy was performed to confirm the synthesis of the alkynated biotin (appendix C). The vibrational band localized at  $1680\text{ cm}^{-1}$  is characteristic of stretching mode of C=O bond in the amide group present in the biotin. The bands at  $3300\text{ cm}^{-1}$  and  $2115\text{ cm}^{-1}$  correspond respectively to the stretching modes of the  $\text{C}\equiv\text{C-H}$  and  $\text{C}\equiv\text{C}$  bands. The band at  $3300\text{ cm}^{-1}$  is not visible because of the strong and wide O-H band ascribed to water. Moreover,  $^1\text{H}$  NMR display signals which agree with the desired product (appendix C).

Alkynated biotin was grafted at the surface of azido-terminated nanoparticles supported on the gold substrate by performing CuAAC “click” reaction in a similar way as reported in Chapter II. The nanoparticle assembly was dipped for 24 h under reflux into a THF solution of alkynated molecules which contains Cu-catalyst and trimethylamine. After the reaction, the substrate was rinsed with THF and exposed for 1 minute to ultrasounds in order to remove any adsorbed species. The substrate was then dried under air stream and packed for further characterization.

## b) *Characterizations*

The grafting of biotin on the nanoparticle surface was controlled by using several characterization techniques. The microscopy techniques give information on the spatial arrangement of the nanoparticles and on the topography of the surface while spectroscopy techniques and water contact angle measurement allow the chemical characterization of the surface.

### (1) Microscopy characterizations

SEM images (figure IV-3) show the surface of the nanoparticle film before and after grafting the biotin groups. The image becomes smoother after grafting the biotin, despite the same acquisition parameters. It can be due to the presence of larger amount of organic species at the surface which disrupts the detection. The contamination by organic species leads to a loss of the conduction of the electron beam which induces a strong heating. Such an increase of temperature alters locally the sample and results in blurry images.

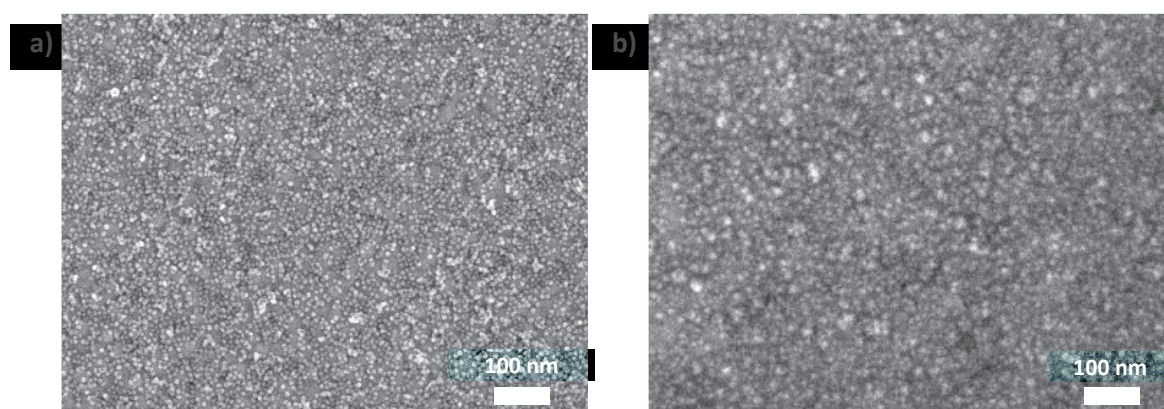
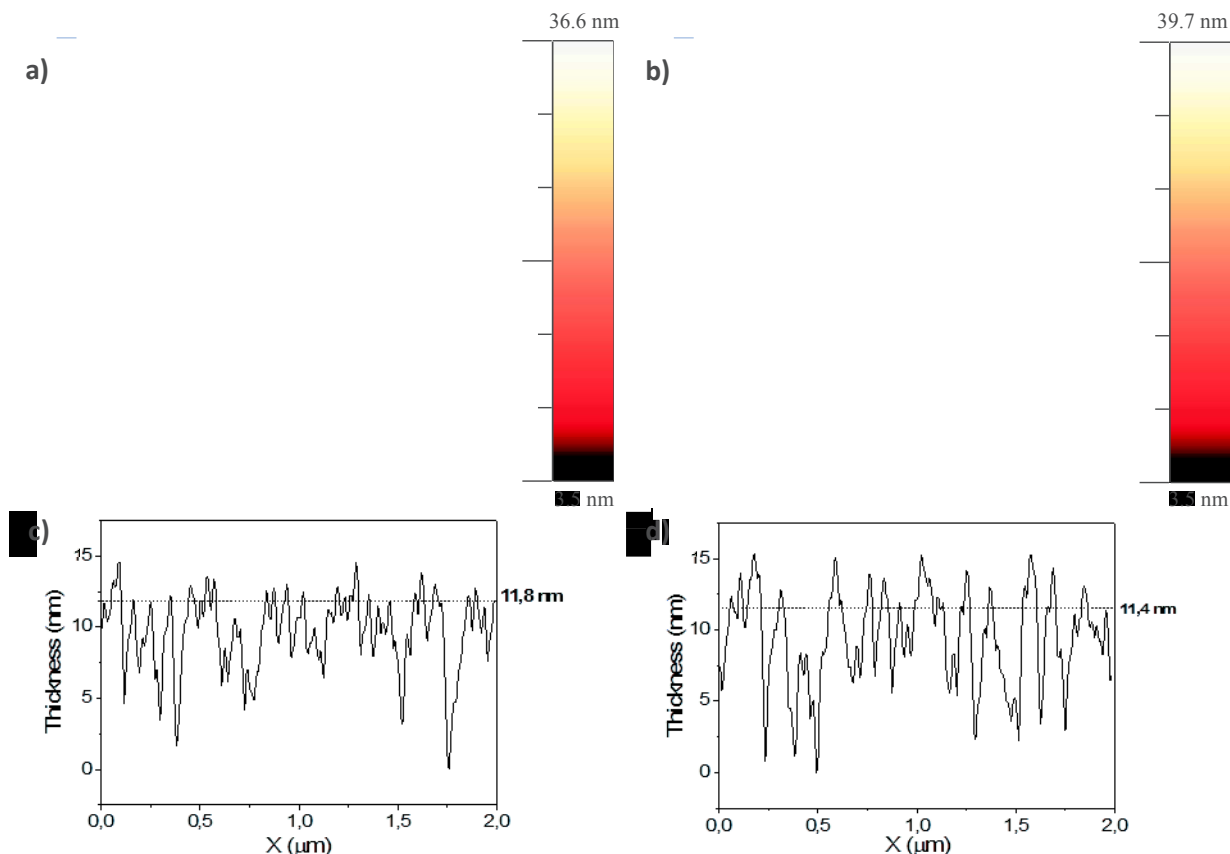


Figure 0-3. SEM images of the film of nanoparticles (a) before and (b) after grafting the biotin. Magnification X50000

The surface coverage by nanoparticles can be evaluated before and after grafting the biotin groups. The density of nanoparticles is estimated by counting the nanoparticles on twelve different areas for different samples and averaged at  $3385 \pm 205$  NPs/ $\mu\text{m}^2$  and  $3035 \pm 215$  NPs/ $\mu\text{m}^2$  before and after grafting respectively. Such a slight decrease about 10% can be attributed by the removal of physisorbed nanoparticles.



**Figure 0-4. AFM images of the surface topography and profile cross-sections along the line of the surface before (a,c) and after (b,d) grafting of biotin**

AFM images show similar topographies of the surface before and after the grafting of the biotin groups (figure IV-4). The topographic profiles (blue line) display similar average heights about 11.8 nm and 11.4 nm before and after grafting, respectively. The average roughness slightly increases from 3.1 nm to 4.0 nm which can be related to the removal of nanoparticles.

SEM images do not show a remarkable change at the surface. The immobilization of biotin groups does not significantly affect the structuration of the nanoparticle film which agrees with the formation of covalent bonds between nanoparticles and the SAM onto gold substrates.

## (2) Water Contact Angle

An easy and efficient way to determine the correct functionalization of the nanoparticle surface was to measure water contact angle (WCA). The grafting of biotin groups induces a change in the surface hydrophobicity. The measurement was done by depositing a 5  $\mu\text{L}$  water droplet on the substrate. Pictures of both samples were taken after one minute of stabilization. An alkyne chain terminated with azide groups shows a water contact angle of  $100^\circ$  (figure IV-5.a) which is coherent

with a hydrophobic surface. The grafting of biotin derivatives is demonstrated by the decrease of the contact angle down to 50° which agree with a hydrophilic surface (figure IV-5.b). It is consistent with the replacement of alkyne groups by biotin.<sup>[16, 17]</sup>

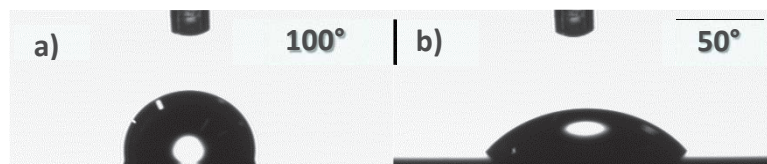


Figure 0-5. Pictures of a drop of water deposited onto a) the azido-terminated and b) the biotin-terminated nanoparticle assemblies supported onto a gold substrate

### (3) X-Ray Photoelectron Spectroscopy

X-Ray photoelectron spectroscopy (XPS) was performed in order to identify the chemical elements at the surface of nanoparticle assembly. Figure IV-6.a shows the N<sub>1s</sub> binding energy region, binding energies at 405.3 eV (N=N=N) and 401.8 eV (N=N=N) with a peak area ratio close to 1:2 was attributed to azide groups.<sup>[10, 18, 19]</sup> After performing CuAAC, the signal at 405.3 eV totally disappeared while a component a new signal at 400.5 eV was attributed to amine groups present in the biotin.<sup>[17]</sup> The component at 400.8 eV was attributed to (N-C) bonds which agreed with the formation of the triazole bridge.<sup>[20]</sup> The C<sub>1s</sub> region (figure IV-6.b) showed components at 285.3 eV and 286.9 eV corresponding respectively to the C-H binding in the aliphatic carbon chains and the C-N in the triazole bridge, respectively. The component at 288.7 eV can be attributed to the C=O bond in the biotin groups.<sup>[21]</sup> These results confirmed the total replacement of azide groups on the nanoparticle surface by biotin groups.

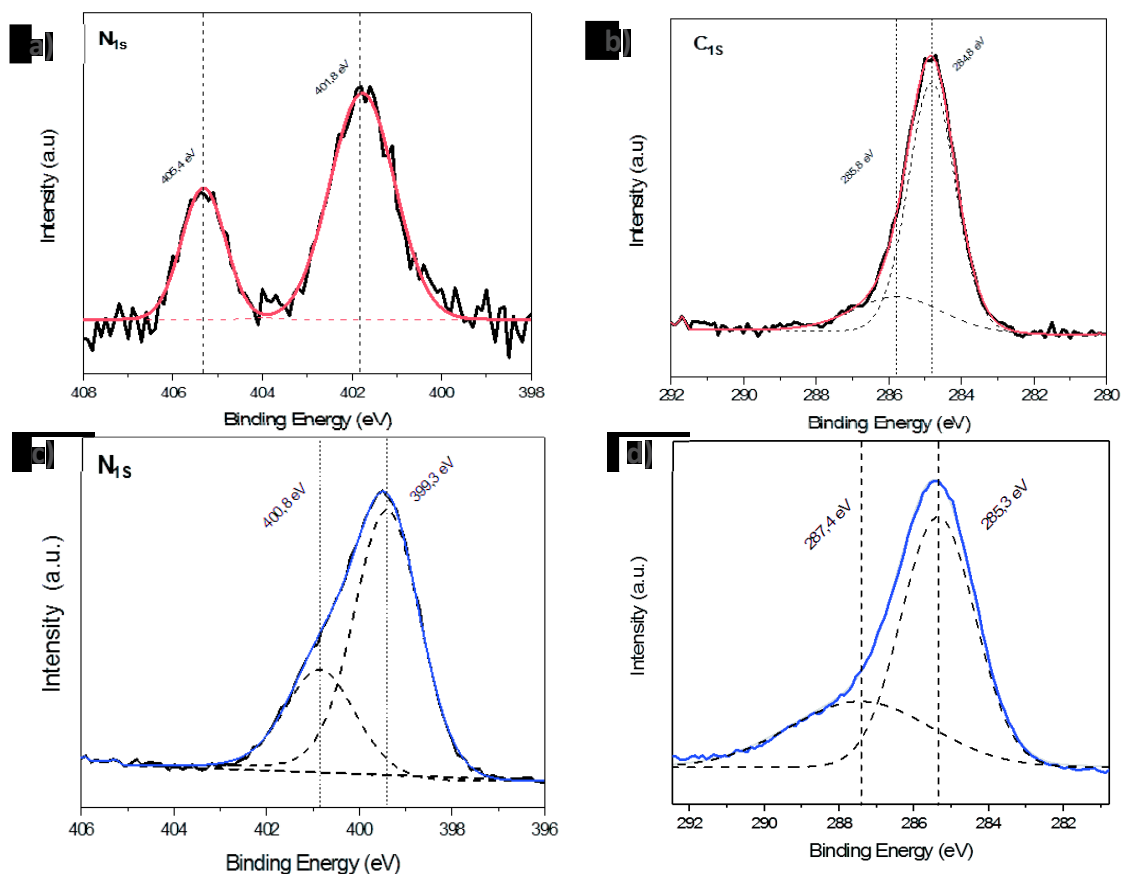


Figure 0-6. XPS measurements on a,c) the azido-terminated and b,d) the biotin-terminated nanoparticle assembly supported onto a gold substrate. N<sub>1s</sub> (a,c) and C<sub>1s</sub> (b,d) core level

#### (4) Phase Modulation Infrared Reflection Absorption Spectroscopy measurements

Phase Modulation Infrared Reflection Absorption Spectroscopy (PM-IRRAS) was performed to measure low amount of organic compounds such as a monolayer of biotin groups at the nanoparticle surface. Figure IV-7.a shows the spectra recorded before (red curve) and after (blue curve) functionalization with alkynated biotin. Given the SEM and AFM results, the quantity of phosphonic acid groups localized at the nanoparticle surface is expected to be unchanged after the functionalization step. Therefore, both spectra were normalized to the area of the  $\nu(\text{Fe-O-P})$  at  $1082 \text{ cm}^{-1}$ .

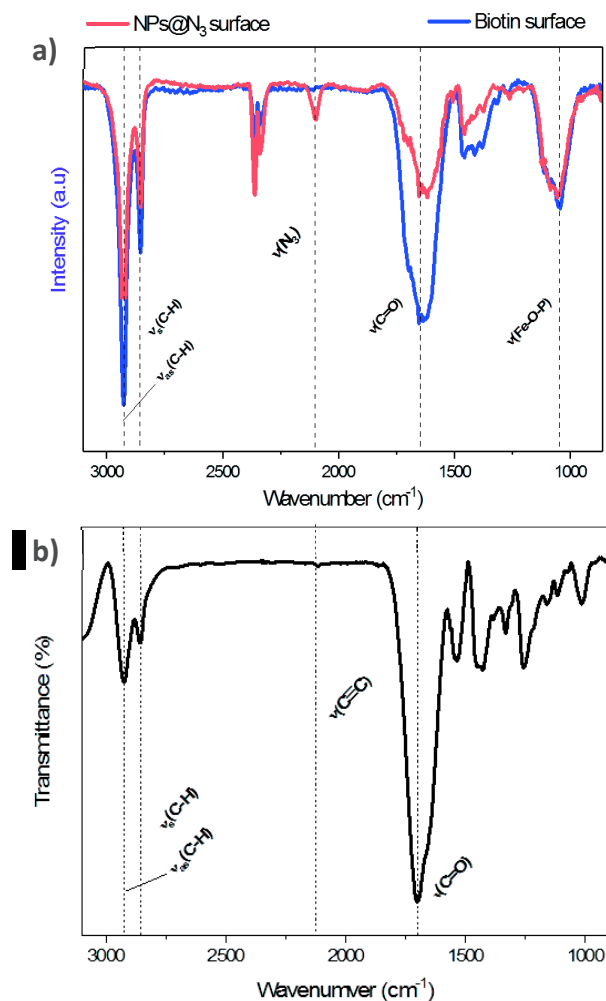


Figure 0-7. a) PM-IRRAS spectra recorded before (red) and after (blue) biotin functionalization. b) FT-IR spectrum of the derivative alkynated biotin molecule

The disappearance of the azide band  $\nu(\text{N}_3)$  at  $2100 \text{ cm}^{-1}$  and the presence of a supplementary contribution of the carboxylic acid band  $\nu(\text{C}=\text{O})$  at  $1660 \text{ cm}^{-1}$ ,<sup>[22]</sup> agree with the reaction of the azide terminal group with the alkynated biotin derivative. The presence of biotin groups was also correlated to the broad band ( $1750\text{-}1550 \text{ cm}^{-1}$ ) corresponding to amide I and II ( $\nu(\text{C}=\text{O})$  and  $\nu(\text{N-H})$ ) vibrations as observed for the alkynated biotin molecule (figure IV-7.b).

To summarize, the large panel of characterization techniques we have used, shows the replacement of azide groups by biotin groups at the surface of nanoparticle assembly. Furthermore, our building strategy based on the CuAAC reaction allows preserving the structure of nanoparticle assemblies as a monolayer of nanoparticles.

c) *Monitoring of the bio-platform build-up by surface plasmon resonance measurements*

The SPR signal of the gold substrate being highly sensitive to the variation of the local refractive index at its surface (see chapter I for details), the SPR measurements were performed to monitor the construction of the film.

The film construction includes several steps which increase the refractive index at the surface of the sample:

- Gold naked substrate (Au)
- Gold substrate functionalized with alkyne-SAM (SAM-CC)
- Assembly of nanoparticles functionalized with azide groups onto the SAM (NP@N<sub>3</sub>)
- Assembly of nanoparticles functionalized with alkynated biotin (Biotin)

The SPR measurements were performed at two different wavelengths by using Bionavis© apparatus. The reflectivity measured as function of the incident angle at 670 nm and 785 nm is shown in figure IV-8.

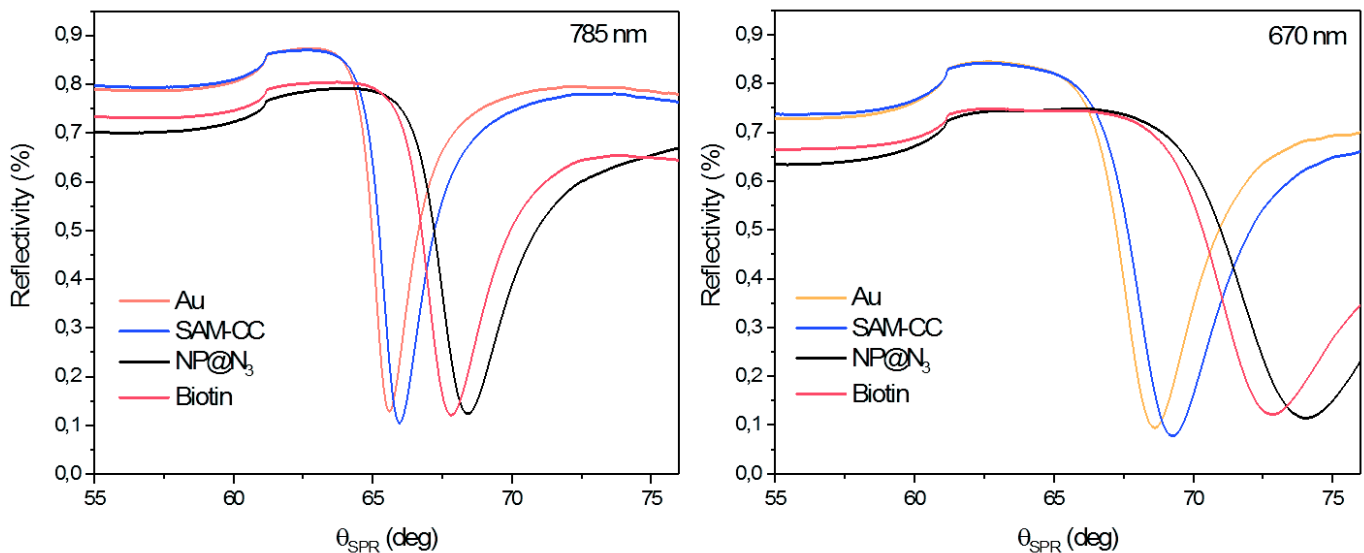


Figure 0-8. SPR reflectivity measurements versus angular response  $\theta$  with an excitation wavelength of a) 670 nm and b) 785 nm

As explained in chapter I, the angular position of the resonance peak is dependent of the wavelength at which the measurement is performed. As mentioned before, for the shortest wavelength, the position of the resonance peak and the sensitivity are overestimated due to the largest imaginary part of the metal permittivity which is correlated to the absorption of light by the gold thin film. It results in the enlargement of the resonance peaks recorded at 670 nm.<sup>[23]</sup> The theoretical positions of the peaks are determined by the resonance condition equation:

$$n \sin(\theta) = \sqrt{\frac{\epsilon_d \epsilon_m}{\epsilon_d + \epsilon_m}} \quad \text{Equation VI.1}$$

If we consider the refractive index of the water  $n_{\text{water}} = \sqrt{\epsilon_{\text{water}}} = 1.33$ , the prism refractive index and the metal permittivity given for the working wavelength,<sup>[24]</sup> we can calculate the theoretical value of the resonance angle. These calculations are made with the approximation that the gold film is thick

enough to not disrupt the peak position. This calculated value can then be compared to the experimental value of the resonance angle. The measurements performed with the Bionavis® apparatus allow an error of 0.001° for the experimental values. These values are summarized in the table IV-1 for a naked gold substrate if we consider water as the dielectric medium.

**Table 0-1. Values of theoretical and experimental resonance angle for naked gold film (Au)**

	670 nm	785 nm
Prism refractive index $n_p$	<b>1.520</b>	<b>1.516</b>
Metal permittivity <sup>5</sup> $\epsilon_m$	<b>-14.358</b>	<b>-22.855</b>
Theoretical resonance angle $\theta_{th}$	<b>69.574°</b>	<b>66.326°</b>
Experimental resonance angle $\theta_{exp}$	<b>68.627°</b>	<b>65.598°</b>

The experimental and theoretical values of the resonance angle are close, the deviation normalized to the experimental value measured at 670 nm is about 1.4% whereas at 785 nm, it is below 1.1%.

These values were calculated by considering that the dielectric at the gold surface is water occupying the whole sensing volume. In our case, this model becomes more complicated because the refractive index combines organic and inorganic parts with different ratios after each step. Therefore, a model with multilayers of different permittivities has to be taken into account. Nevertheless, the position of the resonance angle can be determined experimentally. The values of the minima for each step of the platform build-up are summarized in the table IV-2.

**Table 0-2. Angular peak positions measured for each step of the platform build-up for both operating wavelengths**

Wavelength	Au	SAM	NPs@N <sub>3</sub>	Biotin
<b>670 nm</b>	68.627°	69.260°	74.029°	72.845°
<b>785 nm</b>	65.598°	65.960°	68.410°	67.832°

After each step, the grafting of an organic or inorganic element increases the refractive index at the gold surface which results in the increase of the resonance angle. Iron oxide nanoparticles result in the largest shift of the resonance angle because of the largest change of refractive index ( $n_{organic} = 1.42$  and  $n_{Fe_3O_4} = 2.36$  at 670 nm) and the largest quantity deposited at the gold surface.

However, the grafting of the biotin derivative on the nanoparticle surface resulted in a negative shift of the resonance angle (-1.184° for 670 nm and -0.578° for 785 nm). This change is obviously correlated to the decrease of the refractive index at the gold surface. In order to verify the possibility of the material removal, the film of nanoparticles was refluxed in the same condition of the “click” reaction for 24 hours without addition of biotin derivative. The film before and after refluxing was characterized in order to see the potential desorption of nanoparticles at the surface.

<sup>5</sup> According to the value measured experimentally from Johnson et al.<sup>[21]</sup>

SEM and AFM measurements did not show significant changes of the nanoparticle density and the topography as observed in the presence of biotin (IV.A.1.b). However, these microscopy analyses are not accurate to determine precisely such a small variation of nanoparticle density. The SPR measurements are more sensitive of any change at the surface. Therefore, the film of nanoparticles was characterized by SPR measurement before and after refluxing in the condition of click reaction without adding alkynated biotin in the medium.

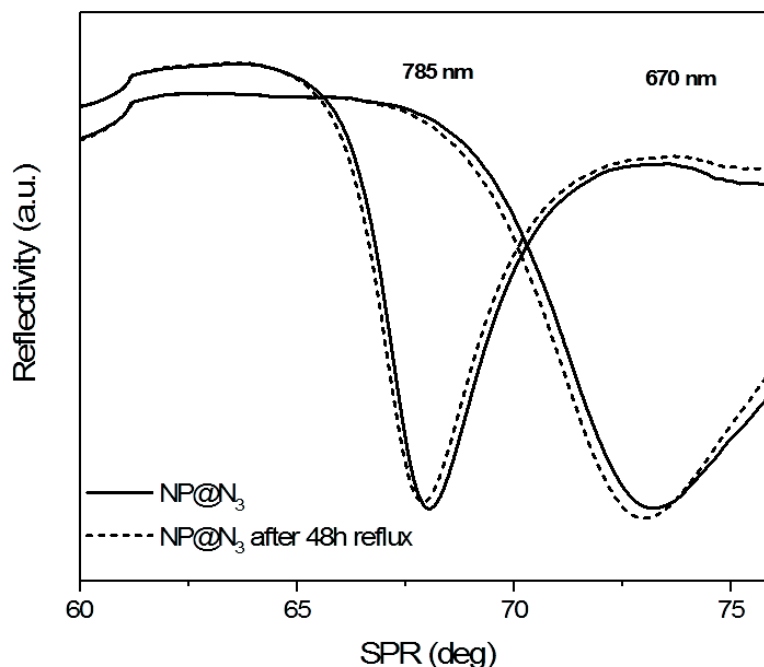


Figure 0-9. SPR measurements performed on an azido-terminated nanoparticle assembly supported onto a gold substrate before (solid curve) and after (dotted curve) being exposed to CuAAC reaction conditions without alkynated biotin derivative.

Figure IV-9 shows the resonance angle recorded for the nanoparticle assembly before and after refluxing for 24 hours. For each wavelength, the resonance angle decreases ( $-0.226^\circ$  and  $-0.145^\circ$  for 670 nm and 785 nm respectively). It is lower than for the sample with biotin; however, this change can be attributed to the difference of density in nanoparticles and the presence of more or less aggregates at the surface which can induce different removal of the nanoparticles. Nevertheless, these results proved the change of refractive index at the surface which can be explained by the desorption of the nanoparticles on the surface during the refluxing process. This desorption can be caused by the removal of physisorbed nanoparticles although the sample was exposed to ultrasounds after nanoparticles were assembled.

#### d) *Performing SPR measurements to determine nanoparticle density*

Here we focus on a new way to measure nanoparticle density onto which is usually measured by SEM. Although SEM provides directly information on the spatial arrangement of nanoparticles, it may be time consuming in the case of a large number of samples to study. Furthermore, as we showed above, it may not be accurate to detect small variations in nanoparticle density on large surface areas. Therefore, we decided to use SPR measurement to measure nanoparticle density

Knowing the refractive index of iron oxide nanoparticles for a given wavelength, the position of the resonance peak allows determining the density of nanoparticles. Samples with different densities of nanoparticles (with a mean diameter of 10.4 nm) were prepared by performing “click” reaction for different times. The position of the SPR peak measured at 785 nm and the nanoparticle density measured from SEM micrographs were plotted as function the reaction time (figure IV-10).

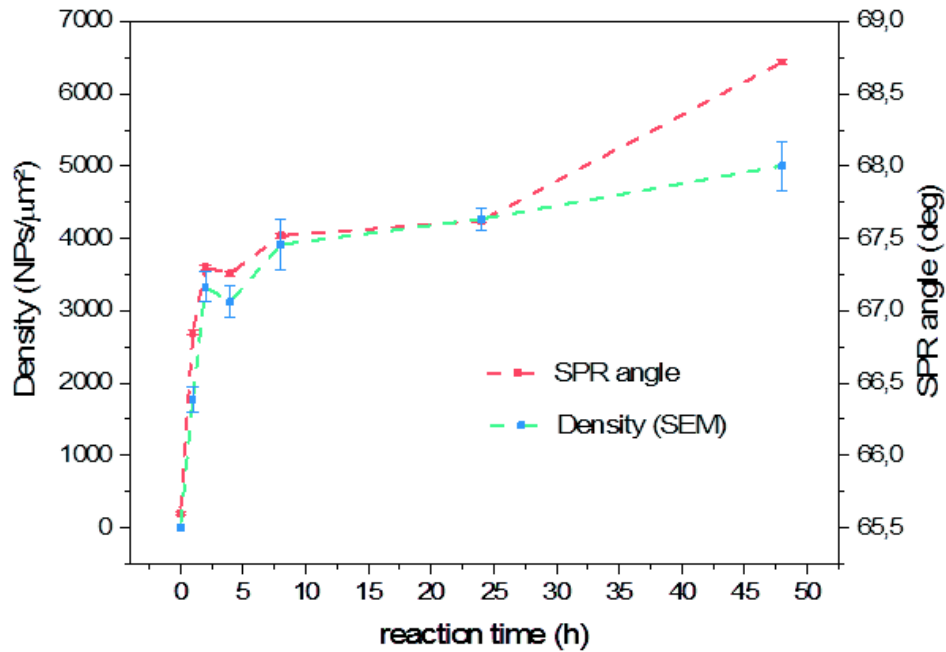


Figure 0-10. Density and SPR angle position for samples prepared after different CuAAC reaction times

Both curves are rather similar and show two different regions which correspond to the fast assembly of nanoparticles for reaction times below 3 hours which levels off but continue to increase until 48 hours. The slower kinetic of the assembly reaction after 3 hours results from the reduction of the available surface by 60 %. We can see that SPR provides a much better precision on nanoparticle density than SEM in the case of the fast kinetics. The larger value of the SPR peak position after 48 hours in comparison with density can be attributed to aggregates on the surface which make the counting of nanoparticles difficult.

The SPR peak can then be plotted as function of the density of these samples and confronted to a theoretical model (detailed in appendix A) shown on figure IV-11.

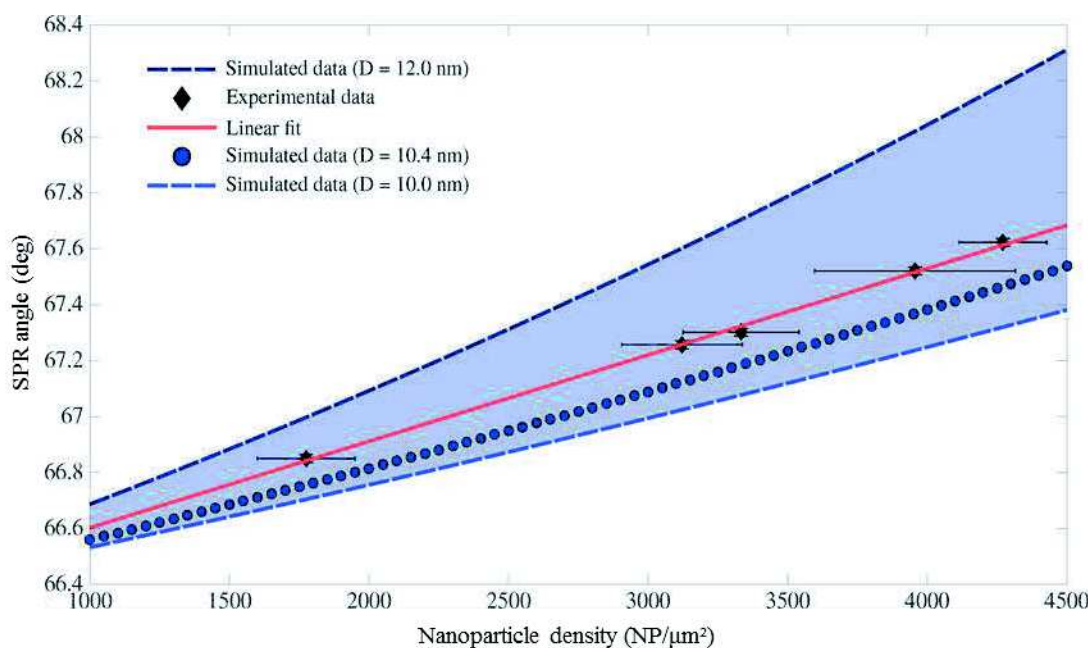


Figure 0-11. SPR peak position at 785 nm plotted with density of nanoparticles

The experimental points show a linear dependence between the SPR and the density of nanoparticles at the gold thin film surface. The values measured after 48 hours of reaction are not shown because of the presence of aggregates of nanoparticles at the surface. This linear fit shows a direct correlation which allows us determining the nanoparticle density by knowing the SPR peak position. Moreover, the simulated data for the considered size (10.4 nm, blue dotted curve) shows a similar behavior of the experimental points. However, the simulated curve exhibits an offset of few millidegrees. This offset may result from the size distribution of nanoparticles which can generate a distribution of angle. Thus, simulated data were performed with different values of  $D$  between 10 nm and 12 nm and can represent a fictive size distribution (colored area). Moreover, this simulation for several sizes shows that the evolution is not perfectly linear. Another reason of the offset may be due to the approximation of the model where the nanoparticle assembly constitutes a layer with an effective dielectric constant. This dielectric constant is determined by using the effective thickness of the nanoparticle layer and therefore using the filling factor  $f$ . The filling factor is defined by the volume fraction of nanoparticles:

$$f = \frac{V_{NPs}}{V_T} \quad \text{Equation VI.2}$$

with  $V_{NPs}$  the volume occupied by the nanoparticles (determined from the density and the volume of a nanoparticle) and  $V_T$  the volume total with a surface of  $1 \mu\text{m}^2$  and a height corresponding to the penetration depth of the evanescent wave  $\delta$  (see chapter I). This approximation implies to consider a total volume with a homogenous permittivity. However, the nanoparticles are not spread all over the sensing volume but localized at the vicinity of the metal surface which influences the value of  $\theta$ .<sup>[25]</sup> Nevertheless, this calibration curve allows determining the density of nanoparticles onto the gold thin film by knowing the SPR peak position.

In this part, a nanostructured recognition platform has been elaborated and the different characterization techniques demonstrated unambiguously the grafting of biotin derivatives at the nanoparticle surface. Moreover, SPR was demonstrated to be very efficient to monitor the build-up of our detection platform. Furthermore, the high sensitivity of SPR properties to change of refractive

index can be used as an alternative to microscopy techniques to quantify precisely nanoparticles assembled onto a gold thin film.

## 2. Detection of streptavidin

In order to prove the efficiency of our sensor, we studied the adsorption of streptavidin by taking advantage of the high tunability of our detection platform. Several structural parameters (nanoparticle density, nanoparticle size, amount of bioreceptors) were investigated to build the most efficient detection platform. We used two different techniques to measure the SPR properties of the gold film which are the most reported in the literature: the angular interrogation (at fixed wavelength of 785 nm) and the spectral interrogation (at fixed angle of 74°).

### a) *Influence of nanoparticle assembly on the detection*

The detection will be studied with two different SPR systems presenting the same Kretschmann configuration to couple incident light with surface plasmons at the interface between metallic substrate and dielectric (see chapter I). The incident wave goes through the prism made of BK7 glass and hit the gold substrate. The minimum of reflection on the surface can be measured as function of the incident wavelength or the incident angle. Therefore, the two systems are defined and used as function of their response:

- A home-made SPR experiment allowing different configurations which was used to study the spectral interrogation to get information on the incident resonance wavelength. In this case, the substrate was deposited directly onto the prism and to ensure the refractive index continuity between the prism and the sample, a coupling oil ( $n = 1.51$ ) is deposited. A gold thin film is deposited by sputtering onto a glass plate with an anchoring layer of titanium (2-3 nm). The thickness of the gold film used is 30 nm or 50 nm.<sup>6</sup>
- A Bionavis© commercial system working at a fixed wavelength allowed studying the angular interrogation by changing the resonance angle position.<sup>7</sup> Here, there was no control on the prism, commercial substrates were inserted inside the system after building up of the detection platform. This system was combined to a microfluidic device which was also used to study the kinetics of the recognition process. Commercial substrates consist in a gold layer of 50 nm deposited onto a glass plate with an adhesion layer of chromium about 2-3 nm.

In the following measurements, streptavidin was extracted from the *Streptomyces avidinii* bacteria. A buffer solution is commonly used for the protein stabilization and to avoid denaturation or conformation change during the storage. Here, the streptavidin was used in pure water to avoid unspecific adsorption of salt on the surface which may hamper the recognition process. The

---

<sup>6</sup> Collaboration with J-F. Bryche,  
G. Barbillon C2N, Orsay  
J. Moreau, IOGS, Orsay

<sup>7</sup> Collaboration with F. Boulmedais, ICS, Strasbourg

recognition process will be performed on biotin terminated assemblies of 10 nm-sized nanoparticles with different densities.

(1) Detection of streptavidin by performing angular interrogation

Angular interrogation was performed by using the Bionavis© system. The sample was settled in the SPR device and the streptavidin solution was injected by using a microfluidic channel. The incubation process was performed for a given time and concentration of streptavidin. Preliminary studies showed that the angular shift reached its maximum value only few minutes after injection of a streptavidin solution with a concentration of 100  $\mu\text{g}/\text{mL}$  (see part VI.A.4.1). 250  $\mu\text{L}$  of streptavidin solution were injected with a flow rate of 50  $\mu\text{L}/\text{min}$ . The sample was rinsed further by injecting pure water.

The effect of the nanoparticles on the adsorption of the streptavidin was studied by measuring the SPR signal at 785 nm (figure VI-12). Two samples were studied: i) a gold thin film without nanoparticles was prepared by grafting azide-PEG3-biotin onto an alkyne terminated SAM by performing CuAAC “click” reaction (appendix C for characterizations) ii) a gold thin film fully covered by 10 nm-sized nanoparticles decorated with biotin groups at their surface was prepared as mentioned in the previous section of this chapter.<sup>8</sup>

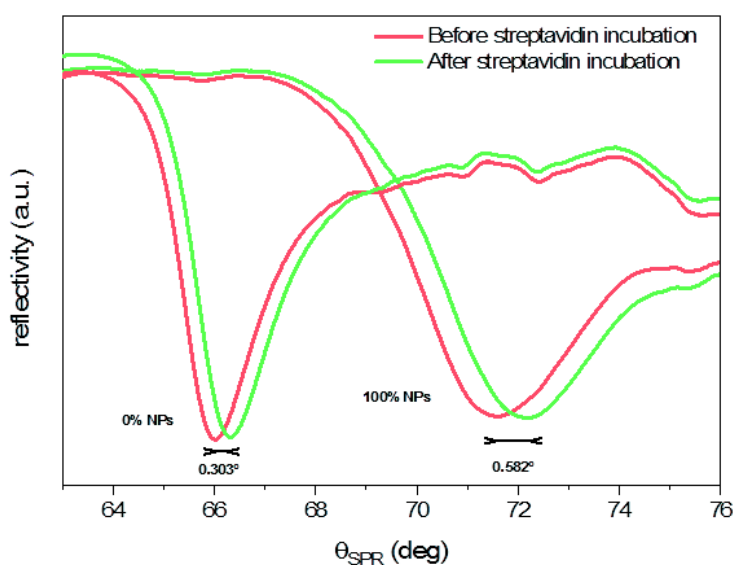


Figure 0-12. SPR measurements at 785 nm before (red curve) and after (green curve) adsorption of streptavidin on a) a gold thin film b) a gold thin film covered by 10 nm nanoparticles.

Figure IV-11 shows the adsorption of streptavidin onto a gold thin film with and without nanoparticles. As expected, the injection of streptavidin onto both biotinylated surfaces induces a shift of the resonance angle corresponding to the adsorption of streptavidin on the surface. The main difference between both samples is the larger SPR angle shift observed in the presence of nanoparticles. The shift passes from  $0.303 \pm 0.002^\circ$  to  $0.582 \pm 0.002^\circ$ , meaning an increase about twice by adding the nanoparticles on the surface. The broadening of the peak for the surface covered by nanoparticles can be explained by the heterogeneity of the film caused by the nanostructures. The

<sup>8</sup> The measurements were performed at both wavelengths. We chose to study the 785 nm since the resonance peak is sharper. Moreover, the position at lower angle is more convenient for the grafting of nanoparticles.

small change in the minimum reflectivity is also probably due to the absorption of the light by the iron oxide.<sup>[26]</sup> Furthermore, we can notice that the specific detection of streptavidin by using biotin receptors was not affected by the presence of iron oxide nanoparticles. The adsorption is followed by a rinsing step with water. The streptavidin was not desorbed (see part VI.A.4.1) which demonstrates that our sensing platform preserves strong biomolecular interactions.

## (2) Detection of streptavidin by performing spectral interrogation

The same experiment was conducted by using a different SPR system which is based on spectral interrogation. The fixed angle was settled at 74° which was the optimized position to monitor the adsorption of streptavidin. Here, the streptavidin was not injected with a microfluidic channel. The substrate was immersed in the streptavidin solution at 100 µg/mL for 30 minutes to conduct measurements in "static" mode. The substrates were then rinsed with pure water and immersed 10 seconds in an ultrasonic bath in order to avoid non-specific deposition of the streptavidin on the nanoparticle surface. The SPR measurements before and after streptavidin adsorption were performed for different surface coverages with nanoparticles. Three samples were considered; i) without nanoparticles (0%), ii) an intermediate coverage of the gold thin film which mainly consists in isolated nanoparticles (15%) and iii) a fully covered gold thin film by nanoparticles (100%)(figure IV-13). The intermediate coverage of nanoparticles was controlled by adjusting the reaction time of CuAAC (cf. chapter II).

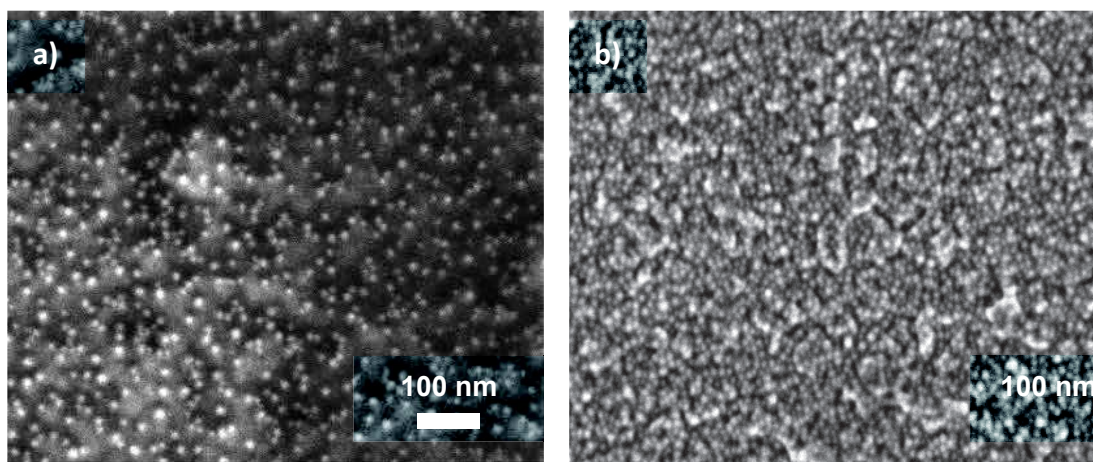


Figure 0-13. SEM images showing the coverage of the gold substrate by nanoparticles corresponding to a) 15% and b) 100 % of a full monolayer after performing CuAAC "click" reaction. Scale bar: 100 nm

The SPR measurements are shown on figure IV-14 the curves are corrected because the minimum of reflectivity changes with the presence of nanoparticles as observed for the angular measurements. This loss in intensity was observed in the case of deposited material on a gold thin film<sup>[27, 28]</sup> and is caused by the absorption of the iron oxide nanoparticles. The sample fully covered with nanoparticles exhibits the largest shift of the resonance peak up to 41 nm. In contrast, a lower density in nanoparticles corresponding to 15 % coverage of the gold substrate resulted in an intermediate shift of 7 nm. The sample without any nanoparticles at the surface presents the smallest shift of 3 nm after immersion in the streptavidin solution. The broadening of the resonance peak in this case is less pronounced than for the measure with angular response. However, the same behavior

is observed since the presence of the nanoparticles on the surface give an enhancement of the response after exposition to the protein.

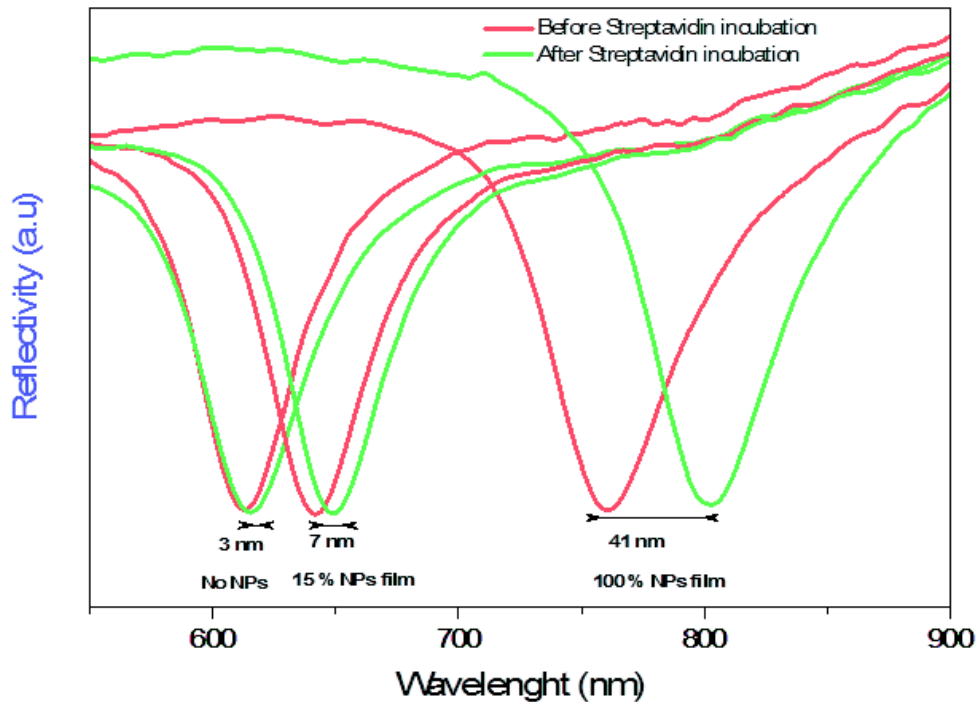


Figure 0-14. SPR measurements at 74° (internal angle) performed before (red curve) and after (green curve) exposition to streptavidin for different surface coverages of the gold substrate by nanoparticles

Both angular and spectral interrogations allow us concluding that the spectral shift is enhanced with the presence of nanoparticles on gold thin film, and that the largest density of nanoparticles is the most effective.

#### b) *Understanding the role of nanoparticle assembly on the detection*

The response of the sensor is dependent of the intrinsic optical properties of the gold thin film and of the chemical functionalization of the nanoparticle surface. To understand the influence of the nanoparticles on the sensitivity of the system and its ability to detect streptavidin, we studied all parameters given by equation (IV.3) on which the response  $R$  (angular or spectral shift) is dependent (cf. chapter I):<sup>[29]</sup>

$$R = m \cdot \Delta n \cdot \left[ 1 - e^{\frac{-2d}{l_d}} \right] \quad \text{Equation IV.3}$$

The enhancement of the SPR response can result from:

- The decrease of the decay length  $l_d$ ;
- The increase of the sensitivity factor  $m$ ;
- The increase of surface area;
- The increase of the accessibility of functional groups;

The presence of nanoparticles impacts these factors which explained the increase of the shift. These different parameters are studied in order to understand their influence on the sensors sensitivity.

(a) *Decay length*

The evanescent electromagnetic field decay length (which is half of the penetration depth) is dependent on two parameters: the operating wavelength and the refractive index of the dielectric at the surface of the gold thin film (equation IV.4).

$$l_d = 2\delta = \frac{\lambda}{2\pi} \sqrt{\left| \frac{\varepsilon_m + \varepsilon_d}{\varepsilon_d^2} \right|} \quad \text{Equation IV.4}$$

The angular interrogation being performed at a fixed wavelength, the decay length is expected to change only because of the increase of refractive index. Nevertheless, it is weakly affected (variation of 7 %) as shown by measurements performed with or without nanoparticles (300 nm and 322 nm, respectively).

In contrast, in the case of the spectral interrogation, the decay length is expected to be significantly increased at longer wavelengths. The decay length increased almost two times from without nanoparticles (160 nm) to with nanoparticles (302 nm).

Therefore, the decay length is more influenced by the operating wavelength than by the refractive index. Indeed, a larger penetration depth increases the sensing volume which hampers the contribution of the refractive index. Therefore, we would have expected that the presence of nanoparticles would disfavor the SPR shift with a strong increase of  $l_d$ . However, our experimental results show that the effect of the decay length on the SPR shift is minor and the significant increase of  $l_d$  is compensated by others parameters.

(b) *Sensitivity factor*

(i) *Angular interrogation*

The sensitivity factor  $m$  is calculated from calibration curves which were recorded by measuring the shift position of the SPR peak as function of the refractive index (RI) of different surrounding media.<sup>[30, 31]</sup>  $m$  can then be extracted from the slope of these curves. Calibration curves have been recorded with the Bionavis system for each sample with and without nanoparticles (figure IV-15). The shift of the resonance peak was measured for several aqueous solutions of sucrose at different concentrations which were correlated to different refractive index.

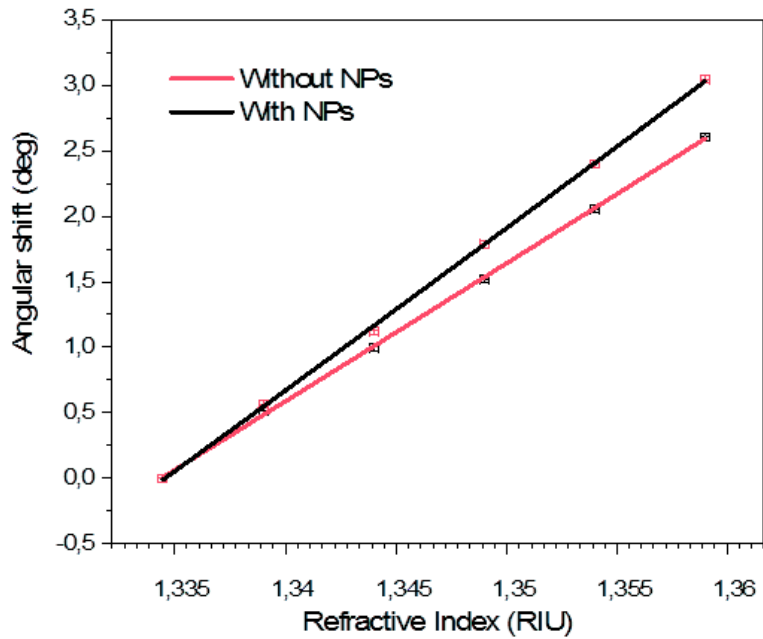


Figure 0-15. Calibration curves recorded at 785 nm for a gold thin film uncovered (red curve) and covered (blue curve) by a full monolayer of nanoparticles

The calibration curves present different slopes without ( $105.4 \pm 2.1^\circ/\text{RIU}$ ) and with nanoparticles ( $115.7 \pm 3.3^\circ/\text{RIU}$ ). This important result shows that the sensitivity of the surface plasmon is slightly increased by the presence of nanoparticles (15%). It may result from the weak interaction of nanoparticles with the light at 785 nm.

The sensitivity is measured for different densities of nanoparticles at the gold surface in order to determine the sensitivity as function of the resonance angle. The shift of the resonance angle is measured after the injection of aqueous solution of sucrose at 0.1 mol/L (meaning a variation of refractive index of  $5.10^{-5}$  RIU). Therefore, the sensitivity can be deduced with  $m = \Delta\theta/\Delta n$  and represented on figure IV-16.

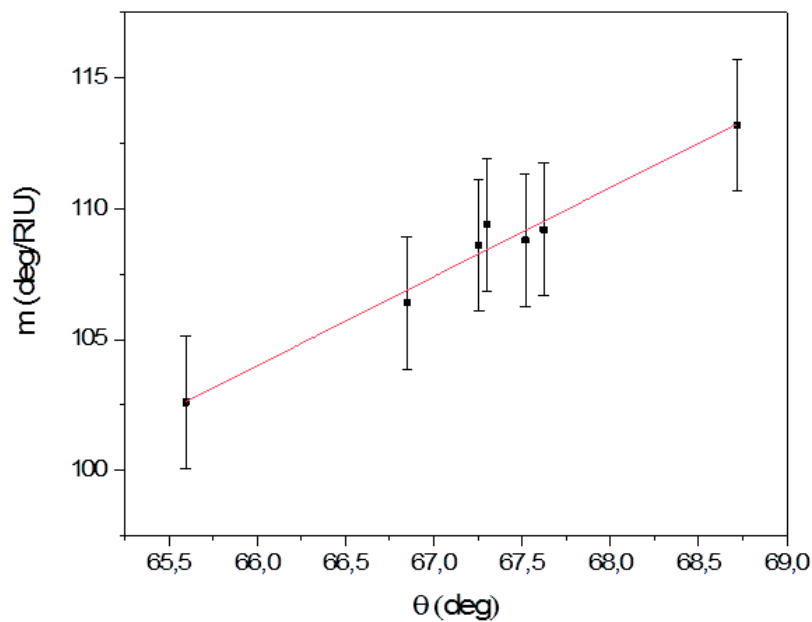


Figure 0-16. Sensitivity factor as function of the incident angle measured on a gold film with a 50 nm thickness for different nanoparticles densities

The slight variation of the sensitivity is shown with the linear fit of the data for different nanoparticle densities. The low increase of the sensitivity shows that the influence of the peak resonance is weakly important on the global sensitivity of the sensor. Nevertheless, it shows that the nanoparticles have a slight influence on this factor. This behavior is similar to the one of a multilayer system where the over layer on the gold surface increases the sensitivity as shown in the literature.<sup>[23, 32]</sup>

(ii) Spectral interrogation

In the case of the spectral interrogation,  $m$  was calculated on film of 30 nm and 50 nm of gold thickness for different wavelengths by changing the refractive index with aqueous solution of sucrose. A polynomial adjustment was done to calculate the sensitivity for every wavelengths (figure IV-17).<sup>9</sup>

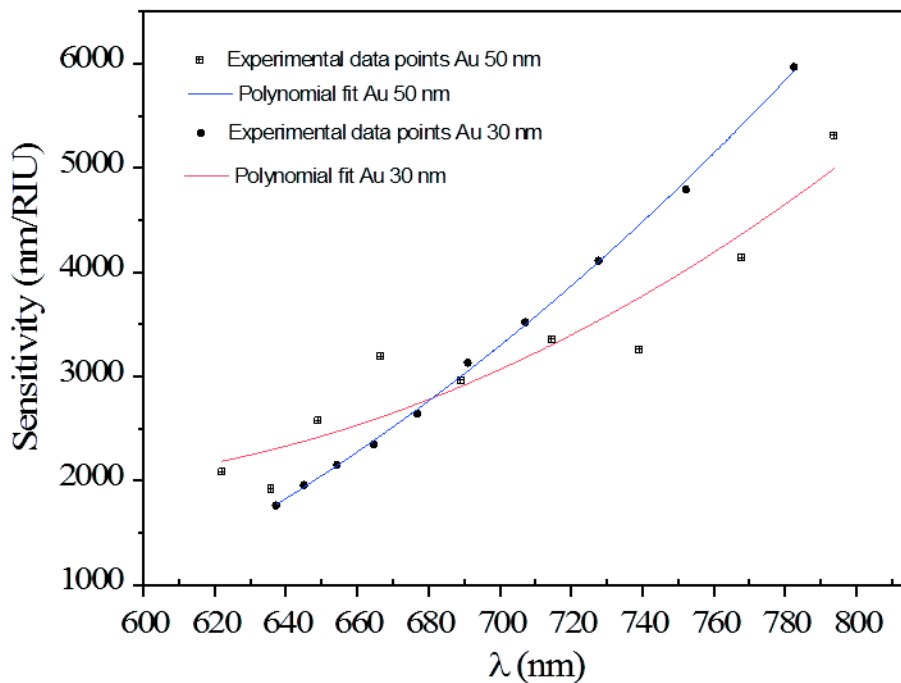


Figure 0-17. Sensitivity factor as function of the wavelength measured on a gold film with a 30 nm (red curve) and 50 nm (blue curve) thicknesses

The resonance angle has slight influence on  $m$ , but here, only the wavelength can have an impact on the sensitivity. Therefore, the sensitivity can be calculated for different wavelength which will correspond to different densities of nanoparticles. In our study,  $m$  dramatically increased with nanoparticle density and was directly correlated to the red shift of the SPR peak from 611 to 760 nm which was reported for similar systems.<sup>[16]</sup>  $m$  is the largest for the gold film fully covered by iron oxide nanoparticles (5600 nm/RIU) in comparison with the sample with nanoparticle density representing 15 % of the theoretical maximal coverage and without nanoparticles (2020 nm/RIU and 1580 nm respectively).

<sup>9</sup> Collaboration with Julien Moreau, IOGS

These experiments have shown that the sensitivity factor  $m$  of the sensors is slightly dependent of the position of the resonance angle (correlated to the deposition of nanoparticles) and strongly dependent of the incident wavelength. Indeed the nanoparticles do not influence this factor directly but indirectly in the case of the spectral interrogation by displacing the resonance peak. For the spectral interrogation system we can easily see the difference of the sensitivity, but in the case of the angular interrogation where the wavelength has no influence, others parameters should influence the larger shift with nanoparticles.

(c) *Available surface area*

Besides the intrinsic parameters of the gold thin film, the sensitivity can be increased by the surface functionalization.<sup>[10, 33]</sup> Indeed, the modulation of surface area and topography resulting from nanoparticles may markedly increase the amount and the accessibility of biotin groups. Investigation of the theoretical quantity of adsorbed streptavidin will be compared with the experimental determination of thickness and mass of streptavidin.

(i) *Number of streptavidin adsorbed*

The surface area is increased with the presence of the nanoparticles due to their high surface/volume ratio. The calculation of the number of available biotin groups can be estimated knowing the occupied surface by alkane thiol molecules on a gold thin film ( $24 \text{ \AA}^2$ ) and by the alkane phosphonate molecules on the iron oxide surface ( $26 \text{ \AA}^2$ ). The number of biotin groups was calculated on a gold thin film fully covered by 10 nm-sized nanoparticles and was compared with a gold thin film without nanoparticles. The number of biotin groups was calculated on the assumption that all azide groups reacted with alkynated biotin derivatives as demonstrated at the beginning of this chapter.

**Table 0-3. Biotin groups per surface unit onto a thin gold film and on a thin gold film fully covered by a 10 nm-sized nanoparticles**

	Flat surface	100% NPs
Surface available per $\mu\text{m}^2$	<b><math>1,0 \cdot 10^{-12} \mu\text{m}^2</math></b>	<b><math>1,86 \cdot 10^{-12} \mu\text{m}^2</math></b>
Number of biotin groups available	<b><math>4,17 \cdot 10^6</math></b>	<b><math>3,10 \cdot 10^6</math></b>

Table IV-3 showed that the number of biotin groups per surface unit decreases by 25 % which is unexpected. Furthermore, nanoparticles being grafted onto the gold thin film, we estimated that biotin groups were grafted on only half of their surface.

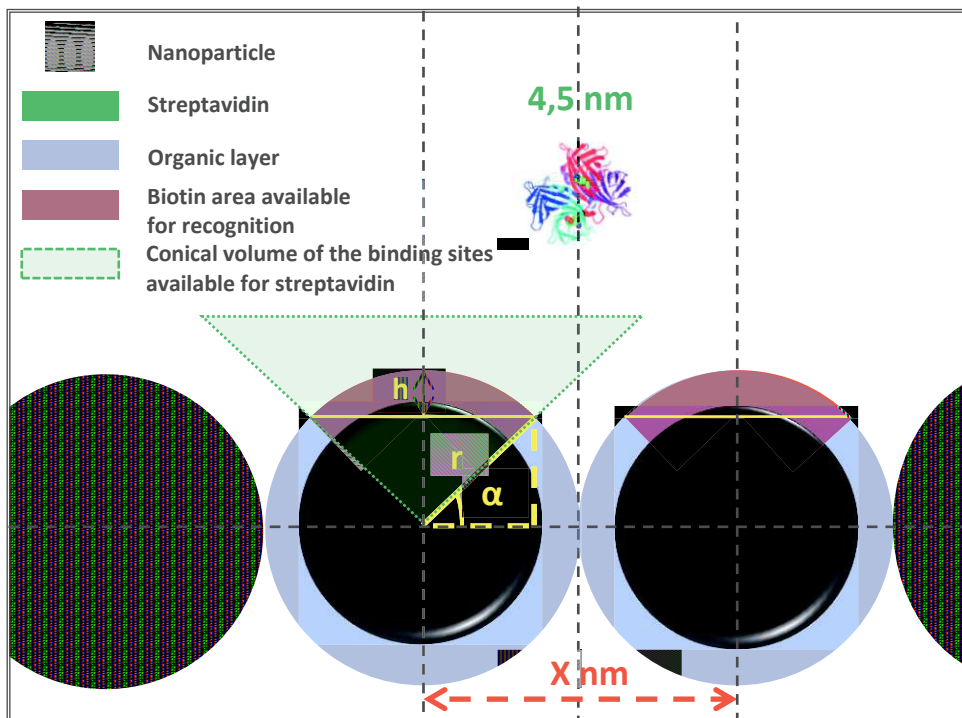


Figure 0-18. Schematic representation of the available area of biotin for the adsorption of streptavidin

Moreover, the number of “available” biotin groups should be considered with the size of the streptavidin which will induce steric hindrance at the surface. Indeed, when the nanoparticles are grafted on the surface, a part of the azide groups already reacted with the SAM and others are not accessible because of the tight packing of the nanoparticles. If we consider the surface available for the streptavidin in the case of a dense monolayer of nanoparticles, only few streptavidin can be adsorbed at the nanoparticle surface. Indeed, the steric hindrance of the streptavidin on the surface of the nanoparticles does not allow its adsorption on the total surface of nanoparticles when tightly packed. The figure VI-18 shows the geometrically area where the available biotin groups are localized for the adsorption of the streptavidin.

The red area corresponds to the surface where are localized the available biotin groups. With this representation, it is obvious that the spacing between nanoparticles can increase the red area and therefore allow the adsorption of a larger amount of streptavidin. The figure IV-19 presents the theoretically maximum number of streptavidin per nanoparticle which can be adsorbed onto the nanoparticle assembly as function of the inter-particle distance considering a streptavidin surface area of  $20.25 \text{ nm}^2$ <sup>[34]</sup> and 10 nm-sized nanoparticles.

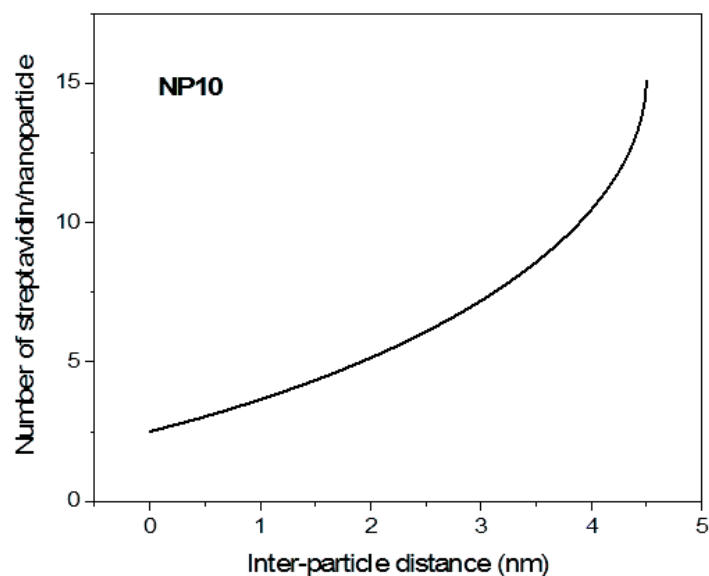


Figure 0-19. Number of streptavidin which can be adsorbed onto a nanoparticle as function of the inter-particle distance in the case of 10 nm-sized nanoparticles

As we can see the number of streptavidin per nanoparticle for a close packed nanoparticle assemblies (and therefore considering an inter-particle distance null) is about 4 streptavidin/nanoparticle. This value agree with the surface available of each nanoparticle for streptavidin adsorption (appendix A) and the surface occupied by each streptavidin.<sup>[15]</sup> In our case, a surface covered with 5 800 NPs/ $\mu\text{m}^2$  corresponds to a full coverage of 10 nm-sized nanoparticles with an organic shell of 2 nm. Therefore, the maximal theoretical number of streptavidin grafted should be 23 200 streptavidin/ $\mu\text{m}^2$ . In the case of a coverage of 15 % by nanoparticles, the average inter-particle distance is about 15 nm which is more than the size of the streptavidin. Therefore, we can consider that neighboring nanoparticles will do hamper the grafting of the streptavidin and reach the value of 15 streptavidin/nanoparticle. However, the surface is only covered with 15 % in density which corresponds to 870 nanoparticles/ $\mu\text{m}^2$  and leads to a theoretical detection of 13050 streptavidin/ $\mu\text{m}^2$ .

As we can see, the number of streptavidin detected does not increase linearly with the quantity of nanoparticles at the surface. Therefore, it should exists an optimum density of nanoparticle which can favor the adsorption of a maximum of streptavidin (see part IV.A.3).

(ii) *Determination of thickness and mass of streptavidin adsorbed*

Experimentally, the effective thickness of the adsorbate layer can be determined with the equation of the sensor response (equation IV.3). Indeed, knowing the sensitivity factor and the decay length, we can determine the effective thickness of the streptavidin which was adsorbed as function of the measured response:

$$d = \frac{-l_d}{2} \ln\left(1 - \frac{1}{m} \frac{R}{\Delta n}\right) \quad \text{Equation IV.5}$$

with  $\Delta n = (n_{\text{adsorbate}} - n_{\text{solvent}}) = 0.24$  for the streptavidin.<sup>[35, 36]</sup>

The spectral shift observed without nanoparticles gives a streptavidin thickness of 0.8 nm. Considering the size of a streptavidin ( $4.5 \times 4.5 \text{ nm}^2$ )<sup>[34]</sup> the surface covered by the protein is less than

20%. This low value can be explained by low accessibility of biotin groups which are tightly packed at the surface of gold thin film. Indeed, steric hindrance hampers the recognition of the streptavidin.<sup>[37]</sup> However, this value is very low and may have to be reconsidered. In contrast, the angular shift measured for the same sample gives a thickness of 1.9 nm which is higher but still low in comparison of the size streptavidin. In the case of the sample fully covered with nanoparticles, the streptavidin thicknesses are 4.6 nm and 3.2 nm for the system with spectral and angular interrogation, respectively. The thickness in the case of the spectral shift is surprisingly high and may represent a full layer of streptavidin at the surface of the nanoparticles.

The effective thickness can be correlated to the mass of protein per unit area which can be determined by using the Freiter equation<sup>[38]</sup> which gives the relation between the response and the mass of adsorbed analyte:

$$\Gamma = \frac{\Delta n \cdot d}{\frac{\partial n}{\partial c}} \quad \text{Equation IV.6}$$

with  $\Delta n$  the variation of the refractive index at the surface,  $d$  the thickness of the adsorbate layer and  $\frac{\partial n}{\partial c}$  the variation of the refractive index as function of the protein concentration ( $\frac{\partial n}{\partial c} = 0.212 \text{ g} \cdot \text{cm}^{-3}$  for the streptavidin).<sup>[39]</sup>

The surface coverage is determined for the samples with and without nanoparticles (table IV-4).

**Table 0-4. Summarize of surface coverage and number of streptavidin per surface area determined by the angular shift**

	$\Delta\theta$	$\Delta\lambda$	$\Gamma$	Streptavidin/ $\mu\text{m}^2$
<b>Without NPs</b>	0.304°		215.1 ng/cm <sup>2</sup>	24 500
		3	90.6 ng/cm <sup>2</sup>	10 400
<b>With NPs</b>	0.512°		362.3 ng/cm <sup>2</sup>	41 300
		41	520.8 ng/cm <sup>2</sup>	59 300

The values of the mass led to the same conclusion than for the thickness. The system with angular interrogation shows an increase of almost twice with the presence of nanoparticles and the system with spectral interrogation exhibit six times more streptavidin with the nanoparticles.

Moreover, the mass coverage allows determining the number of streptavidin per micrometer square. Knowing the number of streptavidin per nanoparticle (4.3 streptavidin/nanoparticles) determined by theoretically and corresponding to a density of nanoparticles (5800 NPs/ $\mu\text{m}^2$ ), we can also determine the number of streptavidin per surface area. Nevertheless, the theoretical maximum coverage is approximated to 25 000 streptavidin/ $\mu\text{m}^2$ . This value represents only half of the streptavidin determined experimentally and may put questions on the reliability of the measurements. Complementary characterization techniques such as quartz microbalance would help concluding on the quantity of streptavidin at the surface.

The table IV-5 summarizes the different parameters for the both systems.

**Table 0-5. Summarize of the characteristics measured from angular and spectral interrogations**

	785 nm Sans NPs	785 nm Avec NPs	74° Sans NPs	74° 15 % NPs	74° 100 % NPs
Angular response of the sensor $\Delta\theta$	<b>0.304°</b>	<b>0.582°</b>	/	/	/
Spectral response of the sensor $\Delta\lambda$	/	/	<b>3 nm</b>	<b>7 nm</b>	<b>41 nm</b>
Decay length $l_d$	<b>322 nm</b>	<b>300 nm</b>	<b>160 nm</b>	<b>186 nm</b>	<b>302 nm</b>
Sensitivity factor $m$	<b>105.4°/RIU</b>	<b>115.6°/RIU</b>	<b>1 300nm/RIU</b>	<b>2 020 nm/RIU</b>	<b>5 600 nm/RIU</b>
Effective thickness $d$	<b>1.9 nm</b>	<b>3.2 nm</b>	<b>0.8 nm</b>	<b>1.4 nm</b>	<b>4.6 nm</b>
Mass coverage $\Gamma$	<b>215.1 ng/cm<sup>2</sup></b>	<b>362.3 ng/cm<sup>2</sup></b>	<b>90.6 ng/cm<sup>2</sup></b>	<b>158.5 ng/cm<sup>2</sup></b>	<b>520.8 ng/cm<sup>2</sup></b>

In conclusion, the presence of nanoparticles significantly influences on the intrinsic optical properties of the gold thin film and contributes actively to enhance the sensitivity to change in refractive index resulting from the adsorption of streptavidin. The use of two different configurations allowed us to distinguish the contribution of the parameters on the sensitivity. The system with spectral interrogation showed that the presence of nanoparticles increases the penetration depth which should decrease the response of the sensor. However, this effect is minor in comparison with the large enhancement of the sensitivity factor. Nevertheless, these effects are mainly due to the operating wavelength. The use of angular interrogation with a fixed wavelength allows showing the effect of the surface functionalization without modifying significantly the penetration depth and sensitivity factor. The presence of nanoparticles does not increase the number of biotin groups available for the recognition of the streptavidin. However, the accessibility is increased since almost twice streptavidin molecules are detected according to the increase of the thickness and mass of protein.

### 3. Detection platform optimization

The optimization of our detection platform is related to the structure of the nanoparticle assembly. Moreover, it has been shown that the immobilization of the streptavidin onto biotin surface is affected by the concentration of the biotin groups and their availability at the surface.<sup>[37, 40-42]</sup> The accessibility of biotin groups which is directly dependent on their packing may be enhanced by dilution at the nanoparticle surface.

#### a) Influence of the spatial distribution of biotin groups at the nanoparticle surface

(1) Preliminary study: influence of the accessibility of the biotin groups on a gold surface

To assess the accessibility of biotin groups on a gold thin film, they were diluted with alkane chains. This control experiment is first performed on a gold thin film without nanoparticles. First, a mixed SAM was prepared by immersing a gold substrate in an equimolar ethanolic solution of (11-Undec-1-ynyl)thiol and dodecanethiol in a molar ratio 50/50 with a total concentration of 10 mM. Second, the alkynated biotin derivative was grafted in the standard conditions.

SPR measurements were performed by injecting an aqueous solution of streptavidin (100  $\mu\text{g}/\text{mL}$ ) in standard conditions (figure IV-20).

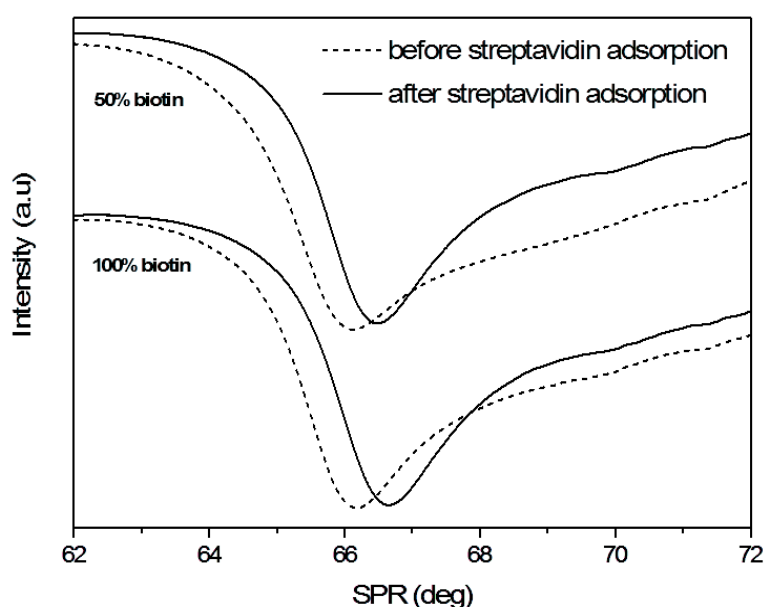


Figure 0-20. SPR measurements of the gold thin film functionalized with 100% and 50% of biotin groups without nanoparticles

The initial position of the resonance angle is similar for both samples (66.128° and 66.175° for the 50% and 100% density of biotin groups, respectively). The slightly higher value for the sample with 100% biotin may result from the thicker organic layer implying a higher refractive index. More interestingly, after exposition to streptavidin solution, the shift is significantly larger for the sample with 50% biotin ( $\Delta\theta_{50\%} = 0.477^\circ$ ) than with 100% biotin ( $\Delta\theta_{100\%} = 0.349^\circ$ ). Although the density of biotin groups is half, its dilution significantly enhances their accessibility to streptavidin. The close packed biotin groups do not allow the good recognition of the streptavidin in contrast with separated biotin groups favor a better recognition.

In order to study the influence of the density of biotin groups on nanoparticles, several samples with different amounts of biotin at the nanoparticle surface have been performed.

The method consists in grafting a mixture of alkynated biotin and hex-1-yne molecules at the surface of nanoparticle assemblies in order to prepare several samples with the same density of nanoparticles. Hex-1-yne was chosen because it is inactive and as a similar length to alkynated biotin derivative. Therefore, biotin groups were diluted with methylene groups at the surface of nanoparticle. The biotin/hex-1-yne molar ratios studied were 5%, 20%, 50%, 80% and 100%. The nanoparticles

assembled were characterized by SEM and PM-IRRAS in order to control the nanoparticle density and the CH<sub>3</sub>/biotin ratio at their surface.

(a) SEM analysis

The SEM images show that the spatial arrangement of nanoparticle assemblies is very similar whatever biotin/hex-1-yne ratio (figure IV-21). The densities of nanoparticles are the same for each sample (with an average of  $44.8 \pm 3.8$  % of the theoretical full density). The nanoparticles on the surface are not fully packed, nevertheless the same density over the sample ensure the same position of the resonance peak. Moreover, this result shows the high reproducibility of “click” chemistry approach for nanoparticle assembly and their functionalization by biomolecules.

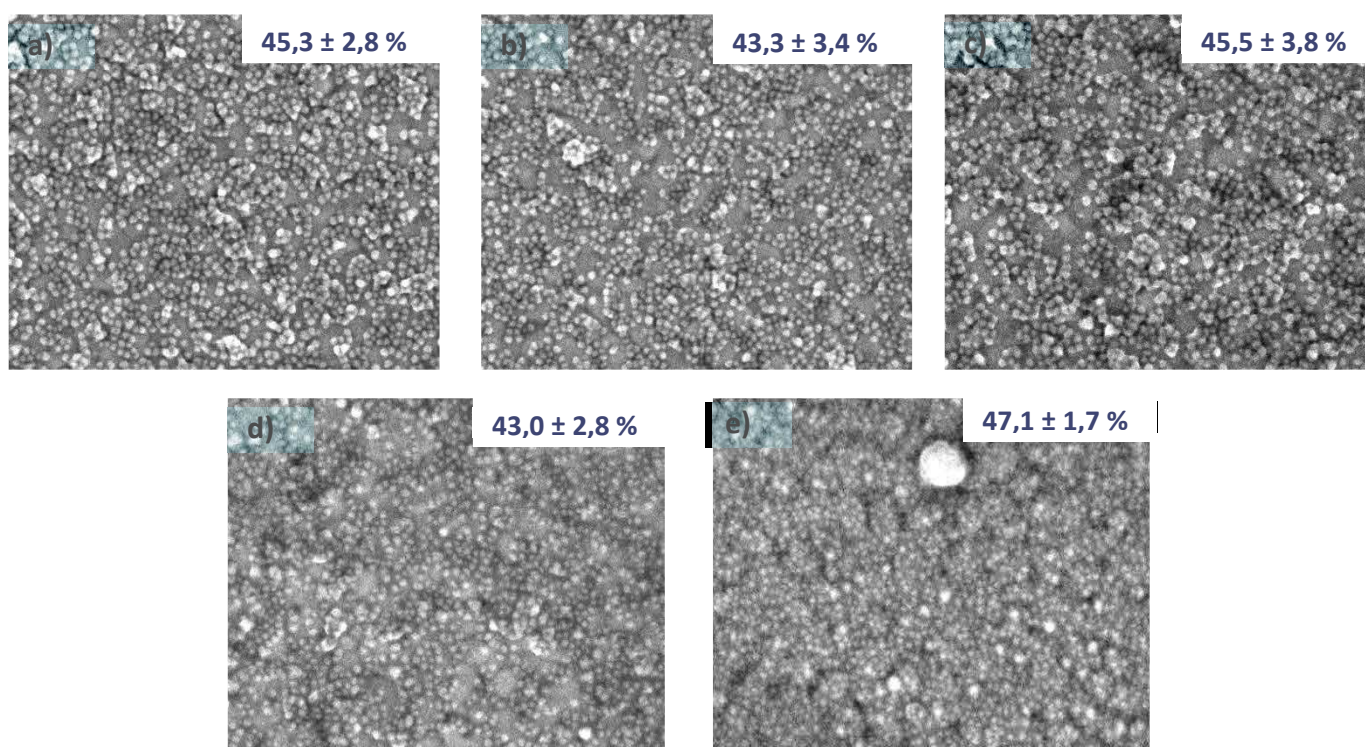


Figure 0-21. SEM images of the sample with different ratio biotin/hex-1-yne a) 5%, b) 20%, c) 50%, d) 80% and e) 100% (inset: density of nanoparticles)

(b) PM-IRRAS measurements

PM-IRRAS measurements were performed in order to control the functionalization at the surface. The figure IV-22 showed the results on the surface functionalized with the different biotin/hex-1-yne ratios.

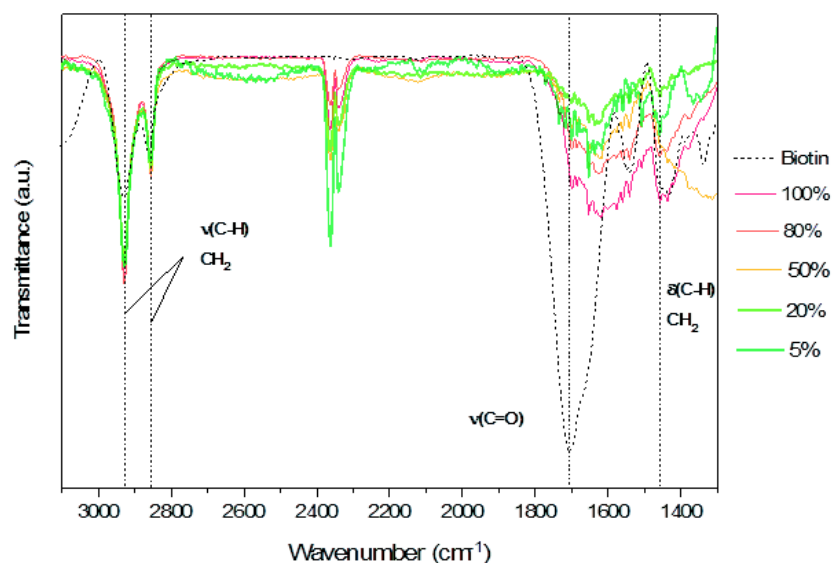


Figure 0-22. PM-IRRAS measurements of nanoparticle assemblies functionalized with different biotin/hex-1-yne ratios

Unfortunately, interferences during the measurement did not allow recording vibrational modes below  $1300\text{ cm}^{-1}$  which corresponds to the phosphonate area. The numbers of  $\text{CH}_2$  groups being similar in the biotin and the hex-1-yne, the spectra were then normalized on the area of the  $\nu(\text{C-H})$  band. Bands around  $2300 - 2400\text{ cm}^{-1}$  were ascribed to  $\nu(\text{CO}_2)$  from the environment during the measurement. The large bands in the  $1500 - 1700\text{ cm}^{-1}$  correspond to the amide bands of the biotin groups as mentioned above (cf. IV.A.1.b.4)). Moreover, the presence of the phosphonic acid band at  $1600\text{ cm}^{-1}$  contributes to the enlargement of this band. Therefore, the quantitative determination of amide groups is complicated. However, the relative evolution of these bands with respect to the biotin/hex-1-yne ratios shows the increase of biotin groups. The figure IV-23 shows the evolution of the surface area of the  $\nu(\text{C=O})$  band expected at  $1680\text{ cm}^{-1}$  with respect to the  $\nu(\text{C-H})$  band at  $2950\text{ cm}^{-1}$ .

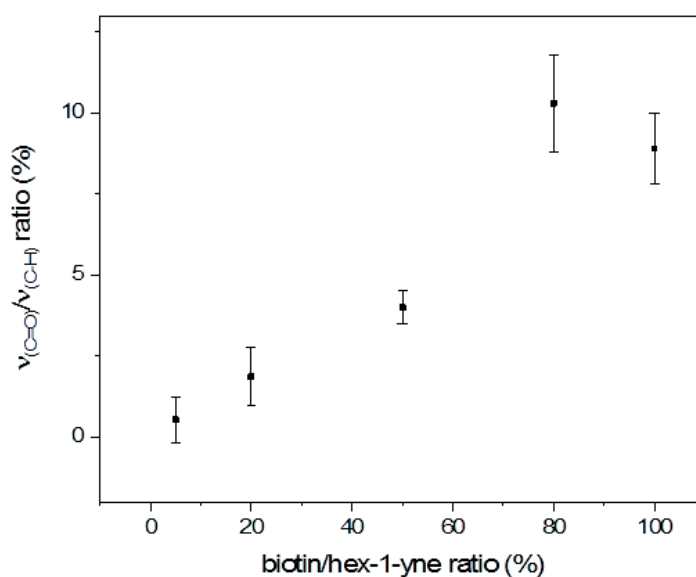


Figure 0-23. Evolution of the area surface ratio between  $\nu(\text{C=O})$  and  $\nu(\text{C-H})$  bands as function of the biotin/hex-1-yne ratio

The increase of  $v_{(C=O)}/v_{(C-H)}$  ratio with the biotin/hex-1-yne ratio in the reaction medium shows the linear increase of biotin at the surface of the nanoparticle assembly (excepted for 80%).

(c) SPR measurements

The SPR measurements were performed as function of the incident angle on the five samples with different ratios of biotin. The streptavidin was adsorbed by dipping the samples in an aqueous solution of streptavidin at a concentration of 100  $\mu\text{g/mL}$ . The results are presented on figure IV-24.

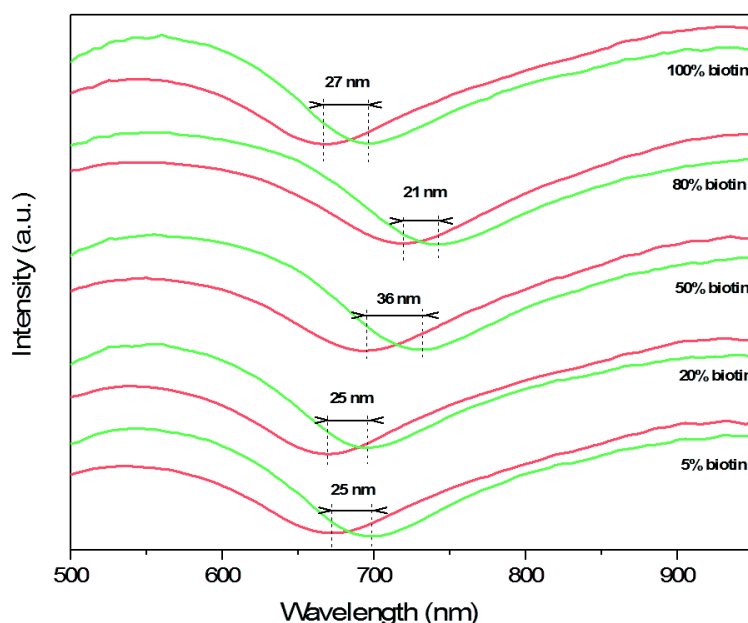


Figure 0-24. SPR measurements before (red) and after (green) exposition of the samples containing different biotin/hex-1-yne ratios in a streptavidin solution

Before adsorption of streptavidin the SPR peak is centered to 670 nm which agree with a density about 45%. Some slight differences on the sample at 50% and 80% can be observed where the peak position is slightly higher. These differences can be caused by the presence of aggregates on the nanoparticle layer.

The shift induced by the adsorption of the streptavidin is similar for most of the samples (around 25 nm). Nevertheless, the shift is larger for the sample with 50% of biotin and reaches 36 nm and a little bit lower for the sample with 80% of biotin (21 nm). The higher shift could be expected due to a lower steric hindrance thanks to dilution. However, the sample with 80% of biotin groups does not seem to follow this trend.

The effective thickness of these samples with an average resonance peak at 670 nm and a shift of 25 nm is about 4.2 nm. It represents almost a full coverage of streptavidin with less density than the previous sample fully covered. Moreover, we expected the sample with only 5% biotin to be less sensitive, however, the shift is similar to other samples. Furthermore, this sample and the one with 100% of biotin resulted in similar shifts which agree with similar amounts of adsorbed streptavidin.

In conclusion, even low quantity of biotin at the nanoparticle surface affords the similar amount adsorption of the streptavidin. This suggests only few biotin groups are required for the recognition. Moreover, the effect of the diluted groups at the nanoparticle surface can be observed since the recognition is performed no matter the quantity of biotin groups. The sample with 50% presents a larger shift which may suggest a better accessibility for the streptavidin.

(2) Variation of the size of the nanoparticles

The amount of biotin being directly dependent on the surface of nanoparticles, we have used assemblies of nanoparticles of 6 and 22 nm. Furthermore, the nanoparticle sizes control the packing of biotin groups because of curvature and facets which become predominant in the case of 20 nm sized nanoparticles. These features are expected to influence steric hindrance of biotin groups. For each nanoparticle size, two assemblies with different nanoparticle densities were prepared. An assembly with 10 nm-sized nanoparticles with high density was also prepared. The diameters and densities are summarized in table IV-6 and the SEM images are shown in figure IV-25.

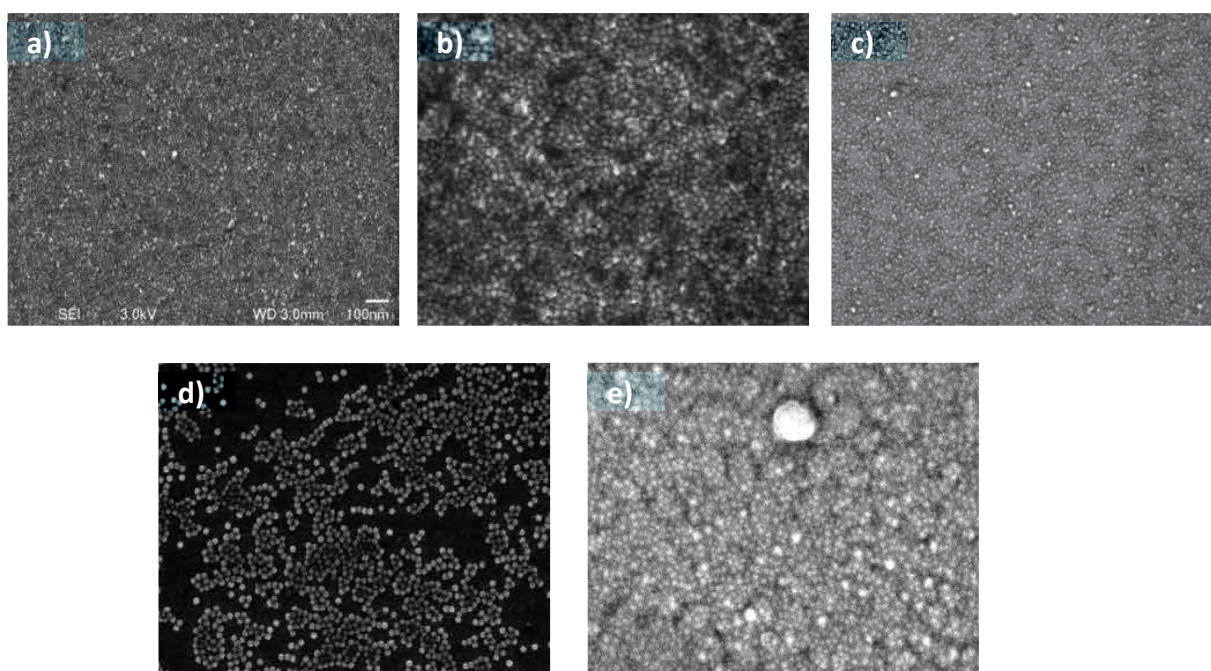


Figure 0-25. SEM images of nanoparticle assembly of a,c) 6 nm and b,d) 22 nm with a,b) high and c,d) low coverage and e) 10 nm. Magnification X50000

Table 0-6. Diameters and densities of the corresponding sample with SEM images

	Diameter (nm)	Density (%)
a)	$5.7 \pm 0.9$ nm	18%
b)	$21.9 \pm 1.6$ nm	100%
c)	$5.7 \pm 0.9$ nm	36%

d)	$21.9 \pm 1.6 \text{ nm}$	26%
e)	$10.1 \pm 1.1 \text{ nm}$	47%

These assemblies were then functionalized with the alkynated biotin derivative in order to perform the SPR measurements before and after the immersion for 30 minutes in an aqueous solution of streptavidin at 100  $\mu\text{g/mL}$  (figure IV-26). The sample e) is shown on the figure IV-25.

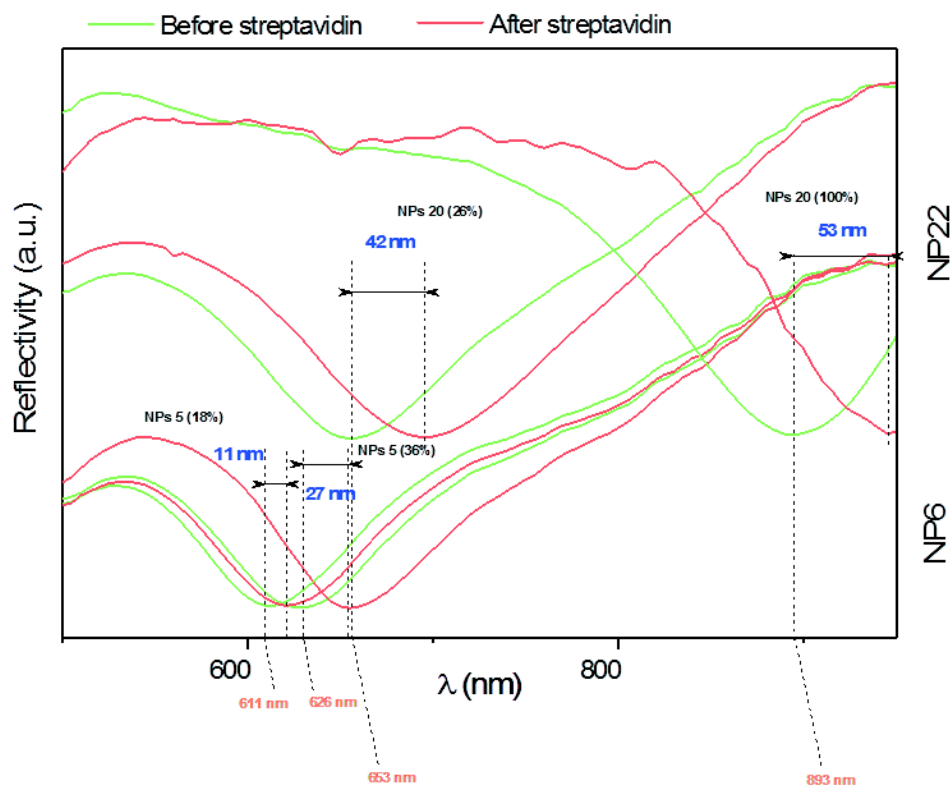


Figure 0-26. SPR measurements before (green) and after (red) dipping in a solution of streptavidin of samples with different size and density of nanoparticles

The values of the resonance plasmon shifts and other parameters are summarized in table IV-7. Before dipping in the streptavidin solution, the SPR peak is shifted to longer wavelengths with larger nanoparticle sizes and densities as expected.

Nevertheless, the shifts of resonance plasmon observed after streptavidin adsorption are unexpected. Indeed, the shifts are not linearly increasing with the incident wavelength. The sample of 6 nm-sized nanoparticles with high coverage and the sample of 22 nm-sized nanoparticles with low coverage exhibit larger shifts than expected (27 nm and 42 nm respectively).

Table 0-7. Summarize of the different parameters of the sample with different volume of iron oxide at the surface

	NP6 18%	NP6 36%	NP22 26%	NP22 100%	NP10 60%
Peak position	611 nm	626 nm	653 nm	893 nm	668 nm
Spectral response of the sensor $\Delta\lambda$	11 nm	27 nm	42 nm	53 nm	27 nm

Decay length $l_d$	158 nm	172 nm	198 nm	440 nm	210 nm
Sensitivity factor $m$	2115nm/RIU	2220 nm/RIU	2460 nm/RIU	8070 nm/RIU	2630 nm/RIU
Effective thickness $d$	1.7 nm	4.5 nm	7.3 nm	6.1 nm	4.6 nm

For the 6 nm-sized nanoparticles, the SPR shift significantly increases from 11 to 27 when the density doubles (from 18% to 36% of the maximal theoretical value). This important variation cannot be caused by the incident wavelength which slightly increases (+15 nm). To understand this phenomenon, the determination of the number of streptavidin per nanoparticle as function of the inter-particle distance and the size of the nanoparticles is necessary (figure IV-27).

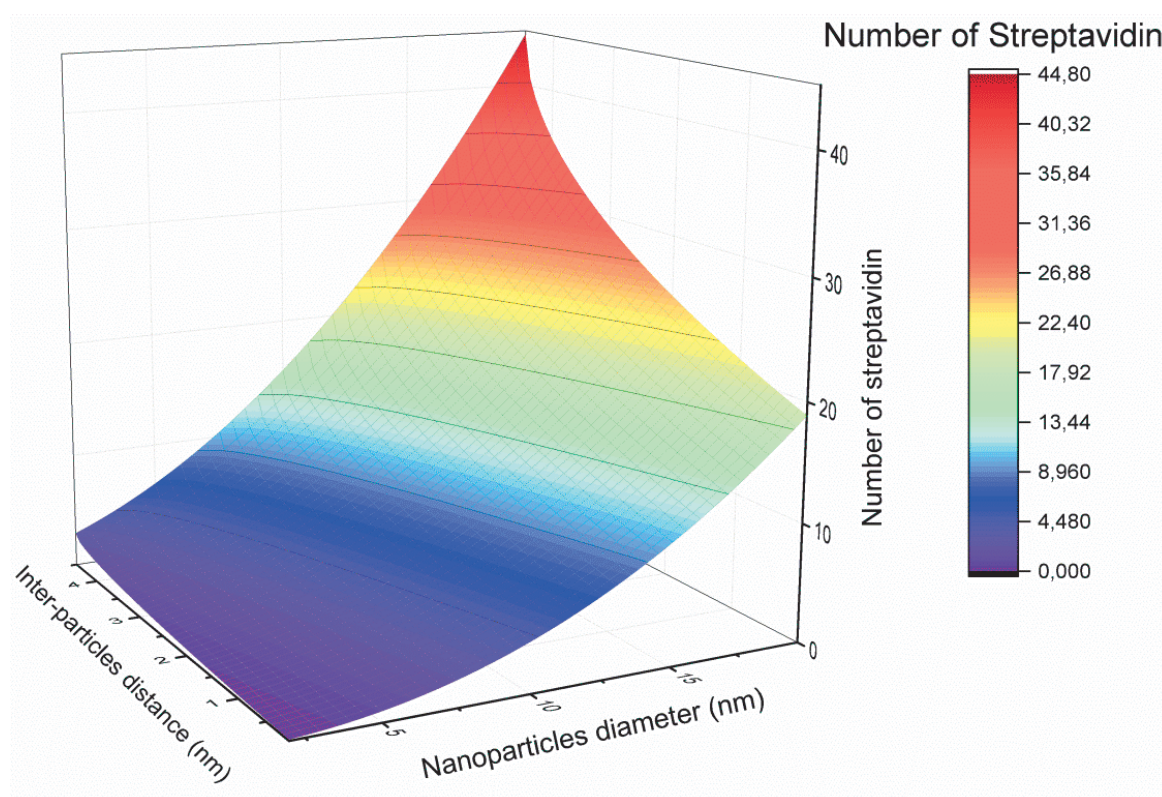


Figure 0-27. Number of streptavidin per nanoparticle as function of the size of nanoparticles and the inter-particle distance.

The low coverage of the gold thin film by 6 nm-sized nanoparticles implies large inter-particle distances as observed on the SEM images. An average inter-particle distance of 10 nm and 6 nm were calculated for samples with 36 % and 18 % in densities, respectively. These inter-particle distances correspond to the maximum of streptavidin adsorbed on the nanoparticles (7.5 streptavidin/nanoparticle for nanoparticles with a diameter of 5.7 nm). Indeed, the maximum of streptavidin per nanoparticles was reached with inter-particles distances up to 4.5 nm corresponding to the size of the streptavidin. Moreover, as shown in the chapter II, the assembly of small nanoparticles presents isolated nanoparticles which promote the high adsorption of streptavidin. The

largest shift observed in the case of the sample with the highest density is then caused by the increase of nanoparticle at the surface and therefore number of streptavidin:

$$\begin{aligned} 18 \% (2210 \text{ NPs}/\mu\text{m}^2) &\rightarrow 7.5 \text{ streptavidin/NPs} \rightarrow 16\,600 \text{ streptavidin}/\mu\text{m}^2 \\ 36 \% (4420 \text{ NPs}/\mu\text{m}^2) &\rightarrow 7.5 \text{ streptavidin/NPs} \rightarrow 33\,200 \text{ streptavidin}/\mu\text{m}^2 \end{aligned}$$

In the case of the 22 nm-sized nanoparticles, the large shift of 53 nm observed for the sample with high density coverage is due to the high sensitivity factor at this wavelength up to 8070 nm/RIU. In contrast, the sample with low coverage of 22 nm nanoparticles exhibits also a large shift of 42 nm, whereas the sensitivity factor is far lower (2460 nm/RIU). This large shift may result from the accessibility of the streptavidin at the nanoparticle surface. Indeed, the quantity of streptavidin per nanoparticles increases strongly (up to 52 streptavidin per nanoparticle for distance inter-particles larger than 4.5 nm):

$$\begin{aligned} 26 \% (450 \text{ NPs}/\mu\text{m}^2) &\rightarrow 52 \text{ streptavidin/NPs} \rightarrow 23\,300 \text{ streptavidin}/\mu\text{m}^2 \\ 100 \% (1710 \text{ NPs}/\mu\text{m}^2) &\rightarrow 20 \text{ streptavidin/NPs} \rightarrow 34\,900 \text{ streptavidin}/\mu\text{m}^2 \end{aligned}$$

Even though, the assembly of 22 nm-sized nanoparticles is driven by dipolar interactions (See chapter II) and form alignment as shown on the SEM images. However, the accessibility of biotin groups seems better for this sample.

Nevertheless, the effective thickness calculated (7.3 nm) for the sample with 22 nm-sized nanoparticle low coverage shows an overestimation of this value.

In conclusion, the sensitivity of the sensor is improved by the intrinsic optical properties such as the incident wavelength which can be tuned by the nanoparticle size and density in the case of a spectral interrogation system.<sup>[2]</sup> Therefore, the presence of nanoparticles improved the sensitivity by tuning the position of the plasmon resonance, however, the nanoparticles allow to increase the surface topography and the filling factor shows a strong influence on the sensitivity of the platform. A good compromise is a large active surface with large inter-particles distance to promote the highest sensitivity of the sensor.

#### 4. Kinetics measurements

One of the main advantages of SPR biosensing is the determination of the kinetics of biomolecular interactions. In this case, the interaction  $A + B \rightarrow AB$  can be followed in real time, where  $A$  is the analyte and  $B$  the receptor molecule immobilized on the sensor surface. The rate constants provide information on the strength of association and the tendency to dissociation. These rates are dependent of several parameters such as the temperature or the flow rate.<sup>[43]</sup> Table IV-8 summarizes the kinetic parameters and the association/dissociation constants.

**Table 0-8. Definition of the rate and affinity constants**

	Association		Dissociation	
	Association rate constant, $k_{on}$	Association constant, $K_A$	Dissociation rate constant, $k_{off}$	Dissociation constant, $K_D$
<b>Definition</b>	$A + B \rightarrow AB$	$\frac{[AB]}{[A][B]} = \frac{k_{on}}{k_{off}}$	$AB \rightarrow A + B$	$\frac{[A][B]}{[AB]} = \frac{k_{off}}{k_{on}}$
<b>Description</b>	number of AB complexes formed per unit time and unit concentration A and B	Affinity to association	number of AB complexes dissociated per unit time	Stability of AB
<b>Units</b>	$\text{l. mol}^{-1} \cdot \text{s}^{-1}$	$\text{l. mol}^{-1}$	$\text{s}^{-1}$	$\text{mol. l}^{-1}$
<b>Typical range</b>	$10^3 - 10^7$	$10^5 - 10^{12}$	$10^{-1} - 10^{-6}$	$10^{-5} - 10^{-12}$

The determination of these kinetic parameters will ensure the understanding of the interaction mechanisms between the receptor molecules and the specific proteins.

The kinetic of the recognition process were studied by measuring the angular shift as function of time. The microfluidic system allows performing injection of proteins in real time and monitoring the recognition process. The experimental conditions were set at a constant flow rate (50  $\mu\text{L}/\text{min}$ ) and a constant temperature (21°C). These measurements allow the determination of different parameters of the biosensors such as the limit of detection (LoD), the association and dissociation constants and the concentration of the analyte.

To determine these parameters, it is important to define the factors of the adsorption event. The analyte in solution ( $A_0$ ) has to be transported to the surface ( $A_s$ ) and then to interact with the recognition element ( $B$ ) to form the adsorbate ( $AB$ ). The equation IV.7 gives the two regimes: (i) transport (driven by the flow rate coefficients  $k_m$  and  $k_{-m}$ ) and (ii) reaction (driven by the rate coefficients  $k_{on}$  and  $k_{off}$ ).



The determination of the binding affinity may lead to error if the mass transport limitation (MTL) is unaccounted. The MTL occurs when the reaction flux is higher than the transport flux and may influence the adsorption mechanisms. In this part, the flow rate will be fixed for the set of experiments in order to avoid the mass transport limitation.<sup>[43]</sup>

The fluidic system is composed of an injection loop with two positions; position 1 “load” where the solution is injected inside the loop and position 2 “injection” where the solution contained in the loop is pushed on the surface of the sample (figure IV-28).

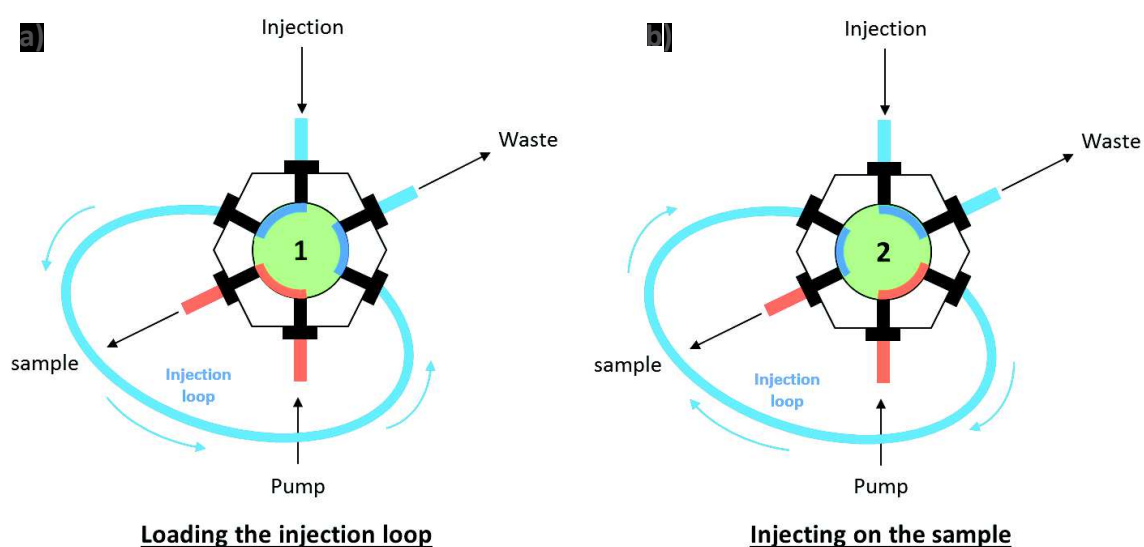


Figure 0-28. Schematic representation of the injection loop with the a) loading and b) injecting position

The degasser is pumping the solution onto the surface of the sample. The flow rate can be tuned to control the speed of the analyte on the surface. The flow rate is an important factor here since it determines the kinetic of the recognition process. It is important to limit the diffusion of the analyte at the surface and in the same time that the analyte have time to bind at the surface. These kinetics of diffusion have been studied and the mechanisms of recognition are dependent of them.<sup>[43]</sup>

- (1) Kinetic measurement and determination of the limit of detection of the Streptavidin

The kinetic measurements are described by the sensorgram which measure the angular position of the resonance peak as function of time. This sensorgram allows observing separately the association, equilibrium and dissociation phases (figure IV-29).

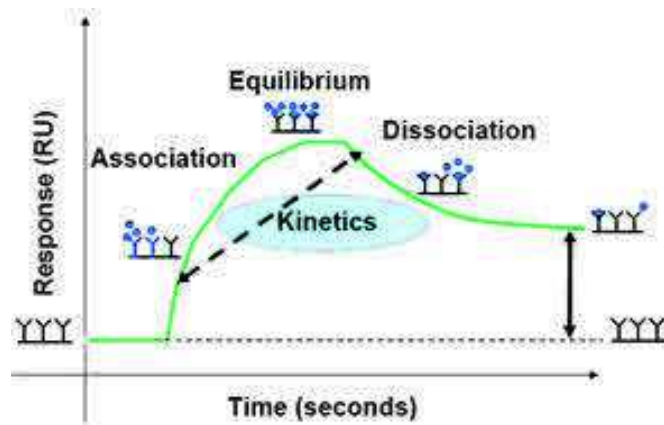


Figure 0-29. Schematic representation of a sensorgram correlated to the different phases. Extracted from [30]

The reaction kinetics was studied onto a thin gold film fully covered by 10 nm iron oxide nanoparticles decorated with biotin groups. The sensorgram was recorded by using a wavelength of 785 nm (figure IV-30).

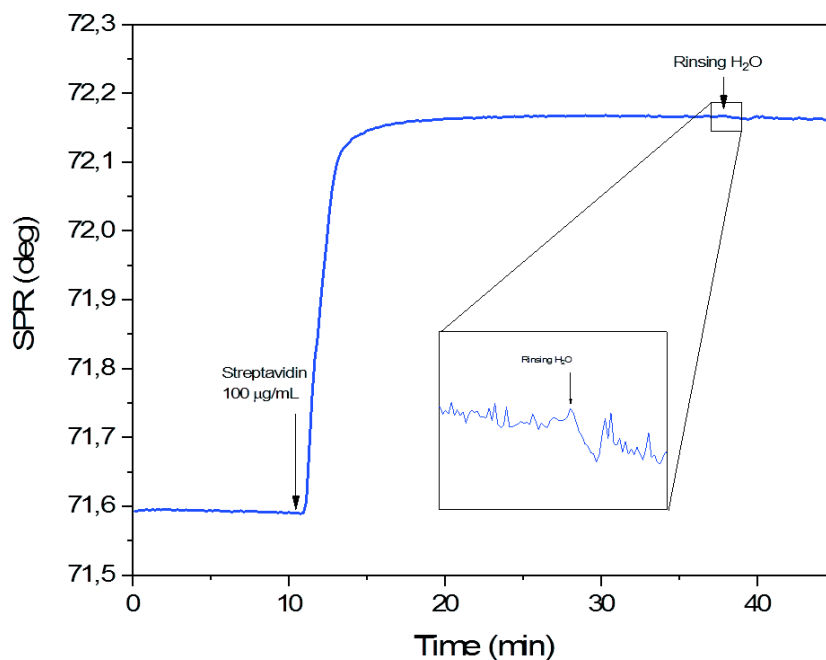


Figure 0-30. Sensorgram of the nanoparticle surface functionalized with biotin recorded after the injection of streptavidin

The injection of streptavidin with a concentration of 100  $\mu\text{g}/\text{mL}$  in pure water shows a strong change of the refractive index. A large shift about  $0.6^\circ$  is reached in less than two minutes meaning a fast adsorption onto the surface. Pure water was injected to remove non-specific adsorbed proteins. The rinsing step affects only slightly the position of resonance peak meaning that the streptavidin is strongly bound to the biotin groups through specific interactions.

The experiment was conducted several times with different concentrations of aqueous solution of streptavidin to investigate the limit of detection of the platform. In parallel, the same experiment was performed with a gold surface directly functionalized with biotin groups (no nanoparticles) in order to determine the influence of the nanoparticle assembly on the kinetics. The figure IV-31 shows the corresponding sensorgrams.

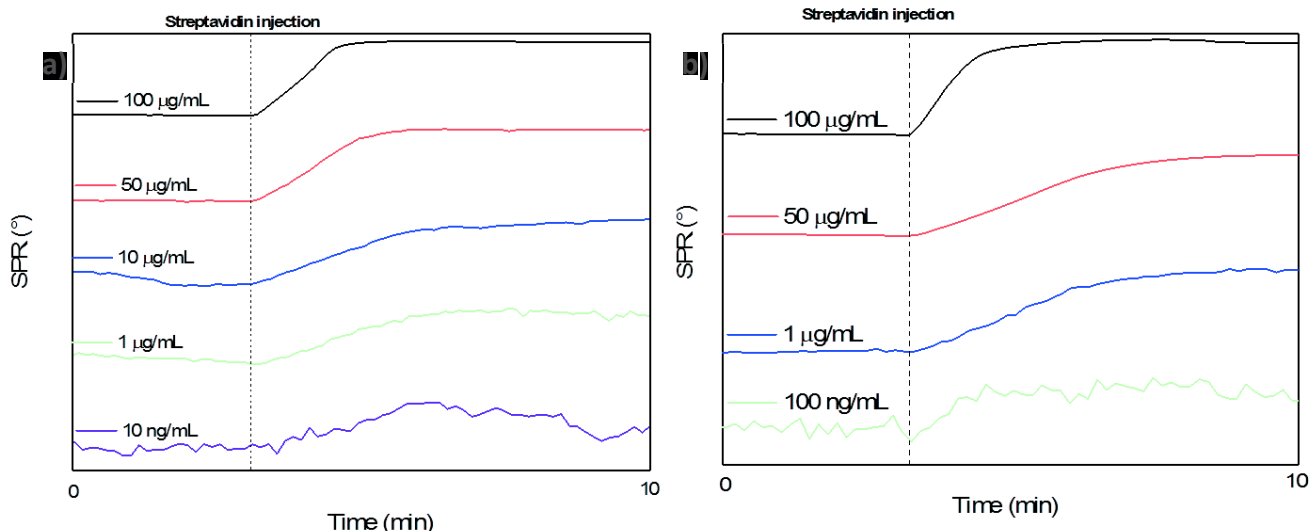


Figure 0-31. Sensorgram measured for different concentrations onto a) nanoparticle assemblies functionalized with biotin and b) a gold thin film directly functionalized with biotin.

All the curves show an increase of the resonance angle followed by a plateau in few minutes after streptavidin injection. The sensorgrams indicate that the shifts of SPR angle decrease with lower streptavidin concentration. The shifts observed for a concentration of 100 µg/mL are coherent with the ones reported on the SPR curves presented in section A.2.a.1 ( $0.589 \pm 0.028^\circ$  and  $0.453 \pm 0.028^\circ$  for surface with and without nanoparticles, respectively). With low concentrations, the shifts decrease until the signal to noise ratio becomes very low which agree with the limit of detection. The sample with the nanoparticle assembly allowed reaching a concentration of 10 ng/mL (189.4 pM) for streptavidin detection, whereas the surface without nanoparticles allowed reaching a concentration of 100 ng/mL (1.89 nM). The nanoparticle assembly seems to improve the LoD which decreases of one magnitude order. Thereafter the limit of detection will be determined more precisely.

Moreover, these typical sensorgrams allow determining the association and dissociation constants and evaluating precisely the limit of detection of the system. For this, two methods are used by fitting calibration curves with the rate and the shifts after injection of the protein.

- (2) Determination of the association constant by the coefficient rate method

An approach to determine the association and dissociation constants is to calculate the rate constants ( $k_{on}$  and  $k_{off}$ ) and therefore determine the affinity constant  $K_A$  defined by equation IV.8:

$$K_A = \frac{1}{K_D} = \frac{k_{on}}{k_{off}} \quad \text{Equation IV.8}$$

These coefficient rate constants can be extracted from a calibration based on the initial reaction rate as function of the concentration. The slope coefficient extracted after each injection of the protein corresponds to the rate constant of the system noted  $k_{obs}$ . The rate being dependent of the concentration of streptavidin in solution, the rate constants were fitted with a linear curve as function of the concentration with a good regression coefficient (0.992). The kinetics analysis allows

determining  $k_{obs}$  which is the rate of the reaction observed and can be defined as function of the concentration by:

$$k_{obs} = k_{on}[C] + k_{off} \quad \text{Equation IV.9}$$

Therefore, a calibration curve was obtained for a fixed flowing rate at 50  $\mu\text{L}/\text{min}$  (figure IV-32).

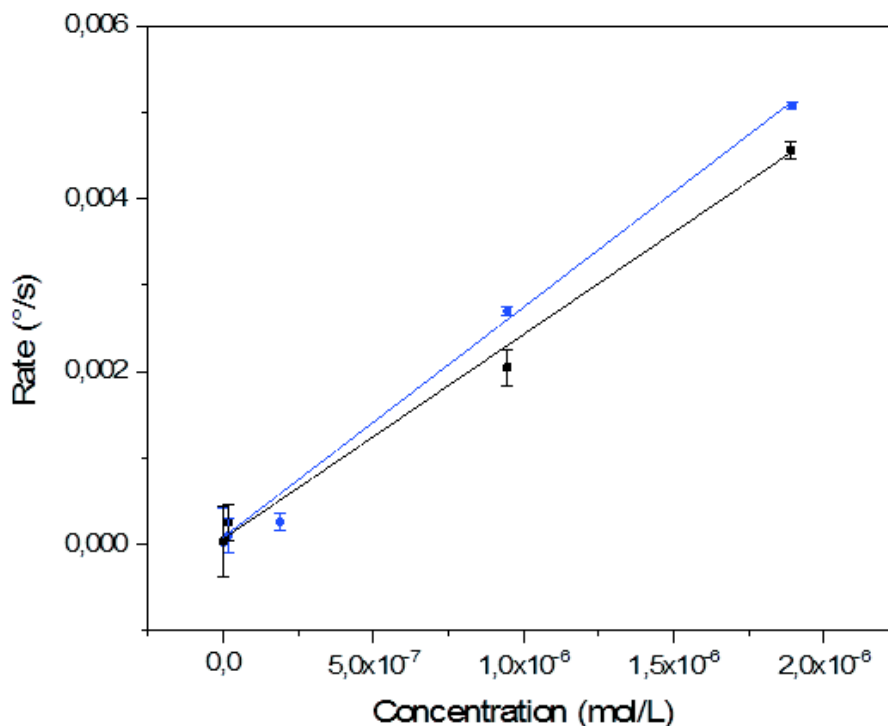


Figure 0-32. Rate coefficient plotted with the analyte concentration onto a surface with (blue curve) and without (black curve) nanoparticles

The slope of the curve corresponds to the rate association coefficient and the intercept corresponds to the rate dissociation constant. They can be determined as function of the concentration of streptavidin. Here, the values of the rate coefficients are summarized in table IV-9.

Table 0-9. Summarize of the association and dissociation rate constants for the biotin/streptavidin couple

	$k_{on}$ ( $^{\circ} \cdot \text{s}^{-1} \cdot \text{M}^{-1}$ )	$k_{off}$ ( $^{\circ} \cdot \text{s}^{-1}$ )	$K_A$ ( $\text{M}^{-1}$ )	$K_D$ ( $\text{M}$ )
With nanoparticles	$(2,663 \pm 0,109) \times 10^3$	$(8,299 \pm 0,157) \times 10^{-5}$	$(3,209 \pm 0,131) \times 10^7$	$(3,116 \pm 0,127) \times 10^{-8}$
Without nanoparticles	$(2,326 \pm 0,131) \times 10^3$	$(6,165 \pm 0,138) \times 10^{-5}$	$(3,773 \pm 0,297) \times 10^7$	$(2,651 \pm 0,209) \times 10^{-8}$

The values of association and dissociation rate constants are similar for the gold films covered with and without nanoparticles. The nanoparticles do not seem to impact significantly the adsorption of streptavidin. The high value of  $k_{on}$  indicates a fast binding reaction whereas the low value of  $k_{off}$  is reliable to a strong stability of the complex. Moreover, the association and dissociation constants are comparable with values found in literature for biotin/streptavidin interaction onto a substrate ( $K_A = 10^6\text{-}10^7 \text{ M}^{-1}$ )<sup>[44-46]</sup>

(3) Determination of the association constant by the Langmuir binding isotherm

Another method can be used to determine the affinity constants, by using the angular shifts measured at different concentrations. The affinity constant of the couple can be determined by the Langmuir binding isotherm which is a non-linear regression defined by equation IV.10:

$$R_{eq} = \frac{[C]}{[C]+K_D} R_{max} \quad \text{Equation IV.10}$$

with  $[C]$  the analyte concentration,  $K_D$  the dissociation constant,  $R_{max}$  the maximum binding capacity of the sensor when all the binding sites are occupied and  $R_{eq}$  the response of the system at the equilibrium. The different concentrations used to determine the calibration curve are used to perform the binding isotherm showed on figure IV-33.

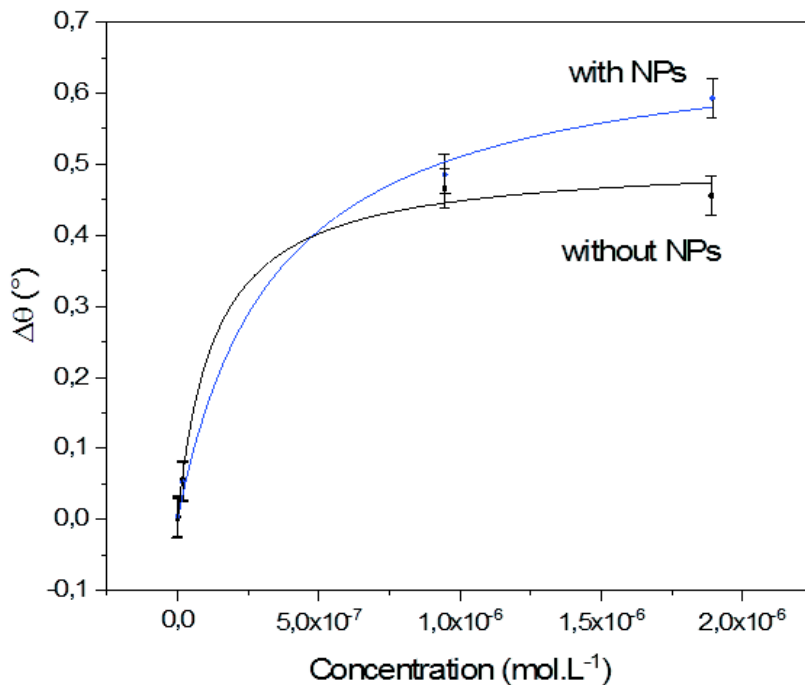


Figure 0-33. Langmuir binding isotherms calculated for a surface with (blue curve) and without (black curve) nanoparticles

The binding isotherm allows determining directly the dissociation constant and the maximum binding capacity of our system. The values of  $R_{max}$  extracted from these curves are different for the samples with and without nanoparticles which was expected from the previous results. The maximum binding capacities for the samples with and without nanoparticles are  $0.685 \pm 0.049^\circ$  and  $0,506 \pm 0,021^\circ$ , respectively. We can observe that the plateau where all the binding sites are occupied is reached faster when there are no nanoparticles at the surface. It can probably be explained by the fact that the streptavidin molecules have more difficulties to reach all the binding sites on a rough surface. The values of  $K_D$  and  $K_A$  determined by the Langmuir binding isotherm model are summarized in table IV-10.

**Table 0-10. Summarize of the value of the rate coefficients and affinity constants for the biotin/streptavidin**

	$K_A$ ( $M^{-1}$ )	$K_D$ ( $M$ )
With nanoparticles	$(2,311 \pm 0,608) \times 10^6$	$(4,327 \pm 1,136) \times 10^{-7}$
Without nanoparticles	$(7,716 \pm 2,417) \times 10^6$	$(1,296 \pm 0,406) \times 10^{-7}$

The values of the affinity constants are in the range of what is found in the literature.<sup>[45, 46]</sup> However, the values calculated with this method differ from the one previously calculated. The determination of  $K_A$  and  $K_D$  by the rate constant method gives affinity constants with an order higher than the one obtained with Langmuir binding isotherm. This behavior has already been observed<sup>[43]</sup> and the reason is linked to the mass transport limitation. Indeed, Schuck and Minton have reported that the MTL influence the  $k_{obs}$  vs  $[C]$  plot. Even with the low flow rate used (50  $\mu$ L/min), the transport flux of the analyte at the surface can influence the binding. Therefore, the Langmuir binding isotherm seems to be the more convincing method.

Moreover, the limit of detection of the system can be extracted from these curves. A linear regression can be performed for low concentrations and give the sensitivity  $k$  of the system ( $k = 1.89 \times 10^6$  and  $k = 2.83 \times 10^6$  for the system with and without nanoparticles respectively). The LoD is defined by the equation IV.11:

$$LoD = \frac{3\sigma}{k} \quad \text{Equation IV.11}$$

with  $\sigma$  the error on the SPR system (0.001°). Thank to this, the LoD for both systems can be determined and are 1.6 nM and 1.1 nM for surface with and without nanoparticles respectively. Finally, the system without nanoparticles presents the lowest LoD.

The SPR technique is a powerful tool to study precisely the effect of nanoparticle assemblies on the kinetics of the recognition process between streptavidine and biotin groups. Several parameters such as association and dissociation constants and limit of detection were calculated. The determination of the affinity constant  $K_A$  and  $K_D$  has been done by the rate coefficient and the Langmuir binding isotherm methods. The rate coefficient method is limited by the transportation of the analyte at the surface. Therefore, the Langmuir binding isotherm is the most accurate technique to determine precisely the association and dissociation constants. The determination of the LoD of the system showed that the nanoparticles do not improve the system.

## 5. Biofouling

The biofouling constitutes a critical point in biosensing. Indeed, the interaction between the molecular receptor and the analyte has to be highly specific in order to avoid non-specific recognition. Therefore, control experiments were performed to study the specificity of our sensing platform. The streptavidin has a strong affinity with most of organic groups. Moreover, hydrophilic groups may favor the physisorption of the streptavidin onto the nanoparticle surface. It can be demonstrated by the injection of streptavidin in the presence of sample which correspond to each step of the sensor construction.

The control experiments were performed by injection of an aqueous solution of streptavidin (100 µg/mL) on the alkyno-terminated gold thin film (SAM-CC), the azido-terminated nanoparticle assembly (NP@N<sub>3</sub>). Finally, a non-recognition protein to the biotin was injected onto a surface of nanoparticles functionalized with biotin groups: the bovin serum albumin (BSA).

The figure IV-34 presents the sensorgrams of the injection of aqueous solution of streptavidin onto the SAM alkyne, the nanoparticle assembly which is not functionalized with biotin groups and injection of aqueous solution BSA onto biotin-terminated nanoparticle assembly.

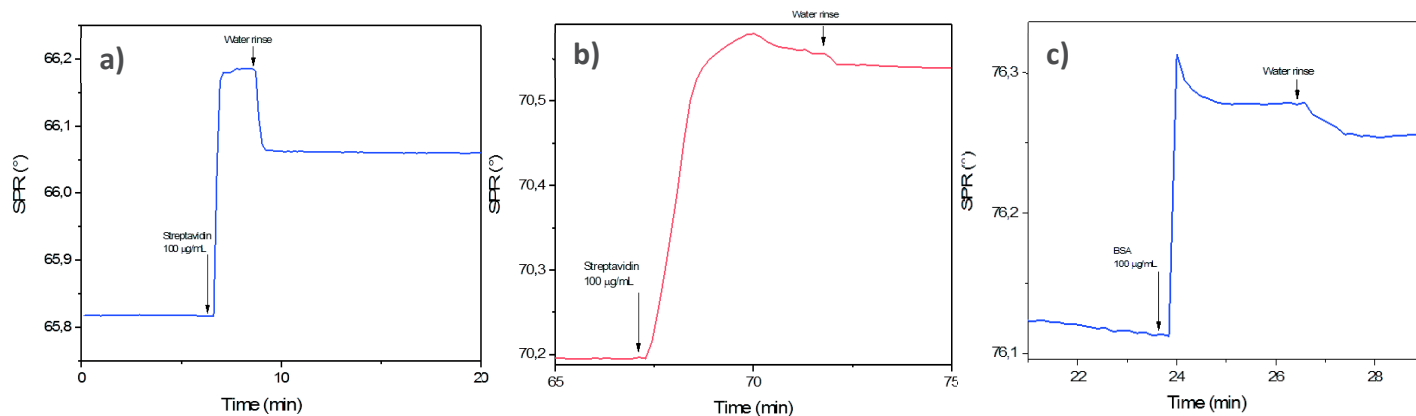


**Figure 0-34. Sensorgrams of the adsorption of streptavidin onto a) SAM-CC and b) nanoparticle assembly and c) adsorption of BSA onto nanoparticle assembly functionalized with biotin**

In the case of the SAM-CC, the adsorption of the streptavidin is shown by the change of the angular peak position demonstrating the adsorption of the protein on the surface. However, the rinsing step showed a partial desorption of the protein which is relevant of non-specific interactions. The streptavidin may probably be physisorbed on the alkyne chains at the surface.

In the case of the azido-terminated nanoparticle assembly, the SPR signal showed an effect of streptavidin injection characterized by the change of the angular peak position. Nevertheless, the increase of the position is followed by a slight diminution which could represent a non-specific recognition at the surface. This recognition is different to the SAM alkyne.

Finally, the adsorption of BSA onto biotin-terminated nanoparticle assembly showed another behavior. A fast increase is observed immediately followed by a rapid decrease.

These control experiments present different values of the rate and the shift after streptavidin or BSA injection. These values are summarized in table IV-11.

**Table 0-11. Summarize of the rate and shift of the control experiments**

	SAM-CC	NP@N <sub>3</sub>	Biotin	BSA
Rate (°/s)	<b>1.09 ± 0.14</b>	<b>0.26 ± 0.01</b>	<b>0.303 ± 0.006</b>	<b>1.24 ± 0.04</b>
Shift (°)	<b>0.247 ± 0.03</b>	<b>0.347 ± 0.03</b>	<b>0.595 ± 0.03</b>	<b>0.166 ± 0.03</b>

The binding rate and shift of the resonance peak values are not corresponding to the adsorption between biotin and streptavidin. The angular shift after injection of the streptavidin is lower on the SAM-CC and on the nanoparticle assembly without grafting of the biotin. Moreover, the rates of the binding are much higher in the case of the SAM-CC and the BSA onto the biotinylated surface. The fast desorption of the streptavidin and the BSA after the rinsing step confirms the non-specific interactions.

## 6. Conclusion

The SPR systems constitute a strong tool to study the mechanisms of molecular recognition. Here, the assembly of nanoparticles has been used as a platform to tune the signal of the surface plasmon. The change of the optical properties allows increasing significantly the sensitivity of the signal. Moreover, the presence of the nanoparticles influenced the surface chemistry and promoted a higher accessibility of the receptor molecules by the analytes which increase more the sensitivity. It has been confirmed by the change of the surface chemistry by varying the number of receptor molecules at the surface and the size and density of nanoparticle assembly. The use of a microfluidic device allowed understanding the mechanisms of detection between the biotin and the streptavidin and identifying the rates of the recognition process. Finally, control experiments have been performed to ensure the specificity of our platform. This specificity was highlighted with the shifts and rates of different binding events.

## E. Iminosugar – Glycosidase

After using the biotin/streptavidin couple as a model system to demonstrate and to optimize our nanostructured SPR platform, we decided to focus on the molecular recognition process between an iminosugar and the  $\alpha$ -Mannosidase (Jack Bean).<sup>10</sup>

### 1. Context and motivation

The interest in glycosidase expands since these enzymes play a key role in many biological processes.<sup>[47]</sup> Indeed, these enzymes are able to cleave the glycosidic bond between two saccharide molecules. The lack or dysfunction of glycosidase is involved in several diseases such as diabetes, Gaucher disease, cancer, cystic fibrosis among others. Therefore, glycosidases inhibitors are used in the treatments of these metabolic disorder and viral infections. Among different classes of glycosidases inhibitors such as disaccharides, carbasugars or thiosugars, iminosugar are very attractive because of their strong inhibition and their better oral bioavailability.<sup>[47]</sup>

Therefore, we can take advantage of such efficient inhibitors for detection of enzymes. On the basis of previous works reported by P. Compain's group we have focused on the interaction between an iminosugar and the  $\alpha$ -Mannosidase which has two recognition sites.<sup>[7-9]</sup> The grafting of the iminosugar onto the surface of the nanoparticle assembly allowed us demonstrating the versatility of our SPR platform as well as studying precisely the recognition mechanisms between the iminosugar and the  $\alpha$ -mannosidase.

### 2. Substrate post functionalization by iminosugar

One more time, we are taking advantage of our SPR bio-platform which consists in a nanoparticle assembly grafted onto a gold substrate and which exhibit azide groups. In a similar way we reported for biotin groups, the azide-terminated nanoparticle assembly was functionalized with an alkyne modified iminosugar (DNJ-Alcyne)<sup>11</sup> by performing the CuAAC reaction. In the light of the previous results obtained with the biotin and streptavidin, 10 nm-sized nanoparticles were used in order to compare the obtained results.

#### a) *Experimental protocol*

A dense monolayer of nanoparticles with a diameter centered at  $10.4 \pm 0.7$  nm ( $5570 \pm 260$  NPs/ $\mu\text{m}^2$ ) was prepared prior to graft the alkynated iminosugar at the surface (figure IV-35). The iminosugar was grafted on the surface of the nanoparticle assembly by performing the CuAAC reaction.

---

<sup>10</sup> Work conducted with P. Compain's group, SYBIO, Strasbourg

<sup>11</sup> The (2R,3R,4R,5S)-2-(hydroxymethyl)-1-(6-(prop-2-yn-1-yloxy)hexyl)piperidine-3,4,5-triol (DNJ Alcyne) iminosugar is provided by the team of P. Compain.

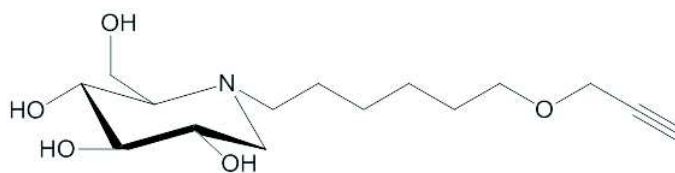


Figure 0-35. Schematic representation of the alkyne-terminated iminosugar

CuAAC “Click” reaction of the alkyne-terminated iminosugar on the surface of NP@N<sub>3</sub> assembly was realized as reported in chapter II. 6,5 mg of CuBr(PPh<sub>3</sub>)<sub>3</sub> and 0,5 mL of Et<sub>3</sub>N were mixed with 5 mL of THF. 10 mg of alkyne-terminated iminosugar were added. The nanoparticle assembly was immersed in the solution and refluxed for 24 h under argon. After the reaction, the substrate was rinsed extensively with THF and exposed for 1 minute to ultrasounds. The substrate was then dried by air stream and stored in a box for further characterizations.

## b) Characterizations

### (1) Scanning electron microscopy

SEM images (figure IV-36) show the surface of the nanoparticle assembly before and after grafting of the alkyne-terminated iminosugar.

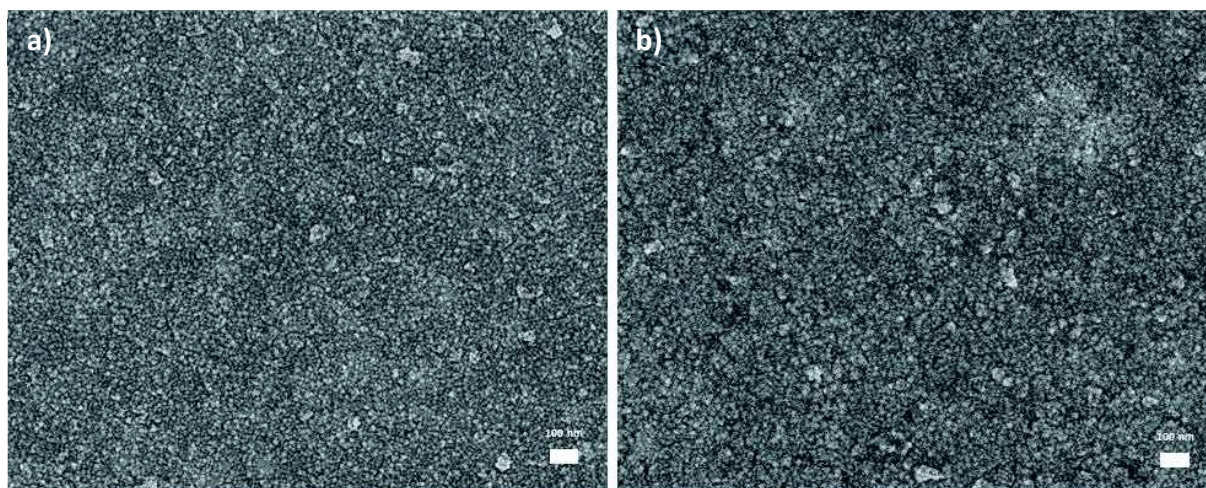


Figure 0-36. SEM images of the nanoparticle assembly (a) before and (b) after grafting of the iminosugar. Magnification X50000

The density of nanoparticles is estimated by counting the nanoparticles on twelve different areas for different samples and averaged at  $5115 \pm 315$  NPs/ $\mu\text{m}^2$  and  $4985 \pm 240$  NPs/ $\mu\text{m}^2$  before and after grafting respectively. As observed for the biotin grafting, a slight decrease of the number of nanoparticles can be noticed. However, both values are very close (below the standard deviation).

## (2) Water contact angle

Water contact angle measurements were performed before and after iminosugar grafting (figure IV-37). The value for the azide terminated nanoparticles is  $99.7 \pm 0.4^\circ$  which is in accordance with the value obtained on previous samples. After iminosugar grafting, the contact angle value decreased significantly ( $52.9 \pm 0.6^\circ$ ) which agrees with a more hydrophilic surface due to the polar groups in the iminosugar.

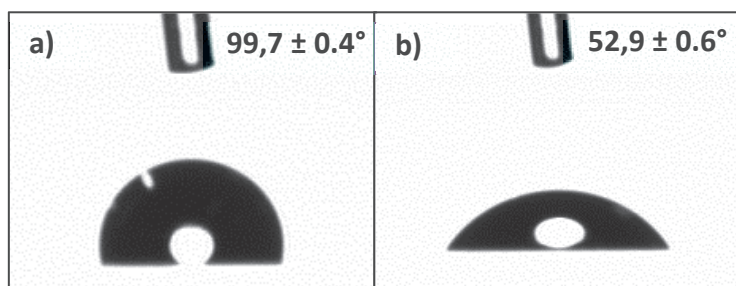


Figure 0-37. Water contact angle measurements of a) NP@N<sub>3</sub> surface and b) iminosugar surface

## (3) XPS

XPS measurements were performed before and after the immobilization of the iminosugar in order to study the grafting of the iminosugar at the surface of the nanoparticle assembly (figure IV-38).

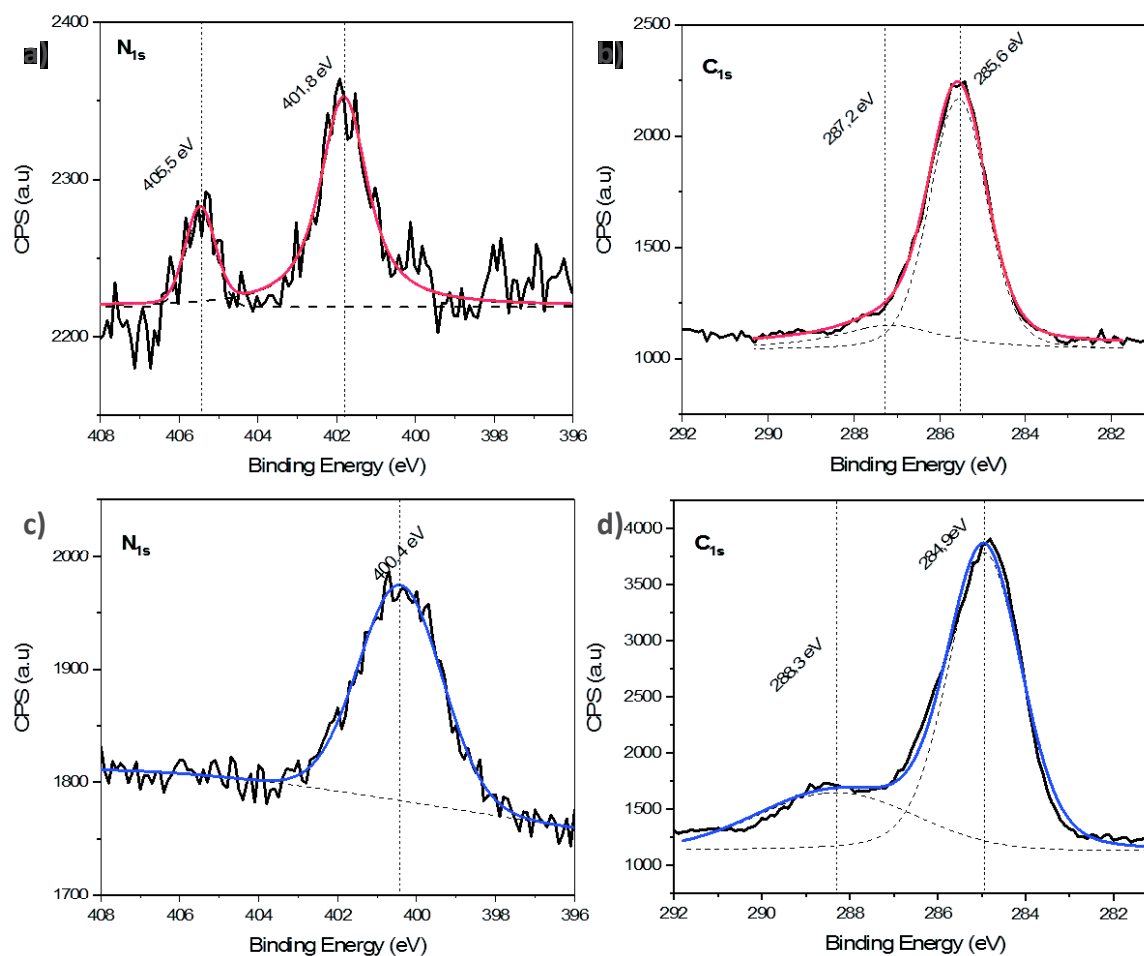


Figure 0-38. XPS measurements of the NP@N<sub>3</sub> surface (a,b) and iminosugar surface (c,d) of the N<sub>1s</sub> (a,c) and C<sub>1s</sub> core (b,d) level.

After the grafting of the iminosugar, the N<sub>1s</sub> core level region shows a single peak centered at 400.4 eV. The absence of peak at 405.5 eV indicates the azide groups are no longer present at the surface meaning a total reaction with the alkyne groups. The peak located at 400.4 eV can be attributed to the triazole bridge formed during the click reaction. The N-C bonds within the iminosugar can also be convoluted in this peak. The C<sub>1s</sub> region show two components located at 284.9 eV and 288.3 eV and can be attributed to C-H and C-C binding and O-C-O binding, respectively.<sup>[48]</sup>

#### (4) PM-IRRAS

PM-IRRAS measurements have also been performed on the surface before and after iminosugar immobilization and showed on figure IV-39. The disappearance of the azide vibrational band at 2100 cm<sup>-1</sup> confirms the absence of azide groups at the nanoparticle surface after the “click” reaction. The apparition of the strong vibrational band of the ether group  $\nu(\text{C-O-C})$  at 1100 cm<sup>-1</sup> present in the iminosugar also, indicates the correct grafting of the receptor at the surface. Moreover, no signal of the alkyne band is observed after the immobilization of the iminosugar meaning a specific grafting through the CuAAC “click” reaction.

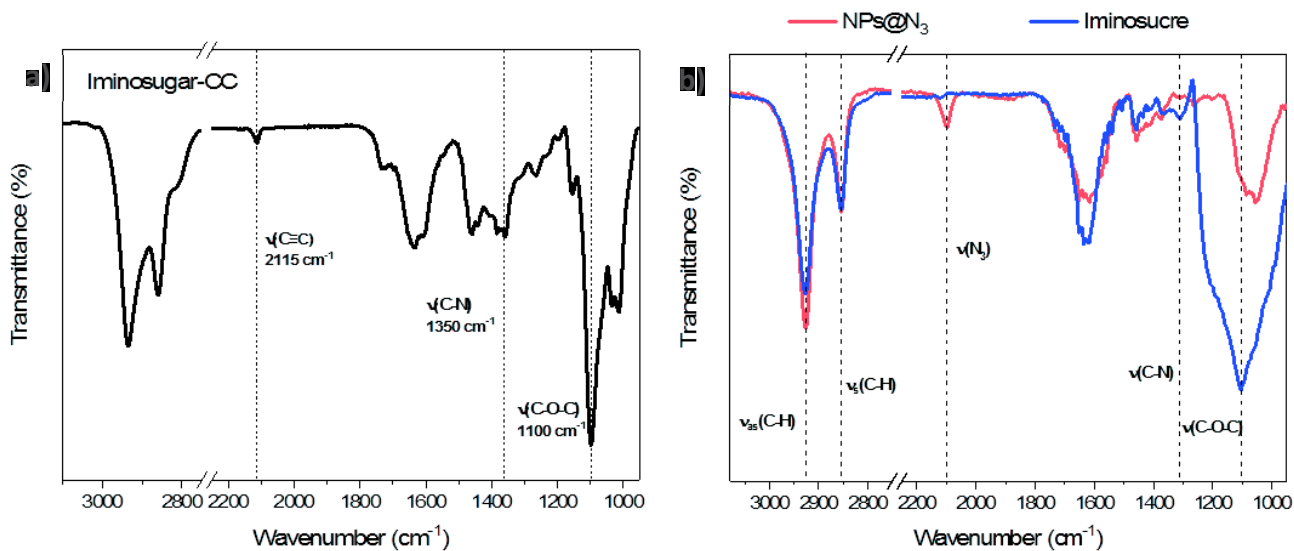


Figure 0-39. a) FT-IR spectrum of the alkynated iminosugar and b) PM-IRRAS spectra of the film of azide terminated nanoparticles (red curve) and after the grafting of iminosugar (blue curve)

(5) Construction of the film followed by Surface Plasmon Resonance Measurements

The different steps of the bio-platform have also been characterized with SPR measurements to monitor the construction of the film. As for the biotin, the film construction includes several steps which increase the refractive index at the surface of the gold thin film:

- Gold naked substrate (Au)
- Gold substrate functionalized with alkyne-SAM (SAM-CC)
- Assembly of nanoparticles functionalized with azide groups onto the SAM (NPs@N<sub>3</sub>)
- Assembly of nanoparticles functionalized with alkynated iminosugar (Iminosugar)

The SPR measurements were performed at a fixed wavelength of 785 nm. The reflectivity as function of the incident angle is shown on figure IV-40 and the values of the resonance angles are summarized in table IV-12.

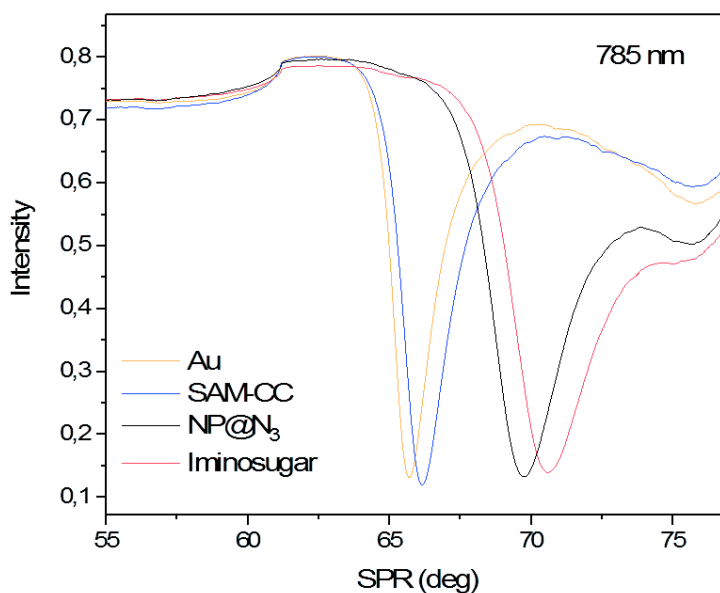


Figure 0-40. SPR reflectivity measurements with angular response at a fixed wavelength of 785 nm

The values measured for the naked gold thin film and the alkyne-terminated SAM are similar from the values obtained previously. The small shift ( $< 0.05^\circ$ ) agrees with the SAM formation. The position of the resonance angle for the assembly of nanoparticles is  $69.764^\circ$  and corresponds to a full monolayer for 10 nm-sized nanoparticles. Surprisingly, the grafting of the iminosugar on the assembly of nanoparticles does not induce a blue shift as observed for the grafting of biotin. The red-shift of about  $0.8^\circ$  may correspond to a more stable assembly with less physisorbed nanoparticles.

Table 0-12. Summarize of the angular peak position for each step of the film construction

Wavelength	Au	SAM	NPs@N <sub>3</sub>	Iminosugar
785 nm	65.698°	66.163°	69.764°	70.596°

To conclude, the different surface characterizations demonstrated the stability and the reproducibility of the grafting of the iminosugar derivative on the surface of nanoparticle assembly. Moreover, the total replacement of the azide groups at the surface by the iminosugar has been highlighted thanks to XPS and PM-IRRAS measurements leading to an available surface for detection of the  $\alpha$ -mannosidase.

### 3. SPR measurements for the glycosidase

#### a) $\alpha$ -Mannosidase solution preparation

In the following measurements,  $\alpha$ -Mannosidase was used from *Canavalia ensiformis* (Jack Bean). The protein is used in a buffer solution for a better stabilization. The buffer solution is sodium acetate at 0.2 M fixed at pH 5 which is optimum for the enzyme stabilization.

The  $\alpha$ -Mannosidase solution was then prepared with different concentrations starting with a 100  $\mu\text{g}/\text{mL}$  solution and then diluted down to 10  $\text{ng}/\text{mL}$ . The error on the measurement increases for each dilution with really small amounts of protein because it can be adsorbed on the laboratory equipment.

### b) SPR measurements

The SPR measurements were performed on the iminosugar functionalized platform before and after the injection of  $\alpha$ -mannosidase at 100  $\mu\text{g}/\text{mL}$  with a flow rate 50  $\mu\text{L}/\text{min}$ . The figure IV-41 shows the measurements performed at 785 nm.

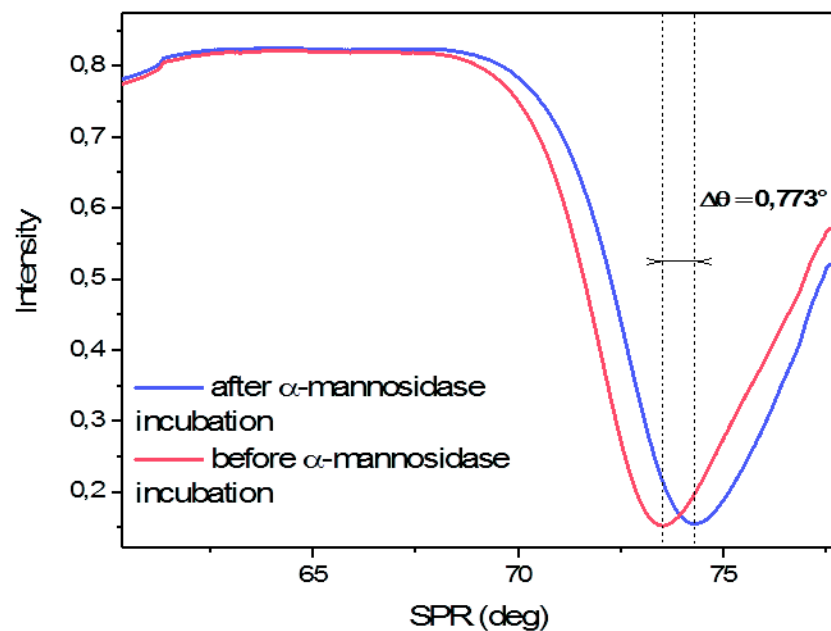


Figure 0-41. SPR measurements performed at 785 nm before (red curve) and after (purple curve) adsorption of  $\alpha$ -mannosidase

A shift of the resonance peak is observed after the injection of the  $\alpha$ -mannosidase which confirms the adsorption of the enzyme and the accessibility of the iminosugar at the surface of the nanoparticle assembly. The immobilization of the  $\alpha$ -mannosidase resulted in an angular shift of  $0.773 \pm 0.002^\circ$ .

The increment refractive index  $\frac{\partial n}{\partial c}$  of the  $\alpha$ -mannosidase has not been calculated. The used of Freiter equation is therefore not possible. However, the mass of the adsorbed enzyme can be estimated with good approximation by using the factor conversion  $0.0001 \approx 0.038 \text{ ng}/\text{cm}^2$  corresponding at the biotin/streptavidin couple. Considering the molecular weight of the  $\alpha$ -mannosidase (MW = 220,000  $\text{g}/\text{mol}$ ), 1.4 enzyme per nanoparticles were estimated. As previously seen with the streptavidin, this value may be overestimate. SEM images reported by Lepage and al. showed that the surface occupied by of  $\alpha$ -mannosidase on cyclopeptides is about  $10 \times 10 \text{ nm}^2$ .<sup>[7]</sup> Moreover, granulometry measurements by DLS have been performed to estimate the radius of the  $\alpha$ -mannosidase in aqueous solution with a concentration of 50  $\mu\text{g}/\text{mL}$  (figure IV-42).

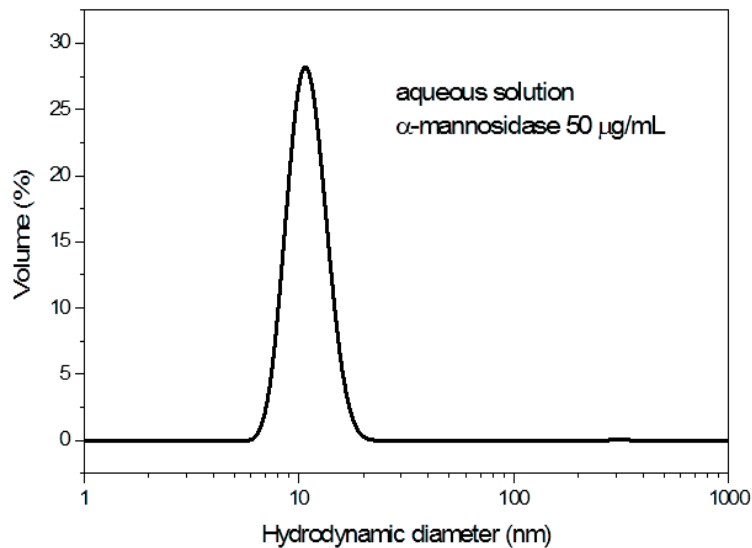


Figure 0-42. Granulometry measurements in volume of the  $\alpha$ -mannosidase in aqueous solution

The size of the enzyme is centered to 10.1 nm which is in accordance with the size shown by SEM analysis. Therefore, the  $\alpha$ -mannosidase can be considered as an enzyme with a gyration radius about 5 nm. Thus, the approximation of the surface occupied by an enzyme is about 78.5 nm<sup>2</sup>. According to our calculation (see part IV.A.4.), for a dense packed assembly of nanoparticles of 10.4 nm, the theoretical maximum coverage is 1.2  $\alpha$ -mannosidase per nanoparticle. Furthermore, the conformation of the enzyme at the surface of the nanoparticle may allow more adsorption, for example the formation of dimers.<sup>[7]</sup> The figure IV-43 gives an example of different configurations of the  $\alpha$ -mannosidase adsorption on the nanoparticle surface.

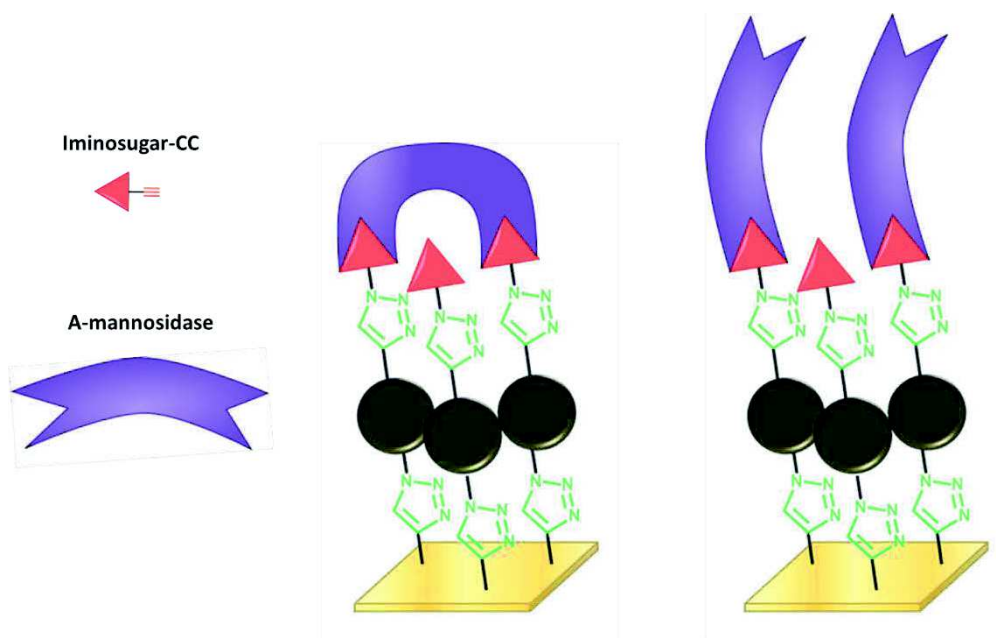


Figure 0-43. Schematic representation of two configuration examples of the  $\alpha$ -mannosidase adsorption at the nanoparticle surface

c) *Kinetics measurements*

(1) Sensorgrams

A sensorgram allows monitoring the adsorption of the analyte to the surface. The sensorgram corresponding to the injection of  $\alpha$ -mannosidase on the iminosugar modified platform is studied and presented on figure IV-44.

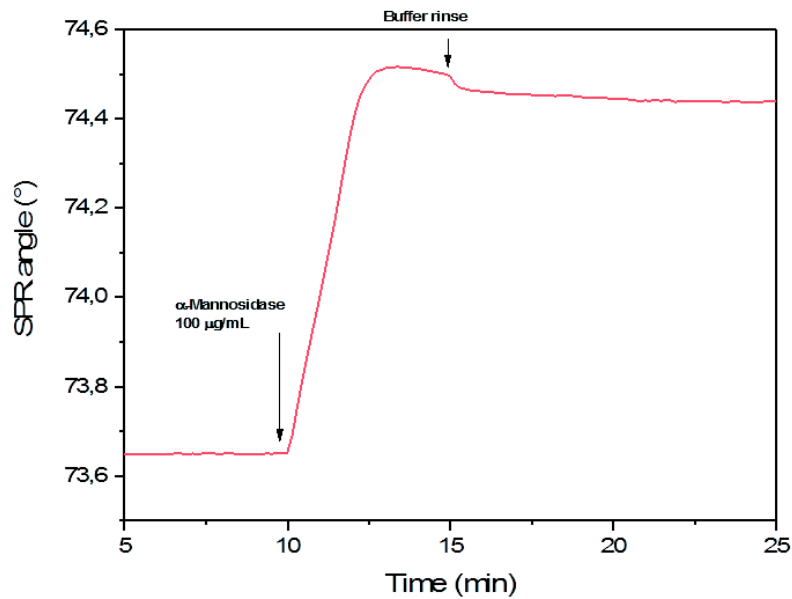


Figure 0-44. Sensorgram of  $\alpha$ -mannosidase adsorbed on the iminosugar modified platform

A significant shift of the resonance angle was immediately observed after the injection of the  $\alpha$ -mannosidase. The shift reached  $0.864^\circ$  and leveled off after 2 minutes meaning a fast adsorption. After rinsing with the buffer solution, a small shift to the lower angle was observed. This behavior can be explained by the non-specific adsorption at the surface, the buffer has the effect to remove these non-specific grafted proteins. This behavior is slightly different from the recognition between biotin and streptavidin and can be relevant of a physisorption of the  $\alpha$ -mannosidase at the surface of the nanoparticle assembly.

In the same way that for the streptavidin, the limit of detection and the affinity constants of the system can be determined by injection of  $\alpha$ -mannosidase solutions with different concentrations (figure IV-45).

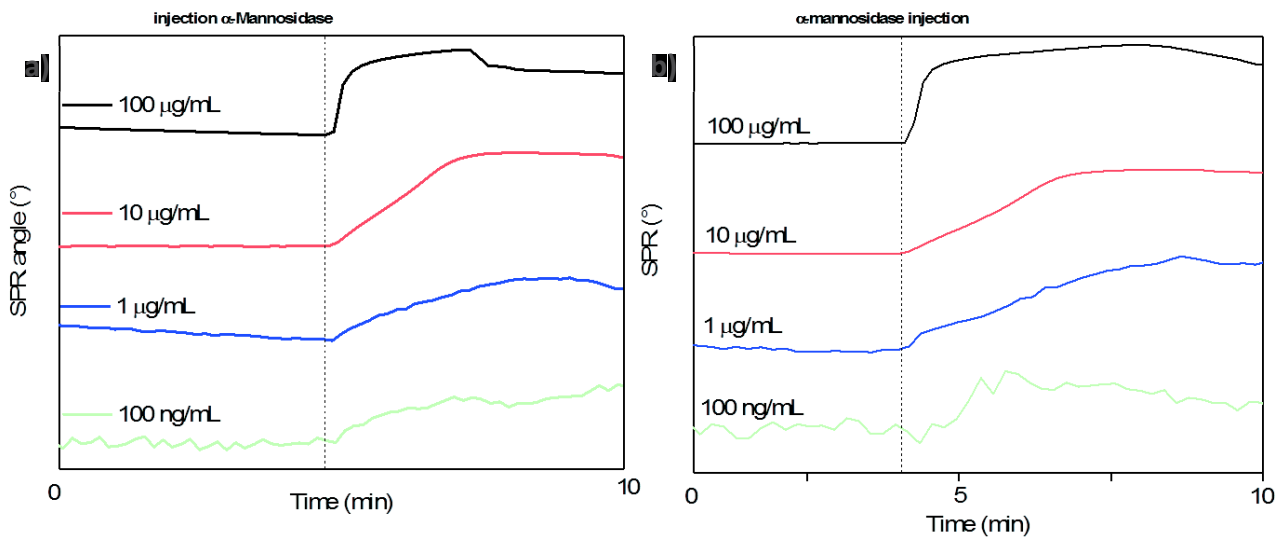


Figure 0-45. Sensorgrams after injection of the  $\alpha$ -mannosidase with different concentrations onto a) nanoparticle assembly functionalized with iminosugars and b) iminosugars directly grafted onto a SAM-CC

The system is responding to the range of concentration from 100  $\mu\text{g/mL}$  down to 100  $\text{ng/mL}$  at which the signal to noise ratio becomes too low. When the nanoparticle assembly functionalized by alkynated iminosugar is subjected to a concentration of  $\alpha$ -mannosidase of 100  $\mu\text{g/mL}$ , a large shift is observed ( $0.925 \pm 0.014^\circ$ ). This shift is in accordance with the previous shift observed and the slight variations observed are caused by the difference in the quantity of nanoparticles at the surface. In the case of the surface without nanoparticles, for the same concentration the angular shift is twice shorter  $0.449 \pm 0.014^\circ$ . Moreover, for each concentration, the angular shifts are lower for the surface without nanoparticles than the film. This behavior is similar to the biotin/streptavidin couple where the sensitivity is higher on the nanoparticle assembly. The angular shifts can be detected down to a concentration of 100  $\text{ng/mL}$  which corresponds to 454  $\text{pM}$  whatever the presence of nanoparticles.

(2) Determination of the rate constant affinity of the iminosugar and  $\alpha$ -mannosidase couple

As seen previously, the binding affinity constant can be calculated by two different methods. The rate of the binding reaction allowed determining the rate constant of the recognition process between the iminosugar and the  $\alpha$ -mannosidase. The slope and angular shift were extracted from sensorgram recorded for each concentration (table IV-13).

Table 0-13. Angular shift and the corresponding measured slope for different concentrations of  $\alpha$ -mannosidase

	With Nanoparticles			Without Nanoparticles		
	Angular shift ( $^\circ$ )	Slope ( $^\circ/\text{min}$ )	Correlation coefficient	Angular shift ( $^\circ$ )	Slope ( $^\circ/\text{min}$ )	Correlation coefficient
100 $\mu\text{g/mL}$	<b>0,9245</b>	<b>3,18</b>	<b>0,9998</b>	<b>0.449</b>	<b>0.74</b>	<b>0.956</b>
10 $\mu\text{g/mL}$	<b>0,7926</b>	<b>0,37</b>	<b>0,9973</b>	<b>0.265</b>	<b>0.079</b>	<b>0.995</b>
1 $\mu\text{g/mL}$	<b>0,0948</b>	<b>0,0117</b>	<b>0,9832</b>	<b>0.0212</b>	<b>0.0048</b>	<b>0.988</b>
0.1 $\mu\text{g/mL}$	<b>0,0122</b>	<b>0,0075</b>	<b>0,9137</b>	<b>0.0032</b>	<b>0.0033</b>	<b>0.874</b>

The figure IV-46 presents the curve of the rate of binding events versus the concentration of the analyte.

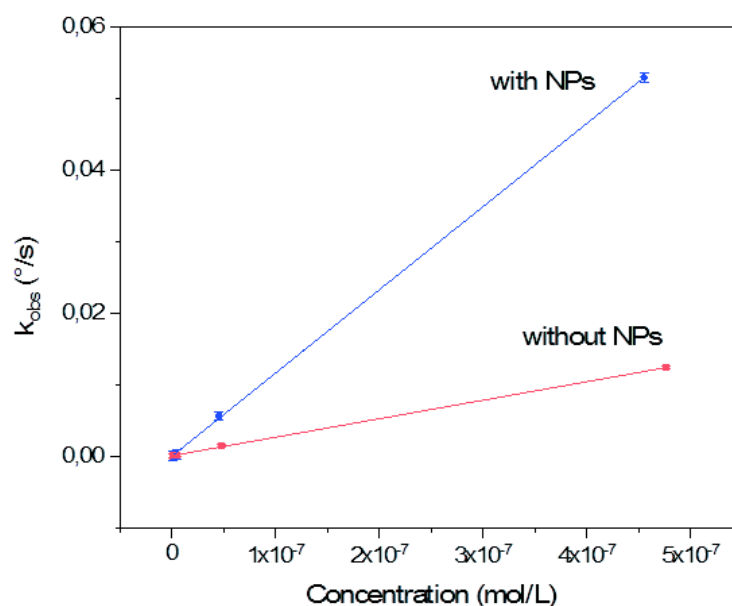


Figure 0-46. Rate coefficient calculated for different concentrations of  $\alpha$ -mannosidase with (blue curve) and without (red curve) nanoparticles

The first observation is a different behavior between the samples with and without nanoparticles. The association rate constant is much higher in the case of the nanoparticle film assembly implying a faster binding reaction than for flat surface. The rate association and dissociation coefficient  $k_{on}$  and  $k_{off}$  were determined by the slope and intercept of the curve and are summarized in table IV-14.

Table 0-14. Summarize of the value of association and dissociation rate constant for the biotin/streptavidin couple

	$k_{on}$ ( $^{\circ}.s^{-1}.M^{-1}$ )	$k_{off}$ ( $^{\circ}.s^{-1}$ )	$K_A$ ( $M^{-1}$ )	$K_D$ ( $M$ )
With nanoparticles	$(1,162 \pm 0,081) \times 10^5$	$(1,788 \pm 0,198) \times 10^{-5}$	$(6,499 \pm 1,173) \times 10^9$	$(1,549 \pm 0,278) \times 10^{-10}$
Without nanoparticles	$(2,586 \pm 0,042) \times 10^4$	$(8,681 \pm 3,962) \times 10^{-5}$	$(2,979 \pm 1,407) \times 10^8$	$(3,357 \pm 1,586) \times 10^{-9}$

The affinity constants determined here are different for the sample with and without nanoparticles. The highest association constant and lowest dissociation constant for the sample with nanoparticles show a higher affinity and stability of the iminosugar with the  $\alpha$ -mannosidase. In contrary to the biotin/streptavidin couple, the nanoparticle assembly here seems having an effect of the association of the enzyme. The important size and steric hindrance generated by the enzyme may be responsible of the difference between a flat surface and a rough surface.

In another hand, the measure of the shift at the equilibrium versus the concentration of the analyte (Langmuir binding isotherm) allows the determination of the dissociation constant and the limit of detection of the system (figure IV-47).

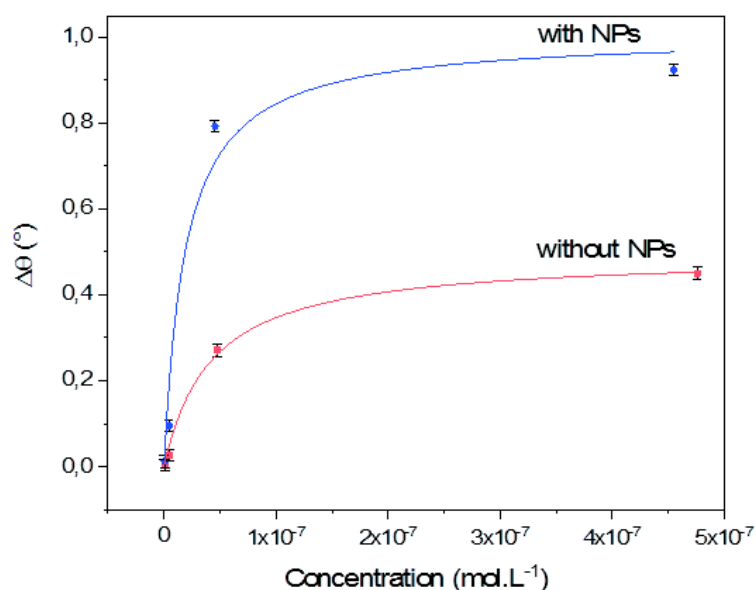


Figure 0-47. Langmuir binding isotherm calculated for a surface with nanoparticles (blue curve) and without (red curve)

The binding isotherm allows determining directly the dissociation constant and the maximum binding capacity of our system. The values of  $R_{max}$  extracted from these curves are  $1.006 \pm 0.108^\circ$  and  $0.493 \pm 0.024^\circ$  for samples with and without nanoparticles, respectively. Here, the nanoparticle assembly results in an increase about twice the maximum binding capacity. This means a more favorable surface for adsorption of the enzyme. The values of  $K_D$  and  $K_A$  determined by the Langmuir binding isotherm model and from the  $k_{on}$  and  $k_{off}$  values are summarized in table IV-15.

Table 0-15. Summarize of the affinity and rate constants

	$K_A$ ( $M^{-1}$ )	$K_D$ ( $M$ )
With nanoparticles	$(5.26 \pm 2.60) \cdot 10^7$	$(1.90 \pm 0.94) \cdot 10^{-8}$
Without nanoparticles	$(2,37 \pm 0.46) \times 10^7$	$(4,21 \pm 0,79) \times 10^{-8}$

The values of the  $K_D$  and  $K_a$  determined by the rate curves differ from the ones determined with the binding isotherm. As discussed previously, the rate constant method is very sensitive to MTL limitation and therefore can induce a difference of about one order of magnitude for the affinity constants.<sup>[47]</sup> The Langmuir binding isotherm gives us  $K_D$  values of  $1.90 \times 10^{-8}$  mol/L and  $4.21 \times 10^{-8}$  mol/L. These values can be compared to the values of systems using the same couple in solution  $K_D = 1.0 - 33.0 \cdot 10^{-7}$  mol/L.<sup>[8]</sup> The major difference is the immobilization on the surface of the iminosugar in our system which can modify the stability of the complex. Therefore, the inhibition of the iminosugar is stronger when it is located onto a substrate than in solution.

The LoD for both systems can also be determined and are 1.2 nM and 4.6 nM for surfaces with and without nanoparticles, respectively. Comparable values are obtained whatever the presence of nanoparticles. In contrary, to the biotin/streptavidin couple, the system with nanoparticles has a better LoD.

#### d) Competitive association

The injection of a competitive substrate in solution will allow understanding the interaction between  $\alpha$ -mannosidase and the inhibiting agent. Therefore, the adsorption of  $\alpha$ -mannosidase is followed by the injection of an aqueous solution of methyl  $\alpha$ -D-mannopyranoside at 10 mM.<sup>[49, 50]</sup> The injection of the competitive substrate to iminosugar is followed by a rinsing step with pure water. The figure IV-48 presents the sensorgram of the experiment.

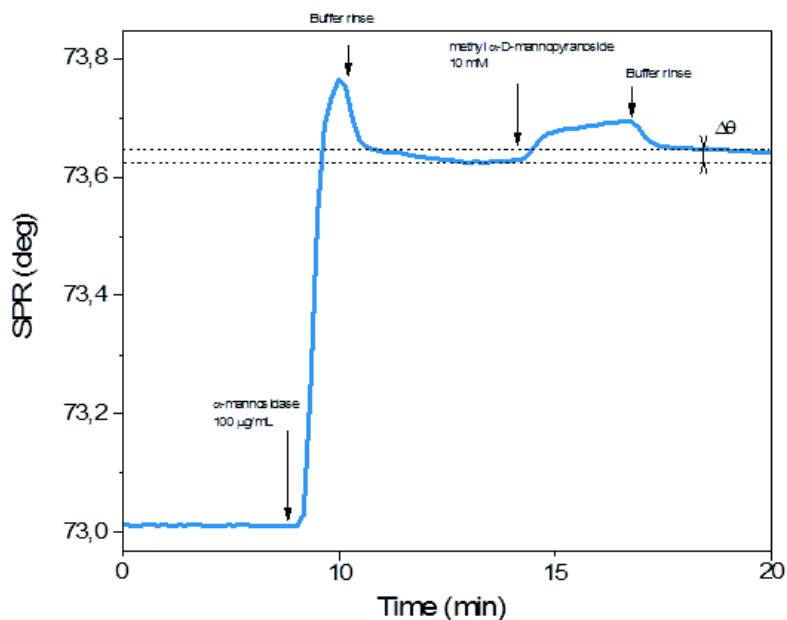


Figure 0-48. Sensorgram after the injection  $\alpha$ -mannosidase and methyl  $\alpha$ -D-mannopyranoside

The injection of methyl  $\alpha$ -D-mannopyranoside at 10 mM with a flow rate of 50  $\mu$ L/min on the surface covered with  $\alpha$ -mannosidase showed a change of the angular position. However, the rinsing step decreases the angular position of the resonance peak. Few conclusions can be deduced from this observation: first, the methyl  $\alpha$ -D-mannopyranoside does not remove the enzyme from the surface by replacing the iminosugar. Indeed, the constant association between the iminosugar and the enzyme seems larger than with this substrate. Second, the rinsing step removed most of the  $\alpha$ -mannopyranoside from the surface. However, a slight difference is observed after the injection of the substrate (about 0.023°) meaning an immobilization of the substrate. Indeed, the molecular recognition of  $\alpha$ -mannosidase may happen from two specific sites. This information indicates that both sites are not necessarily involved in the interaction with iminosugar. Therefore,  $\alpha$ -mannosidase may be adsorbed at the surface of nanoparticle assembly through only one binding site (figure IV-49).

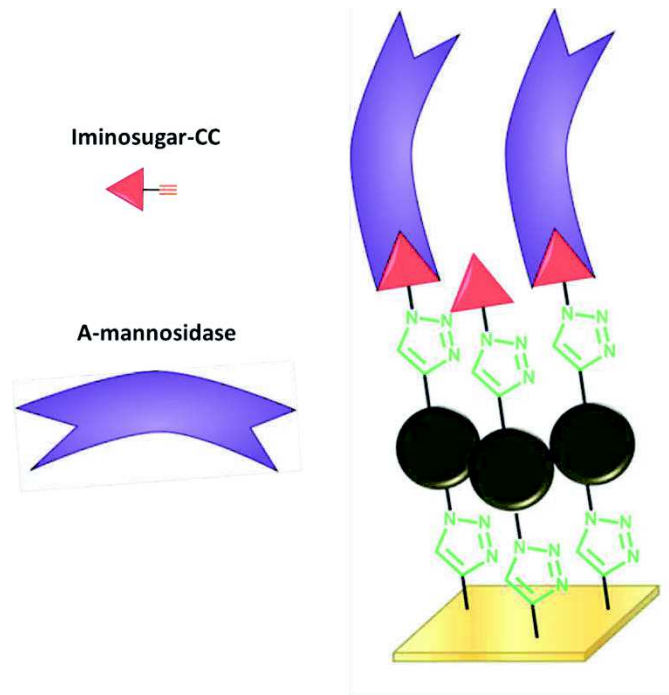


Figure 0-49. Schematic representation of the most favorable configuration of the  $\alpha$ -mannosidase adsorption at the nanoparticle surface

#### e) *Regeneration of the surface*

One of the current challenges on biosensing is the possibility to regenerate sensing surfaces in order to develop reusable devices. The regeneration of the sensors requires the desorption of the enzyme. Some studies showed the use of acidic medium to break bonds between enzyme and sugar.<sup>[33]</sup> Here, we used a solution of phosphoric acid at 0.02 M and pH 2.5 which are subsequently injected after the  $\alpha$ -mannosidase injection onto a SAM functionalized with iminosugar. A second injection of  $\alpha$ -mannosidase was performed thereafter to see the correct binding. These experiments were conducted first in the absence of nanoparticles, the iminosugar was directly grafted on the alkyne-terminated gold thin film (figure IV-50).

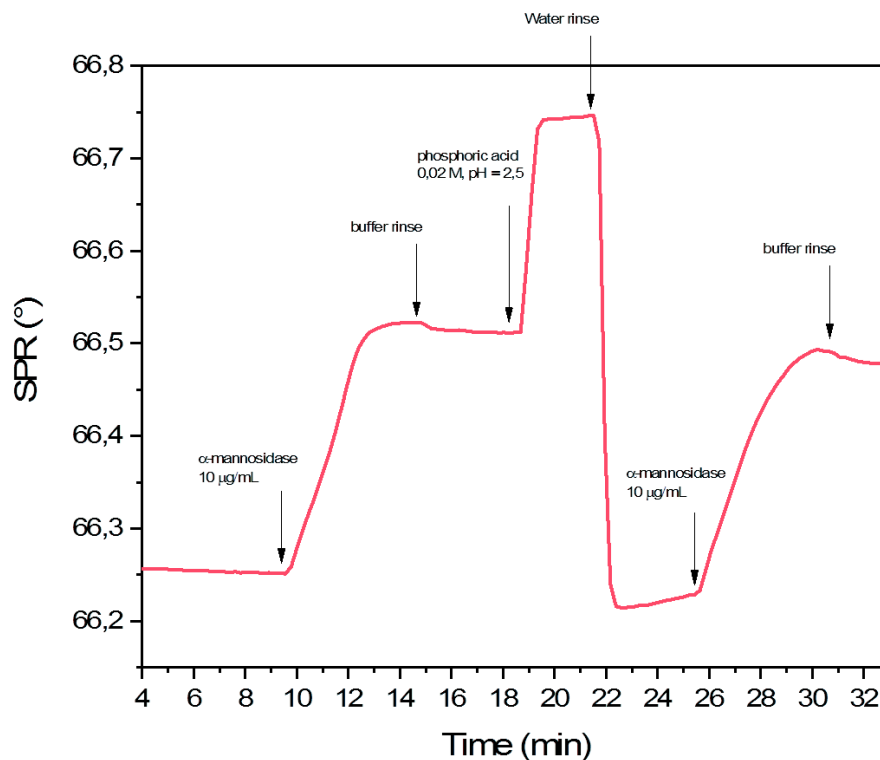


Figure 0-50. Sensorgram after  $\alpha$ -mannosidase injection and regeneration with phosphoric acid onto SAM functionalized with iminosugar

The first injection of  $\alpha$ -mannosidase at 10  $\mu$ g/mL with a 50  $\mu$ L/min flow led to a shift of 0.271° as expected for this concentration. After the rinsing step with the buffer, the phosphoric acid solution was injected. The injection was immediately followed by a strong and fast angular shift. This shift is observed because of the change of refractive index of the solution of acid phosphoric ( $n = 1.341 \pm 0.001$ ). After rinsing with pure water, the resonance angle dropped fast to the initial value before enzyme injection meaning a successful desorption of the glycosidase. A second injection was performed in order to control the non-destruction of the iminosugar surface. The second angular shift observed was about 0.265° which is quite close from the first one. Moreover, the binding rates were calculated and were 0.091°/min and 0.081°/min for the first and second injections, respectively. These results show the possibility to regenerate the surface. Nevertheless, some complementary characterizations are required to control the presence of iminosugar at the surface after the acid injection.

The same experiment was performed onto a gold thin film covered with nanoparticles and the sensorgram is presented in figure IV-51.

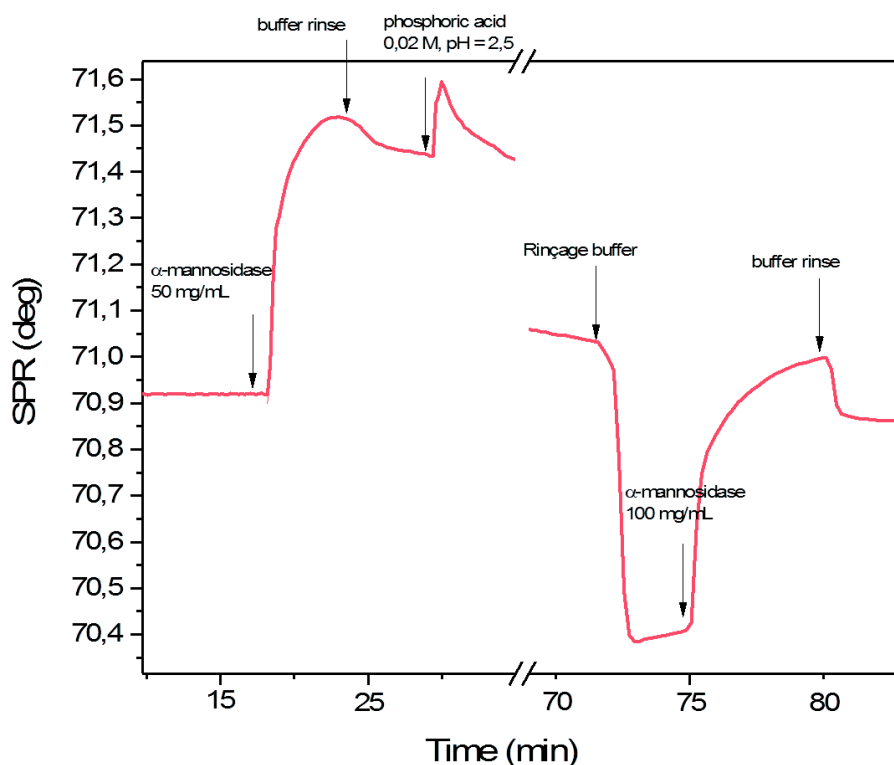


Figure 0-51. Sensorgram after  $\alpha$ -mannosidase injection and regeneration with phosphoric acid onto nanoparticle assembly functionalized with iminosugar

Here the sensorgram shows that after the injection with phosphonic acid the value of the resonance angle drops below its initial value. Although SEM images show that nanoparticles are still present at the surface, such a decrease of the SPR angle may be ascribed to the partial dissolution of iron oxide nanoparticle in solution with low pH (< 5).

Nevertheless, the second injection of  $\alpha$ -mannosidase resulted in the similar angular shift to the first injection of enzyme. It may correspond to non-specific interactions at the surface of iron oxide nanoparticles. Some additional experiments (use of pH > 5) and characterizations (XPS, PM-IRRAS, AFM) are required to study the way the phosphoric acid affects the iron oxide nanoparticles and the organic layer at their surface. Nevertheless, the study in the absence of nanoparticles showed that phosphoric acid is very promising in the development of reusable sensors.

#### 4. Biofouling

The specific recognition between the receptor molecule and the analyte is a key parameter as we saw previously. Different control experiments have been performed in order to testify the specificity of the recognition.

##### a) Control experiment: $\alpha$ -mannosidase on NPs@N<sub>3</sub> surface

The injection of  $\alpha$ -mannosidase in a buffer solution of sodium acetate at 100  $\mu\text{g}/\text{mL}$  was first performed onto a nanoparticle assembly without functionalization with iminosugar. The azide surface should not be specific for the enzyme recognition. The sensorgram was performed and presented on figure IV-52.

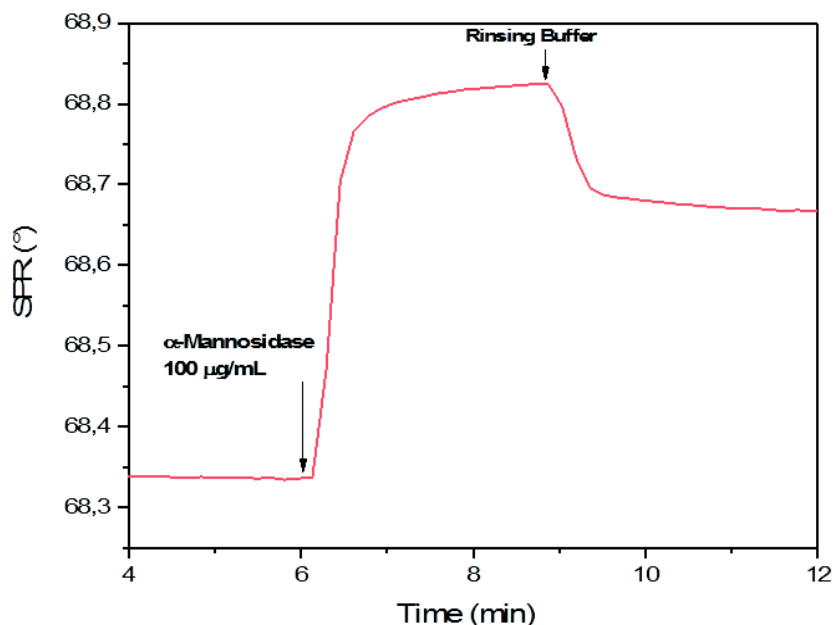


Figure 0-52. Sensorgram after the injection of  $\alpha$ -mannosidase onto nanoparticle assembly surface

The shift of the resonance angle ( $\Delta\theta_{\text{NP@N}_3} = 0.487^{\circ}$ ) shows the adsorption of  $\alpha$ -mannosidase. After the rinsing step, the desorption of species can be observed by the change of the resonance angle. As observed for the streptavidin, the  $\alpha$ -mannosidase was immobilized on the surface of azide terminated nanoparticles. Nevertheless, the kinetics of the reaction is different from that in the presence of iminosugars. Indeed, the shift of the resonance angle is twice lower ( $\Delta\theta_{\text{NP@N}_3} = 0.487^{\circ}$  and  $\Delta\theta_{\text{iminosugar}} = 0.924^{\circ}$ ) for injections at the same concentration. The same difference is observed for the rate of the reaction with  $k_{on}$  values of  $1.13^{\circ}/\text{min}$  and  $3.03^{\circ}/\text{min}$  for the surface without and with iminosugar respectively. Therefore, the interaction between  $\alpha$ -mannosidase and an azido terminated surface is not specific.

#### b) *Control experiment: BSA on iminosugar surface*

The injection of BSA onto a nanoparticle assembly functionalized by iminosugars has been performed in order to control the specificity of the recognition. An aqueous solution of BSA at 1  $\text{mg}/\text{mL}$  was injected with a flow rate of 50  $\mu\text{L}/\text{min}$  and the sensorgram is presented on figure IV-53.

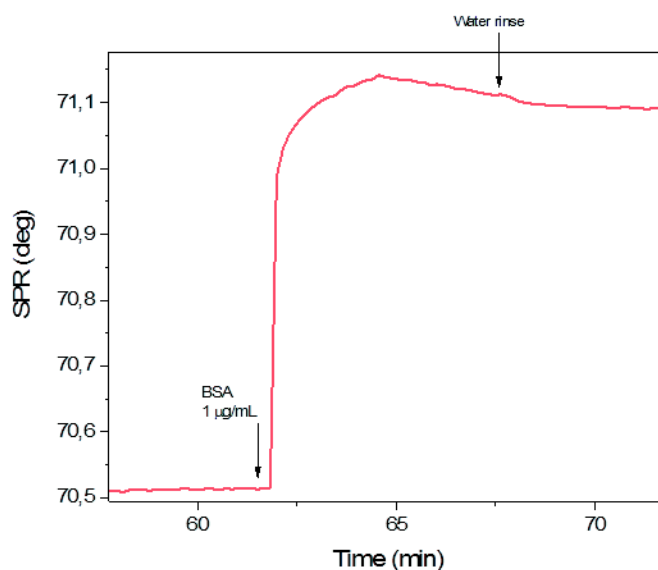


Figure 0-53. Sensorgram of the injection of BSA onto NP@N<sub>3</sub> surface functionalized with iminosugar

The injection of BSA was noticed by an angular shift of 0.624° and a rate of 1.59°/min which are also different from the α-mannosidase onto the same surface.

The biofouling is highlighted by different rates and shifts which allow the control of non-specific recognition (table IV-16).

Table 0-16. Summarize of the rate and shift of the control experiment

	NP@N <sub>3</sub>	Iminosugar	BSA
Rate (°/s)	<b>1.13 ± 0.02</b>	<b>3.03 ± 0.01</b>	<b>1.59 ± 0.04</b>
Shift (°)	<b>0.487 ± 0.002</b>	<b>0.864 ± 0.002</b>	<b>0.6264 ± 0.002</b>

As observed for the biotin/streptavidin, the angular shift and rate after α-mannosidase injection are lower in the case of the azide-terminated nanoparticle assembly. The same behavior is observed for the adsorption of BSA onto iminosugar-terminated nanoparticle assembly even if, in this case, the shift and rate are slightly higher.

## 5. Conclusion

The SPR allowed understanding the mechanism of recognition of the couple between α-mannosidase and one of its natural inhibitor iminosugar. The use of our bio-platform showed that in contrary to the biotin/streptavidin couple, the nanoparticles have an influence on the binding of the enzyme. Moreover, the interaction between the iminosugar and the enzyme seems to be stronger when the inhibitor is immobilized onto a substrate than in solution. This result has been highlighted with the comparison with similar system in solution.<sup>[7-9]</sup>

Experiment with a competitive substrate gave us indications on the configuration of the binding of the α-mannosidase. Moreover, preliminary experiment on the regeneration of the surface showed that the system is promising and require more optimization and supplementary characterizations.

## F. General conclusion

The assembly of nanoparticles allowed designing a bio-platform with post-functionalization of receptor molecules. The different surface characterizations permitted to confirm the grafting of biotin and iminosugar.

The SPR measurements allowed monitoring the detection of streptavidin. Moreover, the use of this couple allowed investigating the sensitivity of our bio-platform and studying the recognition mechanisms. The comparison between gold films covered with and without nanoparticles has shown the enhancement of the sensitivity of the sensors. The use of different configurations permitted to understand the origin of this enhancement. The control of the structuration of assemblies of iron oxide nanoparticles allowed tuning the plasmonic resonance of gold substrates to enhance the sensitivity factor. Moreover, the accessibility of functional groups at their surface increased in comparison with flat surface to permit adsorbing a larger quantity of analyte.

The kinetic measurements in real-time allowed determining the affinity constants between biotin and streptavidin. This kinetic study was also studied for the coupling between an enzyme, the  $\alpha$ -mannosidase, and iminosugar, one of its natural inhibitors. The recognition process monitored by SPR showed that the affinity constants when the inhibitor is immobilized on a substrate are larger than in solution.

## H. Bibliography

- [1] Teramura, Y.; Arima, Y.; Iwata, H., *Analytical biochemistry*, (2006) **357**, 208.
- [2] Pichon, B. P.; Barbillon, G.; Marie, P.; Pauly, M.; Begin-Colin, S., *Nanoscale*, (2011) **3**, 4696.
- [3] L. Hausling and H. Ringsdorf, F.-J. S. a. W. K., *Langmuir*, (1991),
- [4] J. Spinke, M. L., H.-J. Guder, L. Angermaier and W. Knoll, *Langmuir*, (1993),
- [5] Rempel, B. P.; Withers, S. G., *Glycobiology*, (2008) **18**, 570.
- [6] Borges de Melo, E.; da Silveira Gomes, A.; Carvalho, I., *Tetrahedron*, (2006) **62**, 10277.
- [7] Lepage, M. L.; Schneider, J. P.; Bodlenner, A.; Meli, A.; De Riccardis, F.; Schmitt, M.; Tarnus, C.; Nguyen-Huynh, N. T.; Francois, Y. N.; Leize-Wagner, E.; Birck, C.; Cousido-Siah, A.; Podjarny, A.; Izzo, I.; Compain, P., *Chemistry*, (2016) **22**, 5151.
- [8] Decroocq, C.; Joosten, A.; Sergent, R.; Mena Barragan, T.; Ortiz Mellet, C.; Compain, P., *Chembiochem : a European journal of chemical biology*, (2013) **14**, 2038.
- [9] Bonduelle, C.; Huang, J.; Mena-Barragan, T.; Ortiz Mellet, C.; Decroocq, C.; Etame, E.; Heise, A.; Compain, P.; Lecommandoux, S., *Chem Commun (Camb)*, (2014) **50**, 3350.
- [10] Gouget-Laemmel, A. C.; Yang, J.; Lodhi, M. A.; Siriwardena, A.; Aureau, D.; Boukherroub, R.; Chazalviel, J. N.; Ozanam, F.; Szunerits, S., *The Journal of Physical Chemistry C*, (2013) **117**, 368.
- [11] Spinke, J.; Liley, M.; Schmitt, F. J.; Guder, H. J.; Angermaier, L.; Knoll, W., *The Journal of Chemical Physics*, (1993) **99**, 7012.
- [12] Victor H. Perez-Luna, M. J. O. B., Kimberly A. Opperman, Philip D. Hampton, Gabriel P. Lopez, Lisa A. Klumb, and Patrick S. Stayton, *JACS*, (1999),
- [13] Marinakos, S. M.; Chen, S.; Chilkoti, A., *Anal Chem*, (2007) **79**, 5278.
- [14] Nath, N.; Chilkoti, A., *Anal Chem*, (2002) **74**, 504.
- [15] D'Agata, R.; Palladino, P.; Spoto, G., *Beilstein journal of nanotechnology*, (2017) **8**, 1.
- [16] Rios, F.; Smirnov, S., *ACS applied materials & interfaces*, (2009) **1**, 768.
- [17] Williams, E. H.; Davydov, A. V.; Motayed, A.; Sundaresan, S. G.; Bocchini, P.; Richter, L. J.; Stan, G.; Steffens, K.; Zangmeister, R.; Schreifels, J. A.; Rao, M. V., *Applied Surface Science*, (2012) **258**, 6056.
- [18] James P. Collman, N. K. D., Todd P. A. Eberspacher, and Christopher E. D. Chidsey, *Langmuir*, (2006) **22**, 2457.
- [19] Claire-Marie Pradier, M. S., Liu Zheng, Gerard Jaouen, *Surface Science* (2002) **502**, 193.
- [20] Liu, Y.; RamaRao, N.; Miller, T.; Hadjipanayis, G.; Teplyakov, A. V., *The Journal of Physical Chemistry C*, (2013) **117**, 19974.
- [21] Gao, S.; Koshizaki, N.; Tokuhisa, H.; Koyama, E.; Sasaki, T.; Kim, J.-K.; Ryu, J.; Kim, D.-S.; Shimizu, Y., *Advanced Functional Materials*, (2010) **20**, 78.
- [22] Lapin, N. A.; Chabal, Y. J., *The journal of physical chemistry. B*, (2009) **113**, 8776.
- [23] A. Lahav, M. A., I. Abdulhalim, *Optics Letters*, (2008) **33**, 2539.
- [24] Christy, P. B. J. a. R. W., *Phys. Rev. B*, (1972) **6**, 4370.
- [25] B. Liedberg, I. L., *Sensors and Actuators B: Chemical*, (1993) **11**, 63.
- [26] B. P. Pichon, A. D., M. Pauly, K. Mouglin, A. Derory, S. Bégin-Colin, *J Phys Chem C*, (2010) **114**, 9041.
- [27] S. Szunerits, R. B., *Langmuir*, (2006) **22**, 1660.
- [28] Wijaya, E.; Lenaerts, C.; Maricot, S.; Hastanin, J.; Habraken, S.; Vilcot, J.-P.; Boukherroub, R.; Szunerits, S., *Current Opinion in Solid State and Materials Science*, (2011) **15**, 208.
- [29] Linda S. Jung, C. T. C., Timothy M. Chinowsky, Mimi N. Mar, and Sinclair S. Yee, *Langmuir*, (1998) **14**, 5636.
- [30] Shalabney, A.; Abdulhalim, I., *Laser & Photonics Reviews*, (2011) **5**, 571.
- [31] Szunerits, S.; Boukherroub, R., *Chem Commun (Camb)*, (2012) **48**, 8999.
- [32] Szunerits, S.; Shalabney, A.; Boukherroub, R.; Abdulhalim, I., *Reviews in Analytical Chemistry*, (2012) **31**,

- [33] Maalouli, N.; Barras, A.; Siriwardena, A.; Bouazaoui, M.; Boukherroub, R.; Szunerits, S., *The Analyst*, (2013) **138**, 805.
- [34] R. Reiter, H. M., W. Knoll, *Langmuir*, (1993) **9**, 2430.
- [35] Barbillon, G.; Faure, A. C.; El Kork, N.; Moretti, P.; Roux, S.; Tillement, O.; Ou, M. G.; Descamps, A.; Perriat, P.; Vial, A.; Bijeon, J. L.; Marquette, C. A.; Jacquier, B., *Nanotechnology*, (2008) **19**, 035705.
- [36] Barbillon, G.; Bijeon, J. L.; Plain, J.; Royer, P., *Thin Solid Films*, (2009) **517**, 2997.
- [37] J. Spinke, M. L., H-J. Guder, L. Angermaier, W. Knoll, *Langmuir*, (1993) **9**, 1821.
- [38] W. M. Albers, I. V.-L., *Nano-Bio-Sensors*, Springer Ed. New York, NY, (2011).
- [39] W. M. Albers, I. V.-L. Ed. *Nano-Bio-Sensing: Surface Plasmon Resonance on Nanoscale Organic Films*, (2011); Vol. p 83.
- [40] V. H. Pérez-Luna, M. J. O. B., K A. Opperman, P. D. Hampton, Gabriel P. Lopez, L A. Klumb, P. S. Stayton, *JACS*, (1999) **121**, 6469.
- [41] Shulei Zhao, D. S. W., W. M. Reichert, *Langmuir*, (1993) **9**, 3166.
- [42] L. S. Jung, K. E. N., C. T. Campbell, P. S. Stayton, S. S. Yee, V. Pérez-Luna, G. P. Lopez, *Sensors and Actuators B*, (1999) **54**, 137.
- [43] R. Schasfoort, A. J. T., *Handbook of Surface Plasmon Resonance*, The Royal Society of Chemistry: (2008).
- [44] Y.Tang, R. M., X. Zeng, *Anal Chem*, (2006) **78**, 1841.
- [45] Tang, Y.; Mernaugh, R.; Zeng, X., *Anal Chem*, (2006) **78**, 1841.
- [46] N. M. Green, E. J. T., *Biochem. J.*, (1970) **118**, 67.
- [47] N. F. Bras, N. M. C., M. J. Ramos, P. A. Fernandes, *Expert Opinion*, (2014) **24**, 1.
- [48] Dhayal, M.; Ratner, D. M., *Langmuir*, (2009) **25**, 2181.
- [49] B. Hultberg, P. K. M., S. Sjoblad, *Biochimica et Biophysica Acta*, (1976) **445**, 398.
- [50] Eiji ICHISHIMA, N. T., Masamichi IKEGUCHI, Yasunori CHIBA, Motoyoshi NAKAMURA, Choko KAWABATA, Takashi INOUE, Koji TAKAHASHI, Toshiki MINETOKI, Kenji OZEKI, Chieko KUMAGAI, Katsuya GOMI, Takashi YOSHIDA, Tasuku NAKAJIMA, *Biochem. J.*, (1999) **339**, 589.

## General Conclusion

The purpose of this work was to control the structuration of nanoparticle assemblies in order to control the magnetic collective properties of these objects and their influence on plasmonic properties carried by a substrate. Therefore, assemblies of nanoparticles onto gold substrates were prepared through specific intermolecular interactions.

The thermal decomposition, by controlling the operating conditions, allowed synthesizing spherical iron oxide nanoparticles with different sizes. The structural and magnetic properties were investigated as function of their diameter. The XRD measurements highlighted the partial oxidation of the nanoparticles, especially in the case of 5 nm-sized nanoparticles. The magnetic measurements showed the superparamagnetic behavior of these nanoparticles at room temperature. The blocking temperature was studied as function of the size of the nanoparticles. The increase of the nanoparticle diameter led to an increase of the magnetic anisotropy which displaces the blocking temperature to higher values.

Thereafter, these nanoparticles were functionalized with a ligand carrying a functional group active for a CuAAC “click” reaction. The infrared spectroscopy and granulometry measurements highlighted the correct grafting of the ligand at the surface of the nanoparticle and the colloidal stability of the suspension after functionalization. Moreover, gold substrates were functionalized with thiol molecules with a complementary head group to form a SAM. The infrared spectroscopy and contact angle measurements of the gold surface showed the presence of the thiol molecules.

The assemblies of the azido-terminated nanoparticles onto the alkyne-terminated SAM were performed by CuAAC “click” reaction and the conditions of reaction were studied. The variation of reaction time allowed controlling the spatial distribution of the nanoparticles on the gold surface from few isolated nanoparticles to dense monolayers. The kinetic of the assembly was studied for two different concentrations and showed a faster kinetic for larger nanoparticles than small nanoparticles which do not reach the full monolayer. The investigation on the colloidal stability of the nanoparticle suspension after different reaction times showed that the aggregation of nanoparticles was favored for larger nanoparticles. The assembly kinetics seems to be driven by the aggregation in suspension and the dipolar interactions especially in the case of 20 nm-sized nanoparticles. Finally, the magnetic properties of assemblies prepared with different sizes and different densities were performed. The measure of the magnetization as function of an applied field and the temperature highlighted that the NP20 present stronger dipolar interactions than the NP5 and NP10 whatever the density of nanoparticles. This behavior confirmed that the assembly is driven by these dipolar interactions and explains the faster kinetic and stronger tight-packing of the NP20.

A new assembly strategy was reported based on specific intermolecular interactions between nucleobases. By taking advantage of the “click” chemistry, the nanoparticles and substrates were post-functionalized with complementary nucleobases. The use of micro-wave irradiations allowed decreasing strongly the reaction time down to few minutes. Alkyne-modified thymine was grafted onto azido-terminated nanoparticles and the control of the spatial arrangement of the functional groups at their surface was performed by diluting the functional groups during the ligand exchange. The control of the quantity of thymine groups at the nanoparticle surface was ensured by infrared spectroscopy and the stability of the suspension was investigated. The nanoparticles functionalized with thymine

groups presented a different stability as function of the solvent used. It was shown that the use of polar solvent favored the stability of thymine-terminated nanoparticles due to the interactions between the thymine molecules and the solvent. The functionalization of the substrate was also performed by grafting azido-modified adenine on the alkyne-terminated SAM. The control of the spatial arrangement was also performed by dilution of the functional groups at the surface. Infrared and photo-electron spectroscopies and contact angle measurements highlighted the presence of the adenine at the surface. The assembly process through multiple hydrogen binding was then performed by dipping the adenine-terminated substrate in the thymine-terminated nanoparticle suspension. The control of the density was investigated as function of the solvent, the quantity of nucleobases and the temperature. The control of these parameter allowed finding the best conditions to favor high coverage of the surface.

In the last part of this work, the assembly of nanoparticles was used to control the plasmonic properties of the gold substrate. The control of the presence of functional groups after the assembly through “click” reaction allowed obtaining a “bio-platform” able to be functionalized with a large variety of receptor molecules. The grafting of biotin, confirmed by infrared and photo-electron spectroscopies, allowed detecting the streptavidin by surface plasmon resonance measurements. The sensitivity and the recognition process were investigated with and without the presence of nanoparticles at the gold thin film surface. The enhancement of the sensitivity with the presence of nanoparticles was highlighted. Investigations on the nature of the enhancement showed the nanoparticles modified the intrinsic optical properties of the gold substrate. Moreover, the nanoparticles gave a better accessibility of the biotin groups at the surface which allowed the detection of a higher number of streptavidin.

This strategy developed for protein was extended to enzyme detection. The recognition process was studied with the biotin/streptavidin as well as iminosugar/glycosidase couple. The alkyne-modified iminosugar was grafted onto the azido-terminated nanoparticle assembly in order to detect the  $\alpha$ -mannosidase. The measure of the surface plasmon resonance as function of the time allowed monitoring in real time the adsorption of the analyte. From these data, affinity constants and limit of detection of the analyte were determined. The results, in comparison with similar study in solution, showed a higher inhibitor power of the iminosugar grafted onto a solid surface than in solution.

## Outlook

This work led to a great number of perspectives. The nanoparticle assembly through nucleobases recognition was studied with nanoparticles functionalized with thymine. However, it is possible to functionalized nanoparticles with adenine. Therefore, the self-assembly of multilayer induce by the external conditions (solvent, temperature,  $\pi$ -stacking) can be imagined.

A preliminary study was done by functionalizing 10 nm-sized nanoparticles with adenine diluted at the surface with a terminal methylene group in a ratio 50/50 (NP@Ade 50%). The suspension of a mixture with nanoparticles functionalized with both type of nucleobases allowed forming aggregation in solution through the base pairing (figure I).

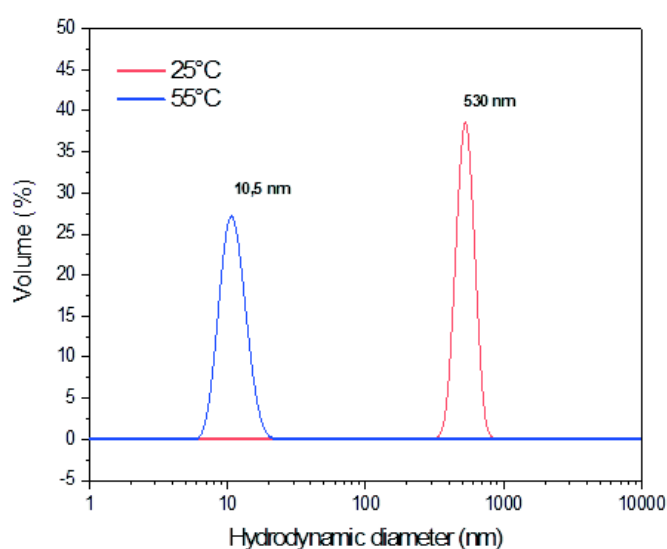


Figure LIV. DLS measurements on a suspension of NP@Thym 50% and NP@Ade 50% in DMF at 25°C (red curve) and 55°C (blue curve)

The control of the solvent and the temperature could control the aggregation since the hydrogen bonds are sufficiently weak. Indeed, granulometry measurements showed that aggregate of NP@Ade 50% and NP@Thym 50% at room temperature do not present aggregation when the temperature reaches 55°C.

Moreover, the assembly of nanoparticles through self-recognition of nucleobases can be extended to larger structures. The assembly of nanoparticle via DNA strands has already been performed in literature. However, most of the studies were done with gold nanoparticles which are easily functionalized in water. Preliminary study showed that the iron oxide nanoparticles can be functionalized with DNA strand mixed with a PEG on their surface to have pseudo stability in a mix

water/ethanol. Moreover, the functionalization of a gold substrate with the complementary DNA strand resulted in the self-assembly of nanoparticles (figure II).<sup>12</sup>

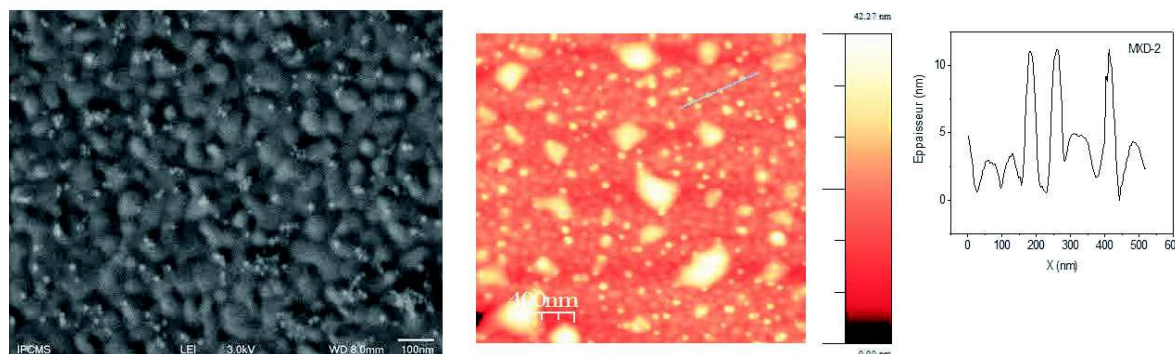


Figure LV. SEM image, AFM image and the corresponding topographic profile of the assembly of NP10 via DNA strands

This experiment showed the feasibility of this system even if the optimization of the operating conditions has to be done.

In the case of the SPR measurement, the bio-platform allowed grafting a large panel of bio-receptors. Therefore, the study of the recognition process of different couples of molecules can be performed. Moreover, the use of different sizes and shapes of nanoparticles could allow finding a perfect configuration to optimize the sensitivity.

Finally, the CuAAC “click” chemistry, thanks to its versatility, allows performing assembly of nanoparticles from different compositions. Therefore, gold nanoparticles which carry plasmonic properties could be grafted onto substrates in order to induce magneto-plasmonic properties.

---

<sup>12</sup> Collaboration X. Cattoën, Institut Néel, Grenoble  
D. Gasparutto, CEA, Grenoble

# Appendix A

## Anisotropy energy of a nanoparticle

The anisotropy energy results of the contribution of different energies:

$$E_a = E_{MC} + E_S + E_F$$

with  $E_{MC}$  the magnetocrystalline anisotropy energy,  $E_S$  the surface anisotropy energy and  $E_F$  the shape energy.

- The magnetocrystalline energy  $E_{MC}$  comes from the interaction between the magnetization and the crystal lattice which try to align the magnetic moments in a direction specific of the material. These crystallographic directions are called magnetic easy axis. For a single nanoparticle, the magnetocrystalline energy at first order is:

$$E_{MC} = KV \sin^2(\theta)$$

- When the size of a nanoparticle decrease, the ratio surface/volume increase strongly this implies a lead of the surface effect. The diminution of neighbor atom at the surface leads to break the symmetry and create disorder of the spin at the surface of the nanoparticle. The direct consequence of this size reduction is the disordered layer at the surface which has a spin glass magnetic behavior where the magnetization of surface atom is different of the one from volume atom. This effect is called spin canting and is responsible of the reduction of saturation magnetization in nanoparticle. The spin canting is strongly dependent of the size of the nanoparticle but also of the synthesis method and the ligand bound on the surface atoms.<sup>[104, 105]</sup>

- When a magnetic field is applied on a nanoparticle, charge appears around the nanostructure which induces a magnetic field opposite of the field applied. This field called demagnetizing field can be written:

$$H_d = -NM$$

where M is the magnetization of the system and N the demagnetizing factor. This field is dependent of the magnetization direction relative to the shape of the sample. The associate energy is given by:

$$E_a^{shape} = \frac{1}{2} \mu_0 V (N_x M_x^2 + N_y M_y^2 + N_z M_z^2)$$

Where  $N_x, N_y, N_z, M_x^2, M_y^2$  and  $M_z^2$  are the component of the demagnetizing factor and the magnetization in the directions  $x, y$  and  $z$  and with  $N_x + N_y + N_z = 1$ ,  $\mu_0$  is the vacuum permeability and  $V$  the nanoparticle volume. In the case of a spherical nanoparticle,  $N_x = N_y = N_z = 1/3$  and does not present shape anisotropy.

The magnetic behavior of a nanoparticle will depend of contribution of these energies. All energies are influenced of by the field applied, the temperature, the shape and size of the nanoparticle. Therefore, the magnetic properties, especially the reversal magnetization dynamic will depend of these parameters.

### **Atomic Absorption Spectroscopy (AAS)**

The determination of concentration of the nanoparticles suspension was performed by atomic absorption spectroscopy.

A calibration curve of absorbance was performed by measuring the absorption of solution with an iron concentration known. The sample of iron oxide nanoparticle suspension was dissolved in hydrochloric acid (12 M). The measure of adsorption is then performed to know the iron concentration [Fe]. The iron oxide concentration [Fe<sub>3</sub>O<sub>4</sub>] is then calculated by multiplying the iron concentration with a factor 1.38.

### **Inter-particle distance**

The inter-particle distance  $d$  is calculated with the approximation that the nanoparticles are homogenous distributed onto the surface and is expressed as:

$$d = \sqrt{\left(\frac{S}{N} - \pi \left(\frac{D}{2}\right)^2\right) \frac{1}{\pi}}$$

with  $S$  the area considered for the density calculus (in our case,  $S$  will always be  $1 \mu\text{m}^2 = 10^6 \text{ nm}^2$ ),  $N$  the number of nanoparticles in the surface  $S$  (determined by SEM) and  $D$ , the nanoparticles diameter.

### **Alkynated biotin synthesis**

Alkynated Biotin was synthesized by a method from Cao and al (2013)<sup>[14]</sup>. N-(3-Dimethylaminopropyl)-N'-ethylcarbodiimide hydrochloride (EDC.HCl) (92 mg, 0.48 mmol) was added to a solution of biotin (100 mg, 0.4 mmol) and N-hydroxysuccinimide (51 mg, 0.448 mmol) in DMF (15 mL) in a round bottom flask. The solution was stirred for 24 h at room temperature under nitrogen and evaporated in vacuum. The crude solid was triturated with methanol several times to form N-hydroxysuccinimidobiotin as a white solid product (73 mg, 54%). Propargylamine (21  $\mu$ L, 0.32 mmol) was added to a solution of this compound (54 mg, 0.16 mmol) and triethylamine (43  $\mu$ L, 0.32 mmol) in DMF (8 mL). The solution was stirred for 24 h at room temperature under nitrogen, concentrated, and purified by column chromatography (silica gel, with a 6:1 chloroform/methanol eluent) to give alkynated biotin as a white solid (57 mg, 94% yield).

### Angular position model

The theoretical position of the resonance angle is determined by:

$$\theta = \arcsin\left(\sqrt{\frac{\varepsilon_d \varepsilon_m}{\varepsilon_d + \varepsilon_m} \frac{1}{n_p}}\right)$$

with  $n_p$ , the prism refractive index,  $\varepsilon_d$  and  $\varepsilon_m$  the dielectric and metal permittivities, respectively. Moreover, the dielectric permittivity  $\varepsilon_d$  is determined with the model of Paletto et al.

$$\varepsilon_{eff} = (1 - f) \frac{9\delta\varepsilon_1^2\varepsilon_2 + (\varepsilon_2 + 2\varepsilon_1)^2(1 - f)\varepsilon_1}{[(\varepsilon_2 + 2\varepsilon_1)(1 - f) + 3\varepsilon_1f]^2} + f \frac{9(1 - f)\varepsilon_2^2\varepsilon_1 + (\varepsilon_1 + 2\varepsilon_2)^2f\varepsilon_2}{[(\varepsilon_1 + 2\varepsilon_2)f + 3\varepsilon_2(1 - f)]^2}$$

with  $f$  and  $1 - f$  the volume percentage of the material 1 and 2, in the layer respectively. In our case, we will consider the first material as iron oxide  $\varepsilon_1 = 5.57$  and the second material as water  $\varepsilon_2 = 1.77$ . The values of  $f$  and  $1 - f$  are calculated by the volume occupied by the nanoparticles in a cube of  $1 \times 1 \times \delta$ . With  $\delta$  the penetration depth of the surface plasmon (figure A-1).

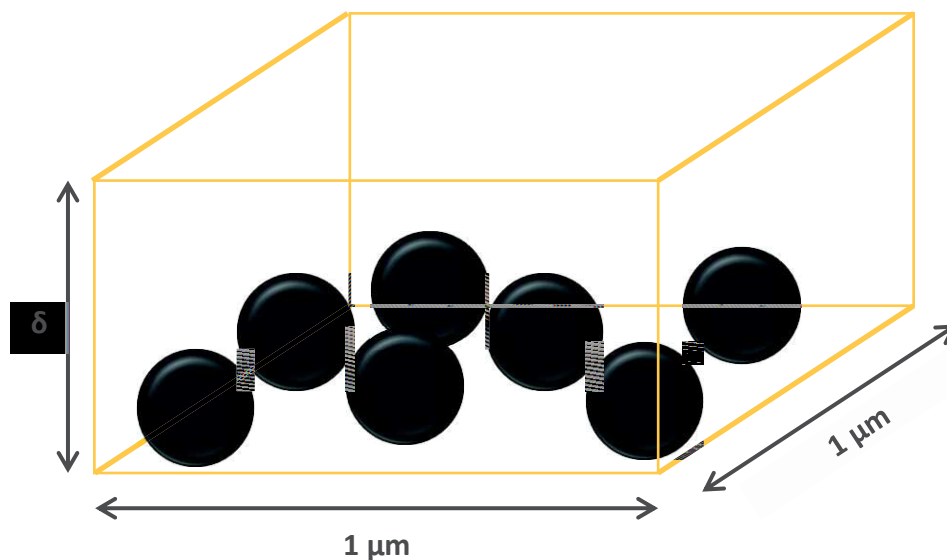


Figure.A 1. Schematic representation of the volume occupied by the nanoparticle

### Determination of the available surface by biotin

The available surface of biotin groups correspond to the spherical cap at the surface of the nanoparticle where the streptavidin can reach. This surface is expressed as:

$$S = \pi D \left( 1 - \sin \left( \arccos \left( \frac{\frac{D - 4.5 + x}{2}}{\frac{D}{2}} \right) \right) \right)$$

with  $D$  the nanoparticle diameter with the organic layer at the surface (2 nm) and  $x$  the inter-particle distance. The number of streptavidin is then determined by division of the area occupied by a streptavidin (20.25 nm<sup>2</sup>).

## Appendice B

In this appendice, we will describe the surface plasmons behavior by using these equations at the metal/dielectric interface.

In free space, the Maxwell equations are defined as:

$$\text{div } \vec{E} = \frac{\rho}{\epsilon_0} \quad \mathbf{3.1}$$

$$\text{div } \vec{B} = 0 \quad \mathbf{3.2}$$

$$\overrightarrow{\text{rot}}(\vec{E}) = \frac{-\partial \vec{B}}{\partial t} \quad \mathbf{3.3}$$

$$\overrightarrow{\text{rot}}(\vec{B}) = \mu_0(\epsilon_0 \frac{\partial \vec{E}}{\partial t} + \vec{j}) \quad \mathbf{3.4}$$

where  $\vec{E}$  represent the electric field,  $\vec{B}$  the induction of the magnetic field,  $\epsilon_0$  the dielectric permittivity in vacuum ( $\epsilon_0 = 8.85 * 10^{-12} \text{A}^2 \cdot \text{s}^4 \cdot \text{kg}^{-1} \cdot \text{m}^{-3}$ ),  $\mu_0$  the magnetic permeability in vacuum ( $\mu_0 = 4\pi \cdot 10^{-7} \text{kg} \cdot \text{m} \cdot \text{A}^{-2} \cdot \text{s}^{-2}$ ),  $\rho$  the charge density and  $\vec{j}$  the current density.

We introduce  $\vec{D}$  and  $\vec{H}$  which are the electric displacement field and magnetic field, for non-magnetic and with an external current density null ( $\mu_r = 1$  and  $\vec{j} = 0$ ), given by:

$$\vec{D} = \epsilon_0 \vec{E} + \vec{P} \quad \mathbf{3.5}$$

$$\vec{H} = \frac{\vec{B}}{\mu_0} - \vec{M} \quad \mathbf{3.6}$$

where  $\vec{P}$  and  $\vec{M}$  represents the electric and magnetic dipolar moments respectively. Here we will consider non-magnetic materials implying  $\vec{M} = 0$  and linear implying that the following expression of  $\vec{P}$  is:

$$\vec{P} = \epsilon_0 \chi_e \vec{E} \quad \mathbf{3.7}$$

with  $\chi_e$  the electric susceptibility

The displacement of the electric field (3.5) and magnetic field (3.6) leads to:

$$\vec{D} = \epsilon_0 \epsilon_r \vec{E} \quad \mathbf{3.8}$$

$$\vec{H} = \frac{\vec{B}}{\mu_0} \quad \mathbf{3.9}$$

with  $\epsilon_r = 1 + \chi_e$  the relative permittivity also called the dielectric constant of the material.

If we consider now two semi-infinite medium, non-magnetic and with a zero external current density ( $\mu_r = 1$  and  $j = 0$ ) as represented on figure B-1. The Maxwell equations for this system are:

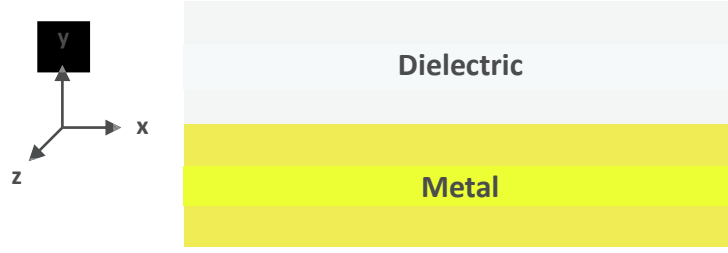


Figure.B 1. Schematic representation of the metal/dielectric interface

$$\operatorname{div} \vec{D} = 0 \quad 3.10$$

$$\operatorname{div} \vec{B} = 0 \quad 3.11$$

$$\overrightarrow{\operatorname{rot}}(\vec{E}) = -\frac{\partial \vec{B}}{\partial t} \quad 3.12$$

$$\overrightarrow{\operatorname{rot}}(\vec{H}) = \epsilon_0 \epsilon_r \frac{\partial \vec{E}}{\partial t} \quad 3.13$$

The wave equations can be expressed with the following equations:

$$\overrightarrow{\operatorname{rot}}(\overrightarrow{\operatorname{rot}}(\vec{E})) = \overrightarrow{\operatorname{rot}}\left(-\frac{\partial \vec{B}}{\partial t}\right) = -\frac{\partial}{\partial t}(\overrightarrow{\operatorname{rot}}(\vec{B})) \quad 3.14$$

$$\operatorname{div}(\operatorname{div} \vec{E}) - \Delta \vec{E} = -\mu_0 \epsilon_0 \epsilon_r \frac{\partial^2 \vec{E}}{\partial t^2} \quad 3.15$$

knowing  $\Delta \vec{E} = \nabla^2 \vec{E}$ , we obtain:

$$\nabla^2 \vec{E} - \frac{\epsilon_r}{c^2} \frac{\partial^2 \vec{E}}{\partial t^2} = 0 \quad 3.16$$

with  $c = \sqrt{\frac{1}{\mu_0 \epsilon_0}}$

The same reasoning can be used for the magnetic field:

$$\nabla^2 \vec{H} - \frac{\epsilon_r}{c^2} \frac{\partial^2 \vec{H}}{\partial t^2} = 0 \quad 3.17$$

Considering the fields to have a harmonic time dependency, the electric field can be expressed as

$$\vec{E} = \vec{E}_0 e^{ik_0 r - i\omega t + \varphi} \quad 3.18$$

with  $\omega = 2\pi f$  the angular frequency,  $r$  the position vector,  $k_0$  the wave number and  $\varphi$  the phase (we will consider  $\varphi = 0$ ). The derivative from time of the electric field becomes  $\frac{\partial^2 \vec{E}}{\partial t^2} = \frac{\partial}{\partial t}(-i\omega \vec{E}) = i^2 \omega^2 \vec{E} = -\omega^2 \vec{E}$  and  $\nabla^2 \vec{E} = \frac{\partial^2 \vec{E}}{\partial x^2} + \frac{\partial^2 \vec{E}}{\partial y^2} + \frac{\partial^2 \vec{E}}{\partial z^2}$ . If we assume that the electric field is propagating along  $x$  axis and invariant on  $z$  axis, we have:  $\frac{\partial^2 \vec{E}}{\partial z^2} = 0$  and the field can be expressed as  $\vec{E} = \vec{E}(y) e^{i\beta x}$  with  $\beta$  the propagation constant of the electric field.

So  $\frac{\partial^2 \vec{E}}{\partial x^2} = \frac{\partial}{\partial x}(i\beta \vec{E}) = i^2 \beta^2 \vec{E} = -\beta^2 \vec{E}$

and (3.16) becomes:

$$\frac{\partial^2 \overline{E}_y}{\partial y^2} - \beta^2 \overline{E}_y + \frac{\varepsilon_r}{c^2} \omega^2 \overline{E}_y = 0 \quad 3.19$$

$$\frac{\partial^2 \overline{E}_y}{\partial y^2} + \overline{E}_y (k_0^2 \varepsilon_r - \beta^2) = 0 \quad 3.20$$

with  $k_0 = \frac{\omega}{c}$

In the same way, we find for the magnetic field:

$$\frac{\partial^2 \overline{H}_y}{\partial y^2} + \overline{H}_y (k_0^2 \varepsilon_r - \beta^2) = 0 \quad 3.21$$

To find the component of the fields  $\vec{E}$  and  $\vec{H}$  we use the equations (3.12) and (3.13) knowing that  $\frac{\partial}{\partial t} = -i\omega$  we can assume the following equations:

$$\begin{cases} \frac{\partial E_y}{\partial z} - \frac{\partial E_z}{\partial y} = i\omega\mu_0 H_x \\ \frac{\partial E_z}{\partial x} - \frac{\partial E_x}{\partial z} = i\omega\mu_0 H_y \\ \frac{\partial E_x}{\partial y} - \frac{\partial E_y}{\partial x} = i\omega\mu_0 H_z \end{cases} \quad \begin{cases} \frac{\partial H_y}{\partial z} - \frac{\partial H_z}{\partial y} = -i\omega\varepsilon_0\varepsilon_r E_x \\ \frac{\partial H_z}{\partial x} - \frac{\partial H_x}{\partial z} = -i\omega\varepsilon_0\varepsilon_r E_y \\ \frac{\partial H_x}{\partial y} - \frac{\partial H_y}{\partial x} = -i\omega\varepsilon_0\varepsilon_r E_z \end{cases}$$

The wave propagation is following the x axis,  $\frac{\partial}{\partial x} = i\beta$  and the system is invariant in z, therefore  $\frac{\partial}{\partial z} = 0$ , conducting to simplified equations:

$$\begin{cases} -\frac{\partial E_z}{\partial y} = i\omega\mu_0 H_x \\ i\beta E_z = i\omega\mu_0 H_y \\ \frac{\partial E_x}{\partial y} - i\beta E_x = i\omega\mu_0 H_z \end{cases} \quad \begin{cases} \frac{\partial H_z}{\partial y} = i\omega\varepsilon_0\varepsilon_r E_x \\ i\beta H_z = -i\omega\varepsilon_0\varepsilon_r E_y \\ \frac{\partial H_x}{\partial y} - i\beta H_y = -i\omega\varepsilon_0\varepsilon_r E_z \end{cases}$$

Two sets of solutions can be obtained, the first represents the transverse magnetic modes (TM) where the magnetic field is polarized perpendicularly to the incidence plane (and the electric field is contained into the incidence plane) where  $H_x = 0$ ,  $E_z = 0$  and therefore  $H_y = 0$ , bringing the equation system to:

$$\begin{cases} \frac{\partial H_z}{\partial y} = i\omega\varepsilon_0\varepsilon_r E_x \\ i\beta H_z = -i\omega\varepsilon_0\varepsilon_r E_y \\ \frac{\partial E_x}{\partial y} - i\beta E_x = i\omega\mu_0 H_z \end{cases}$$

Two solutions can be deduced from this system:

$$E_y = \frac{-\beta}{\omega\varepsilon_0\varepsilon_r} H_z \quad 3.22$$

$$E_x = \frac{-i}{\omega\varepsilon_0\varepsilon_r} \frac{\partial H_z}{\partial y} \quad 3.23$$

By substituting (3.22) in the equation (3.20) we obtain the wave equation for the radial modes TM :

$$\boxed{\frac{\partial^2 \overline{H}_z}{\partial y^2} + \overline{H}_z (k_0^2 \varepsilon_r - \beta^2) = 0} \quad 3.24$$

The second set of solution represent the transverse electric modes (TE) where the electric field is polarized perpendicularly to the incidence plane (and the magnetic field is contained into the incidence plane) where  $E_x = 0$  and therefore  $E_y = 0$  and  $H_z = 0$ , bringing the equation system to:

$$\begin{cases} -\frac{\partial E_z}{\partial y} = i\omega\mu_0 H_x \\ i\beta E_z = i\omega\mu_0 H_y \\ \frac{\partial H_x}{\partial y} - i\beta H_y = -i\omega\varepsilon_0\varepsilon_r E_z \end{cases}$$

$$H_y = \frac{\beta}{\omega\mu_0} E_z \quad 3.25$$

$$H_x = \frac{i}{\omega\mu_0} \frac{\partial E_z}{\partial y} \quad 3.26$$

By substituting (3.25) in the equation (3.21) we obtain the wave equation for the azimuthal modes TE:

$$\boxed{\frac{\partial^2 \vec{E}_z}{\partial y^2} + \vec{E}_z (k_0^2 \varepsilon_r - \beta^2) = 0} \quad 3.27$$

Equations (3.24) and (3.27) allow studying plasmons confined at the interface.

The solution for radial modes (TM) is given by the solution of equation (3.24), then combined with equations (3.22) and (3.23) we obtain the solutions for  $E_y(y)$  and  $E_x(y)$  inside the dielectric ( $y > 0$ ) and inside the metal ( $y < 0$ ).

In the dielectric,  $y > 0$ :

$$H_z(y) = A_d e^{i\beta x} e^{-\gamma_d y} \quad 3.28$$

$$E_x(y) = iA_d \frac{1}{\omega\varepsilon_0\varepsilon_d} \gamma_d e^{i\beta x} e^{-\gamma_d y} \quad 3.29$$

$$E_y(y) = -A_d \frac{1}{\omega\varepsilon_0\varepsilon_d} e^{i\beta x} e^{-\gamma_d y} \quad 3.30$$

In the metal,  $y < 0$ :

$$H_z(y) = A_m e^{i\beta x} e^{\gamma_m y} \quad 3.31$$

$$E_x(y) = -iA_m \frac{1}{\omega\varepsilon_0\varepsilon_m} \gamma_m e^{i\beta x} e^{\gamma_m y} \quad 3.32$$

$$E_y(y) = -A_m \frac{1}{\omega\varepsilon_0\varepsilon_m} e^{i\beta x} e^{\gamma_m y} \quad 3.33$$

with  $A_d$  et  $A_m$  the amplitudes in the dielectric and in the metal respectively and  $\gamma_{d,m} = \beta^2 - k_0^2 \varepsilon_{d,m}$ .

Considering these two media as continuous, the conditions at the limits have to be applied. This imply than the tangential component of the electric field is continuous through the section while the tangential component of the magnetic field is equal to the current density through the interface. The tangential fields at the interface have to be continuous, to satisfy this condition. using equations from (3.28) to (3.33) it implies that:

$$A_m = A_d \quad 3.34$$

$$\boxed{\frac{\gamma_m}{\varepsilon_m} = -\frac{\gamma_d}{\varepsilon_d}} \quad 3.35$$

If we consider a metal without absorption, equation (3.35) implies that the real part of the permittivity has to be of opposite sign. It is effective for a system with a metal/dielectric interface. This relation allows obtaining the dispersion relation for plasmon propagation at the interface:

$$\beta = k_0 \sqrt{\frac{\epsilon_d \epsilon_m}{\epsilon_d + \epsilon_m}} = \frac{\omega}{c} \sqrt{\frac{\epsilon_d \epsilon_m}{\epsilon_d + \epsilon_m}} \quad 3.36$$

In the same way, for the azimuthal modes, these equations allow finding the expression of  $E_z(y)$  and bring to the following relations:

In the dielectric,  $y > 0$ :

$$E_z(y) = A_d e^{i\beta x} e^{-\gamma_d y} \quad 3.37$$

$$H_x(y) = -i A_d \frac{1}{\omega \mu_0} \gamma_d e^{i\beta x} e^{-\gamma_d y} \quad 3.38$$

$$H_y(y) = A_d \frac{1}{\omega \mu_0} e^{i\beta x} e^{-\gamma_d y} \quad 3.39$$

In the metal,  $y < 0$ :

$$E_z(y) = A_m e^{i\beta x} e^{\gamma_m y} \quad 3.40$$

$$H_x(y) = -i A_m \frac{1}{\omega \mu_0} \gamma_m e^{i\beta x} e^{\gamma_m y} \quad 3.41$$

$$H_y(y) = A_m \frac{1}{\omega \mu_0} e^{i\beta x} e^{\gamma_m y} \quad 3.42$$

Respecting the conditions at the limits conduct to:

$$A_m (\gamma_m + \gamma_d) = 0 \quad 3.43$$

The solution for this condition is  $A_m = 0$  and therefore surface plasmons do not exist for the TE polarization.



## Appendix C

### Infrared and granulometry characterization of NP20 and NP5

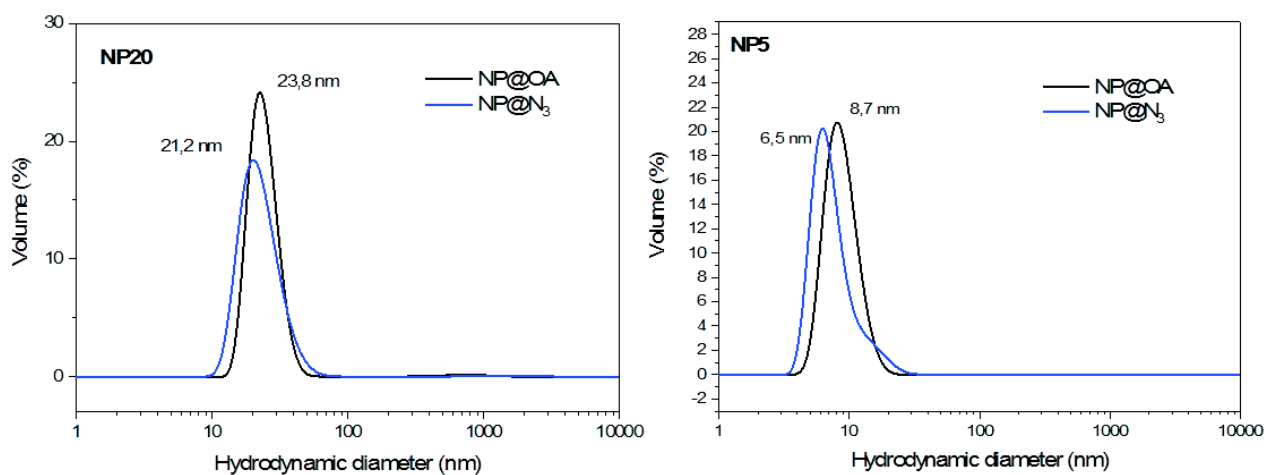


Figure.C 1. Granulometry measurements of the nanoparticles in THF before (black curve) and after (blue curve) ligand exchange for NP20 (left) and NP5 (right)

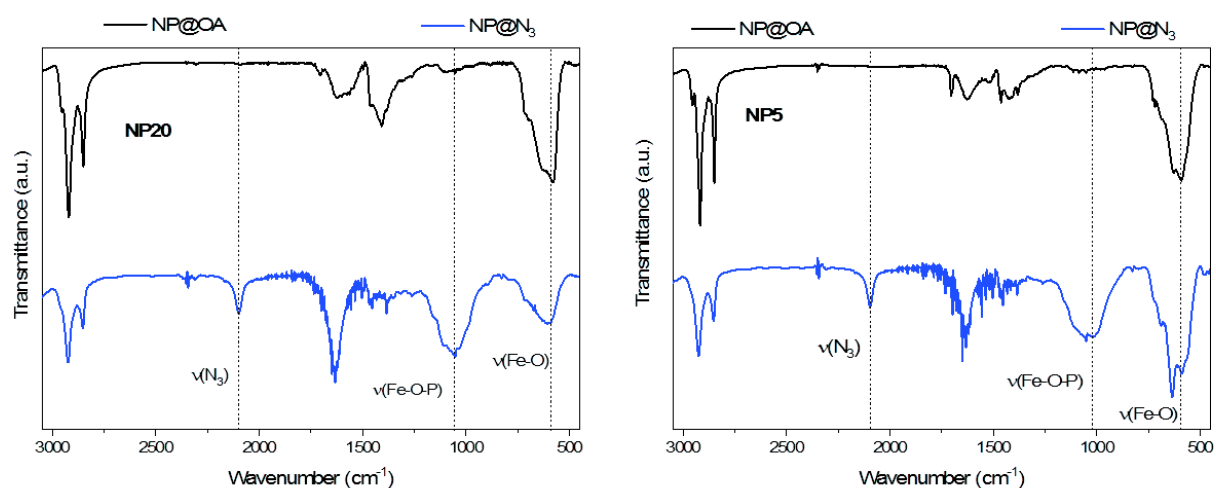


Figure.C 2. Infrared spectra of the nanoparticles with oleic acid (black curve) and the nanoparticles functionalized with the azide phosphonic acid (blue curve) for NP20 (left) and NP5 (right)

### <sup>1</sup>HNMR of 11-mercapto-undecyn

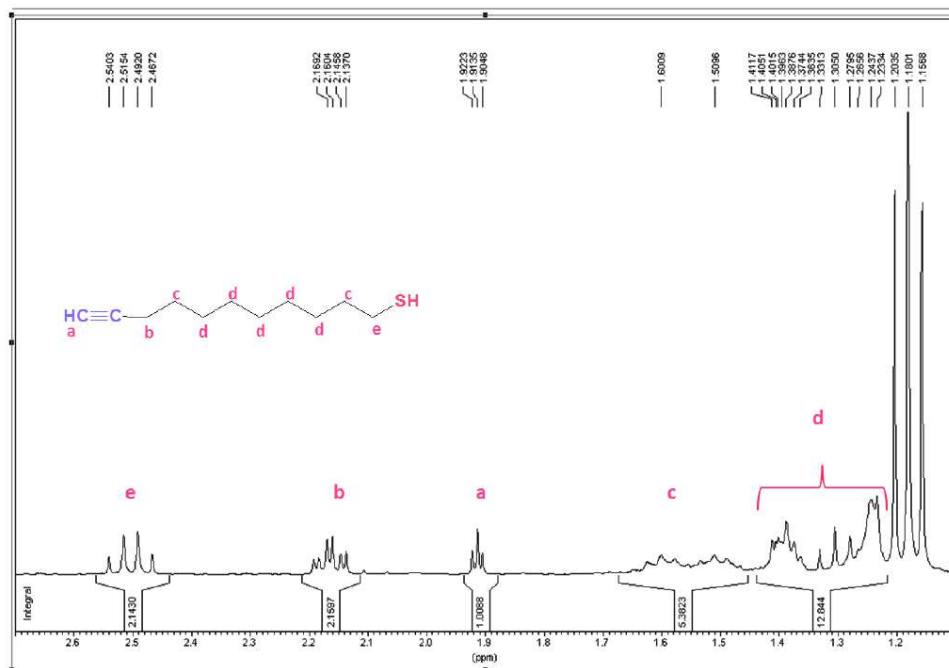


Figure.C 3.  $^1\text{H}$ NMR spectra of the 11-mercapto-undecyn

$^1\text{H}$ NMR ( $\text{CDCl}_3$ , 400 MHz): 2.50 (q,  $J = 7.0$  Hz, 2H); 2.15 ( $t_d$ , 2H); 1.94 (t, 1H); 1.4-1.6 (m, 4H); 1.22-1.41 (m, 14H)

#### FT-IR and $^1\text{H}$ NMR of alkynated biotin

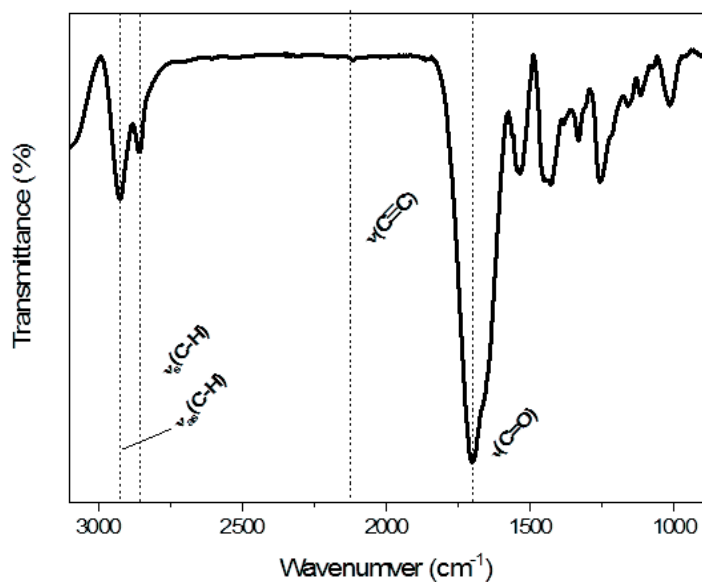


Figure.C 4. FT-IR spectrum of the derivative alkynated biotin molecule

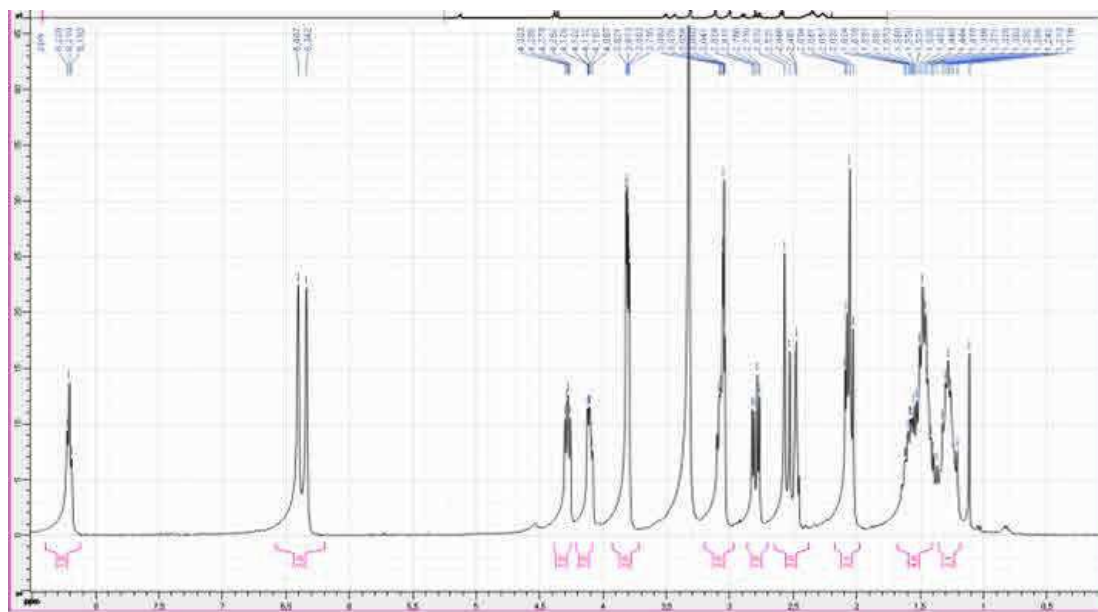


Figure.C 5. <sup>1</sup>HNMR spectra of the alkyated biotin

<sup>1</sup>H NMR (DMSO-d<sub>6</sub>) δH: 1.29–1.33 (m, 2H), 1.44–1.51 (m, 2H), 1.59–1.62 (m, 2H), 2.07–2.10 (d, J = 7.5 Hz, 2H), 2.57–2.59 (d, J = 13.0 Hz, 1H), 2.81–2.84 (dd, J<sub>1</sub> = 4.5 Hz, J<sub>2</sub> = 5.0 Hz, 1H), 3.04–3.09 (m, 2H), 3.83–3.83 (m, 2H), 4.130 (m, 1H), 4.29–4.31 (m, 1H), 6.31 (s, 1H), 6.36 (s, 1H), 8.17 (s, 1H).

### Characterizations for 0% nanoparticle assemblies

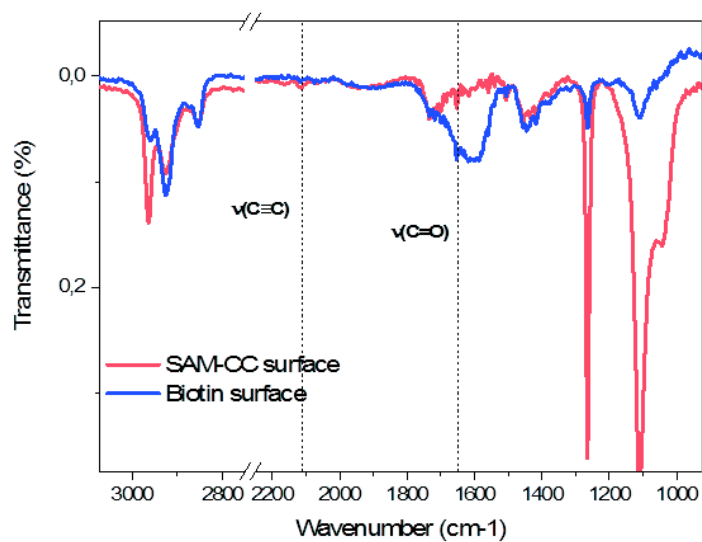


Figure.C 6. PM-IRRAS spectra of SAM-CC (red line) and biotin functionalized film (blue line)



# Résumé de thèse en français

## Chapitre I – Etat de l’art

Le travail effectué dans ce manuscrit porte sur l’intérêt d’assembler des nanoparticules sur des surface dans le but d’étudier les propriétés des nanoparticules ainsi que de la surface en fonction de la structuration de leur assemblage. Plus particulièrement, l’influence de l’assemblage des nanoparticules sur des surface pour permettre d’améliorer les performances de détection de biomolécules a été étudié.

Le control de l’assemblage de nanoparticules sur une surface est primordial puisque leurs propriétés sont dépendantes de leur taille, leur forme et leur composition, mais aussi de leur distance à chacune d’entre elles. De plus leur incorporation dans des dispositifs pour des applications nécessite fréquemment leur immobilisation sur une surface. Il va donc de soi que pour moduler leurs propriétés physiques, dépendantes des interactions individuelles et collectives des nanoparticules, le contrôle de leur arrangement spatial est crucial. L’organisation à la surface d’un substrat va dépendre de la technique de déposition ainsi que de la catégorie d’interactions. Il existe de nombreuses techniques qui permettent d’assembler des nanoparticules sur des surfaces de façon simple et rapide comme les méthodes de déposition dite « externes » tel que le dipping, le drop casting, le spin coating et le dip coating. Ces méthodes permettent d’assembler des nanoparticules sur des grandes surfaces et de façon compactes, néanmoins ces techniques souffrent du manque de spécificité lors des assemblages. D’autres méthodes permettent une spécificité et donc une reconnaissance entre la surface du substrat et des nanoparticules. Pour cela, les surfaces sont fonctionnalisées avec des groupements spécifiques complémentaires qui vont permettre la reconnaissance entre les nanoparticules et le substrat. Cette spécificité permet donc un bon contrôle de l’arrangement spatial des nanoparticules.

L’assemblage de nanoparticules permet d’accéder à un grand nombre d’application, notamment dans le cas de nanoparticules d’oxyde de fer qui présentent des moments magnétiques. Le contrôle de leurs distribution spatial à la surface d’un substrat permet le contrôle des propriétés magnétiques et permet donc de réaliser des dispositifs pour le stockage d’information ainsi que des capteurs magnéto-résistifs. Cependant, au-delà des propriétés intrinsèques des nanoparticules qui peuvent être modulées, les propriétés physiques du substrat sur lequel elles reposent peuvent également être contrôlées. En effet, en utilisant un substrat présentant des propriétés optiques particulières, le dépôt de nanoparticules peut les modifier. En effet, le phénomène de résonance plasmon, qui provient de l’oscillation des électrons de conduction couplé avec une onde lumineuse produit à la surface d’un substrat, une extinction lumineuse. Cette extinction est dépendante de l’angle et de la longueur d’onde incidente de l’onde lumineuse et est également très sensible aux variations d’indice de réfraction à la surface.

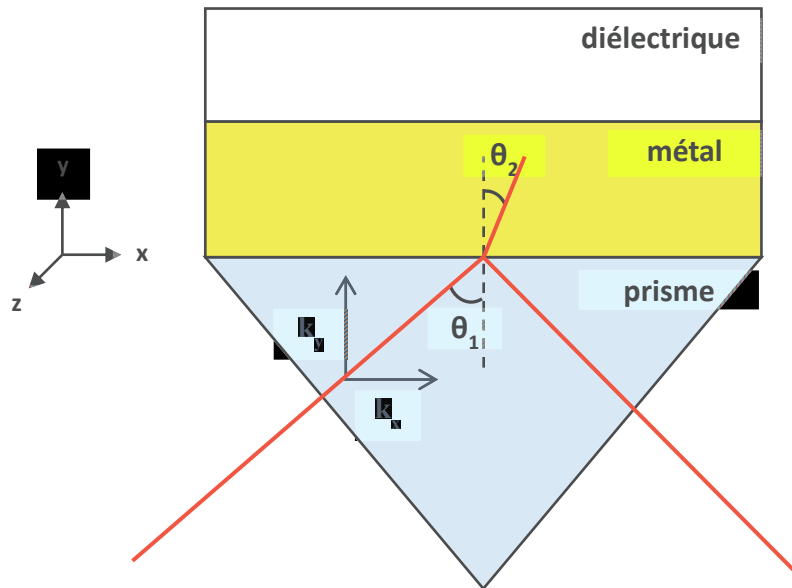


Figure 56. Représentation schématique du phénomène de résonance plasmon en utilisant un prisme dans la configuration de Kretschmann.

En effet, le phénomène de résonance plasmon de surface se produit lorsque le vecteur d'onde d'une onde évanescente transmise à travers un prisme se couple avec l'oscillation des électrons à l'interface entre le métal et un diélectrique (figure 1). Lorsque se phénomène se produit, il y a une brusque diminution de l'onde réfléchi dans le prisme pour un angle précis défini par :

$$\theta_{SPR} = \sin^{-1} \sqrt{\frac{\epsilon_d \epsilon_m}{\epsilon_d + \epsilon_m} \frac{1}{n_{prism}}}$$

Ainsi, la dépendance avec l'indice de réfraction du diélectrique  $n_d^2 = \epsilon_d$  est clairement démontrée. La détection moléculaire va pouvoir avoir lieu entre des molécules réceptrices greffées à la surface du substrat et une espèce à détecter en solution.

La détection plasmonique est aujourd'hui déjà utilisée dans de nombreux domaines (biologie, agroalimentaire, médecine, environnement, sécurité) et présente certains avantages tel que la non nécessité de marquer les éléments à détecter ainsi que le fait d'avoir une détection rapide et en temps réel. Néanmoins, aujourd'hui il reste des limites à ce système de détection, notamment dans le cas de solution extrêmement diluée ou pour des très petites molécules. C'est pourquoi l'augmentation des performances est primordial pour améliorer ce type de dispositifs.

L'utilisation de nanoparticules pour augmenter les performances des capteurs SPR a déjà été étudié principalement en utilisant les nanoparticules pour faire de la détection de type « sandwich » où l'adsorption de l'analyte va induire l'assemblage ou l'agrégation des nanoparticules sur la surface et donc amplifier le signal SPR. Cependant, dans ce manuscrit, on va s'intéresser à l'assemblage des nanoparticules dans un premier lieu pour ensuite permettre l'augmentation des propriétés physique du substrat. Cela passera par la synthèse et fonctionnalisation des nanoparticules dans un premier temps, puis la fonctionnalisation du substrat et l'assemblage des nanoparticules aux travers de liaisons spécifiques avant de pouvoir étudier la détection moléculaire en utilisant des couples de molécules ayant un intérêt biologique.

## **Chapitre II – Structuration de l'assemblage de nanoparticules d'oxyde de fer**

L'intérêt de cette partie est de synthétiser et d'assembler des nanoparticules d'oxyde de fer sur des substrats d'or. La synthèse des nanoparticules par décomposition thermique permet un bon contrôle de leurs tailles et de leurs morphologies permettant ainsi de contrôler leurs propriétés intrinsèques. Les nanoparticules sont ensuite assemblées sur des surfaces au travers de liaisons covalentes réalisées par chimie « click ». Les assemblages sont ensuite étudiés en fonction de la taille des nanoparticules et des conditions opératoires de la réaction de « click ».

### **Synthèse des nanoparticules**

Les nanoparticules sont synthétisées par la méthode de décomposition thermique qui consiste à décomposer un précurseur métallique dans un solvant à haute température d'ébullition en présence d'un tensioactif. L'avantage de cette méthode est la séparation des phases de nucléation et de croissance des germes formées pendant la réaction. Ainsi, le contrôle de la température permet ainsi que la quantité des réactifs permet de modifier la taille et la morphologie des nanoparticules formées. Le stéarate de fer II est ainsi chauffé dans le dioctyléther avec de l'acide oléique en suivant une rampe en température contrôlée par un ordinateur. Plusieurs synthèses sont donc réalisées en modifiant les conditions opératoires pour obtenir des nanoparticules avec un diamètre de 5 nm, 10 nm et 20 nm.

Les synthèses sont ensuite purifiées pour retirer l'acide oléique libre en solution ainsi que les réactifs résiduels. La purification se fait par centrifugation en dispersant les nanoparticules dans un mélange de solvant. Les solvants utilisés sont le chloroforme, qui présente une forte affinité avec les nanoparticules, et l'acétone qui présente une meilleure affinité avec l'acide oléique. Ces étapes de purifications sont suivies par spectroscopie infrarouge (FT-IR) afin de visualiser la disparition des réactifs n'ayant pas réagi et de l'acide oléique libre en solution. Ainsi, après 22 lavages, les bandes vibrationnelles caractéristiques de l'acide oléique libre en solution (située à  $1710\text{ cm}^{-1}$ ) ont totalement disparues. De plus la proportion des bandes vibrationnelles correspondant aux chaînes alkylènes (à  $2920\text{ cm}^{-1}$ ,  $2850\text{ cm}^{-1}$  et  $720\text{ cm}^{-1}$ ) ont considérablement diminuées par rapport aux bandes vibrationnelles correspondant aux liaisons Fe-O de l'oxyde de fer (située entre  $500\text{ cm}^{-1}$  et  $800\text{ cm}^{-1}$ ).

La taille et la morphologie des nanoparticules est ensuite caractérisée par microscopie électronique à transmission. Les images TEM permettent d'observer des nanoparticules sphériques et homogènes en taille pour les trois différentes synthèses. Une mesure statistique est réalisée à l'aide du logiciel imageJ en comptant plus de 200 nanoparticules. La distribution en taille est ensuite fitter à l'aide d'une fonction de Gauss (figure 2). Les distributions en taille sont étroites pour les trois échantillons et sont centrées à  $5.1 \pm 0.8\text{ nm}$ ,  $10.1 \pm 1.1\text{ nm}$  et  $21.2 \pm 1.2\text{ nm}$  pour les nanoparticules qui seront appelées NP5, NP10 et NP20 respectivement.

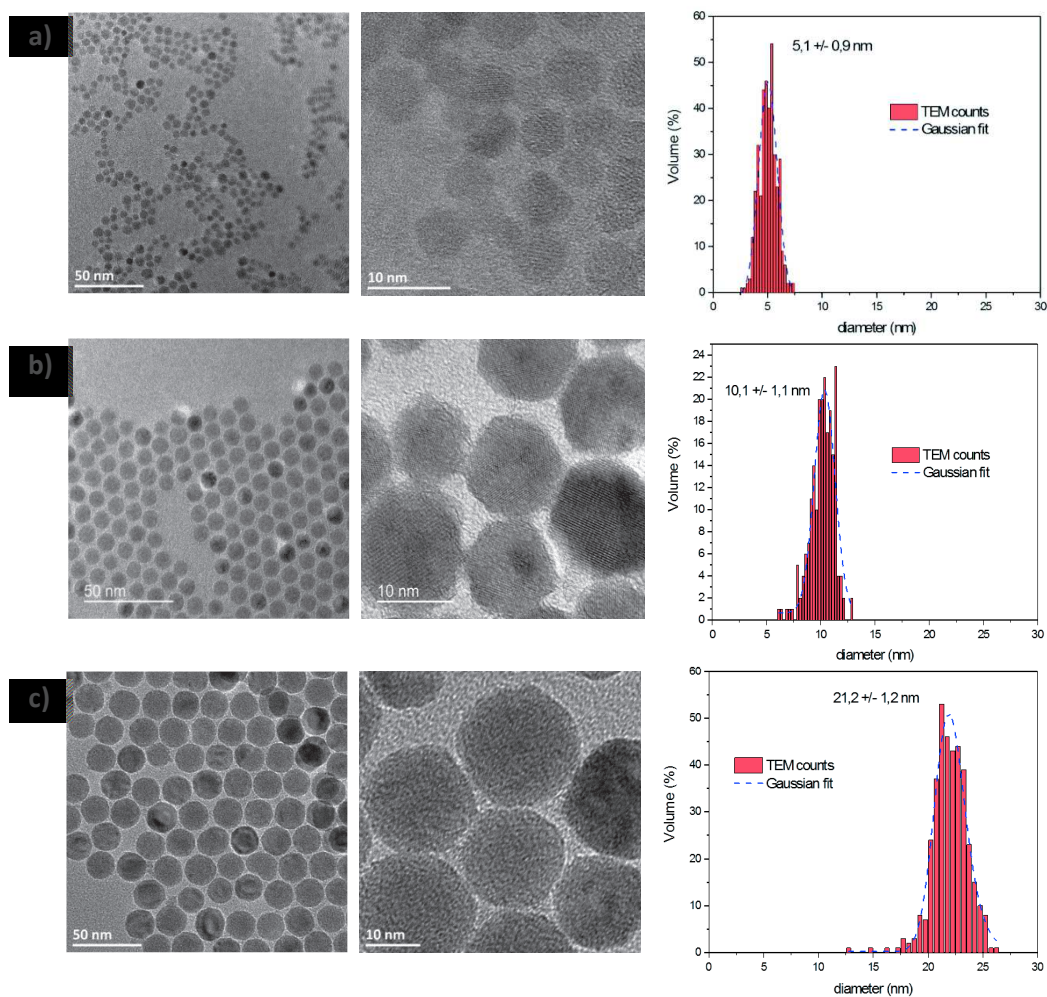


Figure 57. Images TEM des nanoparticules fonctionnalisées par l'acide oléique et la distribution en taille correspondantes. a) NP5, b) NP10 et c) NP20.

La stabilité colloïdale des nanoparticules est vérifiée par des mesures de granulométrie dans le tétrahydrofuran (THF). Les mesure par DLS sont monomodales avec un facteur de polydispersité faible ce qui indique une seule population de nanoparticules en suspension. Les diamètres hydrodynamiques mesurées sont de 8.7 nm, 12.5 nm et 23.8 nm pour les NP5, NP10 et NP20 respectivement. Le léger décalage de 2-3 nm qui peut être observé entre la mesure par TEM et par DLS est expliqué par la mesure du diamètre hydrodynamique dans le cas de la DLS qui inclut les molécules organiques en surface des nanoparticules ainsi que la sphère de solvatation. Dans les trois cas, les nanoparticules présentent une bonne stabilité colloïdale dans le THF.

Les nanoparticules sont également caractérisées par diffraction des rayons X (XRD) afin de déterminer les phases cristallines et leurs compositions. Les diffractogrammes obtenus pour les trois tailles de nanoparticules permettent d'identifier une structure spinelle. Un affinement de Rietveld permet de déterminer avec précision le paramètre de maille des oxydes de fer qui se situe entre les phases de la magnétite ( $8.396 \pm 0.001 \text{ \AA}$ , JCPDS file n°00-019-0629) et de la maghémite ( $8.338 \pm 0.001 \text{ \AA}$ , JCPDS file n°00-013-0458). Cette proportion est plus importante pour les NP5 et NP10, cela s'explique par la plus forte contribution de l'oxydation de surface pour les nanoparticules avec un faible diamètre.

Les propriétés magnétiques des trois tailles de nanoparticules sont ensuite étudiées en utilisant un magnétomètre SQUID. Des cycles d'aimantations mesurant l'aimantation d'un échantillon en fonction d'un champ magnétique appliqué sont réalisés à 300 K et à 5 K. Les cycles d'aimantation fermés à 300 K indiquent un comportement superparamagnétique des nanoparticules. A faible température, l'ouverture des cycles d'aimantation indiquent que les moments magnétiques sont bloqués. L'aimantation à saturation  $M_s$ , le champ coercitif  $H_c$  et le champ rémanent  $H_R$  peuvent être extraits des courbes d'aimantations et sont résumés dans le tableau 1.

**Tableau 1. Champs coercitifs, aimantations rémanentes et aimantations à saturation pour les différentes tailles de nanoparticules à 5K.**

Echantillon	$H_c$ (Oe)	$M_R/M_s$	$M_s$ (emu/g)
NP5	$240 \pm 30$	$0.36 \pm 0.05$	$55 \pm 5$
NP10	$495 \pm 30$	$0.35 \pm 0.05$	$55 \pm 5$
NP20	$330 \pm 30$	$0.16 \pm 0.05$	$75 \pm 5$

L'aimantation à saturation est inférieure à celle de la magnétite à l'état massif (92 emu/g) à cause de la présence d'une couche oxydée en surface des nanoparticules. En effet la maghémite présente une aimantation à saturation plus faible (74 emu/g), et la composition des nanoparticules avec un plus faible diamètre (NP5 et NP10) possédant une plus grande proportion de maghémite que les NP20, leurs aimantations à saturation est donc plus faible. De plus, des défauts à la surface pouvant entraîner un désordre magnétique (canting de spin) peut également diminuer l'aimantation à saturation.

Des mesures d'aimantations en fonction de la température sont ensuite réalisées. Les courbes obtenues passent par un maximum d'aimantation qui est assimilé à la température de blocage  $T_B$  des nanoparticules qui correspond au passage de l'état superparamagnétique à l'état ferromagnétique. Les valeurs de  $T_B$  sont de 20 K, 75 K et 185 K pour les NP5, NP10 et NP20 respectivement. L'augmentation de la température de blocage avec la taille des nanoparticules est attendu. En effet, l'augmentation du volume des nanoparticules augmente leurs énergies magnétocristalline, et l'énergie thermique nécessaire pour retourner les moments magnétiques va donc être plus importante.

### Fonctionnalisation des nanoparticules et du substrat

Pour pouvoir réaliser l'assemblage des nanoparticules sur des substrats au travers de la réaction de chimie « click », il est nécessaire de fonctionnaliser les nanoparticules et les substrats avec des molécules possédant les groupements complémentaires.

Les nanoparticules subissent donc un échange de ligand pour remplacer l'acide oléique en surface par une molécule portant un groupement azoture. Le 12-azido-dodecyl-phosphonic acid ( $AP_{12}N_3$ ) est utilisé, car la fonction acide phosphonique possède une interaction avec l'oxyde de fer plus forte que l'acide oléique. Il va donc spontanément le remplacer lors d'un échange direct de ligand dans le THF. L'échange se fait sous agitation pendant 16 heures. A la fin de l'échange de ligand, la suspension de nanoparticules est purifiée pour éliminer les molécules libres en solution. La purification

se fait par ultrafiltration qui consiste à filtrer la suspension colloïdale sur une membrane de cellulose (30 kDa). Les molécules libres vont ainsi passer à travers la membrane, tandis que les nanoparticules resteront en suspension. La purification est suivie par spectroscopie infrarouge et par granulométrie pour observer la disparition des molécules libres en solution ainsi que la stabilité des suspensions.

La caractérisation par spectroscopie infrarouge montre l'apparition de bandes vibrationnelles caractéristiques des acides phosphoniques entre  $900\text{ cm}^{-1}$  et  $1150\text{ cm}^{-1}$ . De plus, la bande caractéristique des azotures à  $2100\text{ cm}^{-1}$  peut être observée ce qui confirme le greffage des molécules d' $\text{AP}_{12}\text{N}_3$  à la surface des nanoparticules. La mesure DLS montre un diamètre hydrodynamique de 6.5 nm, 11.8 nm et 21.2 nm pour les NP5, NP10 et NP20 respectivement. La légère diminution du diamètre hydrodynamique correspond à la différence de longueur de chaîne entre la molécule  $\text{AP}_{12}\text{N}_3$  et l'acide oléique. Les nanoparticules sont donc correctement fonctionnalisées et présente une bonne stabilité en suspension après l'échange de ligand.

La seconde étape consiste à fonctionnaliser des substrats d'or avec les groupes complémentaires pour la réaction de chimie « click ». Des groupes azotures étant localisés à la surface des nanoparticules, des groupes alcynes doivent être greffés à la surface des substrats. L'utilisation d'une surface d'or permet la formation de monocouche auto-assemblés (SAM) en greffant des thiols. L'arrangement de dérivés thiolés avec des chaînes allyliques permet d'avoir les groupes terminaux accessibles à la surface de la SAM.

La SAM est formée en utilisant le 11-mercapto-undécyn préalablement synthétisé. Les substrats d'or sont nettoyés à l'aide d'un plasma d'oxygène et d'hydrogène pendant 2 minutes pour éliminer les éléments organiques à la surface. Les substrats sont ensuite immergés dans une solution éthanolique à 10 mM de 11-mercapto-undécyn. Les substrats restent dans la solution pendant 24 heures avant d'être rincés à l'éthanol.

Les substrats ainsi fonctionnalisés sont caractérisés par microscopie à force atomique (AFM) pour observer une augmentation de l'épaisseur à la surface correspondant à la présence d'une monocouche de molécules. Les substrats sont ensuite caractérisés par angle de contact (WCA) en déposant une goutte d'eau à la surface. L'angle de contact avant fonctionnalisation est de  $21.7^\circ$  ce qui correspond à la surface très hydrophile de l'or. Il passe à  $84.1^\circ$  après le greffage des thiols, ce qui correspond à une surface relativement hydrophobe causé par la présence des longues chaînes alkylées des thiols. La spectroscopie infrarouge en polarisation de phase (PM-IRRAS) permet de confirmer la présence des molécules à la surface du substrat avec la présence des bandes caractéristiques des groupes alcynes terminaux situés à  $3320\text{ cm}^{-1}$ .

### **Assemblage des nanoparticules par chimie « click »**

Les nanoparticules et les substrats d'or ayant été fonctionnalisés par les groupes complémentaires azotures et alcynes respectivement, l'assemblage des nanoparticules va pouvoir être réalisé. Les SAM sont rincés avec du THF avant d'être introduit dans une solution d'assemblage avec 5 mL de nanoparticules dans le THF, 0.5 mL de triéthylamine et 6.5 mg d'un catalyseur au cuivre ( $\text{CuBr}(\text{PPh}_3)_3$ ). La solution est chauffée à reflux à  $70^\circ\text{C}$  pendant 48 heures avec un réfrigérant sous argon. Une fois la réaction terminée, les substrats sont retirés, puis rincés au THF 1 minute dans un bain à ultrasons pour retirer les nanoparticules physisorbées à la surface.

Les assemblages sont caractérisés par microscopie électronique à balayage (SEM) afin de déterminer la couverture du substrat. Les images SEM permettent de déterminer la densité de nanoparticules à la surface et de la comparer à la densité théorique maximale obtenue dans le cas d'un empilement hexagonal compact (figure 3). Pour les trois tailles de nanoparticules on obtient un taux de couverture de  $13940 \text{ NPs}/\mu\text{m}^2$ ,  $5810 \text{ NPs}/\mu\text{m}^2$  et  $1820 \text{ NPs}/\mu\text{m}^2$  pour les NP5, NP10 et NP20 respectivement.

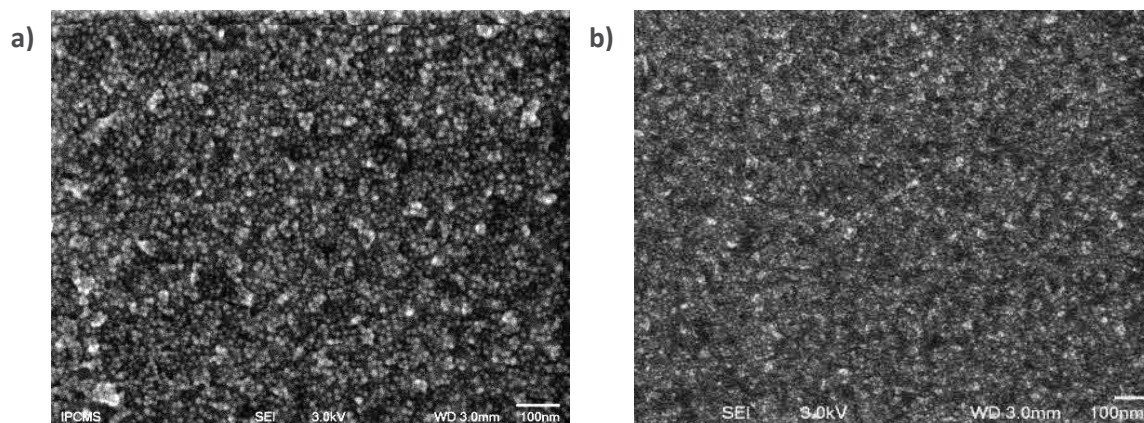


Figure 58. Images SEM des nanoparticules de 10 nm assemblées à la surface de la SAM aux grossissements a) X100000 et b) X50000.

Le contrôle de la structuration de l'assemblage peut se faire en jouant sur la cinétique de la réaction. En effet, des assemblages réalisés avec différents temps de réaction permettent de modifier la densité de nanoparticules à la surface des substrats. Ainsi, pour des temps de réaction courts (inférieur à 4 heures), des nanoparticules isolées sont observées sur la surface des substrats. Néanmoins, la vitesse de recouvrement dépend de la taille des nanoparticules. Dans le cas des NP20, la surface arrive à 80% de la densité théorique maximale après 4 heures de réaction, tandis que pour les NP10 il faut attendre 48 heures. Dans le cas des NP5, après 48 heures de réaction, la densité atteint seulement 40% de la densité théorique maximale. Cela peut s'expliquer par l'influence des interactions dipolaires magnétiques qui est plus importante pour les nanoparticules de 20 nm et qui peut diriger et accélérer l'assemblage.

Pour conclure cette partie, la synthèse par décomposition thermique permet la formation de nanoparticules d'oxyde de fer stable en solution avec un très bon contrôle de la taille et de la morphologie. Trois différentes tailles ont donc été synthétisées :  $5.1 \pm 0.8 \text{ nm}$ ,  $10.1 \pm 1.1 \text{ nm}$  et  $21.2 \pm 1.2 \text{ nm}$ . Les nanoparticules ont été fonctionnalisées avec un groupement azoture tandis que les substrats d'or ont été fonctionnalisés avec un groupement alcynes. L'assemblage des nanoparticules a ainsi pu être réalisé par la réaction de chimie « click ». La variation du temps de réaction a permis de contrôler la distribution spatiale des nanoparticules sur la surface d'or. L'étude de l'assemblage des différentes tailles de nanoparticules a montré l'influence des interactions dipolaires magnétiques sur leurs assemblages.

### Chapitre III – Auto-assemblage des nanoparticules au travers de liaisons hydrogène multiple entre des bases azotées

Dans cette seconde partie, l'assemblage des nanoparticules d'oxyde de fer sera étudié au travers de liaisons hydrogènes multiples. L'auto-assemblage via des liaisons faibles permet une géométrie plus flexible et dynamique que les liaisons covalentes. La stratégie repose sur la fonctionnalisation des nanoparticules et du substrat par des bases azotées complémentaires greffées par l'intermédiaire de la chimie « click ». Le processus de reconnaissance se base sur l'interaction Watson-Crick entre les bases azotées de l'ADN : adénine-thymine (AT). Les bases azotées sont modifiées avec des groupements azotures et alcynes pour pouvoir être greffées à la surface des nanoparticules recouvertes par des azotures et des SAMs alcynes (figure 4).

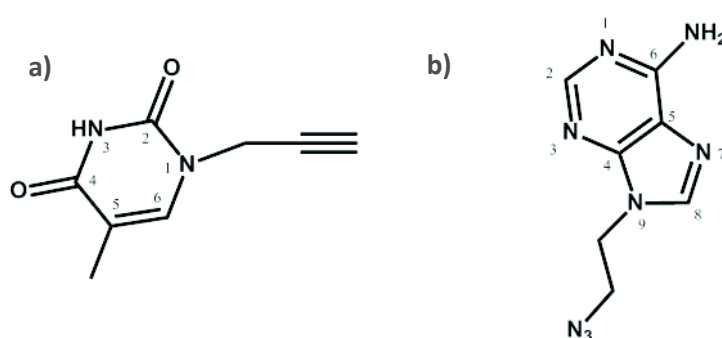


Figure 59. Représentation schématique de a) la thymine modifiée avec un alcyne et b) l'adénine modifiée avec un azoture.

La première étape consiste donc à fonctionnaliser le substrat d'or par l'adénine modifiée avec azoture. Pour cela, une SAM alcyne est immergé dans une solution d'assemblage contenant 10 mg d'adénine-azoture. La réaction se déroule sous irradiation micro-onde, ce qui permet de diminuer fortement le temps de réaction à 30 minutes. Les substrats sont ensuite rincés et séchés à l'air sec. La quantité d'adénine à la surface peut être modifiée en réalisant des SAM avec différentes quantités d'alcyne à leurs surfaces. Ainsi l'alcyne est « dilué » avec une autre molécule : le dodécane-thiol (DDT) ne possédant pas de groupes actifs pour la réaction de « click ». Des SAM avec différents ratio alcyne/DDT sont ainsi préparées : 0%, 20%, 50%, 80% et 100%.

Les SAMs modifiées avec l'adénine sont ensuite caractérisées. La mesure de l'angle de contact permet d'observer une diminution de l'hydrophobicité à la surface avec l'augmentation du ratio alcyne/DDT. Cela confirme une plus grande présence d'adénine, qui possède des groupements polaires et donc un comportement hydrophile, à la surface du substrat. Les SAMs sont caractérisées par spectroscopie des photo-électrons (XPS) et PM-IRRAS pour confirmer la présence de l'adénine à la surface. L'XPS présente un pic intense à 400 eV correspondant aux liaisons N-C et N-H contenus dans l'adénine. De plus, l'analyse par spectroscopie infrarouge présente deux bandes vibrationnelles à 1660  $\text{cm}^{-1}$  et 1580  $\text{cm}^{-1}$  qui correspondent aux bandes caractéristiques des liaisons N-C contenus dans l'adénine et qui confirme sont greffage à la surface de la SAM.

La seconde étape consiste à fonctionnaliser les nanoparticules terminées par un azoture avec la thymine modifiée avec un alcyne. De la même manière que pour les substrats, la thymine à la surface des nanoparticules est diluée avec une autre molécule ne présentant pas de groupes actifs pour la

réaction de « click » : le dodecylphosphonique acid (DPA). Les nanoparticules sont placées dans une solution d'assemblage avec la thymine et la réaction est réalisée sous irradiation micro-onde pendant 5 minutes. Les nanoparticules sont ensuite purifiées par ultrafiltration pour retirer les molécules libres en solution. Ainsi des nanoparticules avec différents ratios thymine/DPA sont obtenues : 20%, 50%, 80%, 100%.

La caractérisation des nanoparticules se fait par spectroscopie infrarouge dans un premier temps. L'apparition des bandes vibrationnelles caractéristiques de la thymine à  $1710\text{ cm}^{-1}$  et  $1660\text{ cm}^{-1}$  (correspondant aux liaisons C=O), ainsi que la disparition de la bande vibrationnelle de l'azoture, permet de confirmer le greffage de la thymine à la surface des nanoparticules. De plus l'analyse infrarouge des nanoparticules recouvertes par l'azoture et le DPA à différents ratios montre une évolution du ratio des bandes vibrationnelles  $\text{N}_3/\text{Fe-O}$  qui augmente avec le ratio azoture/DPA utilisé pour la fonctionnalisation. Cela confirme que la quantité d'azoture est contrôlé à la surface des nanoparticules.

Une mesure DLS est ensuite effectuée pour contrôler la stabilité des nanoparticules recouvertes par la thymine à 100%. La mesure DLS effectuée dans le THF indique un diamètre hydrodynamique centré vers 100 nm indiquant une agrégation des nanoparticules en suspension. Cependant, lorsque la mesure est réalisée dans le diméthylformamide (DMF), le diamètre hydrodynamique est centré à 12 nm indiquant que les nanoparticules ne présentent pas d'agrégation. Ainsi, le solvant joue un rôle prépondérant dans la stabilité des nanoparticules en suspension. Les nanoparticules entièrement recouvertes par la thymine présentent donc de nombreux groupements polaires à leurs surfaces qui sont capable de créer des liaisons hydrogènes avec des atomes électronégatifs. Lorsque ces nanoparticules sont en suspension dans un solvant apolaire ou à faible polarité, comme le THF, elles ne réaliseront pas de liaison avec le solvant et les liaisons formées seront des liaisons thymine-thymine qui permettra la formation d'un réseau de nanoparticules. En revanche, l'utilisation d'un solvant permettant les interactions entre la thymine et le solvant ne permettra pas la formation de ces liaisons thymine-thymine et les nanoparticules conserveront leurs stabilités, c'est le cas du DMF. Cette agrégation contrôlée est parfaitement réversible, de plus, en fonction de la quantité de thymine à la surface des nanoparticules, le solvant permettant une meilleure stabilité va varier. Ainsi, les nanoparticules possédant des ratios thymine/DPA de 100%, 80% et 50% sont stable dans le DMF, tandis que les nanoparticules recouvertes à 20% sont stables dans le chloroforme ( $\text{CHCl}_3$ ).

La surface des nanoparticules et des substrats étant fonctionnalisées par les bases azotées complémentaires, l'assemblage par reconnaissance moléculaire peut être réalisé. Le processus d'assemblage consiste à immerger les substrats fonctionnalisés dans une suspension de nanoparticules à température ambiante. Les substrats sont ensuite retirés de la solution puis rincés au DMF et exposé 15 secondes au bain à ultrasons. Des tests préliminaires ont été effectués avec différents temps d'immersions pour réaliser que le temps d'immersion idéal est de 30 minutes.

L'influence de la quantité de groupes à la surface des nanoparticules et des substrats est étudiée en réalisant différents assemblages en variant la quantité d'adénine à la surface des SAMs et la quantité de thymine à la surface des nanoparticules. Malgré une densité faible observé en SEM pour l'ensemble des échantillons, le meilleur taux de couverture est celui réalisé avec une SAM-adénine à 80% immergée dans une suspension de nanoparticules recouvertes de thymine à 50%. Ainsi, ces conditions sont utilisées pour le reste de l'étude pour limiter le  $\pi$ -stacking qui pourrait réduire la force des interactions des liaisons hydrogènes.

Le second facteur qui est étudié est le solvant, puisqu'il intervient dans la stabilité des nanoparticules. Les assemblages ont été réalisés avec des mélange de solvants à différentes polarités.

Ainsi les substrats 80% ont été immergés dans des suspensions de nanoparticules recouvertes à 50% dans un mélange DMF/CHCl<sub>3</sub> avec différents ratios : [4 :1], [1 :1] et [1 :4]. Les images SEM (figure 5) de ces assemblages montrent une densité de nanoparticules de 20% dans le cas des ratios [4 :1] et [1 :4], alors qu'une densité de 53% est observée dans le cas du ratio [1 :1]. Ces résultats peuvent être reliés à la stabilité en suspension des nanoparticules pour ces différents ratios. Dans le cas du ratio [4:1], les nanoparticules sont parfaitement stables avec un diamètre hydrodynamique centré à 12.6 nm. Dans le cas du ratio [1 :4] les nanoparticules sont complètement agrégées avec un diamètre hydrodynamique supérieur à 1 µm. Tandis que pour le ratio [1 :1], les nanoparticules sont plutôt stables, mais présentent un début d'agrégation avec un diamètre hydrodynamique de 21.3 nm. Cette étude permet de conclure sur l'énergie d'interactions entre les bases azotées et le solvant. En effet, le solvant peut rentrer en compétition avec la formation des liaisons entre l'adénine et la thymine. Cela explique le faible taux de couverture dans le cas du ratio avec un grand volume de DMF [4 :1] qui empêche la reconnaissance entre les bases complémentaires et favorise les liaisons avec le solvant. Au contraire, un ratio faible en DMF [1 :4] va favoriser cette reconnaissance, néanmoins les nanoparticules se retrouvent agrégées dans ce cas et ne seront pas disponibles pour l'assemblage, ce qui explique également le faible taux de couverture. Ainsi, la densité maximale est obtenue en trouvant un équilibre entre les énergies d'interactions de la thymine avec le solvant et l'adénine pour un ratio DMF/CHCl<sub>3</sub> [1 :1].

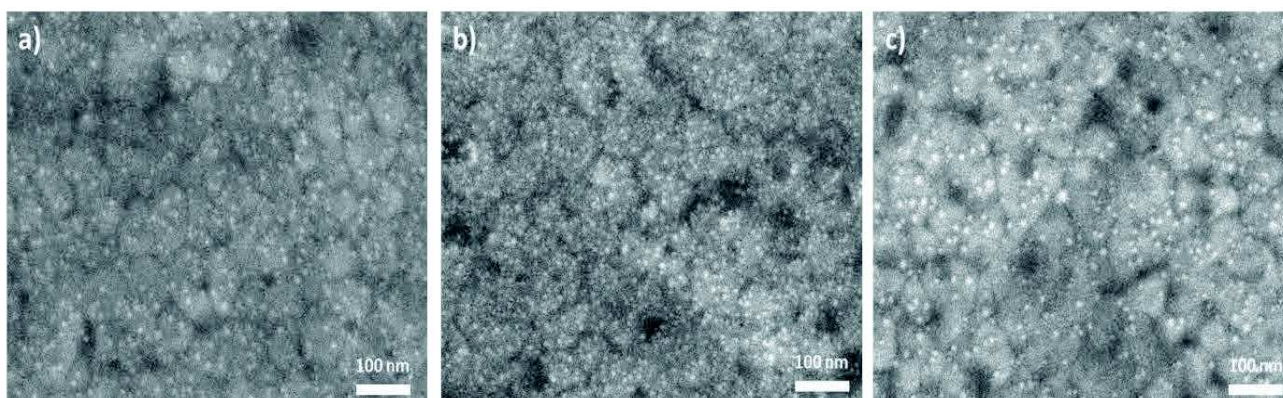


Figure 60. Images SEM de l'assemblage des nanoparticules fonctionnalisées par la thymine à 50% sur une SAM fonctionnalisée par de l'adénine à 80% avec différents ratios DMF/CHCl<sub>3</sub>. a) [4:1], b) [1:1] et c) [1:4].

Le dernier facteur étudié qui influence la reconnaissance des bases azotées est la température. Ainsi, un assemblage réalisé dans les conditions optimales (avec un taux de couverture de 57%) est placé dans le DMF et chauffé à 80°C pendant 2 heures. Les images SEM montrent une diminution de la densité qui passe à 18% de la densité théorique maximale. En effet l'énergie thermique permet de briser les liaisons hydrogènes et donc de désorber les nanoparticules à la surface du substrat.

Pour conclure cette partie, en tirant avantage de la méthode de chimie « click », les nanoparticules et les substrats ont pu être fonctionnalisés par des bases azotées complémentaires. L'utilisation du micro-onde a grandement réduit le temps de réaction de plusieurs heures à quelques minutes. L'assemblage des nanoparticules a pu être réalisé et être étudié en fonction de plusieurs paramètres tel que le  $\pi$ -stacking, le solvant et la température. De plus, le contrôle de la distribution spatiale des nanoparticules est effectué en contrôlant ces différents paramètres.

## Chapitre IV – Reconnaissance biomoléculaires au travers de l’assemblage de nanoparticules d’oxyde de fer déposées sur des films d’or

Dans cette dernière partie, l’assemblage des nanoparticules va être utilisé pour élaborer une plateforme de détection basé sur la résonance plasmon du substrat d’or (figure 6).

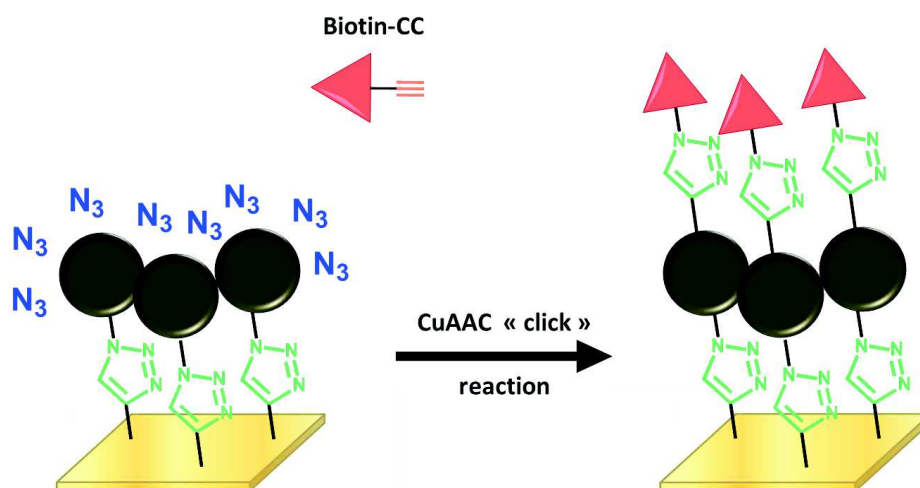


Figure 61. Représentation schématique du greffage d'un bio récepteur modifié avec un alcyne sur la surface de l'assemblage de nanoparticules fonctionnalisées avec un azoture.

En utilisant la réaction de « click » pour moduler la structuration de l’assemblage, les propriétés du substrat peuvent être modulés. De plus, les nanoparticules assemblées possèdent toujours un groupement azoture en surface qui va pouvoir être utilisé pour greffer une molécule réceptrice nécessaire pour la détection. Deux couples récepteur/analyte ont été étudié dans ce manuscrit : biotine-streptavidine et iminosucre- $\alpha$ -mannosidase.

### **Biotine-Streptavidine**

Pour élaborer une bio-plateforme la biotine doit être greffée à la surface de l’assemblage de nanoparticules. Une biotine modifiée avec un groupement alcyne est donc synthétiser (biotin-CC). La biotin-CC est greffer à la surface des nanoparticules de la même manière que les nanoparticules ont été assemblées sur la surface d’or. Le substrat est immergé dans une solution d’assemblage avec 5 mg de biotin-CC et est chauffé à reflux pendant 24 heures. L’échantillon est caractérisé par microscopie pour s’assurer que le greffage de la biotine n’ait pas perturbé l’assemblage de nanoparticules. Les images SEM et AFM montrent en effet que la densité reste inchangée et que les nanoparticules sont toujours homogènement distribuées sur la surface du substrat. La mesure de l’angle de contact avant et après greffage de la biotine montre un brusque changement d’hydrophobicité de la surface qui passe d’une surface hydrophobe ( $100^\circ$ ) due à la présence des longues chaînes alkylènes de l’acide phosphonique, à une surface plus hydrophile ( $50^\circ$ ) expliqué par la présence de la biotine et des groupes polaires contenus dans sa structure. L’analyse XPS permet de montrer la disparition des groupements azotures à la surface des nanoparticules avec la disparition des contributions des liaisons  $N_3$  à 405.3

eV et 401.8 eV pour laisser place à deux contributions à 400.8 eV et 400.5 eV qui correspondent aux liaisons N-C et N-H présentes dans la biotine. De plus une nouvelle contribution apparaît à 287.4 eV qui correspond aux liaisons C=O présente dans le groupement amide de la biotine. L'analyse PM-IRRAS permet de confirmer le remplacement total de l'azoture par la biotine avec la disparition de la bande vibrationnelle caractéristique des azotures à  $2100\text{ cm}^{-1}$  et l'apparition d'une bande large à  $1660\text{ cm}^{-1}$  qui correspond aux liaisons C=O des groupements amides.

Le signal plasmon du substrat d'or étant très sensible aux variations d'indice de réfraction à sa surface, la construction des différentes étapes de la bio-plateforme peut être suivi par mesure SPR. Le tableau 2 résume la position du pic de résonance plasmon pour deux différentes longueurs d'onde pour chaque étape de la construction de la bio-plateforme.

**Tableau 2. Position angulaire des pics de résonance plasmon pour chaque étape de l'élaboration de la plateforme de détection pour deux longueurs d'onde de travail.**

Wavelength	Au	SAM	NPs@N <sub>3</sub>	Biotin
670 nm	68.627°	69.260°	74.029°	72.845°
785 nm	65.598°	65.960°	68.410°	67.832°

Après chaque étape, un shift vers grand angle est observé ce qui confirme le dépôt d'une couche à la surface du substrat. Cependant pour le greffage de la biotine, un shift vers les faibles angles est observé. Ce shift inattendu est le résultat de la désorption des nanoparticules greffées de façon non covalente lors de l'étape de greffage de la biotine.

Pour étudier l'efficacité de la bio-plateforme de détection, l'adsorption de la streptavidine est étudié en fonction de différents paramètres comme la densité de nanoparticules, la taille des nanoparticules et la quantité de biotine. Deux configurations ont été utilisés pour étudier les propriétés SPR : une interrogation spectrale à angle constant (74°) et une interrogation angulaire à longueur d'onde fixe (785 nm). Le protocole de détection se fait en injectant une solution aqueuse de streptavidine à 100 µg/mL sur la surface du substrat.

L'influence des nanoparticules est étudiée en réalisant l'adsorption de la streptavidine sur un substrat avec et sans nanoparticules recouvert de biotine (figure 7).

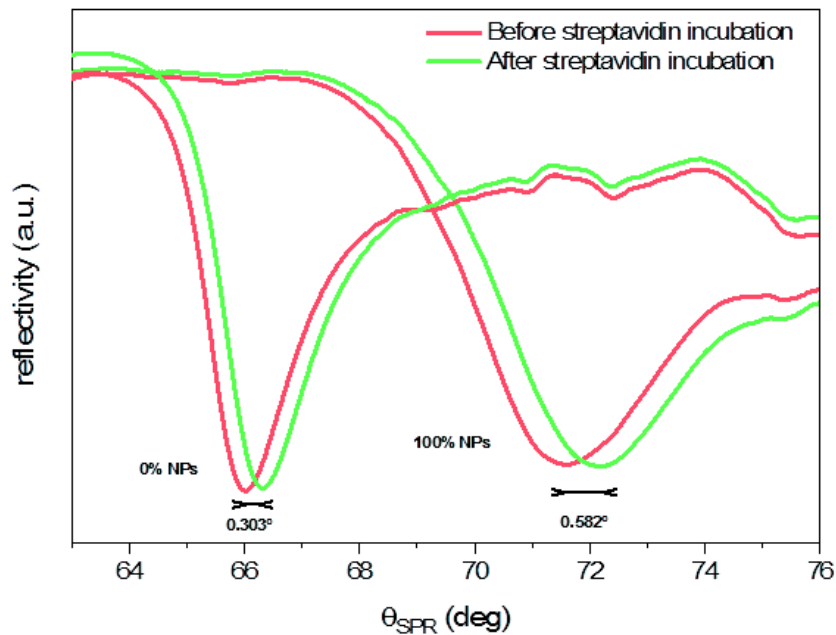


Figure 62. Mesures SPR à 785 nm avant (rouge) et après (vert) adsorption de la streptavidine sur un film mince sans nanoparticules et avec nanoparticules d'oxyde de fer.

Le pic de résonance est décalé de  $0.303^\circ$  dans le cas d'une surface sans nanoparticules et  $0.582^\circ$  dans le cas d'une surface recouverte à 100% de nanoparticules. Le même phénomène se produit avec une interrogation spectrale où l'augmentation du signal est exacerbée avec un décalage lors de la détection de la streptavidine de 3 nm pour une surface sans nanoparticules et 41 nm pour une surface recouverte de nanoparticules. Il convient donc de comprendre le rôle des nanoparticules sur l'augmentation de la sensibilité de détection, pour cela il faut découpler l'origine de l'évolution du signal qui provient des propriétés intrinsèques optiques du capteur et les propriétés de chimie de surface qu'apporte les nanoparticules.

La réponse du signal SPR est donné par la formule suivante :

$$R = m \cdot \Delta n \cdot \left[ 1 - e^{-\frac{2d}{l_d}} \right]$$

La réponse du capteur dépend directement de la variation d'indice de réfraction  $\Delta n$ , mais également des paramètres optiques  $m$  et  $l_d$  qui sont le facteur de sensibilité et la longueur de pénétration respectivement. La valeur de  $l_d$  ne varie quasiment pas avec la présence des nanoparticules, en revanche, le facteur  $m$  lui augmente avec la présence des nanoparticules. La mesure de la sensibilité en fonction de l'angle d'incidence permet de calculer  $m$  avec et sans nanoparticules. La sensibilité augmente légèrement avec la présence des nanoparticules en passant de  $105,4^\circ/\text{RIU}$  à  $115,7^\circ/\text{RIU}$ . Néanmoins la valeur de  $m$  augmente significativement lors de l'interrogation spectrale, car la sensibilité est directement liée à la longueur d'onde incidente. La présence des nanoparticules va décaler le pic de résonance vers les hautes longueurs d'ondes et passera de  $1580 \text{ nm}/\text{RIU}$  à  $5600 \text{ nm}/\text{RIU}$ .

La présence des nanoparticules augmente donc la sensibilité du capteur en modifiant les propriétés optiques intrinsèques de la surface d'or. Cependant, la présence des nanoparticules modifie également la chimie de surface et peut modifier le nombre de groupements et leurs accessibilités pour

la détection de la streptavidine. Le nombre de streptavidine que la surface peut détecter peut être estimé de façon géométrique en fonction de la taille de la protéine de streptavidine et de la surface des nanoparticules accessible. Le nombre de streptavidine détecté dépend ainsi du diamètre des nanoparticules et la distance inter-particules. Une étude a ainsi été menée pour optimiser la plateforme de détection en faisant varier la taille et la densité des nanoparticules à la surface du substrat.

Des échantillons ont donc été réalisés, le diamètre et la densité des nanoparticules à la surface est résumé dans le tableau 3. Trois tailles différentes sont considérées 5.7 nm, 10.1 nm et 21.9 nm qui seront appelées NP6, NP10 et NP22 respectivement.

**Tableau 3. Diamètres et densités des nanoparticules assemblées sur la surface de la SAM.**

	Diameter (nm)	Density (%)
a)	<b>5.7 ± 0.9 nm</b>	<b>18%</b>
b)	<b>21.9 ± 1.6 nm</b>	<b>100%</b>
c)	<b>5.7 ± 0.9 nm</b>	<b>36%</b>
d)	<b>21.9 ± 1.6 nm</b>	<b>26%</b>
e)	<b>10.1 ± 1.1 nm</b>	<b>47%</b>

Ces échantillons sont soumis à une injection de streptavidine et le décalage spectral est mesuré après l'injection. Dans le cas des NP6, le décalage est de 11 nm pour une densité de 18% et 27 nm dans le cas d'une densité de 36%. Pour ces deux densités, la distance inter-particules est très importante et permet l'adsorption d'un maximum de streptavidine (7.5 streptavidine par nanoparticules). De plus le facteur de sensibilité  $m$  est quasiment le même (2115 nm/RIU et 2220 nm/RIU). La seule différence réside dans le nombre de nanoparticules qui est doublé à la surface et donc permet d'adsorber deux fois plus de streptavidine. Dans le cas des NP22, les décalages sont de 42 nm pour une densité de 26% et 53 nm pour une densité de 100%. Ici le facteur de sensibilité est nettement plus important pour l'échantillon recouvert à 100% (8070 nm/RIU par rapport à 2460 nm/RIU). Cependant la détection de streptavidine reste importante malgré le faible facteur de sensibilité. La distance inter-particule est plus élevée dans le cas d'une densité plus faible et permet la détection de 52 streptavidine par nanoparticule pour la densité de 26% et seulement 20 streptavidine par nanoparticule pour la densité de 100%. Ainsi le nombre de streptavidine adsorbé est plus important dans le cas d'une faible densité présentant une distance inter-particules élevée.

Une étude a également été menée pour déterminer l'influence de la quantité de biotine à la surface des nanoparticules. Le greffage de la biotine a donc été diluée avec une autre molécule : l'hex-1-yne. Des ratios biotin/hex-1-yne de 5%, 20%, 50%, 80% et 100% ont été réalisés. Après adsorption de la streptavidine, le décalage spectral est similaire pour chacun des échantillons (25-27 nm). Ainsi, même avec uniquement 5% de biotine à la surface des nanoparticules, la streptavidine est détectée. Cela s'explique par l'augmentation de l'accessibilité à la surface des nanoparticules due à leurs rayons de courbure.

Pour conclure, la sensibilité du facteur est augmentée par les propriétés optiques du substrat qui sont modifiés par l'assemblage des nanoparticules, mais aussi par la quantité et l'accessibilité de la streptavidine sur la surface du capteur.

Les mesures SPR permettent également, en étudiant les cinétiques d'adsorption, de déterminer les processus de reconnaissances tel que les constantes d'association des couples

molécules réceptrices/analytes. Le sensorgramme décrit la mesure de la réponse du capteur en fonction du temps. Il est utilisé pour déterminer les phases d'association, d'équilibre et de dissociation des couples étudiés. Une étude a été réalisée en injectant une solution aqueuse de streptavidine à différentes concentrations à la surface d'un substrat avec et sans nanoparticules couvert de biotine. La valeur des pentes lors de la phase d'association ainsi que la valeur des décalages angulaires en fonction de la concentration sont relevées. La constante d'association  $K_A$  est déterminée de deux manières distinctes en se basant sur la cinétique de réaction et en déterminer la constante effective d'association et de dissociation, respectivement  $k_{on}$  et  $k_{off}$  (avec  $K_A = k_{on}/k_{off}$ ) et en se basant sur la réponse angulaire en utilisant l'isotherme de Langmuir.

$$k_{obs} = k_{on}[C] + k_{off}$$

$$R_{eq} = \frac{[C]}{[C] + K_D} R_{max}$$

Ces deux méthodes nous permettent de trouver des valeurs de  $K_A$  similaires pour la surface recouvertes de nanoparticules et celles sans nanoparticules ( $K_A = 10^{-6}$ - $10^{-7}$ ).

Pour compléter l'étude des contre-tests visant à prouver l'interaction spécifique de la streptavidine sur la surface du substrat ont été réalisés. Ainsi la streptavidine a été injecté sur une surface de nanoparticules ne possédant pas de groupements biotine ainsi que le test complémentaire avec l'injection d'une protéine non spécifique, l'albumine sérique bovine (BSA), sur une surface de nanoparticules recouverte de biotine. Les deux expériences ont montré un décalage angulaire indiquant l'adsorption de la streptavidine. Cependant, la valeur de ces décalages ainsi que la cinétique d'adsorption est plus faible que dans le cas de la reconnaissance entre biotine et streptavidine.

### Iminosucre- $\alpha$ -mannosidase

La même étude a été réalisé en utilisant un couple iminosucre et une glycosidase, l' $\alpha$ -mannosidase, qui est une enzyme impliquée dans le traitement de certaines maladies (maladie de Gaucher, mucoviscidose). La surface de nanoparticules a donc été fonctionnalisées avec un iminosucre modifié avec un groupement alcyne, puis caractérisées avec les différentes techniques d'analyses pour confirmer la présence de l'iminosucre à la surface du substrat.

L' $\alpha$ -mannosidase est une enzyme qui possède deux sites actifs et par conséquent peut former différents types d'accroche avec les iminosucres localisés à la surface des nanoparticules (figure 8). Une configuration existe pour laquelle les deux sites actifs sont inhibés par les sucres et une autre pour laquelle un seul site actif est inhibé laissant le second libre à la surface.

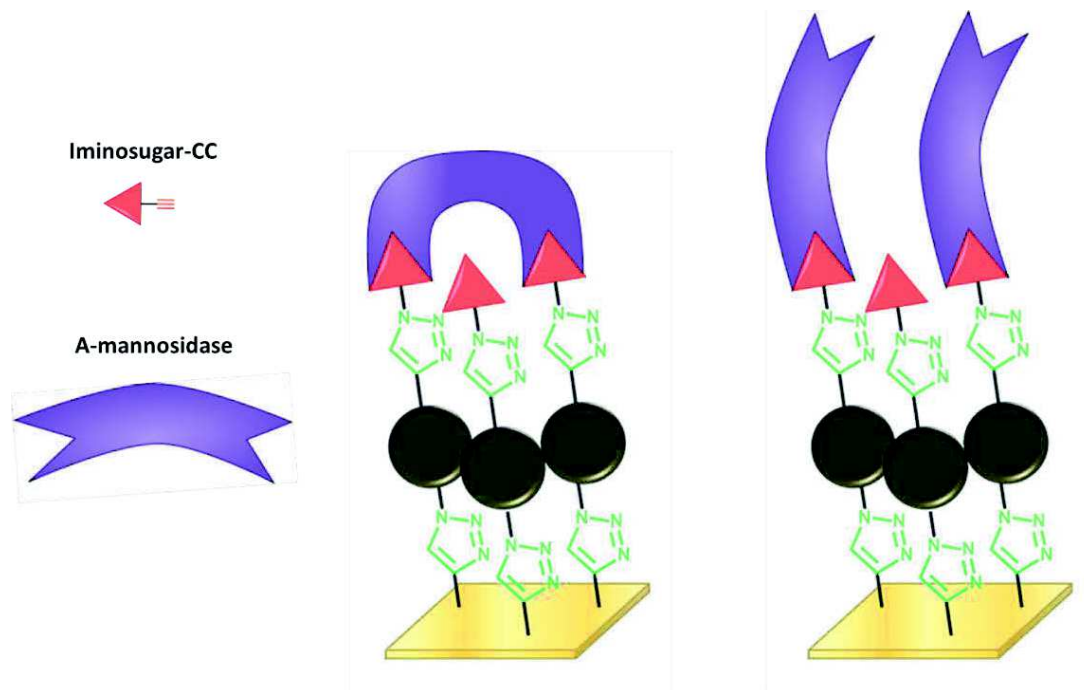


Figure 63. Représentation schématique de deux configurations possibles pour l'adsorption de l' $\alpha$ -mannosidase à la surface des nanoparticules.

La détection de la glycosidase est effectuée en injectant une solution d' $\alpha$ -mannosidase sur la surface du substrat. L'adsorption de l'enzyme est suivie par un sensorgramme qui mesure en temps réel l'angle de résonance. De la même façon que pour la streptavidine, l'enzyme est injectée à différentes concentrations afin de déterminer les constantes d'association sur une surface avec et sans nanoparticules.

Les résultats dans le cas de l' $\alpha$ -mannosidase sont différents de ceux observés avec la streptavidine. En effet, la constante d'association dans le cas d'une surface avec nanoparticules est deux fois plus importante que dans le cas d'une surface plane ( $5,26 \cdot 10^7 \text{ M}^{-1}$  et  $2,37 \cdot 10^7 \text{ M}^{-1}$  respectivement). Cela signifie que la présence des nanoparticules favorise l'adsorption de l'enzyme sur la surface. Le processus impliqué dans cette adsorption n'est pas connu, mais la géométrie d'une surface recouverte de sphères semble accélérer l'accroche de l'enzyme. De plus, les valeurs des constantes d'associations ont été comparées aux études réalisées en solutions sur des couplages multivalents entre l'enzyme et l'iminosucre et l'interaction semble plus forte dans le cas où l'enzyme est immobilisée sur la surface.

D'autre part, une étude a été réalisée en injectant un substrat compétitif pour l'inhibition de l'enzyme, le methyl  $\alpha$ -D-mannopyranoside à 10 mM, après l'injection de l' $\alpha$ -mannosidase. Un décalage de l'angle de résonance plasmon est observé après rinçage, ce qui implique que le substrat s'est déposé sur la surface. L'absence de diminution de l'angle de résonance après injection du sucre compétitif indique qu'il n'a pas désorbé l'enzyme de la surface et donc que l'association entre l' $\alpha$ -mannosidase et l'iminosucre est trop forte. Cependant, le faible décalage de l'angle de résonance indiquant l'adsorption du substrat permet de confirmer qu'il reste des sites actifs de l'enzyme disponible à la surface. Ceci permet de conclure sur les configurations possibles de l' $\alpha$ -mannosidase à la surface des nanoparticules en admettant que celle-ci se greffe en laissant des sites actifs disponibles.

Une étude a également été réalisée pour tenter de régénérer la surface du capteur en désorbant l'enzyme. Pour cela une solution d'acide phosphorique est injectée après l'adsorption de l'enzyme dans le but de pouvoir casser les liaisons avec le sucre. Une solution aqueuse d'acide phosphorique à 0,02 M et à pH 2,5 est donc injecté sur un substrat non recouvert de nanoparticules. Après injection de la solution acide, la position de l'angle de résonance plasmon retrouve sa valeur initiale avant injection de l' $\alpha$ -mannosidase. De plus, une injection de l'enzyme avec la même concentration effectuée par la suite donne une variation de l'angle de résonance identique à la première, ce qui indique que la reconnaissance à la surface peut se faire. Cela indiquerait que le capteur est régénérable en pouvant désorber l'enzyme et laisser la surface active pour une reconnaissance par la suite. L'expérience a également été réalisée avec un substrat recouvert de nanoparticules. Cependant, la valeur de l'angle de résonance est descendue en dessous de sa valeur initiale impliquant la disparition de matériau à la surface. En effet, les nanoparticules d'oxyde de fer sont sensibles aux pH trop acides, et la solution d'acide phosphorique a détérioré la qualité de la surface.

Enfin, une étude sur la reconnaissance spécifique a été réalisée de la même manière que pour la streptavidine en injectant sur une surface de nanoparticules sans iminosucres l' $\alpha$ -mannosidase et en injectant sur une surface de nanoparticules fonctionnalisées par l'iminosucre, une enzyme non spécifique à la reconnaissance, la BSA. Les résultats sont similaires à l'étude précédente avec une réponse du capteur avec des décalage angulaire et des vitesses d'association différentes que pour le couple iminosucre/glycosidase.

Pour conclure, l'assemblage des nanoparticules constitue une plateforme de détection de biomolécules qui peut être facilement fonctionnalisée avec différentes molécules réceptrices pour permettre la reconnaissance d'une analyte. La sensibilité de ce capteur a été étudiée avec et sans nanoparticules pour s'apercevoir que ces dernières ont un rôle prépondérant dans la sensibilité de la détection. Tout d'abord d'un point de vue optique, puisqu'elles modulent le plasmon de surface du substrat sur lequel elles reposent, mais aussi d'un point de vue géométrique où la rugosité qu'elles induisent permet de détecter un plus grand nombre de biomolécules. De plus, les mesures SPR permettent de suivre l'adsorption de protéine ou d'enzyme en temps réel, ce qui a permis de définir les constantes d'association pour les couples biotin/streptavidine et iminosucre/ $\alpha$ -mannosidase. Malgré la reconnaissance spécifique qui nécessite des expériences complémentaires, la plateforme a montré qu'elle pouvait être régénérable avec une solution acide. Le système est donc prometteur mais nécessite une optimisation et des caractérisations supplémentaires.

## Conclusion générale

Le but de ce travail était de contrôler la structuration de l'assemblage de nanoparticules pour contrôler les propriétés magnétiques collectives et individuelles de ces objets ainsi que leurs influences sur les propriétés plasmoniques portées par le substrat sur lequel elles reposent. L'assemblage a été réalisé au travers d'interactions moléculaires spécifiques.

La décomposition thermique a permis, en contrôlant les conditions opératoires, de synthétiser des nanoparticules d'oxyde de fer de différentes tailles. La caractérisation structurale a permis d'identifier un cœur de magnétite avec une coquille de maghémite. Les propriétés magnétiques ont montré que la température de blocage augmentait avec le diamètre des nanoparticules. Par la suite, les nanoparticules ont été fonctionnalisées avec des groupements spécifiques pour la réaction de chimie « click ». Des substrats d'or ont également été fonctionnalisés avec les groupements spécifiques complémentaires. L'assemblage a été réalisé par la réaction de chimie « click » et les conditions d'assemblage ont été étudiées. La variation du temps de réaction a permis de contrôler la distribution spatiale des nanoparticules sur le substrat d'or. Les interactions dipolaires magnétiques entre les nanoparticules a ainsi pu être contrôlées et les propriétés magnétiques des films ont été étudiées. Il a été montré que l'assemblage est dirigé en partie par ces interactions dipolaires notamment dans le cas de nanoparticules avec un diamètre supérieur à 10 nm.

Une nouvelle stratégie d'assemblage a été reportée qui est basée sur la reconnaissance spécifique entre des bases azotées. En prenant avantage de la réaction de chimie « click », les nanoparticules et les substrats ont été fonctionnalisés avec des molécules de thymine et d'adénine. De plus, l'utilisation de l'énergie micro-onde a permis de diminuer drastiquement le temps de réaction. Le contrôle de la distribution spatiale des nanoparticules a été démontré en utilisant les différents paramètres lors de la reconnaissance. Ainsi, le solvant, la température et la quantité de groupements fonctionnels à la surface des nanoparticules et du substrats a été étudiés.

La dernière partie de ce travail a été d'utiliser ces assemblages de nanoparticules pour pouvoir contrôler les propriétés plasmoniques des substrats d'or sur lesquelles elles ont été déposées. Une « bio-plateforme » est ainsi réalisé en greffant des molécules réceptrices à la surface des films de nanoparticules. La détection de la streptavidine ainsi que de l' $\alpha$ -mannosidase a été réalisée et l'augmentation de la sensibilité avec la présence des nanoparticules a été démontrée. Les nanoparticules modulent les propriétés optiques intrinsèques du substrat et donne une meilleure accessibilité aux molécules cibles. De plus, l'utilisation de mesure SPR a permis d'étudier les processus de reconnaissance entre les couples étudiés pour déterminer leurs constantes d'association.

## Design of magnetic iron oxide nanoparticle assemblies supported onto gold thin films for SPR biosensor applications

### Résumé

La bio-détection de molécules reposant sur le phénomène de résonance plasmon permet de détecter des espèces en utilisant les propriétés optiques de films métalliques. L'utilisation de ce type de capteurs nécessite néanmoins l'augmentation de leurs performances afin de détecter des concentrations faibles d'analyte dans des milieux complexes. L'assemblage de nanoparticules d'oxyde de fer sur des substrats d'or, en utilisant des groupements complémentaires spécifiques via la méthode de chimie « click », permet de contrôler leur distribution spatiale à la surface du substrat. Les propriétés magnétiques portées par les nanoparticules sont ainsi étudiées en fonction de leurs distances inter-particules ainsi que de leurs tailles. Par ailleurs, le plasmon de surface du substrat étant directement influencé par l'assemblage des nanoparticules, il sera possible de contrôler la sensibilité du capteur pour étudier la détection de différentes biomolécules impliquées dans des processus biologiques. La présence des nanoparticules augmente les propriétés optiques intrinsèques de la surface du substrat et la géométrie de l'assemblage permet d'augmenter la quantité de biomolécules détectées.

**Mots-clés :** Nanoparticules, Biocapteurs, Plasmon de Surface, Magnétisme, Fonctionnalisation de surface, Détection Moléculaire, Biomolécules.

### Résumé en anglais

Biomolecular detection based on the surface plasmon resonance phenomenon allow detecting species by using the optics properties of metallic thin films. This kind of biosensors require the increase of their performances in order to detect low concentration analyte in complex medium. The assembly of iron oxide nanoparticles on gold substrates by using specific complementary groups via the "click" chemistry technique allows controlling their spatial distribution on the substrate surface. The magnetic properties carried by the nanoparticles are studied as function of their inter-particle distances and their sizes. Moreover, the surface plasmon of the substrate is directly influenced by the nanoparticle assembly and the control of the sensor sensitivity will be possible in order to study the detection of different biomolecules implies in biological processes. The presence of nanoparticles increases the intrinsic optical properties at the substrate surface and the geometry of the assembly allow increasing the number of biomolecules detected.

**Key-words :** Nanoparticles, Biosensors, Surface Plasmon, Magnetism, Surface Functionalization, Molecular Recognition, Biomolecules.